An Experimental Study of Model Two-Dimensional Antiferromagnets

Fiona C. Coomer

MA(Cantab) MSci AMRSC

A thesis presented for the degree of Doctor of Philosophy

The University of Edinburgh

2006

Declaration

I hereby declare that this thesis is of my own composition. It is all my own work, unless otherwise stated, carried out at the University of Edinburgh between October 2002 and July 2006. It has not been submitted for any other degree or professional qualification.

Fiona C. Coomer

Abstract

There is a need to design and synthesise magnetic materials that can be used as models to test our understanding of fundamental magnetic phenomena. Particularly important areas of current interest include the study of systems that model aspects of the magnetic behaviour of the high-T_c superconductors (low-spin Heisenberg antiferromagnets on a square lattice) and of highly frustrated magnetic systems. A family of layered copper salts, $(5CAP)_2CuX_4$, (5CAP = 5-chloro-2-aminopyridine, X = Cl, Br) is a promising model system for the former class of magnet. The ordered magnetic structure of this system has been studied by neutron diffraction, along with (H, T) phase data and appears classical in character; this picture is confirmed by MuSR data, in addition, inelastic neutron scattering gives an indication of the three dimensional nature of the exchange in this system. The jarosite family of minerals, containing kagome lattices of metal ions, commonly Fe^{3+}, are physical realisations of highly frustrated antiferromagnets. The excitation spectra of these materials have been studied using time of flight inelastic neutron scattering. Hydronium iron jarosite appears to behave as a spin liquid to 2 K despite strong antiferromagnetic coupling between homogeneous spin centres, whereas potassium iron jarosite exhibits conventional spin waves for a kagome lattice antiferromagnet, with contributions to the Hamiltonian of either a Dzyaloshinskii-Moriya interaction or crystal field induced single ion anisotropy. SQUID magnetometry measurements made under pressure in order to perturb the system, reveal changes in ordering behaviour in potassium iron jarosite. The mineral volborthite containing a slightly distorted kagome lattice of Cu^{2+} ions is particularly interesting as it combines both high frustration and low spin (S = ½). This system has been studied using various

techniques including SQUID magnetometry, neutron scattering and muon spin relaxation, all of which indicate that the magnetic correlations are highly unconventional. These show that volborthite also possesses strong antiferromagnetic exchange and fluctuations remain significant down to at least 50 mK, despite the build up of short range antiferromagnetic correlations. Experiments looking at ways to minimise the hydrogen content of the various materials studied, to improve the quality of the data from neutron scattering measurements, are also reported.

Acknowledgements

First of all I would like to thank Andrew for all his help, encouragement and support throughout the course of this PhD, none of this would have been possible without you. Thanks for having patience and believing in me, and for all the input and ideas, whilst also encouraging me to be independent.

A whole host of people have been invaluable when performing the neutron and muon experiments, at the various facilities around the world. Their help has ranged from trying to explain complex physics theories to me, helping with the intricacies of data analysis and attempting to resolve the problems of a hydrogen filled sample to providing light relief during the many hours of counting. The following all deserve a special mention, Georg Ehlers, Björn Fåk, Ralf Feyerherm, Peter Fouquet, Jason Gardner, Thomas Hansen, Paul Henry, Adrian Hillier, James Lord, Garry McIntyre, Des McMorrow, Hannu Mutka, Henrik Rønnow, John Stride, Ross Stewart, Anne Stunault, Jon Taylor and Dirk Visser. In addition, I would like to thank the technical support at each of the facilities, in particular the cryogenic teams for the many hours spent fiddling with dilution fridges.

A number of academic and support staff from the University of Edinburgh have helped with this project, from helping set up apparatus, making measurements to discussions about theory, these include Ronnie Brown, Philip Camp, Lorna Eades, Francesca Fabbiani, Stuart Johnstone, Konstantin Kamenev, Stuart Mains and Gavin Whittaker.

A big thank you to all the members of the Harrison group and the various project students I've worked with throughout the course of my PhD; Adrian, Chris, Gaétan, Goran, Keith, Lynne, Marcela, Mark, Phil and Rob, for help with sample prep, being able to bounce ideas off, for putting up with my general chat in the office and for a few great meals.

The work of a PhD does not stop at the door of the lab, therefore I would like to thank those who have helped to put everything in perspective. Those I've lived with, in particular, Catherine, Gwen, Richard and Tony, have probably had to put up with more than their fair share of my project's highs and lows. The 72nd Brownies and all at Nicolson Square Methodist have helped to provide an escape from the stress of a PhD, and have coped with my frequent trips away, often at short notice. A special mention to all those who have been up for a natter over a drink or dinner, trips to the cinema, beach or hills or just a good run.

Finally, I'd like to thank my family for their support throughout, for understanding the good and bad times, for holidays and for believing I could do it.

Contents

1 Introduction

Since the discovery of lodestone, a magnetic iron ore, by the Greeks almost 3000 years ago[1], magnetic materials and their properties have been of great interest. Magnetic materials first attracted attention due to their use as navigational aids, but within the past few hundred years, the uses of magnetic materials have greatly expanded, particularly with the discovery of the relationship between electricity and magnetism. Chadwick's discovery of the neutron in 1932[2], with its magnetic moment, greatly opened up the field of research by providing an incisive probe of magnetism at an atomic and microscopic scale.

Magnetic materials are particularly interesting to study, as magnetism is an easily probed bulk property, arising directly from the co-operative behaviour at an atomic level. The degrees of freedom of magnetic moments can often be thought of as analogous to those of the atoms themselves. Paramagnets, with independent behaviour of the magnetic moments, can be compared with the behaviour of atoms in the gas phase and long range ordered ferro- and antiferromagnets are analogous to crystalline species in the solid state. More exotic magnetic phases can also exist; these include so-called spin liquids[3-5], spin glasses[6] and spin ice[7, 8], which exhibit analogous behaviour to liquids, glasses and ice respectively. An understanding of these different magnetic phases can often lead to a further comprehension of any analogous atomic behaviour.

Magnetism is of particular interest to the chemist, as the magnetic properties of a material such as the dimensionality, strength of interaction, spin state and any spin anisotropy can often be tuned by altering the structure or chemical composition. Even though the bulk magnetic properties of a material can give an insight into its magnetic behaviour at an atomic level, the direct relationship between the two is not always well understood. As a result, there is a large amount of interest from theoreticians in this area. In order to test and improve their models, theoreticians rely on chemists to produce model magnetic systems. The challenge to the chemist is then to design and synthesise materials containing magnetic structures which correspond to the structures for which theories have been produced, and thus to test these theories[9].

The link between electricity and magnetism is particularly important, as the study of magnetic materials can give insights into the electrical and electronic properties of matter. One such link is between the magnetic fluctuations in low dimensional systems and the behaviour of the high-T_c superconductors. In 1973, Anderson proposed that a new electronic state may exist as an alternative to the long range ordered Néel state, for low spin systems[3]. This so-called resonating valence bond (RVB) state consists of a fluid of mobile valence bonds (pairs of spins correlated together in singlets), and is favoured by low spin, low dimensionality and the element of frustration. This will be discussed further in chapter 2. It was later proposed by Anderson[4] that the RVB state may contribute to the mechanism of superconductivity in the high-T_c superconductors. In order to further understand such mechanisms, model systems containing such properties need to be investigated.

Most of the high-T_c superconductors are based on a structure containing two-dimensional (2D) layers of $S = ½$, Cu^{2+} ions occupying a square lattice[10, 11]. The study of model systems containing lattices of this type, but which do not themselves exhibit superconductivity, enables the magnetic mechanisms present in the high-T_c superconductors to be further understood. One such model system is the family of copper salts (5-chloro-2-aminopyridine)$_2$CuX_4 ((5CAP)$_2$CuX_4), where X is a halide ion[12, 13]. The static and dynamic behaviour of these compounds have been studied in more depth in this thesis, including looking at the effect of perturbing such systems by the application of a field or doping the lattice, and details of such experiments can be found in chapter 4.

It is now believed that the ground state of the $S = ½$ square lattice Heisenberg antiferromagnet is largely classical. Therefore, in order to further destabilise these structures, and favour disordered ground states, a further element known as *frustration* can be introduced[14, 15]. Frustration is the term used to describe a system in which the interactions cannot all be simultaneously satisfied, and is commonly manifested in systems containing structures based on the triangular plaquette. This concept is discussed in further detail in chapter 2. The most theoretically interesting frustrated 2D lattice is the so-called *kagome* lattice, consisting of corner sharing triangles. The jarosite family of minerals[16] are the best examples of experimental kagome lattices known to date, and experiments probing their excitation spectra and also the effects of perturbing such systems by the application of pressure are discussed further in chapter 5.

Many different materials with the jarosite structure have been synthesised, but to date there are no examples containing $S = ½$ ions on the kagome lattice sites. In order to maximise the chance of an exotic ground state, the factors of low spin, low dimensionality and frustration should all be combined, and the case of a magnet consisting of $S = ½$ ions on the kagome lattice possesses all of these factors. One such material is the mineral volborthite, containing Cu^{2+} ions on slightly distorted kagome layers[17]. Further details of a variety of experiments performed on this system to probe both the static and dynamic behaviour can be found in chapter 6.

This thesis contains details of how the aforementioned model magnetic systems have been synthesised, perturbed and measured using a variety of techniques. The techniques used to probe the behaviour of these systems include SQUID magnetometry, muon spin relaxation and both elastic and inelastic neutron scattering. Further details of the experimental techniques used throughout the course of this project can be found in chapter 3.

1.1 References

[1] Blundell, S. J., *Magnetism in Condensed Matter*. Oxford Master Series in Condensed Matter Physics, ed. 2001, (Oxford University Press: New York).

[2] Chadwick, J., *Nature*, 1932, **129**: 312.

[3] Anderson, P. W., *Mat. Res. Bull.*, 1973, **8**(2): 153-160.

[4] Anderson, P. W., *Science*, 1987, **235**(4793): 1196-1198.

[5] Chandra, P. and Doucot, B., *Phys. Rev. B*, 1988, **38**(13): 9335 - 9338.

[6] Mydosh, J. A., *Spin Glasses: An Experimental Introduction*, ed. 1993, (Taylor & Francis: London - Washington DC).

[7] Bramwell, S. T. and Harris, M. J., *J. Phys.: Condens. Matter*, 1998, **10**: L215 - L220.

[8] Ramirez, A. P., Hayashi, A., Cava, R. J., Siddharthan, R. and Shastry, B. S., *Nature*, 1999, **399**(6734): 333-335.

[9] Harrison, A., *J. Phys.: Condens. Matter*, 2004, **16**: S553-S572.

[10] Kastner, M. A., Birgenau, R. J., Shirane, G. and Endoh, Y., *Rev. Mod. Phys.*, 1998, **70**(3): 897-928.

[11] Manousakis, E., *Rev. Mod. Phys.*, 1991, **61**: 1-62.

[12] Woodward, F. M., Albrecht, A. S., Wynn, C. M., Landee, C. P. and Turnbull, M. M., *Phys. Rev. B*, 2002, **65**(14): art. no.-144412.

[13] Hammar, P. R., Dender, D. C., Reich, D. H., Albrecht, A. S. and Landee, C. P., *J. Appl. Phys.*, 1997, **81**(8): 4615-4617.

[14] Ramirez, A. P., *Annu. Rev. Mater. Sci.*, 1994, **24**: 453-480.

[15] Greedan, J. E., *J. Mater. Chem.*, 2001, **11**: 37-53.

[16] Hendricks, S. B., *Am. Mineral.*, 1937, **22**: 773-784.

[17] Lafontaine, M. A., Lebail, A. and Ferey, G., *J. Solid State Chem.*, 1990, **85**(2): 220-227.

2 Theory

2.1 Magnetic Moment

The bulk magnetic properties of a material arise from the magnetic field created on an atomic scale. When a current flows around a loop of wire, the movement of the charge creates a magnetic field. On an atomic scale, the movement of an electron spin about the nucleus creates this effect. According to the Pauli Exclusion Principle, if two electrons occupy the same orbital, they must be of opposite spin. In this case the spins cancel each other out, resulting in no net magnetic field. The magnetic field on an atomic scale is therefore created by the motion of unpaired electrons about a nucleus, resulting in a magnetic moment on the atom. This is termed paramagnetism. In addition, all elements exhibit a degree of diamagnetism; a weak, negative magnetic susceptibility, which causes a moment to be induced that opposes any applied field. This effect is quantum mechanical and will not be discussed further here, as the effect is generally on a much smaller scale than any paramagnetism.

The size of the paramagnetic moment is determined by the total angular momentum (J) of the unpaired electrons, which is composed of spin (S) and orbital (L) components. When S and L can be coupled together by Russell-Saunders coupling to give J, the magnitude of the moment, μ_J, is given by the equation:

$$\mu_J = g_J \mu_B \sqrt{J(J+1)}\,, \tag{2.1}$$

where μ_B is the Bohr magneton (= $e\hbar/2m_e$) and g_J is the Landé g factor:

$$g_J = \frac{3}{2} + \frac{S(S+1) - L(L+1)}{2J(J+1)} . \tag{2.2}$$

In the case of many transition metal ions, the ligand field has the effect of removing the degeneracy of the singly occupied orbitals; thereby quenching the orbital angular momentum[1]. In this case S can be equated to J, resulting in a 'spin-only' moment.

When a magnetic field is applied to an isolated paramagnetic ion, Zeeman splitting occurs. This has the effect of splitting the ground state into $(2J + 1)$ m_J substates, which have quantised projections along the direction of the applied field, and have energies, E_{m_J} :

$$E_{m_J} = -m_J g \mu_B H . \tag{2.3}$$

At finite temperatures, the population of these states is governed by the Boltzmann distribution. The net polarisation, $\langle \mu_{m_J} \rangle$ of the ion is therefore given by the average over all these states:

$$\langle \mu_{m_J} \rangle = \frac{\sum_{m_j=-J}^{J} \mu_{m_j} \exp(-E_{m_j} / kT)}{\sum_{m_j=-J}^{J} \exp(-E_{m_j} / kT)} . \tag{2.4}$$

If E_{m_J} is small in comparison with the thermal energy, kT, the occupation of each energy level will be approximately the same and the net magnetic polarisation per ion simplifies to:

$$\left\langle \mu_{m_J} \right\rangle = \frac{g^2 \mu_B{}^2 B_0 J(J+1)}{3kT}, \tag{2.5}$$

where B_0 is the magnetic flux in a vacuum. For one mole of ions, the total magnetisation, M, is equal to $N_A \left\langle \mu_{m_J} \right\rangle$. Experimentally, the quantity that is determined is the susceptibility, χ, which is defined as the ratio of M to the applied field (H):

$$\chi = \frac{M}{H} = \frac{C}{T}, \tag{2.6}$$

where:

$$C = \frac{N_A g^2 \mu_B{}^2 J(J+1)}{3k}. \tag{2.7}$$

C is known as the Curie constant, and this behaviour of the susceptibility is known as the Curie law. Measurement of C enables the size of the magnetic moment on individual ions to be calculated. The Curie law only applies for the perfect paramagnet – when there is no interaction between magnetic moments; a system analogous to an ideal gas.

In most cases, the magnetic ion experiences a field in addition to the external applied field, arising from neighbouring magnetic ions. This leads to a deviation from the Curie law, resulting in the Curie-Weiss law:

$$\chi = \frac{C}{T - \theta_{CW}}, \tag{2.8}$$

where θ_{CW} is known as the Weiss constant. The magnitude of θ_{CW} is governed by the strength of the internal field experienced by each ion, *i.e.* the strength of the interaction between magnetic ions. If θ_{CW} is positive, this indicates that there is a tendency towards a local parallel alignment of spins on neighbouring ions, which is known as ferromagnetism. Similarly, if θ_{CW} is negative, the local alignment of spins on neighbouring ions is predominantly antiparallel; this is known as antiferromagnetism.

In order to quantify both C and θ_{CW}, the susceptibility of a sample is measured as a function of temperature. An ideal paramagnet will exhibit Curie law behaviour for all temperatures. Ferro- and antiferromagnetic materials exhibit Curie-Weiss behaviour above the ordering temperature (known as the Curie point for a ferromagnet and the Néel point for an antiferromagnet). At this temperature, the thermal energy becomes greater than any coupling energy. This causes fluctuations that destroy the internal magnetisation to such a degree that any magnetic order is destroyed. Thus the moments behave in a similar manner to those in a paramagnet above this temperature. Below the ordering temperature, the energy of the interactions is greater than the thermal energy, so the moments are coupled to one another, and therefore the behaviour is not Curie-Weiss like. At these temperatures, the magnetic moments in the sample often freeze into a long-range ordered array, analogous to the arrangements of atoms within a crystal. For an antiferromagnet, the

long range ordered state, known as the Néel state, can be thought of as consisting of two sub-lattices of moments aligned in a parallel fashion. The susceptibility plotted as a function of temperature for perfectly paramagnetic, ferromagnetic and antiferromagnetic materials is shown in figure 2.1.

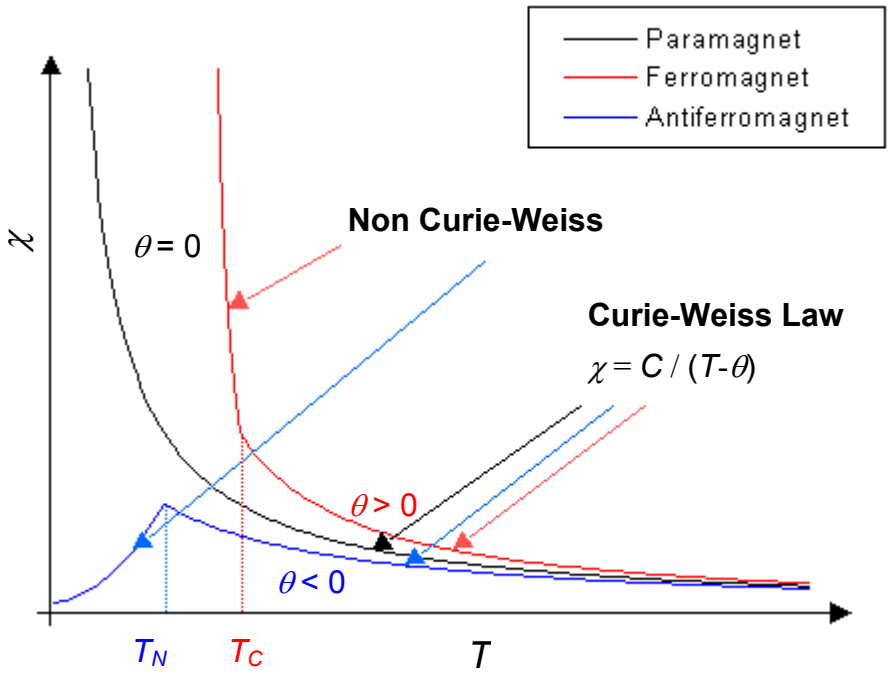

Figure 2.1: Graphs of susceptibility (χ) vs. temperature (T) for an ideal paramagnet, antiferromagnet and ferromagnet.

2.2 Magnetic Exchange

Within a solid, the magnetic moments on different atoms may interact, resulting in deviations from the behaviour exhibited by a perfect paramagnet. The alignment between spins on neighbouring ions can arise through a number of different mechanisms, but is generally termed magnetic exchange. A spin Hamiltonian can be written down to describe the energy of the exchange between two magnetic species:

$$\mathcal{H}_{ij} = -2J_{ij}\boldsymbol{S}_i \cdot \boldsymbol{S}_j , \tag{2.9}$$

where J is the exchange parameter describing both the magnitude and the type of interaction between the two spins at sites i and j. As it involves a scalar product of the two spin vectors, the Hamiltonian is minimised when the two spins are aligned in a co-linear fashion. A positive value of J describes ferromagnetic exchange, and a negative value, antiferromagnetic exchange.

The most obvious interaction that might be expected to play a part in the exchange between magnetic ions is the magnetic dipolar interaction, which is a through-space interaction. The order of magnitude of this effect is so small that it only becomes important over very short ranges or at very low temperatures (< 1 K for two moments of 1 μ_B, a distance of 1 Å apart). This type of interaction therefore does not account for the magnetic exchange in most compounds.

In a conductor, the conduction electrons can mediate the exchange interaction between ions. This effect is known as the RKKY mechanism, after its discoverers Ruderman, Kittel, Kasuya and Yosida. The magnetic moment on an ion spin-polarises the conduction electrons, which then couple to another moment a distance away. This type of interaction is long range, and the sign of the coupling has an oscillatory dependence upon the distance between the moments.

In an insulator, the electrons on neighbouring magnetic ions may interact *via* an exchange interaction; this is known as direct exchange. This arises when the electronic orbitals on the neighbouring atoms weakly interact. This has the effect of lowering the energy of the triplet state, hence favouring ferromagnetic exchange. As

the overlap becomes greater, the Pauli Exclusion Principle comes into play, forbidding the two electrons from having the same spin, thus stabilising the singlet state. Therefore the spins align in an antiparallel fashion (antiferromagnetic exchange), and as the overlap becomes greater, a bond is formed. Direct exchange is not common; as metal ions are rarely close enough in an insulator for direct interactions to occur, although it may come into play for systems containing edge or face sharing MO_6 octahedra.

The most common way in which magnetic exchange occurs in an insulator is *via* the orbitals on an intermediate diamagnetic atom or atoms. This is known as superexchange[2]. Kinetic superexchange stabilises the antiferromagnetic ground state through the overlap of two half-filled d-orbitals (e_g for the σ case and t_{2g} for the π case) with a p-orbital on a diamagnetic ion lying between the two magnetic ions. This occurs, as for the antiferromagnetic case there are two low lying excited states (due to metal-metal charge transfer (M-MCT) and double ligand-metal charge transfer (DL-MCT)) that can mix in with the ground state. This mixing causes the ground state to be lowered. The excited states of the ferromagnetic arrangement are not low enough for mixing with the ground state; as in this case for M-MCT and DL-MCT to occur one spin must be flipped, which is an energetic process. Figure 2.2 shows the case for a partially occupied e_g orbital on the metal ion overlapping in a σ fashion with a fully occupied p orbital on the ligand. Kinetic superexchange can also occur *via* a partially occupied t_{2g} orbital overlapping in a π fashion with the ligand p orbital. As the overlap in this case is weaker, so is the exchange.

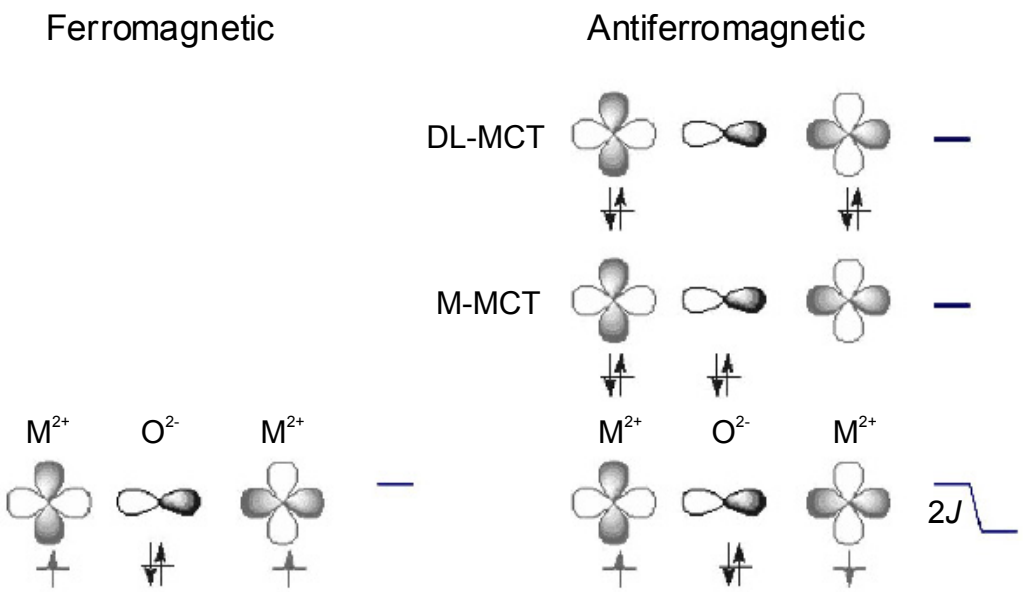

Figure 2.2: Orbital pathways for kinetic superexchange *via* a σ-type interaction through a ligand p orbital.

Potential superexchange occurs when the exchange pathway is *via* two orthogonal p-orbitals on the ligand. In this case the ferromagnetic excited state is lower in energy than the antiferromagnetic excited state, due to Hund's rule, which favours states of higher spin multiplicity. This results in the ferromagnetic ground state being lowered in relation to the antiferromagnetic, favouring ferromagnetic exchange.

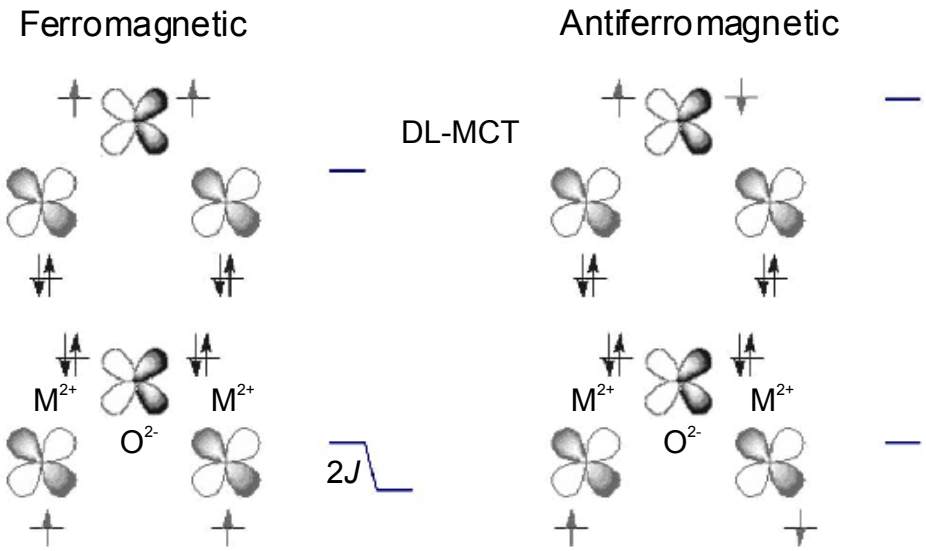

Figure 2.3: Orbital pathways for potential superexchange *via* a σ-type interaction, through orthogonal orbitals (ligand p_x and p_y).

The dominant pathway is almost always the kinetic superexchange pathway and therefore antiferromagnetic exchange dominates. The exception to this is when the metal – ligand – metal bridging angle through the ligand is close to 90º. This leads to ferromagnetic exchange being dominant. The size of the exchange is very sensitive to the degree of orbital overlap; therefore the type of bonding (*e.g.* σ or π), the bond angle and the ionic radius are important factors in determining the nature of the exchange.

2.3 Anisotropy

In some cases the magnetic moment has a preferred direction of alignment, rather than being free to align in any direction. This is known as anisotropy, and has significant implications for the ordering of the magnetic system. Taking into account spin anisotropy, the general case for the exchange Hamiltonian is in fact[3]:

$$\mathcal{H} = -2J\sum_{i>j}\left[a\boldsymbol{S}_i^z\boldsymbol{S}_j^z + b(\boldsymbol{S}_i^x\boldsymbol{S}_j^x + \boldsymbol{S}_i^y\boldsymbol{S}_j^y)\right]. \tag{2.10}$$

In the case when $a = b = 1$, the system is fully isotropic, and therefore the spin is free to align, without preference, in any orientation. This is known as the *Heisenberg* case. If $a = 0$ and $b = 1$, the moment is confined to lie in the *xy*-plane, known in this case as the easy plane; this is known as the *XY* case. Similarly, if $a = 1$ and $b = 0$, the moment is confined to lie along the *z*-axis (easy axis), which corresponds to the *Ising* case. The degree of anisotropy is influenced mainly by the crystal field that the magnetic ion experiences. The crystal field, through spin-orbit coupling, provides a preferred direction of alignment. Also, asymmetry in the available exchange pathways will lead to anisotropic interactions and therefore a preferred alignment direction.

Another interaction that can lead to anisotropy is the Dzyaloshinskii-Moriya (DM) interaction[4, 5]. This interaction is between an excited state of one ion and the ground state of another, and leads to an additional term in the Hamiltonian:

$$\boldsymbol{D}\cdot\left[\boldsymbol{S}_1\times\boldsymbol{S}_2\right]. \tag{2.11}$$

The vector $\boldsymbol{D}$ vanishes when the crystal field has inversion symmetry with respect to the centre of the two ions. If this is not the case, $\boldsymbol{D}$ will lie parallel or perpendicular to the line joining the two ions. In order to minimise this term in the Hamiltonian, the spins will have a tendency to align in a perpendicular fashion to each other (in a

plane perpendicular to ***D***). This has the effect of causing the moments to cant by a small angle, leading to so called Dzyaloshinskii-Moriya ferromagnetism.

The degree of anisotropy in the system, expressed by the parameter D, along with the dimensionality of the system, d, governs the range of magnetic order that can occur in the solid. This is shown in table 2.1:

	One-dimensional $d = 1$	Two-dimensional $d = 2$	Three-dimensional $d = 3$
Ising $D = 1$	Short range order	Long range order	Long range order
XY $D = 2$	Short range order	Medium range order	Long range order
Heisenberg $D = 3$	Short range order	Short range order	Long range order

Table 2.1: Effects of anisotropy and lattice dimensionality on the range of any magnetic ordering.

In reality, a system is rarely ideal, and is usually a mixture of some of the above cases. This is due to the difficulty in eliminating longer range interactions from the system, and the fact that the spin anisotropy rarely conforms exactly to one of the above situations. As can be seen from table 2.1, two-dimensional systems are particularly interesting as the range of their ordering is dependent upon the anisotropy of the moment. The work in this thesis concentrates on various types of approximately two-dimensional systems.

2.4 Spin Waves

At $T = 0$, the atoms within a solid will be ordered on a lattice and to a first approximation will be static (although zero-point fluctuations mean that this is not

quite the case). At finite temperatures, the thermal energy has the effect of disrupting this order by creating lattice vibrations. These vibrations are quantised as *phonons*. The magnetic analogy of these lattice vibrations are spin waves, which are quantised as *magnons*. If we consider a linear chain, at $T = 0$, the magnetic moments on each of the ions will be aligned; for a ferromagnet, in a parallel manner, and in an antiparallel manner for an antiferromagnet, with the precession of the moments all being perfectly in phase. At finite temperatures, thermal fluctuations cause the precession of adjacent moments to be out of phase with respect to their neighbours by a constant amount, ka, where k is a quantum number known as the wavenumber and a is the lattice constant. This results in a spin wave of wavelength $2\pi/k$.

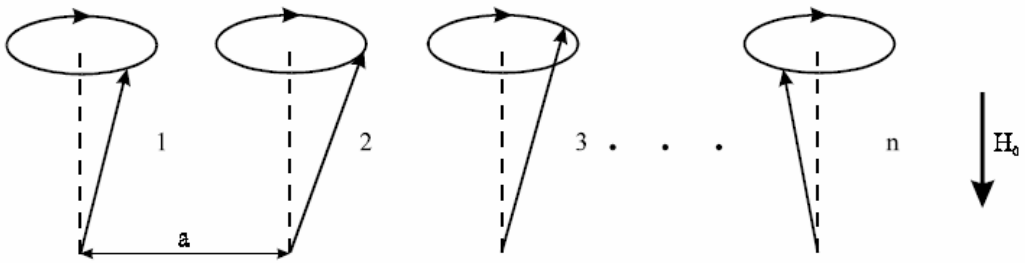

Figure 2.4: Classical picture of a spin wave in a linear ferromagnetic chain of n spins, with a lattice constant a. The arrows represent the spins precessing about the internal field. Figure taken from reference[6].

The energy required to create a spin wave is dependent on the strength of the coupling between the magnetic ions in the structure. The energy input also depends on the wavelength of the spin wave created; for a ferromagnetic chain, a spin wave of infinite wavelength (which is equivalent to one with a wavelength a) will require zero energy input, and the highest energy required will be to create a spin wave of wavelength $2a$, and *vice versa* for an antiferromagnetic chain. The relationship between energy and wavelength (or more commonly wavevector) is known as a

dispersion relation. It can be shown[7] that for a ferromagnetic chain, the dispersion relation is of the form:

$$\hbar\omega = 4JS(1-\cos ka)\,. \tag{2.12}$$

Additional terms in the Hamiltonian, such as spin anisotropy, or additional interactions, will modify the dispersion relation, but by measuring the dispersion, J can often be calculated.

2.5 Two-Dimensional Magnets

Two-dimensional (2D) magnets are particularly interesting as the range of the order in the system depends on the spin anisotropy of the metal ions. Mermin and Wagner[8] showed that there is no long range ordering at T > 0 in the 2D (and also one-dimensional) Heisenberg model, due to the dominance of thermal fluctuations. At T = 0, it is not so clear whether or not there is any long range order, but it is likely[9], as the quantum fluctuations are not strong enough to disturb it. Anderson proposed that instead of the existence of the Néel state in the S = ½ antiferromagnet, a so called resonating valence bond (RVB) state is adopted[10]. The RVB state is a quantum state consisting of a fluid of mobile valence bonds. These valence bonds are pairings of neighbouring spins correlated together to form singlets. The actual ground state consists of a linear combination of all possible nearest-neighbour spin pairings. The RVB state can be thought of in an analogous way to the Kekulé structure of benzene.

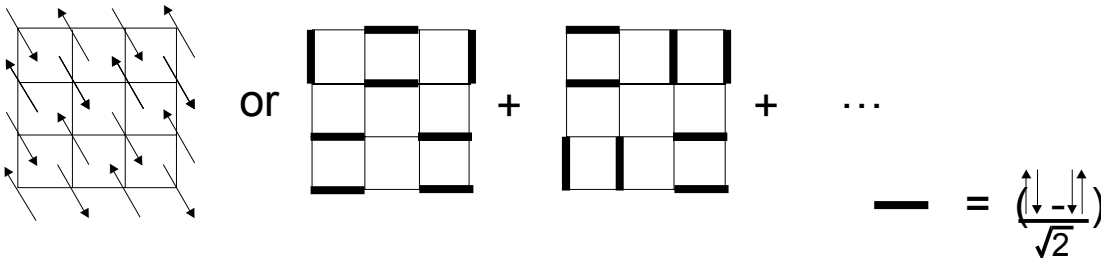

Figure 2.5: The Néel and RVB ground states in a 2D square Heisenberg antiferromagnet. Each bold line represents an antisymmetrised singlet.

The 2D Heisenberg model on a square lattice is particularly important as, for the low spin (quantum) case, it pertains to the behaviour of the high-T_c cuprate superconductors[9, 11, 12]. The high-T_c cuprate superconductors, such as $Ba_xLa_{5-x}Cu_5O_{5(3-y)}$, $YBa_2Cu_3O_{7-y}$ and $HgBa_2Ca_2Cu_3O_{8+y}$ contain square lattices of $S = ½$, Cu^{2+} ions exhibiting Heisenberg spin symmetry. Due to the potential applications of this kind of system, there has been a large amount of theoretical interest. It is found theoretically that on lowering the temperature, there is no onset of long range order at finite temperatures, but there is an increase in the size of the areas of short-range order – increasing the correlation length, ξ. The correlation length diverges exponentially with $1/T$, until long range order is established at $T = 0$[12]. These systems would be expected to behave in a classical manner, and this is observed in terms of their ground state, but experimentally quantum fluctuations may lead to non-classical behaviour particularly in terms of the one-magnon spectrum[13, 14] and behaviour in high applied magnetic fields[15]. Quantum effects lead to non-linear spin wave behaviour near the zone boundary of the one-magnon dispersion, hinting at the existence of RVB-type fluctuations. In fields close to the saturation field, H_s (= $4J$), the spin waves should become unstable to two-magnon decay.

In order to study the behaviour of the 2D Heisenberg model, good model systems are needed. A good model for a two-dimensional system will have well separated layers, typically with a ratio of intraplane to interplane coupling $J/J' \geq 100$. High-T_c superconductors are themselves poor model systems, due to their poor crystallinity, the difficulty in obtaining samples of the precise composition required, and the strong magnetic coupling within these systems which results in an energy scale too high to be experimentally probed. One good model system is copper formate tetradeuterate (CFTD)[16]. This system obeys theory very well, as it has a Hamiltonian close to that expected for the 2D square Heisenberg antiferromagnet, and it has been studied in some detail [13, 16-22]. As the stability of this system is finely balanced, it is often desirable to perturb it in some way (see section 2.8). Unfortunately, due to the size of the coupling in this system (J = 72 K), the magnetic fields required to saturate this system are beyond reach experimentally (H_c = 250 T). Also, it has not been possible to dope this system to a significant level.

A family of compounds with a square lattice of Cu^{2+} ions is the A_2CuX_4 series, where A = 5-chloro-2-aminopyridine (CAP), 5-methyl-2-aminopyridine (MAP) or 5-bromo-2-aminopyridine (BAP) and X = Cl or Br[23-29]. The in-plane coupling in these compounds is smaller than in CFTD, enabling perturbation to occur at experimentally accessible fields. These compounds also appear to be more amenable to chemical doping than CFTD. These materials will be discussed in further detail in chapter 4.

2.6 Frustration

The collective properties of a magnetic system may also be affected by *frustration*. Magnetic frustration is a term that describes the situation in which the magnetic sites on a lattice are subject to competing or contradictory constraints. When this arises from the topology of the lattice, it is termed geometrical frustration. To illustrate this concept, consider a square arrangement of spins (figure 2.6(a)), where only the nearest neighbour interactions are in operation; if the exchange is antiferromagnetic, all the spins can align in their preferred orientation, satisfying all the interactions. On the other hand, for a triangular arrangement of spins (figure 2.6(b)), with three equal antiferromagnetic interactions, only two of the interactions can be simultaneously satisfied. There is no minimisation of all the exchange terms, resulting in one *frustrated* spin. Similarly for a square arrangement with one ferromagnetic and three antiferromagnetic interactions (figure 2.6(c)), only three of these interactions can be satisfied simultaneously, leaving one frustrated spin.

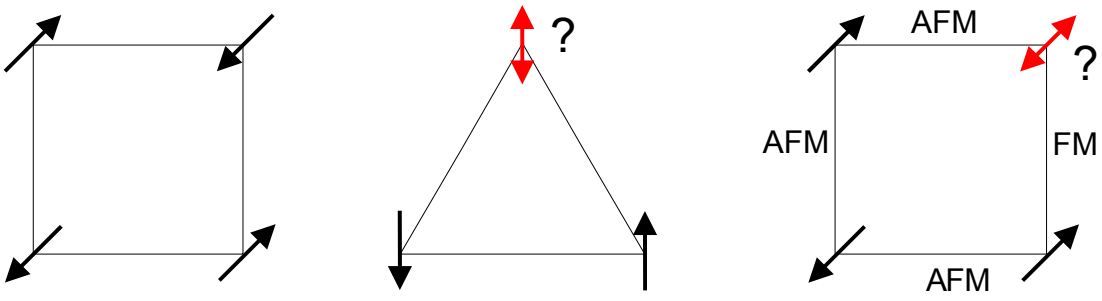

Figure 2.6: (a) A square arrangement of antiferromagnetically coupled spins, (b) frustration on an equilateral triangle, (c) frustration on a square due to one ferromagnetic interaction. In (b) & (c) the red spin is frustrated.

These frustrated plaquettes can be joined together to form lattices, which commonly also exhibit frustration. These frustrated lattices include, in two dimensions, the

triangular lattice of edge sharing equilateral triangles and the kagome lattice of corner sharing equilateral triangles. In three dimensions possible frustrated lattices include the pyrochlore structure of corner sharing tetrahedra and the face centred cubic (FCC) lattice of edge sharing tetrahedra.

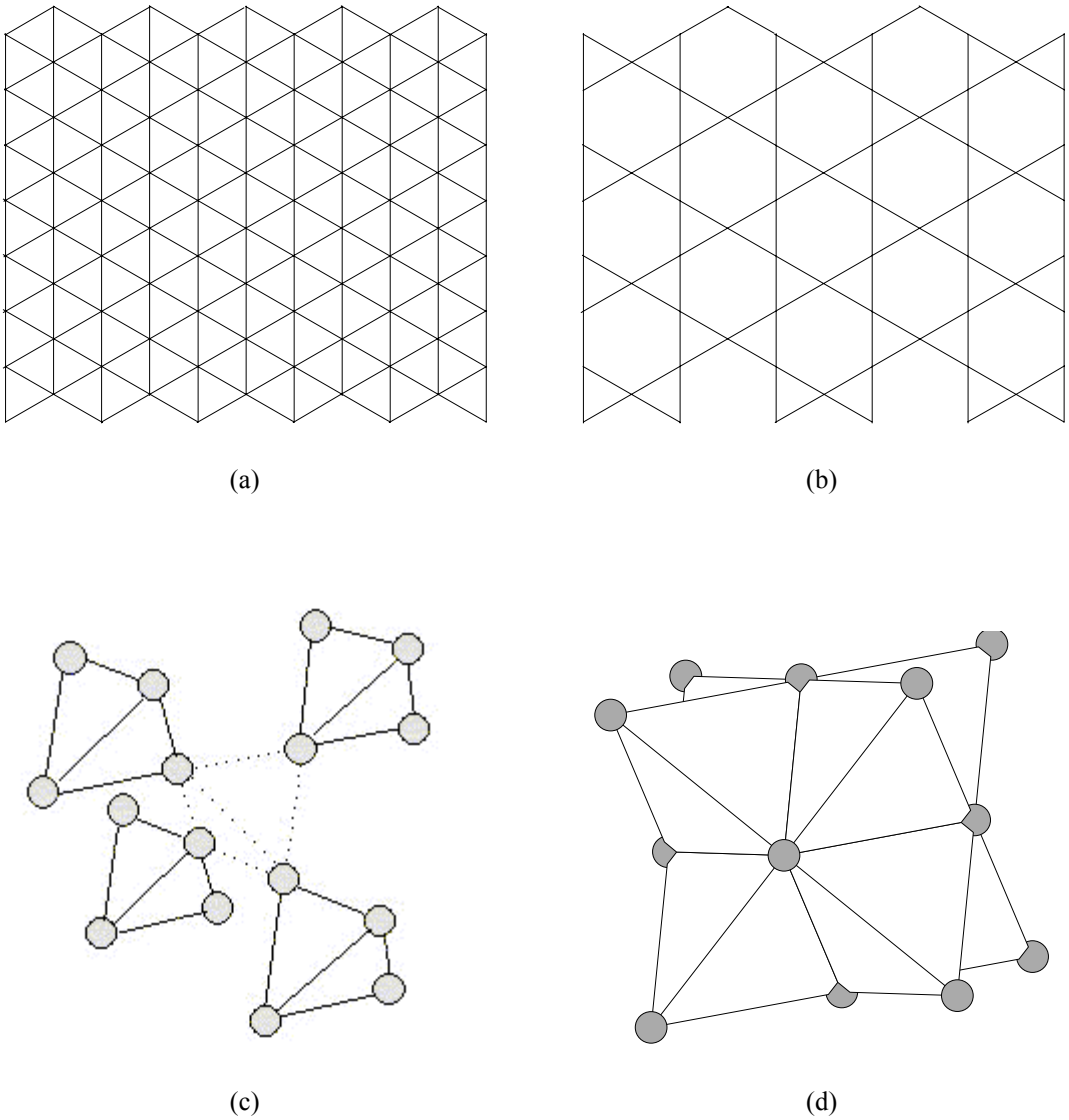

Figure 2.7: (a) Triangular, (b) kagome, (c) pyrochlore and (d) face centred cubic lattices.

The inability to simultaneously satisfy all the interactions in a frustrated lattice suppresses the onset of long range order, lowering the ordering temperature of the system. For an ideal, non-frustrated system, deviations from the Curie-Weiss law

will occur at the Curie-Weiss temperature, θ_{CW}, *i.e.* $T_N = \theta_{CW}$. As the degree of frustration in the system increases, the ordering temperature decreases in relation to θ_{CW}. The degree of frustration, f, is therefore defined as[30]:

$$f = \frac{|\theta_{CW}|}{T_N}. \tag{2.13}$$

For a ferromagnet, f is close to 1, but for a non-frustrated antiferromagnet, f is often greater than 1 and can be as large as 4 or 5[31]. For a truly frustrated system, f is usually larger than 10 and can be even greater than 500[32].

In many cases, when the spins exhibit either Heisenberg or *XY* anisotropy, a compromise spin arrangement of minimum energy is adopted around the plaquette. For the case of the triangular motif, the compromise configuration is the 120º arrangement shown in figure 2.8. In this case, there are two possible compromise configurations; each has a different chirality depending on whether the spins rotate in a clockwise or anticlockwise direction on going around the triangle in a clockwise manner.

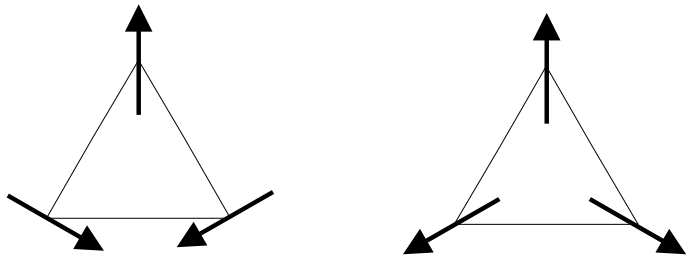

Figure 2.8: Two 120º compromise spin arrangements of minimum energy on a triangular plaquette. The two arrangements are of opposite chirality.

If two triangles are joined together in an edge-sharing fashion, the spin configuration on one triangle unambiguously determines the orientation of the spins on the next triangle (see figure 2.9(a)), and any chiral information is passed on. On the contrary, if the triangles are joined together by their corners, the spin configuration around the first triangle allows two possible minimum energy configurations on the second triangle, each of opposite chirality. In this case, the chiral information is not passed on.

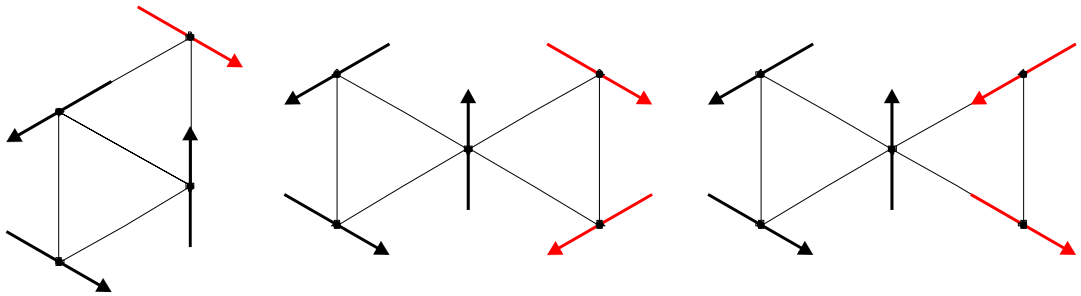

(a) (b) (c)

Figure 2.9: (a) Edge sharing triangles showing the unique orientation of the red spin in order to satisfy the 120° minimum energy configuration, (b) & (c) corner sharing triangles showing the two possible orientations of the red spins satisfying the 120° minimum energy configuration.

When single triangular motifs are joined by their edges to form a triangular lattice, the chirality of the spins on one triangle determines the chirality of the spins on the neighbouring triangles, as two of the spins are shared. Therefore the chiral information is carried throughout the entire lattice, and the ground state is determined by the spins around one triangle. On the other hand, for the kagome lattice, as the neighbouring triangles only share one spin between them, the next triangle can adopt a spin arrangement of either chirality. This means that the chiral information is not passed on throughout the entire lattice. There is therefore no unique ground state,

but a number of degenerate ground states of the spin structure. Two of these states that exhibit long range order are the so-called '**q** = 0' and '√3 x √3' structures.

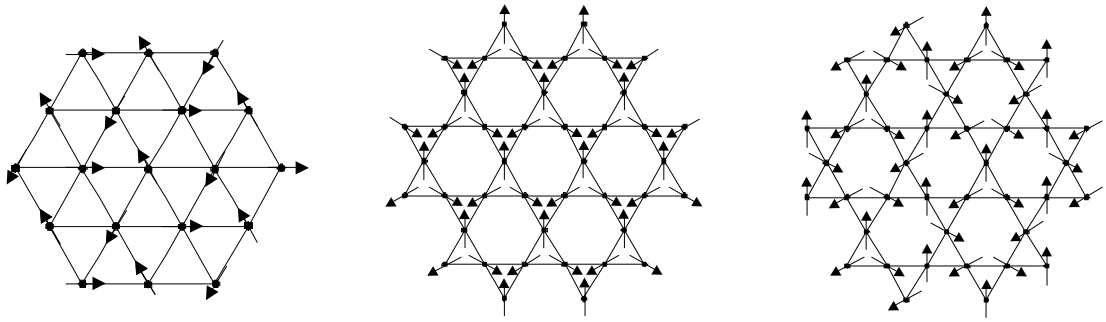

(a) (b) (c)

Figure 2.10: 120º compromise arrangements on lattices: (a) triangular lattice, (b) **q** = 0 arrangement on the kagome lattice and (c) √3 x √3 arrangement on the kagome lattice.

Similarly, in three dimensions, the pyrochlore lattice of corner sharing tetrahedra, shows no unique ground state, unlike the FCC lattice.

A consequence of the competing interactions in a frustrated lattice is that these materials often do not exhibit long range order, but more exotic ground states may be observed. These may include spin glasses, spin ices and spin liquids. A spin glass is a state in which the spins are frozen into a pattern not exhibiting any long-range order. There is a distinct freezing temperature at which this occurs, known as the glass transition temperature, T_g. Below this temperature one of many degenerate spin structures, each separated by very small energy differences, will be adopted. The spin structure adopted will be determined by the instantaneous arrangement just before freezing; therefore the ground state will be determined by the exact experimental conditions, and hysteresis is often observed. Signatures of spin glass behaviour include the divergence of field cooled (FC) and zero field cooled (ZFC) measurements of susceptibility at T_g, a frequency dependence in the a.c.

susceptibility and a strong slowing down of the spin dynamics below T_g, but an absence of long range order. A spin liquid is a system in which the spins remain dynamic down to the lowest temperatures, despite correlations between spins. Spin liquids are often referred to in the case of quantum (S = ½) systems, where the RVB ground state may be important. A spin ice is a state that may be formed from Ising spins on the pyrochlore lattice[33, 34], where the spin orientations are analogous to the proton arrangements around the oxygen atoms in ice[35].

In order to study the properties of frustrated lattices, suitable model systems must be found[36]. There are many different approaches to this problem. The first is to look for examples of materials already in existence, these may include naturally occurring minerals or materials previously synthesised. A second approach is to hope that a suitable sample may be produced serendipitously – but this can be very time consuming, with no guaranteed results. A third option is to try and design a material, often based on building up a material from smaller 'building units', of the required topology, or by modifying the structure of an existing material, by adding vacancies or interstitials.

2.7 Kagome Lattices

As discussed in the previous section, the kagome lattice is a particularly interesting structure due to its large degree of frustration and lack of well defined ground state structure. It has therefore attracted a large amount of interest – both theoretically and experimentally.

A kagome lattice with classical Heisenberg spins will have a large number of degenerate ground states if only nearest neighbour exchange is considered[37]. It is found that this degeneracy can be lifted by considering any small perturbation, *e.g.* next-nearest neighbour interactions, anisotropy and structural distortions. Even for the Heisenberg case, it has been shown that the ground state will consist of a planar arrangement of spins, due to the effects of thermal fluctuations[38, 39]. Calculations have shown that thermal fluctuations remove the degeneracy of the ground state, and in the Heisenberg case, the $\sqrt{3}$ x $\sqrt{3}$ structure is adopted[40] when only nearest neighbour interactions are considered. When further neighbour interactions are considered, the degeneracy of the ground state is either partially or fully lifted[41] depending on the nature of the interaction.

Despite the large amount of theoretical work concentrated on the kagome lattice, there are very few physical representations of the lattice with which to test the theory. Two families of minerals containing metal atoms arranged in kagome lattices have been studied and will be discussed later in this thesis. The jarosite[42] family of minerals contain perfect kagome planes of metal atoms and will be discussed further in chapter 5. The mineral volborthite[43] contains a planar lattice of copper atoms in a slightly distorted kagome arrangement, and will be discussed in chapter 6.

In addition to these materials, a small number of other materials containing kagome lattices have been synthesised and studied. One well studied compound commonly used to model the kagome lattice is $SrCr_{9p}Ga_{12-9p}O_{19}$ (SCGO). The Cr^{3+} ions in this compound adopt a structure consisting of slightly distorted kagome lattices

interleaved with triangular lattices. The occupation of the kagome lattice is less than 100 %, and the distortion of the co-ordination octahedra about the Cr atoms, leads to magnetic exchange anisotropy. These factors all mean that, although SCGO is a highly frustrated system[44], exhibiting spin glass behaviour, it is not an accurate model of the kagome lattice[45]. The related material $Ba_2Sn_2ZnGa_3Cr_7O_{22}$ (BSZGCO)[46] does not contain magnetic ions in the intermediary layers that are present in SCGO, making this compound more 2D in character, resulting in a higher degree of frustration. Recently synthesised systems, which could provide a good starting point for further investigation include the mineral herbertsmithite[47] containing kagome layers of S = ½ Cu^{2+} ions separated by layers containing diamagnetic Zn. To date, there is no evidence of long range ordering in this system. There are a few examples of materials containing kagome lattices of metals templated by organic ligands, these include the S = 1, Ni^{2+} containing compound $[C_6N_2H_8][NH_4]_2[Ni_3F_6(SO_4)_2]$ [48], and the S = ½ compound $\{Cu_3(titmb)_2(OCOCH_3)_6\}\cdot H_2O$ (titmb = 1,3,5-*tris*(imidazol-1-ylmethyl)-2,4,6-trimethylbenzene)[49]. These materials both present a problem with making samples suitable for study by neutron scattering techniques, due to the difficulty and expense associated with producing perdeuterated samples.

2.8 Perturbing Magnetic Systems

In order to probe the magnetic properties of a system and test models of fundamental magnetism it is common to perturb the system in some way, measure the response and compare with predictions of the model. This is particularly desirable for systems such as those studied as part of this project, where the stability of the system is

delicately balanced. There are many ways of perturbing a system, the most commonly used ways being the variation of temperature and applied magnetic field. Other ways of perturbing a system can include making systematic structural changes (*e.g.* changing the ionic radius of a counter ion), doping the magnetic lattice with diamagnetic ions or applying pressure to the system.

2.8.1 Dilution

Doping the magnetic lattice with diamagnetic ions (or diamagnetic dilution) has the effect of randomly introducing site vacancies in the lattice. Dilution is usually carried out with a diamagnetic element possessing a similar size and chemical properties to the paramagnetic ion. This minimises distortion of the lattice, and ensures that the doping is random in nature. If the level of dilution is great enough, the exchange pathways across the lattice will be broken, preventing long-range order. This will occur at the percolation threshold p_c[50]. Up to this point, the range of ordering will be affected by the level of dilution, as will the transition temperature. By altering the level of doping, these properties can be tuned.

2.8.2 Pressure

Another way of perturbing a system is by applying pressure to it, which in the case of a solid can result in structural distortions. As has been discussed earlier, the co-operative magnetic properties of a system are highly sensitive to the local co-ordination of each individual magnetic ion, particularly to factors such as bond angle and length. The structural distortions caused by the application of pressure

may therefore result in the alteration of the magnetic interactions. Structural distortions are often introduced into a material by altering the ionic radius of one or more of the components, by replacement with another (this is often referred to as 'chemical pressure'). This technique is not always satisfactory as the replacement may cause a completely different structure or compound to form. Also, the structural distortions can only be created in discrete steps (depending on the radii of the ions available), rather than being varied continuously. There are therefore many advantages in introducing structural distortions by the application of pressure; structural distortions can be introduced in a continuous manner to a sample of known structure and magnetic properties, without the need to synthesise a new compound, and all the problems associated with that. Applying pressure to a system, and measuring the corresponding structural and magnetic changes should increase our knowledge of the mechanisms leading to and affecting magnetic exchange.

Considering the obvious information that can be obtained by looking at the effects of pressure on the structural and magnetic properties of a system, remarkably little work has been carried out in this field. Most of the work done to date has been concerned with the study of pressure on the magnetic properties of alloys. Early work on magnetic insulators investigated the pressure dependence of both structural and magnetic properties, resulting in a relationship between the strength of the superexchange, J, and the distance between the magnetic moments, r[51-55]:

$$J \propto r^{-n}, \tag{2.14}$$

where n is ~ 10. More recent studies have involved using pressure as another tool to probe materials that are of current interest in solid state magnetism. These include materials related to the high-T_c superconductors[56, 57], colossal magnetoresistors[58-60], and other materials where the effect of pressure on the Jahn-Teller distortion may affect the magnetic ordering[61-64]. The effect of pressure on frustrated systems has also been investigated. One such system is the pyrochlore lattice spin liquid, $Tb_2Ti_2O_7$[65, 66]. The application of pressure to this system induces long range magnetic order, and it has been found that the Néel temperature and ordered magnetic moment may be tuned by the direction of any anisotropic pressure component.

2.9 References

[1] Carlin, R. L., *Magnetochemistry*, ed. 1986, (Springer-Verlag: Berlin).

[2] Anderson, P. W., *Phys. Rev.*, 1950, **79**(2): 350 - 356.

[3] de Jongh, L. J. and Miedema, A. R., *Advances in Physics*, 1974, **23**(1): 1-247.

[4] Dzyaloshinsky, I., *J. Phys. Chem. Solids*, 1958, **4**(4): 241 - 255.

[5] Moriya, T., *Phys. Rev.*, 1960, **120**(1): 91 - 98.

[6] Wills, A. S., *PhD Thesis*. 1996, University of Edinburgh.

[7] Blundell, S. J., *Magnetism in Condensed Matter*. Oxford Master Series in Condensed Matter Physics, ed. 2001, (Oxford University Press: New York).

[8] Mermin, N. D. and Wagner, H., *Phys. Rev. Lett.*, 1966, **17**(22): 1133-1136.

[9] Manousakis, E., *Rev. Mod. Phys.*, 1991, **61**: 1-62.

[10] Anderson, P. W., *Mat. Res. Bull.*, 1973, **8**(2): 153-160.

[11] Anderson, P. W., *Science*, 1987, **235**(4793): 1196-1198.

[12] Kastner, M. A., Birgenau, R. J., Shirane, G. and Endoh, Y., *Rev. Mod. Phys.*, 1998, **70**(3): 897-928.

[13] Rønnow, H. M., McMorrow, D. F., Coldea, R., Harrison, A., Youngson, I. D., Perring, T. G. *et al.*, *Phys. Rev. Lett.*, 2001, **87**(3): art. no.-037202.

[14] Kim, Y. J., Aharony, A., Birgenau, R. J., Chou, F. C., Entin-Wohlman, O., Erwin, R. W. *et al.*, *Phys. Rev. Lett.*, 1999, **83**(4): 852 - 855.

[15] Zhitomirsky, M. E. and Chernyshev, A. L., *Phys. Rev. Lett.*, 1999, **82**(22): 4536-4539.

[16] Clarke, S. J., *DPhil Thesis*. 1994, University of Oxford.

[17] Harrison, A., Clarke, S. J., Mason, T. E. and Visser, D., *J. Magn. Magn. Mater.*, 1992, **104**: 557-558.

[18] Rønnow, H. M., McMorrow, D. F., Harrison, A., Youngson, I. D., Coldea, R., Perring, T. G. *et al.*, *J. Magn. Magn. Mater.*, 2001, **236**(1-2): 4-5.

[19] Clarke, S. J., Harrison, A., Mason, T. E. and Visser, D., *Solid State Commun.*, 1999, **112**(10): 561-564.

[20] Rønnow, H. M., McMorrow, D. F. and Harrison, A., *Phys. Rev. Lett.*, 1999, **82**(15): 3152-3155.

[21] Clarke, S. J. and Harrison, A., *J. Magn. Magn. Mater.*, 1995, **140**: 1627-1628.

[22] Clarke, S. J. and Harrison, A., *J. Phys.-Condes. Matter*, 1992, **4**(29): 6217-6226.

[23] Coffey, T. J., Landee, C. P., Robinson, W. T., Turnbull, M. M., Winn, M. and Woodward, F. M., *Inorg. Chim. Acta*, 2000, **303**(1): 54-60.

[24] Hammar, P. R., Dender, D. C., Reich, D. H., Albrecht, A. S. and Landee, C. P., *J. Appl. Phys.*, 1997, **81**(8): 4615-4617.

[25] Matsumoto, T., Miyazaki, Y., Albrecht, A. S., Landee, C. P., Turnbull, M. M. and Sorai, M., *J. Phys. Chem. B*, 2000, **104**(43): 9993-10000.

[26] Place, H. and Willett, R. D., *Acta Crystallogr. Sect. C-Cryst. Struct. Commun.*, 1987, **43**: 1050-1053.

[27] Woodward, F. M., Albrecht, A. S., Wynn, C. M., Landee, C. P. and Turnbull, M. M., *Phys. Rev. B*, 2002, **65**(14): art. no.-144412.

[28] Woodward, F. M., Landee, C. P., Giantsidis, J., Turnbull, M. M. and Richardson, C., *Inorg. Chim. Acta*, 2001, **324**(1-2): 324-330.

[29] Woodward, F. M., Albrecht, A. S., Wynn, C. M., Landee, C. P. and Turnbull, M. M., *cond-mat*, 2001: 0107483.

[30] Ramirez, A. P., *Annu. Rev. Mater. Sci.*, 1994, **24**: 453-480.

[31] Greedan, J. E., *J. Mater. Chem.*, 2001, **11**: 37-53.

[32] Hirakawa, K., Kadowaki, H. and Ubukoshi, K., *J. Phys. Soc. Jpn.*, 1985, **54**(9): 3526-3536.

[33] Bramwell, S. T. and Harris, M. J., *J. Phys.: Condens. Matter*, 1998, **10**: L215 - L220.

[34] Ramirez, A. P., Hayashi, A., Cava, R. J., Siddharthan, R. and Shastry, B. S., *Nature*, 1999, **399**(6734): 333-335.

[35] Pauling, L., *The Nature of the Chemical Bond*, 3rd ed, ed. 1960, (Cornell University Press: Ithaca, NY). pp. 465 - 468.

[36] Harrison, A., *J. Phys.: Condens. Matter*, 2004, **16**: S553-S572.

[37] Marston, J. B. and Zeng, C., *J. Appl. Phys.*, 1991, **69**(8): 5962-5964.

[38] Chalker, J. T., Holdsworth, P. C. W. and Shender, E. F., *Phys. Rev. Lett.*, 1992, **68**(6): 855-858.

[39] Shender, E. F., Cherepanov, V. B., Holdsworth, P. C. W. and Berlinsky, A. J., *Phys. Rev. Lett.*, 1993, **70**(24): 3812-3815.

[40] Harris, A. B., Kallin, C. and Berlinsky, A. J., *Phys. Rev. B*, 1992, **45**(6): 2899-2919.

[41] Ballou, R., Canals, B., Elhajal, M., Lacroix, C. and Wills, A. S., *Phys. Stat. Sol. (b)*, 2003, **236**(2): 240-245.

[42] Hendricks, S. B., *Am. Mineral.*, 1937, **22**: 773-784.

[43] Lafontaine, M. A., Lebail, A. and Ferey, G., *J. Solid State Chem.*, 1990, **85**(2): 220-227.

[44] Ramirez, A. P., Espinosa, G. P. and Cooper, A. S., *Phys. Rev. Lett.*, 1990, **64**(17): 2070-2073.

[45] Lee, S. H., Broholm, C., Aeppli, G., Perring, T. G., Hessen, B. and Taylor, A., *Phys. Rev. Lett.*, 1996, **76**(23): 4424-4427.

[46] Hagemann, I. S., Huang, Q., Gao, X. P. A., Ramirez, A. P. and Cava, R. J., *Phys. Rev. Lett.*, 2001, **86**(5): 894-897.

[47] Shores, M. P., Nytko, E. A., Bartlett, B. M. and Nocera, D. G., *J. Am. Chem. Soc.*, 2005, **127**: 13462-3.

[48] Behera, J. N. and Rao, C. N. R., *J. Am. Chem. Soc.*, 2006, **128**(29): 9334-9335.

[49] Honda, Z., Katsumata, K. and Yamada, K., *Physica B*, 2003, **329-333**: 1032-1033.

[50] Collins, M. F., *Magnetic Critical Scattering*. Oxford Series on Neutron Scattering in Condensed Matter, ed. 1989, (Oxford University Press: New York).

[51] Bloch, D., *J. Phys. Chem. Solids*, 1966, **27**(5): 881.

[52] Bloch, D., *Ann. Phys.*, 1966, **1**(1-2): 93.

[53] Bloch, D., Chaisse, F. and Pauthene.R, *J. Appl. Phys.*, 1966, **37**(3): 1401.

[54] Bloch, D. and Vettier, C., *J. Magn. Magn. Mater.*, 1980, **15-8**(JAN-): 589-592.

[55] de Jongh, L. J. and Block, R., *Physica B & C*, 1975, **79**(6): 568-593.

[56] Aronson, M. C., Dierker, S. B., Dennis, B. S., Cheong, S. W. and Fisk, Z., *Phys. Rev. B*, 1991, **44**(9): 4657-4660.

[57] Doroshev, V., Krivoruchko, V., Savosta, M., Shestakov, A. and Tarasenko, T., *J. Magn. Magn. Mater.*, 1996, **158**: 669-670.

[58] Moritomo, Y., Kuwahara, H., Tomioka, Y. and Tokura, Y., *Phys. Rev. B*, 1997, **55**(12): 7549-7556.

[59] Imada, M., Fujimori, A. and Tokura, Y., *Rev. Mod. Phys.*, 1998, **70**(4): 1039-1263.

[60] Kamenev, K. V., Lees, M. R., Balakrishnan, G., Paul, D. M., Marshall, W. G., Tissen, V. G. *et al.*, *Phys. Rev. Lett.*, 2000, **84**(12): 2710-2713.

[61] Ishizuka, M., Terai, M., Endo, S., Hidaka, M., Yamada, I. and Shimomura, O., *J. Magn. Magn. Mater.*, 1998, **177**: 725-726.

[62] Ishizuka, M., Terai, M., Hidaka, M., Endo, S., Yamada, I. and Shimomura, O., *Phys. Rev. B*, 1998, **57**(1): 64-67.

[63] Ishizuka, M., Yamada, I., Amaya, K. and Endo, S., *J. Phys. Soc. Jpn.*, 1996, **65**(7): 1927-1929.

[64] Manaka, H., Yamada, I., Kitazawa, T., Kobayashi, M., Ishizuka, M. and Endo, S., *J. Phys. Soc. Jpn.*, 1997, **66**(10): 2989-2992.

[65] Mirebeau, I., Goncharenko, I. N., Cadavez-Peres, P., Bramwell, S. T., Gingras, M. J. P. and Gardner, J. S., *Nature*, 2002, **420**: 54-57.

[66] Mirebeau, I. and Goncharenko, I. N., *J. Phys.: Condens. Matter*, 2005, **17**(11): S771-S782.

3 Experimental Methods

This chapter contains details of a number of the experimental techniques used to study both the static and the dynamic nature of any magnetism in a sample, along with techniques that can also be used to gain information about the structure of materials.

3.1 SQUID Magnetometry

In order to measure the magnetic susceptibility (χ) of a material, a known magnetic field (H) needs to be applied to a sample, and the magnetisation (M) measured. One of the most sensitive ways of doing this is to use a Superconducting QUantum Interference Device (SQUID) magnetometer[1]. The SQUID itself consists of a superconducting loop containing two Josephson junctions in the loop's current path. A Josephson junction is a device based on an electron tunnelling effect and consists of a thin layer of insulating material in a superconducting circuit. This allows the direct observation of quantum electrodynamic phenomena.

The SQUID does not measure the magnetic response from the sample directly, but *via* a superconducting circuit. The sample is moved through superconducting detection coils, which are connected to one of the Josephson junctions on the SQUID by means of superconducting wires. If the sample has a magnetic moment, the movement of this through the detection coils induces a current in the coils. The wires allow the current from the detection coils to inductively couple with the SQUID sensor, varying the phase of the wavefunction tunnelling through one of the

junctions. The addition of this to the unaltered wavefunction tunnelling through the other junction creates an interference pattern, which is very sensitive to the magnetic field. As a closed superconducting loop is formed by the detection coils, connecting wires and the SQUID input coil, the change of magnetic flux in the detection coils produces a change in the current in the detection circuit, which is proportional to the change in magnetic flux. The changes in current in the detection coils create variations in the output voltage of the SQUID coil, which are proportional to the magnetic moment of the sample. During a scan, the sample position is varied, in order to alter this output voltage. The output voltage measured as a function of the sample position is then fitted to a theoretical expression in order to give a value of the sample magnetisation[2]. Ideally, the sample will therefore be a point source in a sample holder that has a negligible magnetic moment and is uniform along the length of the scan. For the ambient pressure measurements reported in this thesis, the sample was held in a gelatine capsule fixed in the centre of a plastic straw.

A magnetic field is applied to the sample in the magnetometer by means of a large superconducting magnet, wound in a solenoid configuration. This is shielded from the SQUID detector, in order for it to magnetise the sample but not the detector. The detection coils, which are placed at the centre of this magnet, are configured as a second-order gradiometer, as shown in figure 3.1:

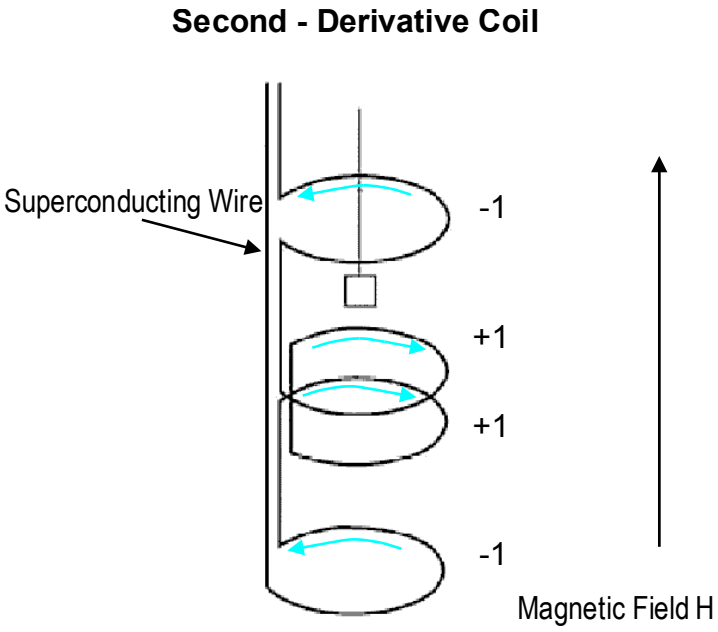

Figure 3.1: Configuration of the second-derivative detection coil in the SQUID magnetometer.

This configuration minimises noise in the detection circuit caused by fluctuations in the large magnetic field of the superconducting magnet. It also minimises the background drifts in the detection circuit caused by the relaxation of the magnetic field. Along with being able to control the magnetic field in the magnetometer, it is also possible to vary the temperature, using a combination of the inbuilt heater and liquid helium cooling system. This enables the magnetisation (and hence susceptibility) to be measured and plotted as a function of temperature or applied field. The susceptibility measurements contained within this thesis were carried out on a Quantum Design $MPMS_2$ magnetometer.

3.1.1 Pressure Cell

In order to determine whether pressure has an influence over the magnetic properties of a material, susceptibility measurements were carried out on a sample held in a

pressure cell. The pressure cell used (shown in figure 3.2) was a clamp cell, made out of a Be-Cu alloy (containing 2 wt % Be). This material was chosen in order to minimise the magnetic background due to the cell as beryllium and copper are both weakly diamagnetic[3], with a combined susceptibility < $7x10^{-9}$ emu g^{-1}[4]. The quantity of Be in the alloy maximises its hardness, enabling high pressures to be obtained, whilst minimising the risk of toxic BeO production. The sample was placed in a PTFE cell, which was filled with 'Daphne 7373' oil[5]. Daphne 7373 is a pure grade hydrocarbon oil and was used as a quasi-hydrostatic pressure transmitting medium. A small amount of lead (tin can also be used) was also placed in the cell in order to calibrate the pressure. At low temperatures Pb exhibits a pressure dependent phase transition to a superconducting phase, resulting in a change in its susceptibility. Therefore measuring the temperature, T_c, at which this occurs, enables the pressure within the cell to be determined.

The pressure within the cell is varied by applying pressure to a small piston within the cell. This is then locked into place by tightening a screw. The pressure cell is then attached to a straw in order for it to be inserted into the magnetometer. The maximum pressures that can be reached using this type of cell are around 10 kbar.

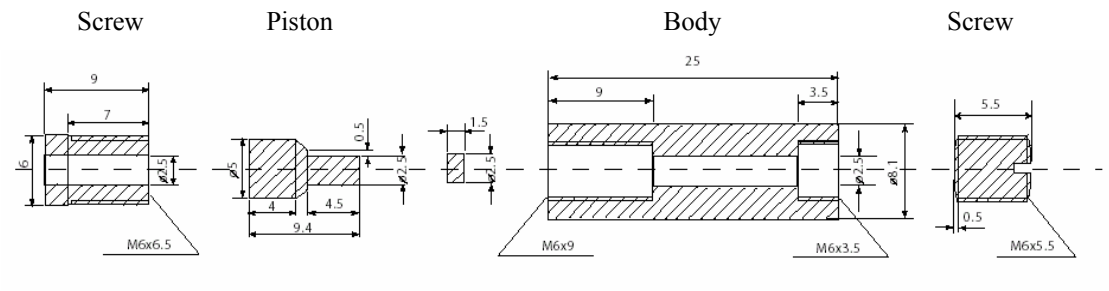

(a)

(b)

Figure 3.2: (a) Diagram and (b) photo of pressure cell for the SQUID.

3.2 Muon Spin Relaxation (MuSR)

A muon is a positively charged spin-½ particle, with a mass approximately 1/9th of that of a proton. Although, in terms of its properties, it is most like a heavy positron (they are both leptons), it can be thought of as a light proton. Muons are a naturally occurring constituent of cosmic rays, but for experimental work muon beams of higher intensity are required. These are created as follows; initially pions are produced when a high energy beam of protons is fired at a target (usually made of graphite) according to equation 3.1:

$$p + p \rightarrow \pi^{+} + p + n\,. \tag{3.1}$$

The pions produced then decay after a half-life of 0.026 μs into muons and muon-neutrinos:

$$\pi^+ \rightarrow \mu^+ + \nu_\mu . \tag{3.2}$$

One property of this decay is that if the pion has zero momentum, then the muons are 100 % spin polarised, with their spin lying anti-parallel to their momenta. In a MuSR experiment, the muons are then implanted into the sample. Due to their positive charge and small size, the muons tend to implant in interstitial sites close to electronegative atoms. If the muon experiences a magnetic field (B), either from within the sample or due to a macroscopic applied field, it will precess about this field with the Larmor frequency:

$$\omega_\mu = \gamma_\mu B , \tag{3.3}$$

where $\gamma_\mu (= ge/2m_\mu)$ is the gyromagnetic ratio of the muon. A muon has a half life of 2.2 μs, after which it decays into a positron, e^+, and two neutrinos:

$$\mu^+ \rightarrow e^+ + \nu_e + \overline{\nu}_\mu . \tag{3.4}$$

The positron is emitted with its momentum lying preferentially along the direction in which the spin of the muon lay when the muon decayed, as shown in figure 3.3.

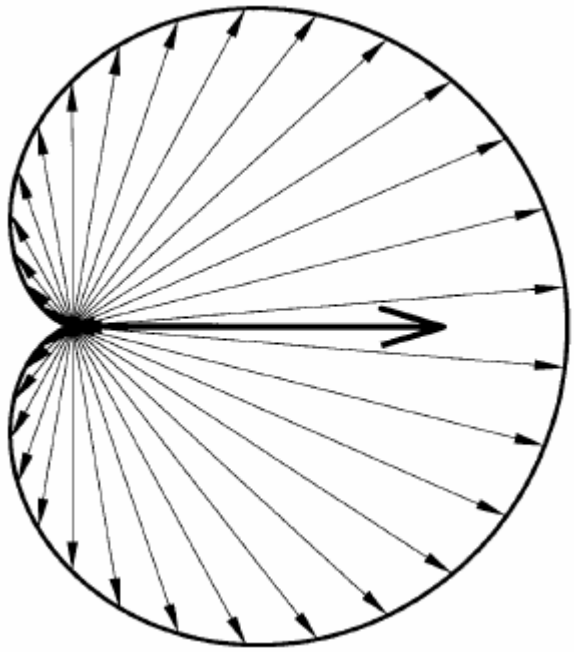

Figure 3.3: The angular distribution of emitted positrons with respect to the initial muon-spin direction. The figure shows the expected distribution for the most energetically emitted positrons. Figure taken from reference [6].

Therefore the direction in which the positron is detected by the detectors gives an indication of the direction in which the muon spin was aligned at the moment of decay.

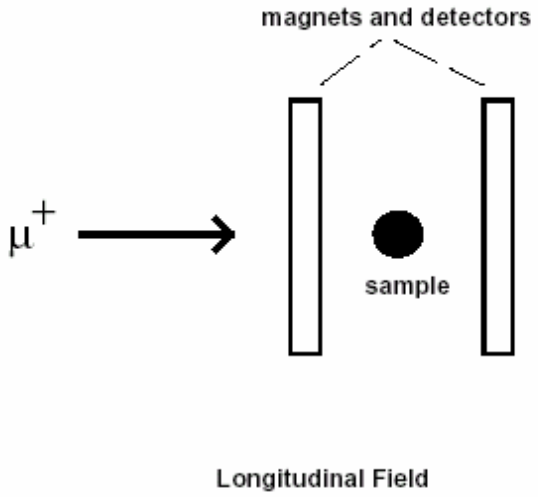

Figure 3.4: Location of magnets and detectors in relation to the sample position and initial muon polarisation direction. Figure taken from reference [6].

In a MuSR experiment, there are normally two banks of detectors; one ahead of the sample, and the other behind, with respect to the incoming muon beam. In a MuSR experiment, the quantity that we wish to know is the time-dependent spin polarisation of the muon, $G(t)$. This is measured as the difference between the number of positrons received at the forward and backward detectors as a function of time, which is normalised in order to account for the exponential decay in signal strength:

$$G(t) \propto \frac{F(t) - \alpha B(t)}{F(t) + \alpha B(t)}. \tag{3.5}$$

In this equation, α is a constant that quantifies the relative efficiencies of the forward and backward detectors for each experimental setup.

When the muon implants into the sample, the local magnetic field will lie at an angle, θ, to the initial muon spin direction. The muon will then precess about a cone of semi-angle θ about this field, which will result in a normalised decay positron asymmetry given by:

$$G(t) = \cos^2\theta + \sin^2\theta \cos(\gamma_\mu B t). \tag{3.6}$$

If the muons all implant into crystallographically equivalent sites within a sample with a static spin structure, each muon will experience the same magnetic field (either arising from the spins within the sample or from the external field applied to the sample), resulting in a unique value of B. If the direction of the local magnetic

field experienced by the muon is completely random as would be the case for a powder sample, then this equation can be averaged over all directions to give:

$$G(t) = \frac{1}{3} + \frac{2}{3}\cos(\gamma_\mu B t)\,. \tag{3.7}$$

This will cause the muons to all precess with the same angular frequency resulting in *G(t)* taking the form of an oscillating function of a single frequency. If the muons implant into two or more well defined sites in a sample with a static spin structure, the muons will precess with two or more well defined frequencies. In this case, $G(t)$ will consist of oscillations of these different frequencies. If the muons experience a distribution of local fields, they precess with a range of different frequencies. This will also cause a depolarisation of the muon spins as they precess, resulting in a loss in amplitude of $G(t)$ with time. The rate of depolarisation is determined by the size of the muon frequency distribution, with a large distribution leading to a rapid loss of amplitude.

If the magnitude of the local field is distributed about zero in the form of a Gaussian with a width Δ / γ_μ, as is the case when the muons experience the nuclear dipolar fields within the sample, it can be shown that the decay asymmetry takes the form of the Kubo-Toyabe function[7]:

$$G(t) = \frac{1}{3} + \frac{2}{3}\exp(-\Delta^2 t^2 / 2)(1 - \Delta^2 t^2)\,. \tag{3.8}$$

In order to minimise the effects of the nuclear dipolar fields, a small longitudinal field can be applied to the sample, which has the effect of aligning all the nuclear dipolar fields in a direction parallel to the initial muon polarisation. It is also important to minimise the depolarisation of the muon spin due to interactions with the nuclear dipolar fields arising from the sample environment. For this reason, silver is commonly used in the construction of the sample holder, as it has a negligible nuclear dipolar field. If the local field experienced by the muon is rapidly changing, either due to the magnetic moments rapidly fluctuating (as in a paramagnet) or the muon hopping through different sites within the sample, the muon spins will become depolarised relative to each other. This loss of polarisation gives a stretched exponential decay in *G(t)*, with the relaxation rate decreasing as the rate of spin fluctuations increase:

$$G(t) = \exp(-\lambda t)^{\beta}. \tag{3.9}$$

For paramagnetic systems, the relaxation corresponds to a simple exponential:

$$G(t) = \exp(-\lambda t). \tag{3.10}$$

In systems such as spin glasses, there are both random static correlations and dynamic components to the magnetic moments in the sample. In order to model this behaviour, Keren[8] has obtained an analytical approximation to the Kubo-Toyabe function in a dynamical magnetic environment, which allows both the static and dynamic components of the local magnetisation to be quantified. The form of this function is an exponential of a function of the longitudinal field strength (ω_L), the

size of the internal field distribution (Δ) and the spin-spin correlation time (ν). In the early time limit, it approximates to a Gaussian relaxation which is dependent on Δ.

The different relaxation functions that can be used to describe $G(t)$ give information about the variation of the local fields within the sample in time and space and can hence be used to study the evolution of magnetic structure within a sample with both temperature and magnetic field.

3.3 Neutron Scattering

A neutron is an uncharged subatomic particle, with a mass similar to that of a proton and is normally found within the nucleus of an atom. Within the nucleus it is a stable particle, but as a free particle it has a half-life of ~ 900 s. Since its discovery by Chadwick in 1932, the neutron has become a useful tool in condensed matter research.

When a neutron is fired at a material, it can either pass straight through it, or be absorbed or scattered by an atomic nucleus within the material. It is the scattering process that we are particularly interested in as it can provide information about the atomic structure and some of the collective excitations of the material. The neutrons that are not absorbed by the atomic nuclei leave the material and can be detected. Experimentally, the most common ways of detecting neutrons are to either use a ^{3}He detector, which works by producing a proton that then creates an electrical signal, or a ZnS detector, which works by the neutron creating a photon that is then detected by a photomultiplier tube.

Property	Value[9]
Mass, m	1.675×10^{-27} kg
Charge	0
Spin, S	½
Magnetic dipole moment, μ_n	$-1.913\ \mu_N$

Table 3.1: Fundamental properties of the neutron.

There are many properties of the neutron that make it a powerful tool for use in condensed matter science. Thermal neutrons have wavelengths of a similar size to typical atomic spacings, allowing them to be diffracted from solids and liquids, in a similar way to X-rays. Unlike X-rays, when neutrons scatter from materials, they do so by interacting with the nucleus rather than with the electron cloud, which can enable accurate atomic positions to be determined. Also, the scattering length, b (how effectively a particular atom scatters), varies independently of atomic number, with different isotopes of the same element scattering differently. This enables light atoms (*e.g.* hydrogen) to be seen, and isotopes of the same element or elements of similar atomic number to be distinguished. As neutrons carry no charge, they interact only weakly with the nuclei in a sample, making them a highly penetrating probe. This enables complex sample environments such as cryostats, cryomagnets or pressure cells to be used, as the neutrons can penetrate them. The energy of a thermal neutron is similar in scale to the energies of many collective atomic and electronic processes, allowing these processes to be probed by the scattering of neutrons. The neutron also has a magnetic moment that can couple to the variation in magnetic field on an atomic scale. This enables the study of both the static and dynamic magnetic structures of solids. Magnetic scattering is of a comparable

magnitude to nuclear scattering, enabling both the nuclear and magnetic structures to be probed simultaneously.

3.3.1 Neutron Formation

There are two main methods of producing free neutrons; these are *via* spallation or using a nuclear reactor. At a spallation source, a high energy pulse of protons is fired at a heavy metal target (*e.g.* tantalum, uranium or tungsten), where the protons effectively 'chip' neutrons off the metal. The neutrons produced at the ISIS Facility, in Oxfordshire (ISIS), are produced in this way. The neutrons at a spallation source such as ISIS are produced in pulses and can only be used with time-of-flight techniques. On the other hand, reactors such as those at the Institut Laue-Langevin (ILL) in Grenoble and the Hahn-Meitner Institute (HMI) in Berlin generate neutrons, by the fission of ^{235}U nuclei, producing a continuous flux of neutrons.

The energy of the neutrons produced is reduced by allowing them to come into thermal equilibrium with a moderator. This is usually a large quantity of matter containing large numbers of light atoms, and held at a known temperature. Cold moderators, containing H_2 or D_2 held at 25 K are used to produce neutrons of a long wavelength. Thermal neutrons are produced by moderators often made of D_2O held at ~ 300 K. In order to produce short wavelength neutrons, a hot moderator will be used, for example graphite held at 2000 K.

3.3.2 Elastic Nuclear Scattering

The scattering of a neutron by the nuclei in a sample is caused by nuclear forces which act over a very short range (10^{-14} – 10^{-15} m) in comparison with the wavelength, λ, of a neutron (~10^{-10} m)[9]. Therefore the nucleus can be considered as a point scatterer, and the scattering will be spherically symmetric. If we define **k** as the wavevector of the incident neutrons, which has a magnitude $k = 2\pi / \lambda$, and the z-axis is taken to be parallel to **k**, and take the scattering nucleus as the origin, the wavefunction of the incident neutrons can be expressed as:

$$\psi_{inc} = \exp(\mathrm{i}kz) . \tag{3.11}$$

As the scattering is spherically symmetric, the wavefunction of the neutrons scattered at a point a distance r from the nucleus is:

$$\psi_{sc} = -\frac{b}{r}\exp(\mathrm{i}kr) , \tag{3.12}$$

where b is the scattering length of the nucleus from which the neutron has been scattered, and is independent of the scattering angle. It is assumed that the nucleus is a weak absorber, and b (in this case a real quantity) independent of the energy of the scattered neutron. This equation assumes that the scattering is completely elastic – that no energy has been gained or lost by the neutron, and therefore that the magnitude of the incident and scattered wavevectors is the same. The value of b is determined by the particular nucleus in question, and on the spin-state of the nucleus-

neutron system. The results of a scattering experiment are expressed in terms of a scattering cross-section, σ. Usually the quantity measured in a scattering experiment is the partial differential cross-section, which is defined as:

$$\frac{\mathrm{d}^2\sigma}{\mathrm{d}\Omega\,\mathrm{d}E'} = \text{(number of neutrons scattered per second into a small solid angle d}\Omega\text{ in the direction }\theta,\phi\text{ with final energy between }E'\text{ and }E'+\mathrm{d}E')\,/\,\Phi\,\mathrm{d}\Omega\,\mathrm{d}E', \qquad (3.13)$$

where Φ is the flux of the neutrons incident on the sample. If the energy of the scattered neutrons is not analysed, but all the neutrons that are scattered into the solid angle dΩ are counted, it is the differential cross section that is measured. This is defined as:

$$\frac{\mathrm{d}\sigma}{\mathrm{d}\Omega} = \text{(number of neutrons scattered per second into d}\Omega\text{ in the direction }\theta,\phi)\,/\,\Phi\,\mathrm{d}\Omega. \qquad (3.14)$$

The total scattering cross-section, σ_{tot}, over all angles is given by:

$$\sigma_{tot} = \text{(total number of neutrons scattered per second)}\,/\,\Phi\,. \qquad (3.15)$$

It can be shown that the total scattered cross-section relates to the scattering length for a point scatterer as follows:

$$\sigma_{tot} = 4\pi b^2\,. \qquad (3.16)$$

In the case when scattering occurs from a single isotope with zero spin, constructive interference occurs, giving rise to Bragg peaks. This is known as *coherent* scattering and the coherent cross section, σ_c, is given by:

$$\sigma_c = 4\pi \left|\bar{b}\right|^2 . \tag{3.17}$$

When the scattering length varies on a particular site due to a distribution of isotopes or a non-zero nuclear spin, *incoherent* scattering occurs, contributing to the background. The incoherent scattering cross-section, σ_i, is given by:

$$\sigma_i = 4\pi \left(\left|b\right|^2 - \left|\bar{b}\right|^2 \right). \tag{3.18}$$

In neutron scattering experiments, it is desirable to minimise the background. This can be done by minimising the number of atoms with large incoherent scattering cross-sections.

	b / fm[10]	σ_c / barns	σ_i / barns
H	-3.7406(11)	1.7583(10)	80.27(6)
D	6.671(4)	5.592(7)	2.05(3)

Table 3.2: Cross sections of hydrogen (H) and deuterium (D)[10].

Hydrogen has a large value of σ_i and a relatively small value of σ_c, whereas deuterium has a small value of σ_i and a larger value of σ_c. For many neutron scattering experiments, it is therefore desirable to replace as many of the hydrogen

atoms as possible in a particular sample with deuterium in order to maximise the number of counts above the background.

For scattering from a collection of *n* nuclei, each situated at a displacement from the origin defined by the vector $\mathbf{r}_n$, the scattering cross section becomes:

$$\frac{d\sigma}{d\Omega} = \left| \sum_n b_n \exp\{i\mathbf{Q}\cdot\mathbf{r}_n\} \right|^2 , \tag{3.19}$$

where **Q** is the scattering vector, defined as being the difference between the wavevectors of the incident and scattered neutrons:

$$\mathbf{Q} = \mathbf{k}_i - \mathbf{k}_f . \tag{3.20}$$

A crystal is a periodic array of atoms, made up of identical building blocks called unit cells. The position of each atom in the unit cell can be described in terms of the fractional coordinates, (*x*, *y*, *z*). When a crystalline material, containing *N* unit cells, is considered, the strength of the scattering from a particular plane of atoms within the unit cell, defined by the Miller indices (*hkl*), is described as:

$$\frac{d\sigma}{d\Omega} = N^2 \left| \sum_d b_d \exp\{2\pi i(hx_d + ky_d + lz_d)\} \right| . \tag{3.21}$$

Strong elastic scattering occurs from a crystalline system when the Bragg condition, for a particular plane, is satisfied:

$$n\lambda = 2d_{hkl}\sin\theta, \tag{3.22}$$

where n is an integer, λ is the wavelength of the radiation, d_{hkl} is the spacing of the crystallographic planes and θ is the scattering angle. In neutron scattering, the relationship between the scattering vector, Q, and the d-spacing is often used:

$$Q = \frac{2\pi}{d_{hkl}}. \tag{3.23}$$

This enables simple comparison between data measured using different wavelength radiation.

3.3.3 Powder Diffraction

If a suitably sized single crystal of the material to be studied is available for an experiment, diffraction from a single plane of atoms will give rise to a single spot in the three-dimensional diffraction pattern. From this diffraction pattern, the structure can often be determined by direct methods, which requires little or no initial information about the structure. If a single crystal is unavailable, a powder must be used. In this case the quantity of powder used will be such as to allow a completely random array of crystallite orientations, relative to the incident beam, to be assumed. If the Bragg condition is satisfied for any of the crystallites, a Bragg peak will be

observed in the diffraction pattern. In the case of a powder, the three-dimensional information gained in the case of single crystal diffraction will be lost, and the diffraction pattern will be one-dimensional. A typical experiment will involve scanning either the wavelength of the incident radiation or the scattering angle and measuring the scattering intensity.

Due to the loss of this three-dimensional information in powder diffraction – often leading to the overlap of different reflections – it then becomes impossible to solve the structure by direct methods. Instead a method known as Rietveld refinement is used in order to find the possible structure[11]. In the Rietveld method, the diffraction pattern obtained is compared quantitatively with that calculated for a closely related model structure. The various parameters that affect the shape of the diffraction pattern will then be allowed to vary by small amounts, in order to minimise least squares (R_{wp}), the weighted (w_i) difference between the observed (y_i(obs)) and calculated (y_i(calc)) patterns:

$$R_{wp} = \left\{ \frac{\sum w_i (y_i(\text{obs}) - y_i(\text{calc}))^2}{\sum w_i (y_i(\text{obs}))^2} \right\}^{1/2} . \qquad (3.24)$$

Such parameters that are varied include the unit cell parameters, atomic positions and occupancies, background function, thermal parameters, and in the case of neutron diffraction, isotope occupancy. This process is continued until the experimenter is satisfied that R_{wp} has been minimised, leading to a refined structure.

As the Rietveld method is a structure refinement process rather than a structure solution method, it relies on having a good starting model for the structure. This means that it can only be used for systems about which a great deal of information is already known. The computer programme used to carry out all the refinements presented in this thesis is the General Structure Analysis System (GSAS)[12].

3.3.4 Magnetic Scattering

A property of the neutron, which is of great significance, is its magnetic moment, which allows it to interact with magnetic ions in a sample. As any magnetic scattering is from the electrons, which are distributed over distances of a similar order of magnitude to that of the neutron wavelength, the scattering is attenuated by a form factor, similar to that observed in X-ray diffraction. For a magnetically ordered structure, additional Bragg peaks will occur in the diffraction pattern. For a ferromagnet, the magnetic Bragg peaks will exactly coincide with the nuclear Bragg peaks, as the magnetic and nuclear unit cells are identical. For other ordered spin structures, *e.g.* an antiferromagnet, the magnetic unit cell is often larger than the nuclear cell, which can give rise to additional Bragg peaks that are absent in the nuclear diffraction pattern. As well as being governed by the magnetic form factor, the magnitude of the magnetic scattering is also affected by the magnitude and direction of the magnetic spin vector. Hence the differential magnetic cross section per unit solid angle, σ_m, for an individual ion, can be expressed as[13]:

$$\mathrm{d}\sigma_m = q^2 S^2 \left(\frac{e^2 \gamma}{mc^2} \right)^2 f^2, \tag{3.25}$$

where f is the magnetic form factor, γ the magnetic moment of the neutron, e the electronic charge, m the electronic mass, c the speed of light, S the spin quantum number of the scattering atom and q the magnitude of the magnetic interaction vector. The magnetic interaction vector, **q**, is defined as:

$$\mathbf{q} = \boldsymbol{\varepsilon}(\boldsymbol{\varepsilon} \cdot \mathbf{K}) - \mathbf{K}, \tag{3.26}$$

where **K** is a unit vector parallel to the atomic moment and **ε** is the scattering vector, a unit vector perpendicular to the scattering planes. Therefore **q** lies in the plane of **ε** and **K** perpendicular to **ε** and with a magnitude $\sin\alpha$. The relationship between the vectors **ε**, **K** and **λ**, the neutron polarisation vector, is shown in figure 3.5:

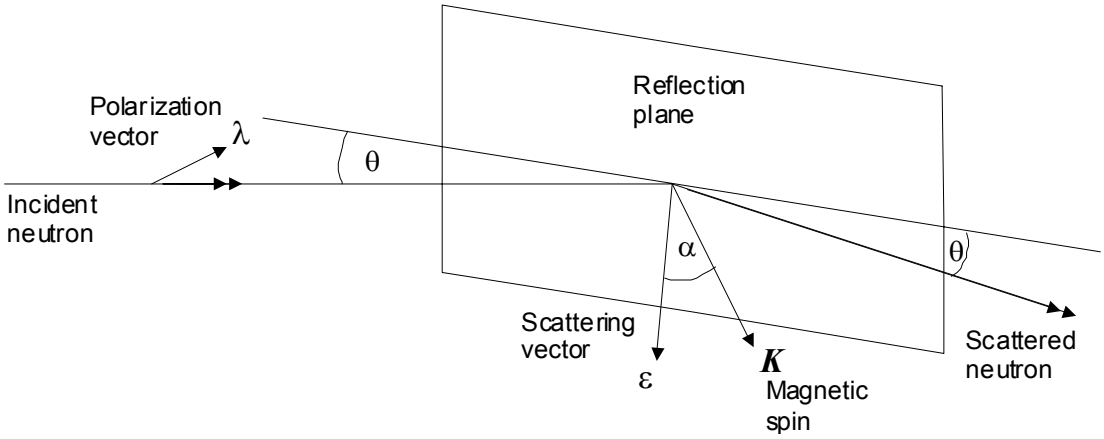

Figure 3.5: Diagram showing the relationship between the various vectors involved in the process of magnetic neutron scattering. Figure taken from reference [13].

This relationship indicates that magnetic neutron scattering arises only from the component of magnetisation lying perpendicular to the scattering vector. If the

magnetic moments in a sample have defined orientations, this leads to coherence between the neutrons scattered by the different individual atoms. Therefore the atoms can also be thought of as having a magnetic scattering length, p, in an analogous way to the nuclear scattering amplitude, b, such that[14]:

$$p = \left(\frac{e^2 \gamma}{mc^2} \right) Sf = 5.4 Sf \times 10^{-15} \text{m} . \tag{3.27}$$

This relationship shows that magnetic scattering is of the same order of magnitude as nuclear scattering.

3.3.5 Inelastic Neutron Scattering

In addition to giving structural information through elastic neutron diffraction, neutrons can also be used to probe the energetic processes within a material. In an inelastic neutron scattering experiment, both the momentum transfer, Q, and the energy transfer, $\hbar\omega$, of the neutron are measured. The intensity of such data is proportional to the double differential cross section (the neutron flux scattered through a small solid angle $d\Omega$ of final neutron energy between E and $E+dE$):

$$\frac{d^2\sigma}{d\Omega dE} = \frac{\mathbf{k}_f}{\mathbf{k}_i} b^2 S(Q,\omega) , \tag{3.28}$$

where $\mathbf{k}_i$ and $\mathbf{k}_f$ are the initial and final momenta of the neutron respectively and $S(Q,\omega)$ is the scattering function.

The energy of a thermal neutron (at 290 K, the energy of a neutron is 25 meV) is of a similar order to many of the excitations that may occur within a material, for example lattice vibrations (phonons) or magnetic excitations (magnons). A neutron scattered from a material may gain energy from or give energy to the material. For coherently scattered neutrons, the neutron energy transfer will be equal to the energy of the process excited within the material. As neutrons have a magnetic moment, the energy of magnons within a sample may be mapped out.

There are two main classes of inelastic neutron scattering instrument that can be used to study such excitations; the triple axis spectrometer (TAS) and the time of flight (TOF) spectrometer.

The type of instrument commonly used at a continuous neutron source is the triple axis spectrometer. This instrument allows the intensity of neutrons scattered with a particular energy transfer and from a particular point in reciprocal space to be measured. A schematic diagram of a triple axis spectrometer is shown in figure 3.6:

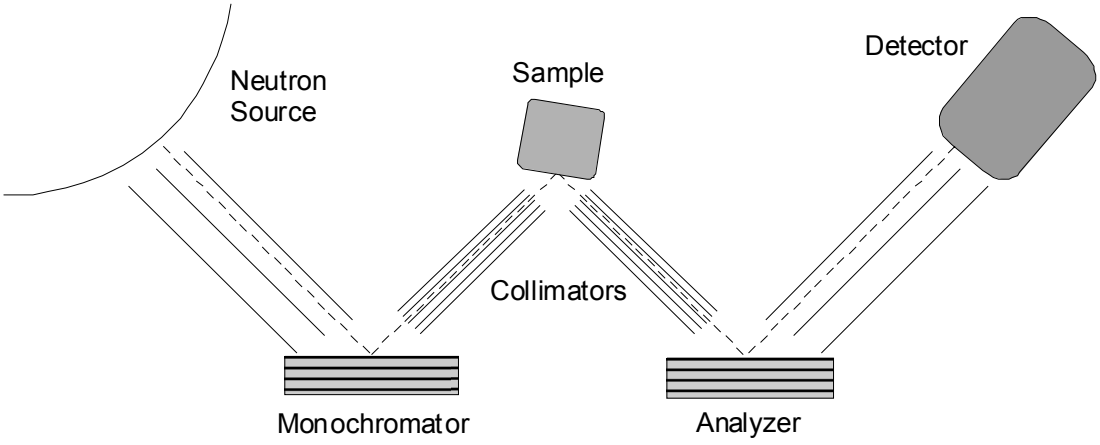

Figure 3.6: Schematic diagram of a triple axis spectrometer.

The incident energy of the neutrons is chosen by Bragg reflection of the 'white' (containing neutrons of a range of different energies) neutron beam from a monochromator crystal as the wavelength, λ, of a neutron is related to its energy, E, by the de Broglie relation:

$$E = \frac{h^2}{2m\lambda^2}. \tag{3.29}$$

The monochromator typically consists of an array of single crystals of copper or pyrolytic graphite. The array can be arranged in such a way as to focus the reflected neutrons onto the sample, thus increasing the effective incident neutron flux.

After the neutron beam is diffracted from the monochromator crystal, it then may be passed through a cooled beryllium filter. This filter removes the longer wavelength neutrons, as neutrons of harmonic wavelengths 2λ, 3λ *etc.* will also be diffracted by the monochromator, and, if left, would cause additional scattering, complicating the data analysis process.

The monochromatic neutron beam then continues to the sample. For a triple axis experiment, this will be in the form of a single crystal (or an aligned array of single crystals). The geometry of the apparatus will have been arranged so that the scattering angle, θ, and therefore momentum transfer, Q, is known, and corresponds to the point of interest in reciprocal space. These scattered neutrons of known Q and incident energy, E_i, are then Bragg diffracted by a further crystal, the analyser crystal. The purpose of the analyser crystal is to select the final energy, E_f, of the

neutrons. The neutrons finally pass into a detector, where the intensity of neutrons scattered with this particular combination of E_i, E_f (and therefore $\hbar\omega$) and Q will be measured. In order to build up a map of a dispersion curve, scans will be made at a number of different values of Q, E_i and E_f by altering the instrument geometry.

In contrast to the TAS technique, the TOF inelastic neutron scattering technique can be used at both pulsed and continuous neutron sources. Powder samples as well as single crystals can also be measured efficiently on these instruments. The TOF technique makes use of the fact that the speed of a neutron is related to its energy. Rather than measuring individual points on the dispersion curve, the time of flight technique allows $S(Q,\omega)$ to be mapped out over a range of values of Q and ω simultaneously.

A pulsed neutron beam is needed for a time of flight neutron experiment. At a spallation source the neutrons are already pulsed, but at a continuous source, the beam needs to be broken into pulses. To do this, the continuous beam passes through a chopper. A chopper is a disc or drum largely made of a neutron absorbing material, with a slit made of a neutron transmitting material. By rapidly rotating the chopper in the path of the neutron beam, the continuous beam is chopped into pulses. These, initially 'white' neutron pulses then pass on to the rest of the instrument. There are two kinds of time of flight spectrometers, termed direct geometry and indirect geometry instruments.

In a direct geometry spectrometer, the pulses of neutrons pass through a further set of choppers, or less commonly, a monochromator crystal, in order to select the initial neutron velocity and therefore the incident energy. These neutrons of known incident energy are then scattered by the sample, altering both the momentum and sometimes also the energy of the neutron. The momentum transfer of the neutron is manifested in a direction change; this is measured by using an array of detectors covering a large solid angle, to calculate the angle through which each neutron has been scattered. The energy change of each neutron results in a velocity change, those increasing in energy, increasing in velocity and *vice versa*. This is calculated by measuring the time that each neutron takes to reach the detector, with the most energetic neutrons arriving first. As the incident velocity and energy of each neutron is known, as is the time of scattering from the sample, the time of arrival at the detector enables the final velocity to be calculated. This further allows E_f and hence $\hbar\omega$ to be determined. A diagram depicting the path of neutrons through a direct geometry spectrometer is shown in figure 3.7:

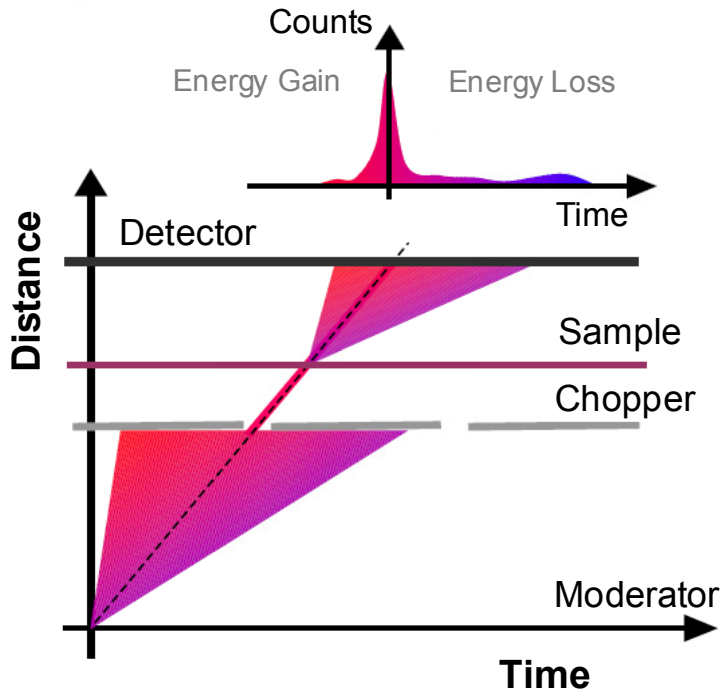

Figure 3.7: Time of flight diagram for a direct geometry chopper spectrometer. Figure taken from reference [15].

Another type of time of flight spectrometer is the indirect geometry spectrometer. In this case a 'white' neutron pulse is scattered by the sample, and then the final energy of the neutrons to be detected is selected by Bragg reflection from a monochromator. The incident energy of the neutrons can be determined from their time of arrival at the detectors. The neutrons with the highest incident energy, and hence the greatest energy loss, will arrive at the detectors first. Any Q dependence of the scattering will be detected by using an area detector. The neutron path through an indirect geometry spectrometer is depicted in figure 3.8:

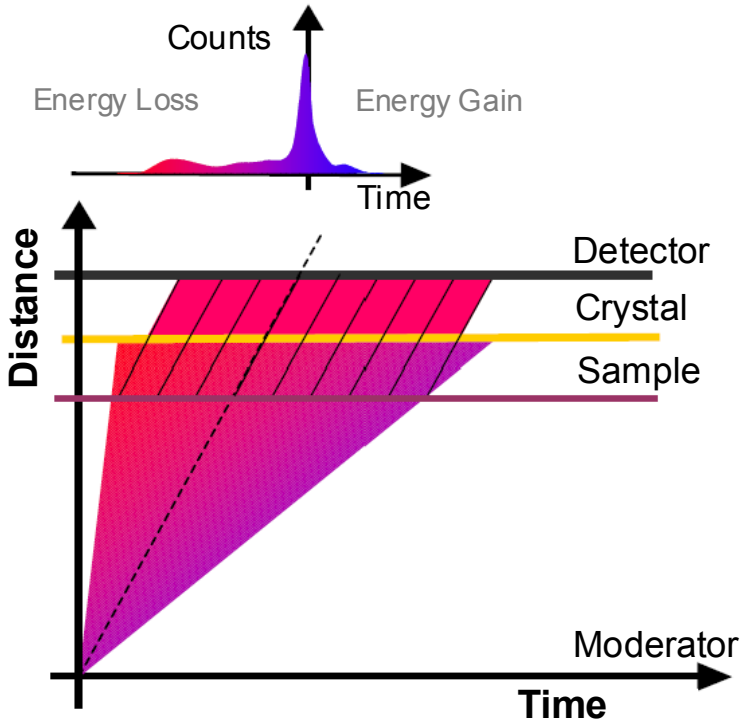

Figure 3.8: Time of flight diagram for an indirect geometry chopper spectrometer. Figure taken from reference [15].

3.3.6 Polarised Neutron Scattering

As a neutron is a spin-½ particle, it has a moment that can align parallel or anti-parallel to an applied magnetic field, therefore it is possible to produce spin polarised beams of neutrons. For a magnetic system where all the magnetic moments are aligned parallel or antiparallel to a particular direction, Halpern and Johnson[14] derived an expression for the differential scattering cross-section:

$$\mathrm{d}\sigma = b^2 + 2bp\boldsymbol{\lambda}\cdot\mathbf{q} + p^2q^2, \tag{3.30}$$

where $\boldsymbol{\lambda}$ is a unit vector in the direction of the spin of the incident neutron. For an unpolarised incident beam, the middle term in this equation will average to zero. On

the other hand, a polarised incident neutron beam will lead to interference between the nuclear and magnetic scattering terms.

The different ways in which neutrons of a particular polarisation interact with magnetic samples enables the neutron scattering to be separated into components arising from nuclear, spin-incoherent and magnetic scattering.

If the geometry of the neutron scattering instrument is designed such that the scattering vector, **q**, is always in the *xy*-plane; by taking different combinations of neutrons whose spin has been flipped or not by the sample in the three possible polarisation directions: *x*, *y* and *z*, it is possible to calculate the degree of scattering from different components of the system, as shown by Schärpf and Capellmann[16]:

$$\left(\frac{\partial^2\sigma}{\partial\Omega\partial E}\right)_{MAG} = 2\left[\left(\frac{\partial^2\sigma}{\partial\Omega\partial E}\right)^{X}_{SF} + \left(\frac{\partial^2\sigma}{\partial\Omega\partial E}\right)^{Y}_{SF} - 2\left(\frac{\partial^2\sigma}{\partial\Omega\partial E}\right)^{Z}_{SF}\right] \tag{3.31}$$

$$\left(\frac{\partial^2\sigma}{\partial\Omega\partial E}\right)_{MAG} = 2\left[2\left(\frac{\partial^2\sigma}{\partial\Omega\partial E}\right)^{Z}_{NSF} - \left(\frac{\partial^2\sigma}{\partial\Omega\partial E}\right)^{X}_{NSF} - \left(\frac{\partial^2\sigma}{\partial\Omega\partial E}\right)^{Y}_{NSF}\right] \tag{3.32}$$

$$\left(\frac{\partial^2\sigma}{\partial\Omega\partial E}\right)_{SI} = \frac{1}{2}\left(\frac{\partial^2\sigma}{\partial\Omega\partial E}\right)_{TSF} - \left(\frac{\partial^2\sigma}{\partial\Omega\partial E}\right)_{MAG} \tag{3.33}$$

$$\left(\frac{\partial^2\sigma}{\partial\Omega\partial E}\right)_{NUC} + \left(\frac{\partial^2\sigma}{\partial\Omega\partial E}\right)_{II} = \frac{1}{6}\left[2\left(\frac{\partial^2\sigma}{\partial\Omega\partial E}\right)_{TNSF} - \left(\frac{\partial^2\sigma}{\partial\Omega\partial E}\right)_{TSF}\right], \tag{3.34}$$

where:
$$\left(\frac{\partial^2\sigma}{\partial\Omega\partial E}\right)_{TSF} = \left(\frac{\partial^2\sigma}{\partial\Omega\partial E}\right)^{X}_{SF} + \left(\frac{\partial^2\sigma}{\partial\Omega\partial E}\right)^{Y}_{SF} + \left(\frac{\partial^2\sigma}{\partial\Omega\partial E}\right)^{Z}_{SF}, \tag{3.35}$$

and:
$$\left(\frac{\partial^2\sigma}{\partial\Omega\partial E}\right)_{TNSF} = \left(\frac{\partial^2\sigma}{\partial\Omega\partial E}\right)^{X}_{NSF} + \left(\frac{\partial^2\sigma}{\partial\Omega\partial E}\right)^{Y}_{NSF} + \left(\frac{\partial^2\sigma}{\partial\Omega\partial E}\right)^{Z}_{NSF}. \tag{3.36}$$

In the above equations, the Cartesian coordinate indicates neutron polarisation in that particular direction, *SF* and *NSF* indicate spin flip and non-spin flip cross sections respectively, *MAG* indicates the magnetic cross section, *SI*, the spin incoherent cross section, *NUC* the nuclear and *II* the isotope incoherent cross sections.

In order to produce a spin-polarised beam of neutrons, various different methods can be used, but for the experiments reported in this thesis, a supermirror bender which provides high polarisation efficiency over a wide wavelength band was employed. A supermirror consists of a number of magnetic / non-magnetic bilayers (*e.g.* Ti / Co) with the magnetic layer magnetised in the plane by permanent magnets. The scattering potential of the magnetised layers is dependent upon the spin direction of

the incident neutron, with spins of one polarisation being reflected satisfying the Bragg condition of the layer thickness, whilst neutrons of the opposite polarisation pass through and are absorbed by a Gd layer. By selecting a range of layer thicknesses throughout the supermirror, the wavelength range for which spin-polarised beams can be produced is extended. In order to ensure that all the neutrons are reflected at least once, supermirrors are curved.

Once a fully polarised neutron beam has been produced, the direction of the beam polarisation can be altered by the use of a spin flipper which will apply a field at a particular angle to the neutron guide field, in order for the neutron spin to precess into a different orientation.

In order to detect whether neutrons are of a particular polarisation, removable supermirrors are placed in front of the detectors, so that only neutrons of a particular polarisation will pass through to the detectors.

3.3.7 Neutron Spin Echo

In traditional inelastic neutron scattering experiments, the neutron energy transfer is determined by measuring the speed of the neutron before and after a scattering event. The finer the energy resolution required, the more accurately the neutron speed needs to be known. As neutrons are produced with a Maxwellian distribution of energies, infinitely high energy resolution therefore comes at a cost of infinitely low neutron flux. Neutron spin echo is an inelastic neutron scattering technique that decouples

the energy resolution from intensity loss. This allows high energy resolution over a large range of energy transfers reaching energy transfers as low as 0.1 neV. The technique was invented in 1972 by Ferenc Mezei[17]. A schematic diagram of the setup for a neutron spin echo experiment is shown in figure 3.9.

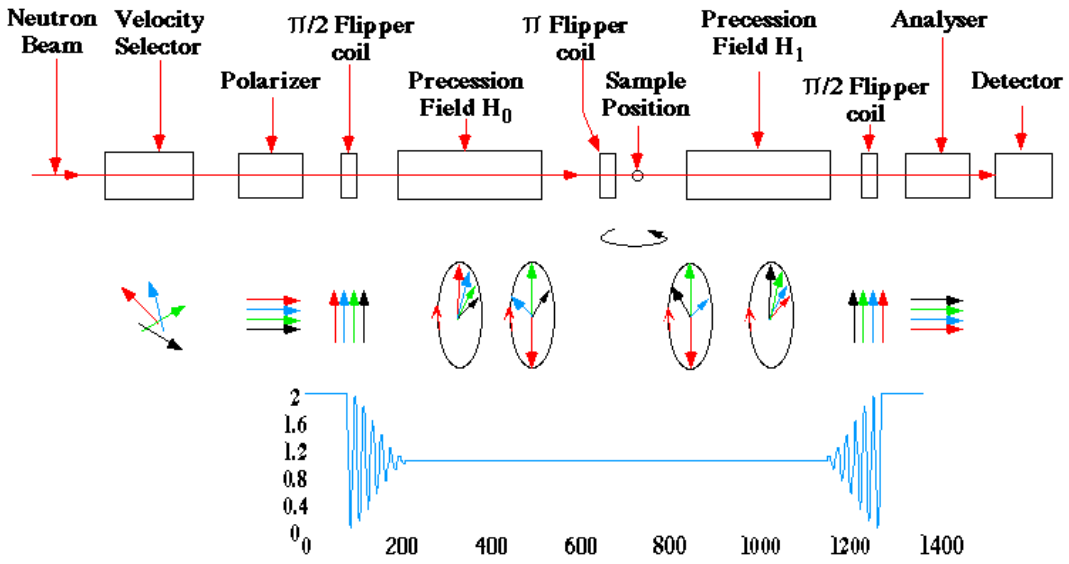

Figure 3.9: Schematic diagram showing the layout of components in a neutron spin echo experiment, along with the relative neutron polarisation and a graphical representation of how the net polarisation varies along the length of the experiment. Figure taken from reference [18].

Initially, a neutron beam is made roughly monochromatic by means of a velocity selector. After this selection, the energy distribution of the neutron beam is typically such that $\Delta\lambda/\lambda$ = 15 % FWHM. The beam of neutrons is then polarised in a direction parallel to the direction of propagation. At a certain point, the neutron polarisation is flipped by means of a π/2 flipper coil, such that the beam polarisation is all in a parallel direction, perpendicular to the direction of propagation. The neutrons then pass into the first precession field, H_0, applied parallel to the neutron beam. The neutron polarisation then precesses around the guide field with the Larmor

frequency. If the first precession field is of magnitude B_1 (= H_0) and length l_1, the total precession angle of the neutron, φ_1, will be:

$$\varphi_1 = \frac{\gamma B_1 l_1}{v_1}, \tag{3.37}$$

where v_1 is the neutron velocity and γ is the gyromagnetic ratio of the neutron. As the neutrons have a distribution of different energies, and therefore velocities; the precession angle of each neutron will be different, leading to a loss of beam polarisation. The neutrons will then scatter from the sample, which in the case of inelastic scattering, will result in a change of velocity. The polarisation will also be flipped by 180° at this point – either by the use of a π flipper, or by the sample itself, this has the effect of reversing the sense of rotation about the second guide field. The neutrons then enter the second guide field, H_1 (= B_2), and precess about it in the opposite sense to the first guide field. This second field is designed such that for elastically scattered neutrons (v_1 = v_2), the total precession angle in the second field will be identical to that in the first (φ_1 = φ_2), therefore $B_1 l_1$ = $B_2 l_2$. The beam polarisation will be completely restored for a sample that only scatters elastically, and any loss in beam polarisation will be as a result of inelastic scattering by the sample. A π/2 flipper then flips the component of the neutron beam where the polarisation has been restored to its original direction, back into a direction parallel to the beam propagation. These neutrons pass through a supermirror analyser and to a detector. By varying the fields in the two precession coils, and measuring how the

resulting polarisation varies, it is possible to measure how the scattering function varies with fourier time: $S(Q, t) / S(Q, 0)$.

3.4 References

[1] McElfresh, M., *Fundamentals of Magnetism and Magnetic Measurements featuring Quantum Design's Magnetic Property Measurement System*, ed. 1994, (Quantum Design: San Diego).

[2] Zieba, A., *Rev. Sci. Instrum.*, 1993, **64**(12): 3357 - 3375.

[3] Wohlleben, D. and Maple, M. B., *Rev. Sci. Instrum.*, 1971, **42**(11): 1573-1578.

[4] Guertin, R. P. and Foner, S., *Rev. Sci. Instrum.*, 1974, **45**(6): 863 - 864.

[5] Murata, K., Yoshino, H., Yadav, H. O., Honda, Y. and Shirakawa, N., *Rev. Sci. Instrum.*, 1997, **68**(6): 2490-2493.

[6] Blundell, S. J., *Contemp. Phys.*, 1999, **40**(3): 175-192.

[7] Kubo, R. and Toyabe, T., in *Magnetic Resonance and Relaxation*, Ed. by: Blinc, R., 1967, (North Holland: Amsterdam). p. 810.

[8] Keren, A., *Phys. Rev. B*, 1994, **50**(14): 10039-10042.

[9] Squires, G. L., *Introduction to the Theory of Thermal Neutron Scattering*, ed. 1978, (Cambridge University Press: New York).

[10] Sears, V. F., *Neutron News*, 1992, **3**(3): 26-36.

[11] Young, R. A., ed. *The Rietveld Method*. IUCr Monographs on Crystallography. 1995, (International Union of Crystallography, Oxford University Press: New York)

[12] Larsen, A. C. and von Dreele, R. B., *GSAS General Structure Analysis System*. 1994: University of California.

[13] Bacon, G. E., *Neutron Diffraction*, Third Edition ed, ed. 1975, (Oxford University Press: London).

[14] Halpern, O. and Johnson, M. H., *Phys. Rev.*, 1939, **55**: 898 - 923.

[15] *ISIS Neutron Training Course Manual*. 2003: Rutherford Appleton Laboratory, Oxfordshire.

[16] Schärpf, O. and Capellmann, H., *Phys. Stat. Sol. (a)*, 1993, **135**: 359 - 379.

[17] Mezei, F., *Z. Physik*, 1972, **255**: 146 - 160.

[18] http://www.ill.fr/YellowBook/IN11/

4 Square Lattice Antiferromagnets

4.1 Introduction

One of the key areas of activity in fundamental solid-state magnetism today concerns the way in which quantum fluctuations lead to non-classical behaviour. Interest in this field enjoyed a resurgence after the discovery of high-temperature superconductivity in layered cuprates whose parent compounds provide model two-dimensional (2D) $S = ½$ (quantum) Heisenberg antiferromagnets on a square lattice (2D QHAFSL). Early magnetic measurements[1, 2] suggested that the ground state of members of this class of magnet might be non-classical, and revived much earlier models and discussions[3] of the nature of magnetic correlations in low-moment, low-dimensional magnets. While subsequent magnetic measurements of various 2D QHAFSLs indicated that the ground state, and indeed many aspects of the one-magnon excitations are essentially classical, with small corrections for quantum fluctuations, there are still surprises[4, 5] particularly when perturbed through the application of a magnetic field[6, 7], or diamagnetic dilution of the magnetic lattice[8-10].

The application of a strong magnetic field may induce mixing of the one-magnon excitations and the two-magnon continuum, destabilising the former[6, 7]. It has been predicted that the spin waves may thus become unstable with respect to two-magnon decay at a critical field H^*. For square and cubic lattices $H^* \cong 0.76\ H_c$, where H_c is the critical field at which the magnetisation is saturated, and is equal to

$(8JS)/(g\mu_B)$[11] for a square antiferromagnet with the following magnetic Hamiltonian:

$$\mathcal{H} = J \sum_{<i,j>} S_i \cdot S_j \,. \tag{4.1}$$

Here the sum is over all spins i and their nearest-neighbours j, and J is the corresponding exchange constant. It is not practical to explore such effects experimentally using layered cuprates on account of the high value of J (≅ 1500 K), requiring fields of the order of 4500 T to bring about saturation. Copper formate tetrahydrate (CFTH), and its deuterated relative (CFTD), have smaller values of J (≅ 72 K), and have allowed in-depth studies of the model 2D QHAFSLs[5, 12-18] but they too would require impractical fields to probe behaviour in the region of H^* (H_{sat} > 200 T).

4.1.1 Previous Work

An alternative model system based on a lattice of Cu^{2+} ions connected magnetically through halide ions has been prepared and characterised[19-21] and shown to have a significantly lower energy scale for J. These materials have the chemical formula $(5CAP)_2CuX_4$ or $(5MAP)_2CuX_4$ (where X = Cl or Br, 5CAP is 2-amino-5-chloropyridinium and 5MAP is 2-amino-5-methylpyridinium). Detailed heat capacity and magnetic susceptibility measurements yielded the magnetic parameters summarised in table 4.1. J takes values in the range 0.76 – 8.5 K, which corresponds to saturation fields in the range 2.3 – 25 T. This promises access to an

unprecedented range of H/J to probe the influence of quantum fluctuations on this class of magnet.

Compound	$J\,k_B^{-1}$ / K	T_N / K	T_N / J	H_c / T	J' / J	Reference
La_2CuO_4	≅ 1500	310	0.21	4500	8.1×10^{-4}	[22, 23]
$Sr_2CuO_2Cl_2$	≅ 1450	251	0.17	4300	1.11×10^{-4}	[24]
$Cu(DCO_2)_2{\cdot}4D_2O$	71.8	16.5	0.23	220	1.9×10^{-3}	[14, 16, 18, 25]
$(5CAP)_2CuBr_4$	8.5	5.20	0.61	25.3	0.26	[20, 21], this work
$(5MAP)_2CuBr_4$	6.5	3.8	0.58	19.4	0.22	[21]
$(5CAP)_2CuCl_4$	1.25	0.754	0.60	3.62	0.25	[19], this work
$(5MAP)_2CuCl_4$	0.76	0.44	0.57	2.26	0.21	[19]

Table 4.1: Magnetic properties of selected S = ½ Heisenberg antiferromagnets on a square lattice; J is the nearest-neighbour in-plane exchange, and H_c is the critical field at which the magnetisation is saturated. Values of J'/J were calculated using an empirical expression based on Quantum Monte Carlo calculations in conjunction with experimental values of T_N and J[26].

This chapter is concerned with measurements made on the 5CAP analogues. This family was chosen as the smaller number of hydrogen atoms in the unit cell mean that it is cheaper and easier to make deuterated samples suitable for study by neutron scattering. A number of experiments have been carried out on both the chloride and bromide analogues in order to characterise these systems. Muon spin rotation (μSR) experiments were performed on fully protonated samples, in order to probe the nature of any magnetic ordering in the samples. Single crystal neutron diffraction experiments gave insight into the magnetic, and also in the case of the bromide analogue, nuclear structures, along with information about the magnetic phase diagram and critical exponents of the sub-lattice magnetisation. Finally, an inelastic neutron scattering experiment was performed on a single crystal of the chloride analogue, to probe the spin-wave excitation spectrum in an applied field and to determine the three-dimensional nature of the magnetic coupling in the system.

4.2 Synthesis

This section describes the syntheses of the samples investigated in the various experiments reported in this chapter. Where possible, fully protonated samples were used, but for neutron scattering experiments it is desirable to minimise the amount of hydrogen in the sample by replacing as much as possible with deuterium. A fully deuterated crystal of $(d_6\text{-}5CAP)_2CuBr_4$ was synthesised prior to the start of this project, and studied (see section 4.4.1), but unfortunately the sample quality degraded before any further experiments could be performed. Due to the expense and technical difficulties associated with the synthesis of fully deuterated 5-chloro-2-aminopyridine (d_6-5CAP), it was not possible to synthesise any more within the timescale and budget of this project; instead a partially deuterated ligand was synthesised.

4.2.1 Synthesis of 2-Amino-5-Chloropyridinium Tetrachlorocuprate Salt ($(5CAP)_2CuCl_4$)

Synthesis of $(5CAP)_2CuCl_4$ was based on an established method[19]. Concentrated (38 %) HCl (1.61ml, 1.9g, 20mmol, Aldrich) was added to $CuCl_2$ (1.34 g, 10 mmol, Aldrich, 99.999 %), followed by 2-amino-5-chloropyridine (5CAP) (2.57 g, 20 mmol, Aldrich, 98 %). H_2O (~ 20 ml) was then added, and the mixture stirred until all the solid had completely dissolved. It was found that adding ~ 1 ml HCl was necessary at this stage in order for the ligand to completely dissolve. The green solution was then filtered into a freshly prepared beaker (washed out with 10 % dimethyldichlorosilane (Aldrich) in ethanol, emptied and washed with acetone and

dried in the oven overnight), and placed in a desiccator containing fresh self-indicating silica gel, with an air flow through the desiccator. The silica gel was regularly replaced, and after a period of approximately six weeks, orange crystals of $(5CAP)_2CuCl_4$ had started to form. These were lozenge-shaped and grew to a size of typically 1 cm^3. Doped samples were made by substituting between 1 mmol and 3 mmol of $MgCl_2$, $CaCl_2$ or $ZnCl_2$ for $CuCl_2$. Flame photometry of the doped samples to calculate the level of doping gave results that were stoichiometrically impossible.

4.2.2 Synthesis of 2-Amino-5-Chloropyridinium Tetrabromocuprate Salt ($(5CAP)_2CuBr_4$)

Synthesis of $(5CAP)_2CuBr_4$ was based on an established method[21]. Concentrated (48 %) HBr (2.265 ml, 3.375 g, 20 mmol, Aldrich) was added to $CuBr_2$ (2.23 g, 10 mmol, Aldrich, 99.999 %), followed by 2-amino-5-chloropyridine (5CAP) (2.57 g, 20 mmol, Aldrich, 98 %). H_2O (~ 20 ml) was then added, the mixture stirred and additional HBr (~ 1 ml) was added until all the solid had completely dissolved. The dark brown solution was then filtered into a freshly prepared beaker (see section 4.2.1), and placed in a desiccator containing fresh self-indicating silica gel, with an air flow through the desiccator. The silica gel was regularly replaced, and after a period of approximately six weeks, dark crystals of $(5CAP)_2CuBr_4$ had started to form. The crystals were of no obvious morphology and were typically ~ 100 mm^3 in size.

4.2.3 Partial Deuteration of 5-Chloro-2-Aminopyridine (d_3-5CAP)

5-chloro-2-aminopyridine (5CAP) (21.3 g, 0.166 mol, Aldrich, 98 %) was added portionwise to D_2SO_4 (100 g, 53 ml, Aldrich, 99.5 % D) cooled in ice and under a flow of nitrogen. The mixture was then heated to 180 ºC for 6 hours, left to cool and then diluted with D_2O (~ 50 ml). NaOD solution was made by adding Na (51 g, 2.22 mol, Aldrich) to D_2O (~ 100 ml, Aldrich, 99.9 % D) under a stream of nitrogen. This was then added to the acid, still under a stream of nitrogen, until the pH had been raised to 12. NaCl was added to saturate the solution, and an extraction was carried out twice in ethyl acetate. The combined organic extracts were dried over $MgCO_3$, then filtered and the solvent evaporated off under vacuum. This left a pale yellow powder of partially deuterated 5CAP (13.05 g). The product was deuterated at the 3-position on the pyridine ring, and also at the two amine proton sites, as determined by ^{1}H NMR.

4.2.4 Synthesis of Partially Deuterated $(5CAP)_2CuCl_4$

Concentrated (37 %) DCl (1.04 ml, 10.26 mmol, Aldrich, 99 %) was added to $CuCl_2$ (0.69 g, 5.13 mmol, Aldrich, 99.999 %), followed by partially deuterated 5-chloro-2-aminopyridine (d_3-5CAP) (1.37 g, 10.26 mmol). D_2O (~ 20 ml, Aldrich, 99.9 % D) was then added, and the mixture stirred until all the solid had completely dissolved. It was found that adding ~ 1 ml DCl was necessary at this stage in order for the ligand to completely dissolve. The green solution was then filtered into a freshly prepared beaker (see section 4.2.1), and placed in a sealed desiccator containing

freshly dried, self-indicating silica gel. The silica gel was regularly replaced and, after a period of approximately six weeks, orange crystals of partially deuterated $(5CAP)_2CuCl_4$ had started to form. These crystals were lozenge-shaped and grew to sizes of the order of 0.5 cm^3.

4.3 Muon Spin Rotation

4.3.1 Experimental

Muon spin rotation (μSR) measurements were made on protonated samples of pure $(5CAP)_2CuX_4$, where X = Cl or Br. Measurements were also made on three samples of $(5CAP)_2CuCl_4$ where a small percentage of the copper had been replaced by group II metal ions. The nominal doping levels, as set by the concentrations of the metal ions in solution, were 20 % Mg, 30 % Mg and 30 % Ca. $MgCl_2$ and $CaCl_2$ were used to replace a fraction of the $CuCl_2$ in the synthesis. Attempts to confirm the doping level by elemental analysis were unsuccessful, as the results obtained did not make stoichiometric sense. Each of the samples was measured in the form of crystalline lumps.

The MuSR instrument at ISIS was used to perform these experiments. This instrument is shown in figure 4.1, and has 32 scintillation detectors – 16 front and 16 back – and frequencies over the range 0.1-10 MHz can be measured (the upper limit is defined by the muon pulse width). A magnetic field of up to 2500 G can be applied longitudinally to the sample; smaller transverse fields (normally used for

calibration) can also be applied. Crystalline pieces of sample were arranged in a 25 mm diameter disc and fixed to a silver sample plate with silicone grease, then covered with two layers of aluminium foil. The bromide sample was measured in an Orange cryostat, enabling measurements to be made at different temperatures between 2.3 and 9 K. The chloride samples were measured in an Oxford Instruments ^{3}He / ^{4}He dilution refrigerator. In this case, crystalline pieces of the sample were arranged in a 25 mm disc and mounted onto a silver plate with GE varnish, and the sample covered with a thin sheet of silver foil. Silver was used as the muons retain their polarisation when passing through silver. Measurements were taken at temperatures between 0.05 K and 1.7 K.

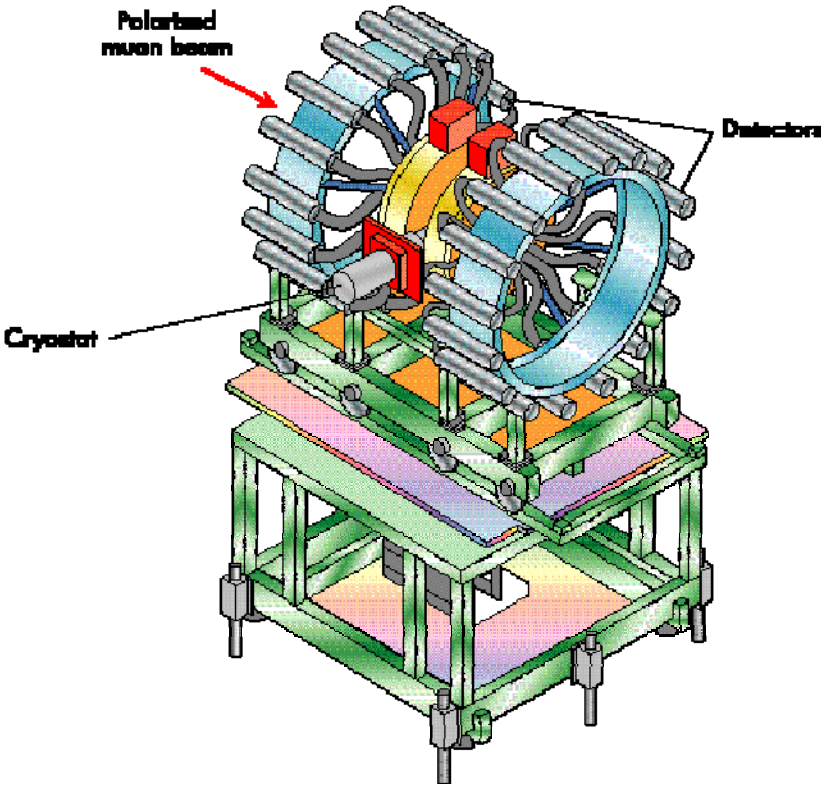

Figure 4.1: Diagram of the MuSR spectrometer at ISIS taken from reference [27].

Initially, the asymmetry of the muon measurement was calibrated. This was performed at 30 K for the bromide and at 6 K for the chloride; temperatures well above the Néel temperature (T_N) for the respective samples. The calibration was performed by applying a transverse magnetic field of 20 G to the sample and looking at the relative response of the forward and backwards detectors. For each of the samples, measurements were made in zero applied field. Measurements were made both above and below T_N, in order to allow the temperature dependence of the signal to be determined. The muon decay asymmetry, *G(t)*, defined as the normalised difference in the counts between the forward and backward detector banks, was plotted as a function of time after the muon pulse had hit the sample.

4.3.2 Results

Above T_N, *G(t)* was found to obey an exponential decay with a Kubo-Toyabe component; this is shown in figure 4.2. An exponential decay is the functional form expected for a paramagnet, and the Kubo-Toyabe component is used to model the muon coupling to the nuclear dipolar spins.

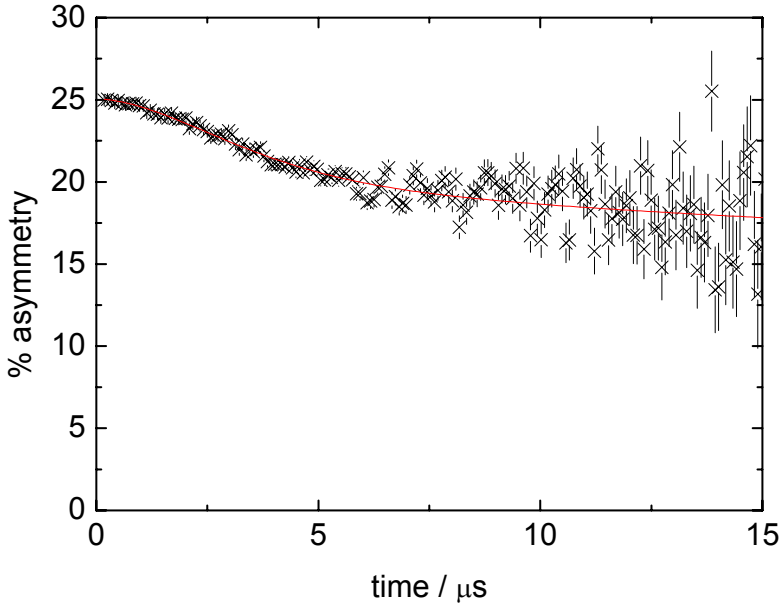

Figure 4.2: Muon decay asymmetry in $(5CAP)_2CuBr_4$ at $T = 6.13$ K (above T_N), shown by the black crosses, with a fit to an exponential decay with a Kubo-Toyabe component shown by the red line.

An oscillatory signal, appearing to contain at least two different components, was observed at temperatures below T_N, in each of the samples; this is shown in figure 4.3(a). Fourier transforms of the data (*e.g.* figure 4.3 (b)) show a distinct peak at frequencies below 1 MHz, and another around 2 MHz; in addition there are less distinct features at higher frequencies. An oscillatory signal is observed when a muon experiences a static magnetic field, with the frequency of oscillation proportional to the magnitude of the field experienced by the muon. The fact that there are at least two oscillation frequencies is indicative of the muons experiencing at least two different static internal magnetic fields. This is probably due to the muon implanting into at least two distinct crystallographic sites. For each of the samples, $G(t)$ was fitted to a function consisting of two distinct oscillation frequencies, each with a Lorentzian decay, and a background of Lorentzian form. Fitting to additional oscillating components did not improve the quality of the fits.

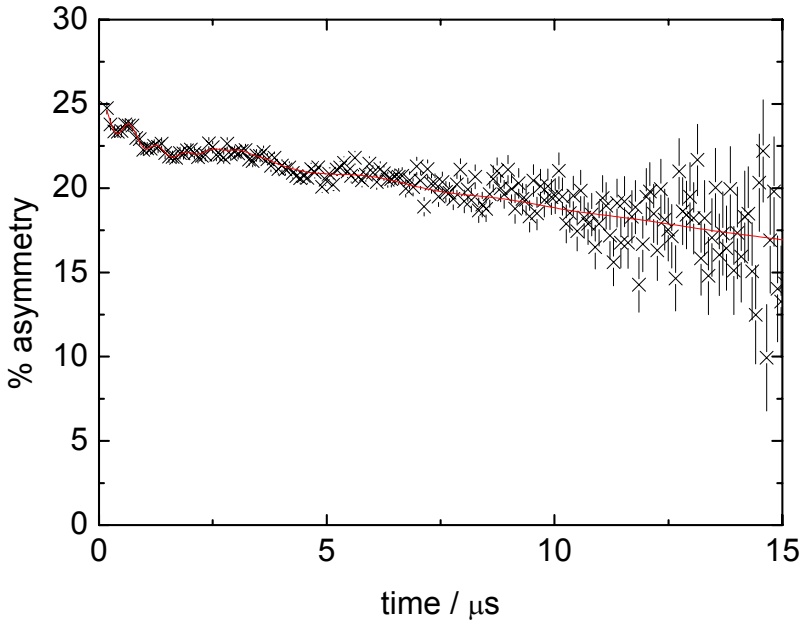

(a)

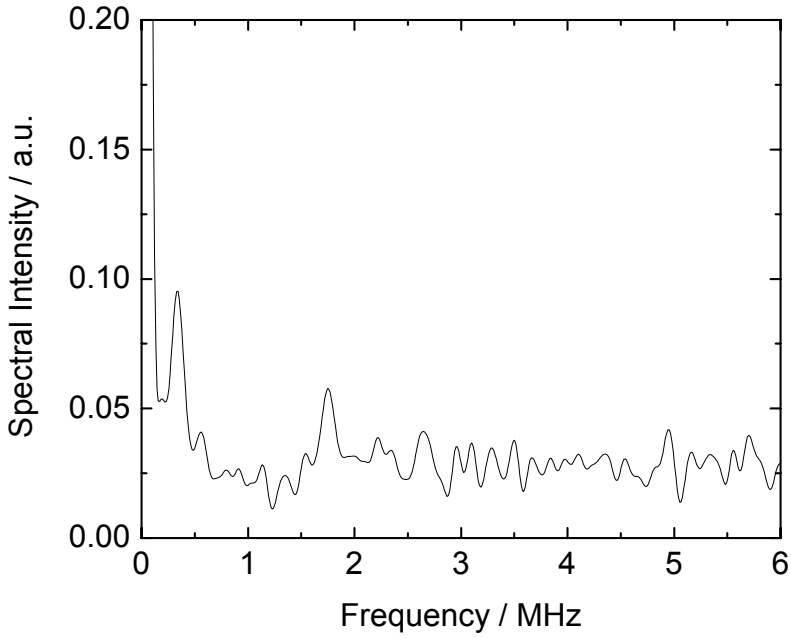

(b)

Figure 4.3: (a) Muon decay asymmetry in $(5CAP)_2CuBr_4$ at $T = 4.987$ K (below T_N), shown by the black crosses, with a fit to two oscillation frequencies with Lorentzian decays on a Lorentzian background shown by the red line and (b) Fourier transform of the same data.

Each oscillation frequency, ν, was then plotted as a function of temperature, T (see figures 4.4 and 4.5). As the temperature was increased towards T_N, both of the

oscillation frequencies decreased, tending towards zero at T_N. This was the same for each of the samples.

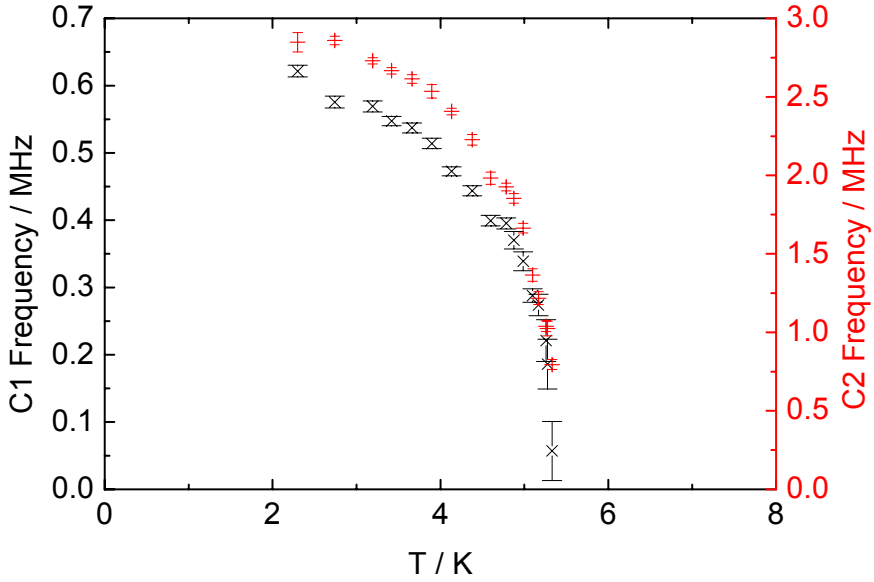

Figure 4.4: Temperature dependence of the two oscillation frequencies in the muon decay asymmetry below T_N for $(5CAP)_2CuBr_4$, with the low (C1) frequency shown by the black crosses and the high (C2) frequency shown by the red plus signs.

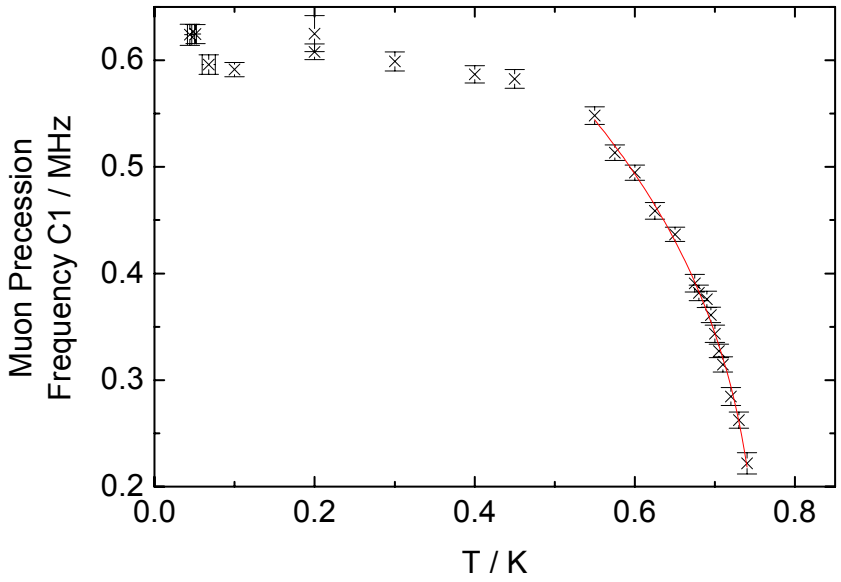

Figure 4.5: Temperature dependence of the low (C1) frequency oscillation in the muon decay asymmetry below T_N for $(5CAP)_2CuCl_4$ shown by the black crosses, with the red line showing the critical exponent fit with $T_N = 0.755(5)$ K and $\beta = 0.349(7)$.

The decrease in frequency with temperature was in accordance with the relation:

$$\nu \propto \left(\frac{T_N - \mathrm{T}}{T_N} \right)^{\beta}, \tag{4.2}$$

where β is the critical exponent for sublattice magnetisation. In order to determine the critical exponent, β; $\log_{10}\nu$ was plotted against $\log_{10}\left(\frac{T_N - \mathrm{T}}{T_N} \right)$, as shown in figure 4.6. The value of the gradient, β, was determined by least squares methods, using Origin™ version 7.5.

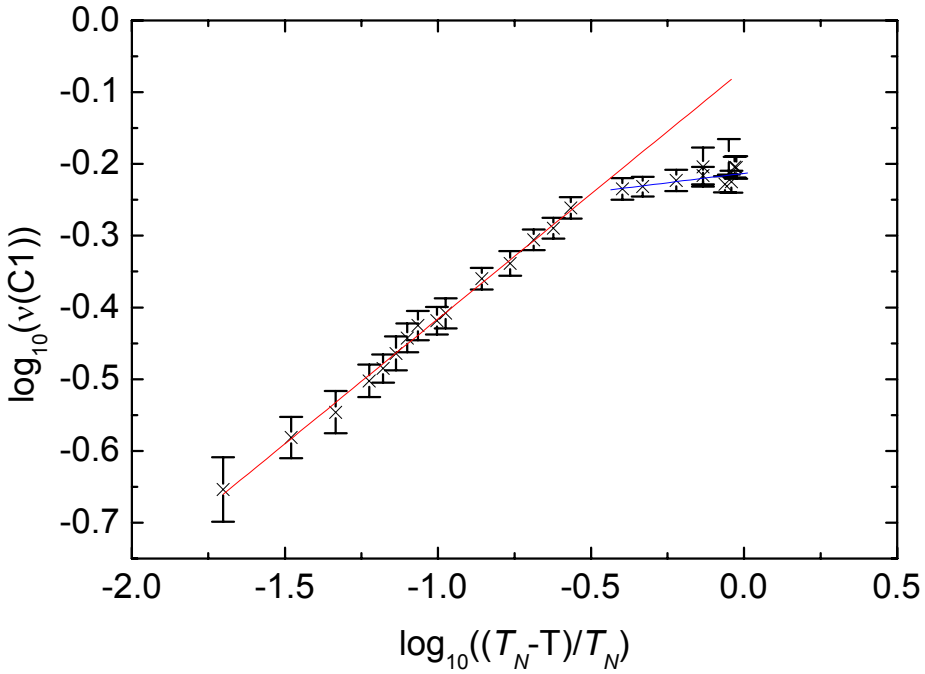

Figure 4.6: Plot of $\log_{10}$(frequency) against $\log_{10}((T_N - \mathrm{T})/T_N)$ for the low (C1) frequency oscillations in the muon decay asymmetry for $(5CAP)_2CuCl_4$, shown by the black crosses. The two lines show the two linear fits in order to determine the critical exponents, β; the red line showing the fit to the low temperature data and the blue line showing the fit to the high temperature data.

For the undoped $(5CAP)_2CuCl_4$ sample, the data were fitted over a temperature range of 0.55 K to 0.74 K; this is shown in figure 4.6. T_N was found to be 0.755(5) K, and the critical exponent, $\beta = 0.349(7)$ for the low frequency oscillation, C1, and for the high frequency oscillation, C2, $\beta = 0.222(2)$. The value of β for C1 is similar to the expected value of β for a Heisenberg magnet of 0.367[28], whereas the value of β found for C2 is close to that predicted by Bramwell and Holdsworth[29] for the 2D *XY* model, and in line with the values found for other 2D QHAFSLs[14, 24, 30]. The data below 0.55 K were also fitted, to give a value of $\beta = 0.05(2)$ for the C1 oscillations and $\beta = 0.056(8)$ for the C2 oscillations, which are both unphysical values.

For $(5CAP)_2CuBr_4$, a value of 5.355 K was used for the T_N. This gave the most realistic values for β. The data were fitted in the range 4.785 K to 5.33 K. A value of $\beta = 0.37(2)$ was found for the low (C1) frequency oscillations, and $\beta = 0.32(2)$ for the high (C2) frequency oscillations. Again, these values correspond well to the expected value for a Heisenberg antiferromagnet. When the data taken at temperatures below and including 4.785 K were analysed, the C1 oscillations resulted in critical exponents of $\beta = 0.28(1)$ and $\beta = 0.25(1)$ for the C2 oscillations. These compare well with the value obtained for $(5CAP)_2CuCl_4$.

For the nominally doped samples of $(5CAP)_2CuCl_4$, the initial asymmetry of the muon signal was much lower than expected. This indicates that there is a relaxation process that is occurring on a much faster timescale than that of the measurement. For all three of the doped samples, T_N was suppressed by a small amount in

comparison with the undoped compound. This is indicative of a very small level of doping in each case. For the nominally 30 % Ca doped $(5CAP)_2CuCl_4$, $T_N = 0.735(7)$ K, the nominally 20 % Mg doped sample, $T_N = 0.743(5)$ K and for the 30 % Mg doped sample, $T_N = 0.724(2)$ K.

4.4 Neutron Diffraction

4.4.1 $(d_6\text{-}5CAP)_2CuBr_4$

4.4.1.1 Experimental

In order to investigate both the nuclear and magnetic structure of $(5CAP)_2CuBr_4$, a single crystal neutron diffraction experiment was performed by other members of our research group[31]. The four-circle diffractometer, D10 at the Institut Laue-Langevin, Grenoble was used to collect these data; a schematic diagram of this instrument is shown in figure 4.7.

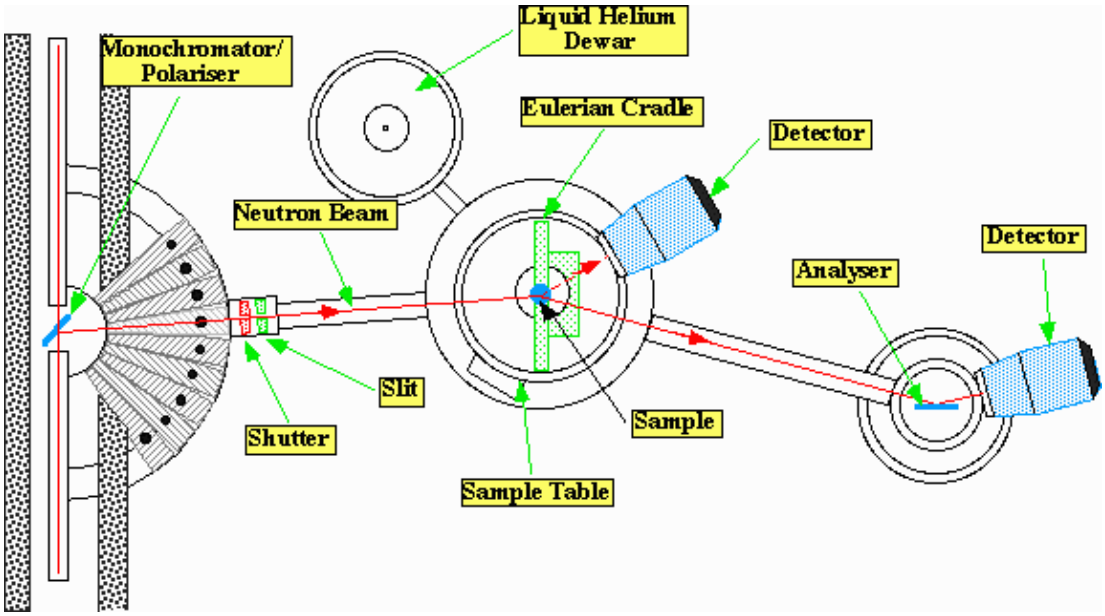

Figure 4.7: Schematic diagram of the D10 diffractometer at the ILL, taken from reference [32].

D10 is located on a thermal neutron guide and incident neutron wavelengths ranging from 1.1 – 6 Å can be selected by use of either a pyrolytic graphite or copper monochromating crystal. This monochromatic beam of neutrons then passes to the sample, which when the instrument is in four-circle mode, is located on an Eulerian cradle, allowing the scattering geometry to be easily altered. After scattering from the sample, the neutrons then pass to a detector – in this case an area detector was used. In order to minimise the incoherent scattering from the sample, a fully deuterated sample was used - $(d_6\text{-}5CAP)_2CuBr_4$. The crystal chosen was the largest available, with dimensions $6.0 \times 1.4 \times 1.8$ mm^3. It was compact in form with clearly defined faces and edges, although the morphology gave no clear indication of the orientation of the crystallographic axes. The sample was glued onto a cadmium sample pin with epoxy resin, and mounted in a He-flow cryostat[33]. This setup allows temperatures down to 2 K to be reached with little loss of four-circle access. The small two-dimensional area detector[34] on D10 was used in order to allow

optimal delineation of the peak from the background. To measure the weak magnetic reflections, a wavelength of 2.3604(6) Å was used, selected using a vertically-curved pyrolytic graphite (0 0 2) monochromator. A shorter wavelength of 1.5318(6) Å using a vertically-focussing multi-element Cu (2 0 0) monochromator was used for measurement of the higher-*Q* structural reflections. Structural refinements were carried out by Garry McIntyre of the ILL, in order to determine both the nuclear and magnetic structures. Details of these refinements can be found in appendix A1. I have carried out the remainder of the analysis on this sample reported in this thesis.

4.4.1.1.1 Magnetic Critical Behaviour

Among the reflections that had significant intensity at 1.8 K but negligible intensity at 10 K, the (1 0 1) reflection was the strongest. This was used to determine the temperature dependence of the sublattice magnetisation from 1.8 K to temperatures in the region of 5 K.

4.4.1.2 Results

4.4.1.2.1 Crystal Structure at 10 K

The geometry and atom numbering of the asymmetric unit of $(d_6\text{-}5CAP)_2CuBr_4$ produced by the structure refinement are shown in figures 4.8 and 4.9. Final atomic positional and equivalent isotropic displacement parameters are given in table A1 in appendix A1 and the anisotropic displacement parameters for the deuterium sites in table A2. Selected interatomic distances and interbond angles are listed in table A3.

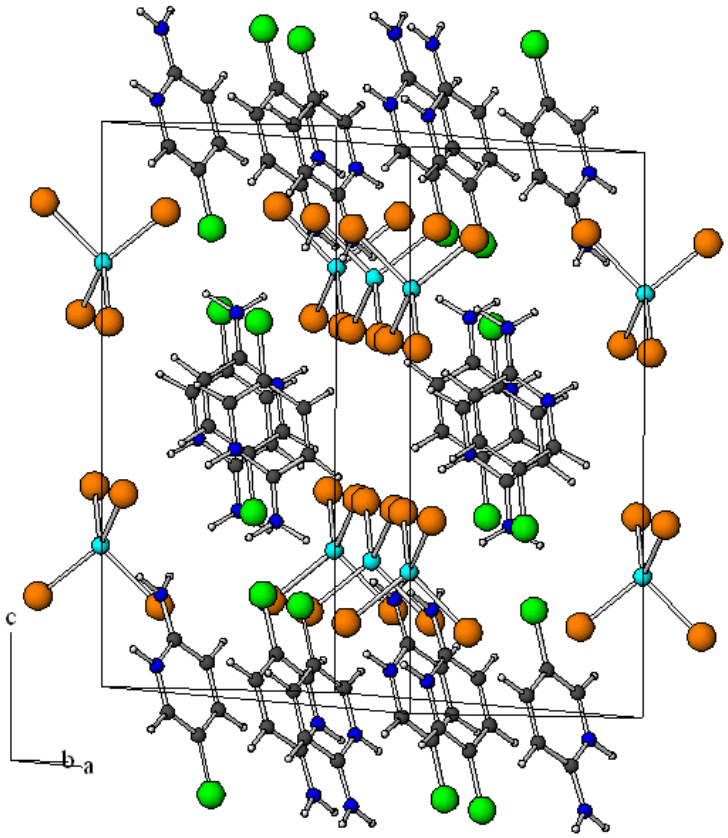

(a)

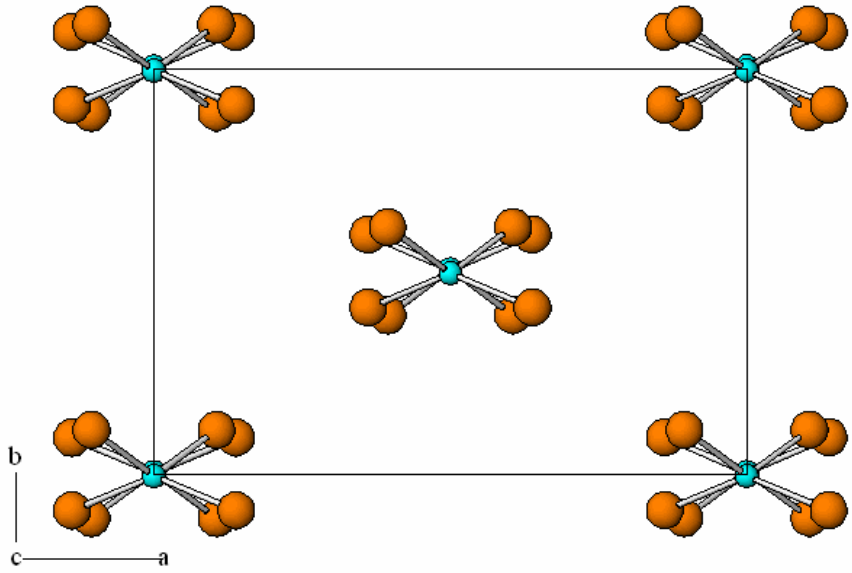

(b)

Figure 4.8: Diagram showing the crystal structure of $(5CAP)_2CuBr_4$, (a) viewed along a direction close to the ***a*** + ***b*** direction with the *c*-axis almost vertical and (b) viewed down the *c*-axis, showing the Cu environment. The atoms are depicted as following: Br – brown, Cl – green, Cu – light blue, N – dark blue, C – black and H/D – white.

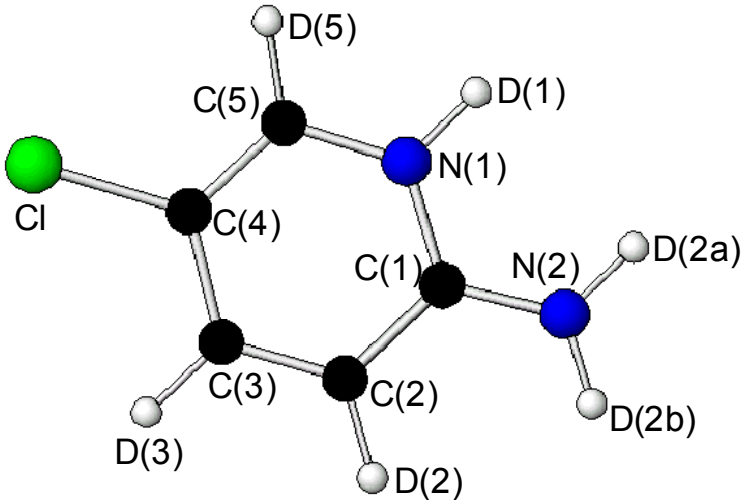

Figure 4.9: Diagram showing the 5-chloro-2-aminopyridinium ion and the numbering scheme used.

The structure at 10 K is essentially the same as that determined at 143 K by X-rays[21], although the deuterium coordinates are found to considerably better precision in the neutron experiment. The large distortion of the $CuBr_4^{2-}$ anion from ideally tetrahedral is observed again at 10 K, although it is not obvious from the stereochemistry why the angular distortion should be so severe. The organic cation is planar to within 0.17 Å, and all bond distances and angles within the cation lie near the average values observed for the same bonds in other compounds[35], indicative of little intermolecular interaction. For the structurally similar 2-amino-5-methylpyridinium copper tetrabromate and tetrachlorate, it was surmised[36] that the crystal-field stabilization energy dominates the electrostatic interaction in the presence of strong hydrogen bonding to give a copper tetrahalide geometry closer to square planar than to tetrahedral. A lesser influence might be repulsion between Br and Cl on the pyridinium ring to maintain the acceptable contact of 4.25(2) Å.

4.4.1.2.2 Magnetic Structure at 1.8 K and Sublattice Magnetisation

There are four Cu sites in the *C*-centred unit cell, related to each other by the *C*-centring and the centre of inversion. The *C*-centring is clearly not satisfied by the magnetic structure, but it is reasonable to initially assume that this might correspond simply to a reversal in the directions of the moments on the sites related by the *C*-centring. The presence of an inversion centre means that all magnetic reflections with $l = 0$ are forbidden. That the (1 0 -1) reflection is much weaker than the (1 0 1) suggests that the Cu moment lies nearly along the [1 0 -1] direction. Refinement against a model with a moment of the same magnitude on all four Cu sites, and a reversal of the directions on sites related by the *C*-centring, gave an acceptable fit with agreement indicators R(F) = 16.6 %, wR(F) = 13.3 % and $\chi^2 = 3.86$. The Cu moment was found to be 0.45(1) μ_B, inclined 47(4)º to the *c*-axis near [1 0 -1] within the *ac*-plane.

The intensity of the strongest magnetic reflection, $I(1\ 0\ 1)$, was determined as a function of temperature and field by fitting to a Gaussian curve, where all the parameters were allowed to vary freely. This resulted in a stable fit with relatively little correlation between fitting parameters, even close to T_N. Figure 4.10 depicts the variation of the height of the Gaussian with temperature. There was no attempt in the final fitting process to correct for scattering from critical fluctuations in the region of T_N[37, 38]. The temperature dependence of $I(1\ 0\ 1)$ was analysed by least-squares fits to the standard expression[37] for the critical exponent β for sublattice magnetisation: $I(1\ 0\ 1) = A \cdot \varepsilon^{2\beta}$, where $\varepsilon = (T_N - T)/T_N$. Optimised values from this

procedure were found to be T_N = 5.18(1) K and β = 0.23(4), for data taken over the temperature range 4.95 – 5.17 K (ε = 0.048 – 0.0057) (inset to figure 4.10).

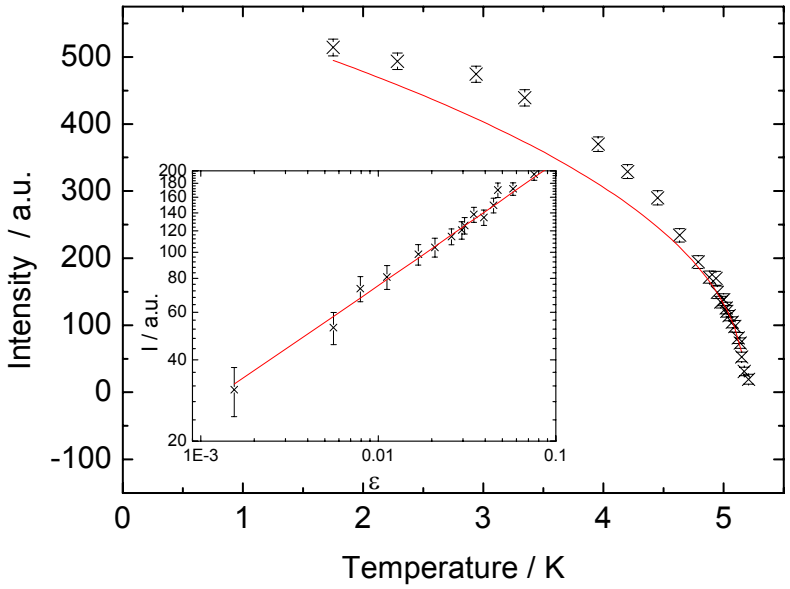

Figure 4.10: Dependence of I(-1 0 -1) on temperature for (5CAP) copper (II) bromide in zero applied field. Data have been corrected for background scattering. The inset to the figure shows a least-squares fit of the temperature dependence of I(1 0 1) for (5CAP) copper (II) bromide to the standard power-law expression $I(T) = A \cdot \varepsilon^{2\beta}$; T_N = 5.18(1) K, β = 0.23(4).

This value of β is similar to that reported for other 2D QHAFSLs: CFTD[14] displays a value of 0.23(1), crossing over to a value of 0.32(2) close to T_N ($\varepsilon < 0.06$). $Sr_2CuO_2Cl_2$[24] yields β = 0.22(1), while for La_2CuO_4[30] the value of 0.28 has been reported. Since the ideal 2D Heisenberg system cannot order at finite temperatures, the 3D order observed in real materials is inevitably due to interlayer coupling. Therefore, 3D critical exponents (0.326, 0.345 and 0.367 for the Ising, *XY* and Heisenberg cases respectively) can be expected sufficiently close to T_N. If the interlayer coupling is assisted by easy-plane anisotropy, at lower temperature a crossover to the Bramwell-Holdsworth value of approximately 0.23 for β [24, 29, 39, 40] might be anticipated. Such a crossover is observed in CFTD, whilst the more 2D

$Sr_2CuO_2Cl_2$ perhaps only reaches 3D exponents closer to T_N than hitherto experimentally accessed. Dedicated critical scattering experiments on $(d_6\text{-}5CAP)_2CuBr_4$ and other model materials would be warranted for a better understanding of the order and extent of crossover regions, as well as the alternatively proposed β = 0.25 due to the proximity of a tri-critical point in La_2CuO_4[41].

There has been some debate on the overall form of $M(T)$ for quantum 2D systems, with the proposal that a $T\ln T$ law is expected as $M(T)$ tends to the T = 0 saturation value, M(0)[29, 39, 42], and a mean-field dependence, with β = 0.5, closer to T_N[40]. Being limited to temperatures higher than 1.75 K (~ T_N / 3) means that the low-temperature limit of $M(T)$ cannot be investigated.

Attempts were also made to observe scattering from short-range correlations above T_N, by scanning in a direction perpendicular to c^* through (0 –1 0.2475) but the scattering was too weak to merit further study with this sample.

4.4.2 $(5CAP)_2CuCl_4$

4.4.2.1 Experimental

In order to study the magnetic structure of $(5CAP)_2CuCl_4$, two single crystal diffraction experiments were carried out on the 2-axis E4 diffractometer (shown in figure 4.11) at the BER-II reactor at the Hahn-Meitner Institute (HMI), Berlin. The

incident neutron wavelength on this diffractometer is selected by Bragg reflection from the (0 0 2) plane of focussing pyrolytic graphite crystals. After diffraction by the sample, the neutrons are then detected by a single ^{3}He detector; this can move to cover a 2θ range of 0° to 120°.

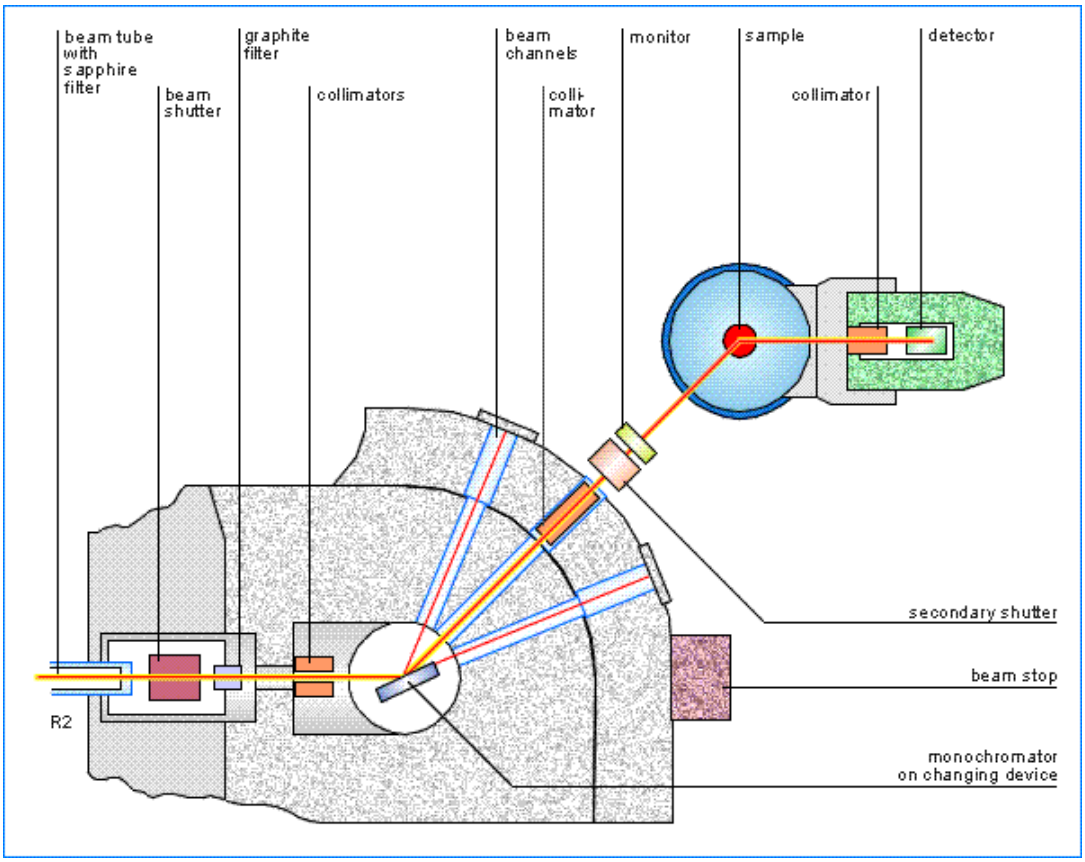

Figure 4.11: Schematic diagram of the E4 diffractometer at HMI, taken from reference [43].

The first experiment reported here was performed by other members of our research group[44]. For this first experiment, the sample of $(d_6\text{-}5CAP)_2CuCl_4$ formed lozenge-shaped crystals such that c^* was perpendicular to the faces with largest area. The largest crystal ($5.0 \times 2.5 \times 1.5$ mm^3) was oriented with a^* and c^* in the horizontal scattering plane of the neutron diffractometer. The sample was then attached to a copper pin with epoxy resin, and the pin and glue shielded with cadmium before mounting in an Oxford Instruments Kelvinox dilution refrigerator,

and placed in the core of the VM2 split-coil, vertical-field magnet (base temperature 0.03 K, maximum field 7 T). The diffractometer was set up with 20' collimation on the beam incident on the sample, 40' collimation in front of the detector and a neutron wavelength of 2.426 Å (PG 0 0 2).

A survey was made of likely magnetic reflections at 0.03 K, scanning positions (h 0 l) for $h = 0 \rightarrow 3$ and $l = -3 \rightarrow 3$ (the limits of these scans being set by the wavelength and the geometry of the instrument). The strongest of those reflections that are forbidden for nuclear scattering in space group $C2/c$ (space group 15 (b1) in the International Tables of Crystallography[45]) was again the (1 0 1) (we have assumed that the space group determined at 143 K by X-ray measurements is still appropriate for these low temperatures[19] and the selection rule for this space group is h or $l = 2n$ for h 0 l reflections). This was then studied as function of temperature to determine T_N, and the evolution of the sublattice magnetisation. Subsequently the variation of T_N with H was mapped out up to 5 T.

A second experiment at HMI, which I was involved in, was performed on the E4 diffractometer in order to study the scattering from the (0 k l) plane. As the crystal used in the first experiment had degraded due to thermal cycling, a second crystal was used. The level of deuteration in this sample was considerably lower than the original sample (~ 67 %). The crystal was also smaller (4 mm × 3 mm × 2 mm) with the c-axis lying along the 3 mm direction. The crystal was mounted on a copper pin with epoxy resin such that the b^* and c^* axes were in the scattering plane. This was then mounted into a DS2 dilution refrigerator, enabling temperatures down to

0.050 K to be reached, and into a vertical field VM1 magnet (maximum field 14 T). A neutron wavelength of 2.444 Å was selected using a pyrolytic graphite (0 0 2) monochromator.

A survey was made of likely magnetic reflections at 50 mK, scanning positions (*0 k l*) for $k = -4 \rightarrow 4$ and $l = 0 \rightarrow 3$ (the limits of these scans being set by the wavelength and the geometry of the instrument). A number of reflections that are forbidden for nuclear scattering in space group *C*2/*c* (space group 15 (b1) in the International Tables of Crystallography[45]) (where the selection rule for this space group is *h* or *l* = *2n* for *h* 0 *l* reflections) were observed in zero field at base temperature (0.05 K); these were the (0 1 1), (0 1 -1), (0 1 3) and (0 1 -3) peaks. The strongest of these was the (0 1 -3) peak; this was then studied as function of *H* up to 8 T in order to look at the response of the system to an applied field.

4.4.2.2 Results

For the first experiment, where scattering was observed in the *a***c**-plane of $(d_6\text{-}5CAP)_2CuCl_4$, significant scattering was observed at (1 0 1), (1 0 -1), (3 0 1) and (3 0 -1), despite being in contravention of the reflection condition for nuclear scattering in Space Group 15 (b1); weaker reflections of this type were also observed at (1 0 3), (1 0 -3) and (3 0 3). The intensity of all of these reflections was reduced to negligible levels by the application of a 5.0 T field perpendicular to the scattering plane, thereby proving their magnetic origin. Similarly in the second experiment, where the scattering was from the *b***c**-plane, significant intensity was found for the

reflections (0 1 1), (0 1 -1), (0 1 3) and (0 1 -3); the intensity of which were also reduced to negligible quantities on the application of 5.0 T.

As the level of deuteration in the sample used in the second experiment was significantly lower than that of the first experiment, the structure factors of the peaks are significantly different. As the overlap between the two datasets is so small, and the quality of the second data set is much poorer due to the smaller crystal size, it was not possible to use both data sets to determine the orientation of the magnetic moment in the magnetically ordered structure to any degree of accuracy; however the fact that the weakest magnetic reflection in the b^*c^*-plane was the (0 1 1) suggests that the component of the magnetic moment lying in the (0 k l) plane lies close to the [0 1 1] direction.

The treatment of data from the measurement of the strongest magnetic reflection, I(1 0 1), as a function of temperature and magnetic field was the same as for the bromide. Figure 4.12 depicts the variation of I(1 0 1) with temperature with the analysis to determine the critical exponent β depicted in the inset. Least-squares fitting of the expression $I(1\ 0\ 1) = A \cdot \varepsilon^{2\beta}$ yielded optimised values T_N = 0.754(1) K and β = 0.28(1) for data taken over the temperature range 0.669 – 0.749 K (ε = 0.113 – 0.0067). As for the bromide, this value of β lies close to the values observed in other 2D QHAFSLs. We were unable to discern any simple power-law dependence of I(1 0 1) of the chloride on reducing temperature further away from T_N.

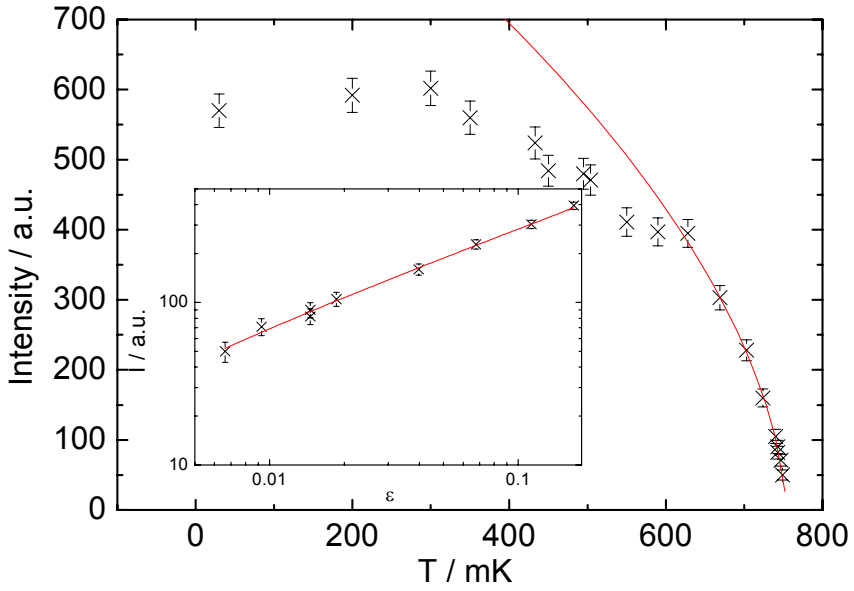

Figure 4.12: Dependence of $I(1\ 0\ 1)$ on temperature for (5CAP) copper (II) chloride in zero applied field. Data have been corrected for background. The inset to the figure shows a least-squares fit of the temperature dependence of $I(1\ 0\ 1)$ for (5CAP) copper (II) chloride to the standard power-law expression $I(T) = A.\varepsilon^{2\beta}$; $T_N = 754(1)$ mK and $\beta = 0.28(1)$.

The dependence of $I(1\ 0\ 1)$ on field perpendicular to the a^*c^*-plane was measured at several fixed temperatures as a function of a field applied perpendicular to the a^*c^*-plane (figure 4.13). At the base temperature of 0.030 K, the intensity disappeared at a field H_c = 3.62(3) T, above which the magnetic moments should be fully polarised with the field. As the temperature was raised towards T_N, H_c decreased towards zero. The corresponding phase diagram is depicted in figure 4.14. Further data were taken at temperatures between 0.670 and 0.754 K, but the weakness of the scattering made it very difficult to determine T_N with sufficient accuracy to contribute usefully to this phase diagram for reasonable counting times. An anomaly is also observed as a function of field at 0.035 K and 0.2 – 0.3 T; this could point to a spin-flop transition as suggested by a.c. susceptibility measurements on the MAP analogue[19].

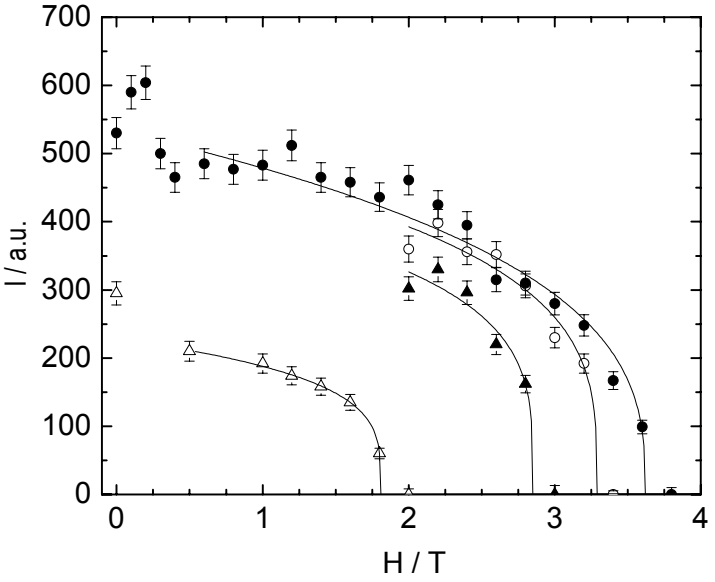

Figure 4.13: Variation of $I(1\ 0\ 1)$ for (5CAP) copper (II) chloride with applied field at selected temperatures denoted by symbols: 0.030 K (closed circles); 0.267 K (open circles); 0.455 K (closed triangles); 0.670 K (open triangles). Black lines are guides to the eye. Data were taken in 0.2 T steps up to and beyond the point where no scattering intensity was observed above background.

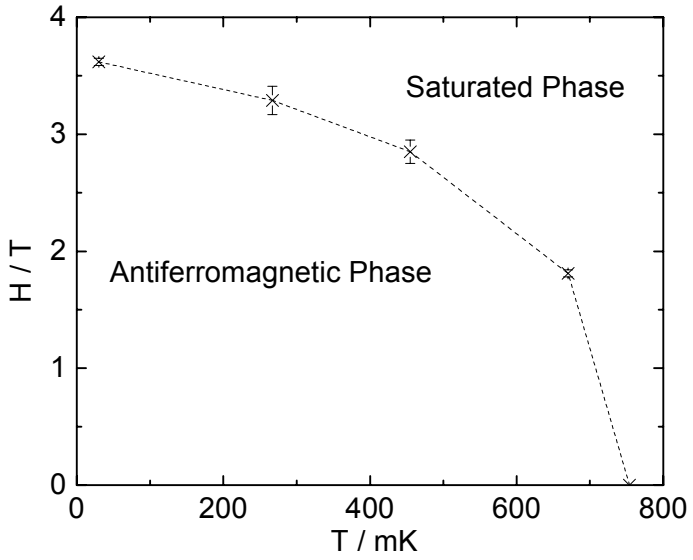

Figure 4.14: *H-T* phase diagram for the transition between the antiferromagnetic state and the state with field-induced saturated magnetisation in (5CAP) copper (II) chloride. The dashed line is a guide to the eye.

4.5 Inelastic Neutron Scattering

4.5.1 Experimental

In order to study the excitation spectrum of $(5CAP)_2CuCl_4$ in an applied magnetic field, an experiment was performed on the IN14 triple-axis spectrometer, which is shown schematically in figure 4.15. This is located on a cold source at the continuous reactor neutron source at the Institut Laue-Langevin (ILL). On this instrument, the incident neutron energy is selected by Bragg reflection from the (0 0 2) plane of a pyrolytic graphite monochromating crystal. The monochromator is curved in order to focus the neutrons onto the sample, therefore maximising the incident neutron flux. For this experiment, an incident neutron wavelength of 1.05 Å was used. High energy neutrons also satisfying the Bragg condition of the monochromator are then removed by a cooled beryllium filter. The neutrons are then scattered by the sample – only neutrons scattered in the horizontal plane can be detected. The scattering angle of the neutrons to be detected is defined by the geometry of the instrument, which can be changed throughout the experiment. The neutrons then pass to a (0 0 2) pyrolytic graphite analyser crystal, where the final energy of the neutrons is selected by Bragg reflection. Finally the neutrons pass to a single ^{3}He detector. The geometry of the instrument is changed throughout the experiment in order to measure the scattered neutron intensity as a function of incident and final neutron energy and scattering angle.

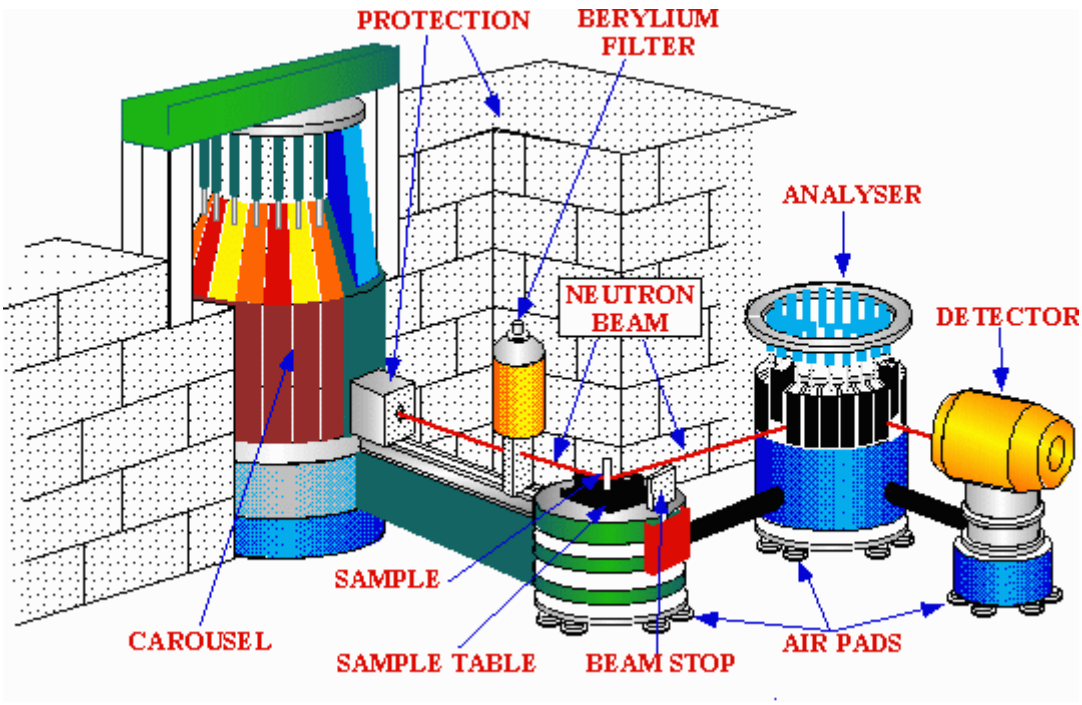

Figure 4.15: Schematic diagram of the IN14 triple-axis spectrometer at ILL, taken from reference [46].

For this experiment, a single crystal of partially deuterated $(5CAP)_2CuCl_4$ was mounted on a copper pin with GE varnish with b^* and c^* in the horizontal scattering plane of the diffractometer. It was then loaded into a cryomagnet capable of reaching fields in excess of 4 T, with a dilution refrigerator insert. The dilution refrigerator insert enabled the sample to be cooled to temperatures below 0.07 K.

4.5.2 Results

Initially scans were made in zero applied field and at base temperature (0.07 K) to investigate the three-dimensional (3D) nature of the dispersion. This was done by scanning along the <0 *k l*> direction for selected values of l = 1.2, 1.0, 0.9, 0.7, 0.6 and 0.5. The energy transfer was fixed at 0.15 meV, and then the position of the magnetic excitation was plotted in the k and l directions (figure 4.16). The shape of

the dispersion showed that the out of plane dispersion is approximately 10 % of the in plane dispersion and hence the inter-plane magnetic coupling is ~ 10 % of the intra-plane coupling.

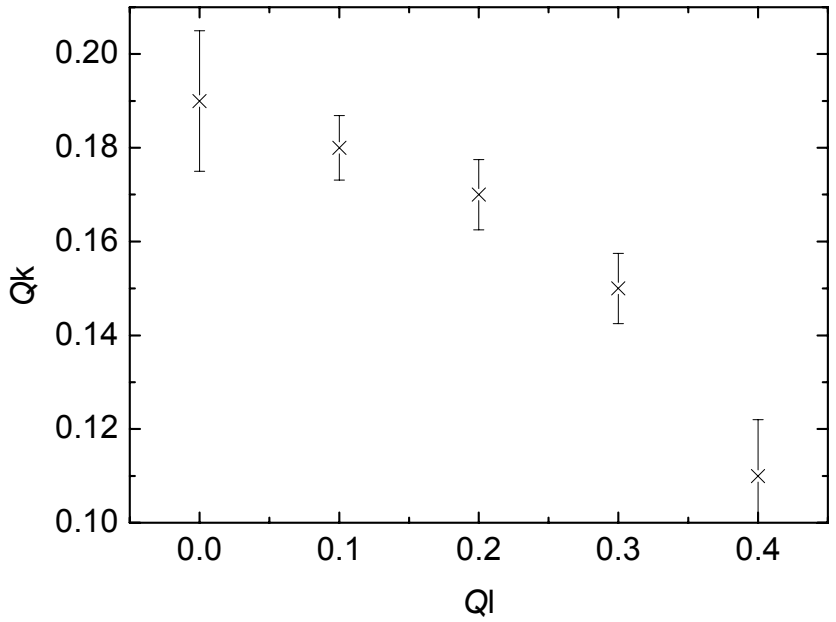

Figure 4.16: The three-dimensional dispersion measured in zero field in $(5CAP)_2CuCl_4$ at an energy transfer of 0.15 meV plotted along the *k* and *l* directions.

The magnetic phase diagram was investigated at 0.07 K in order to investigate the field required to saturate the sample in the ferromagnetic phase, and is shown in figure 4.17. This was done by measuring the intensity of the (0 1 1) magnetic Bragg peak as a function of magnetic field. It was found that the saturating field was less than 4 T.

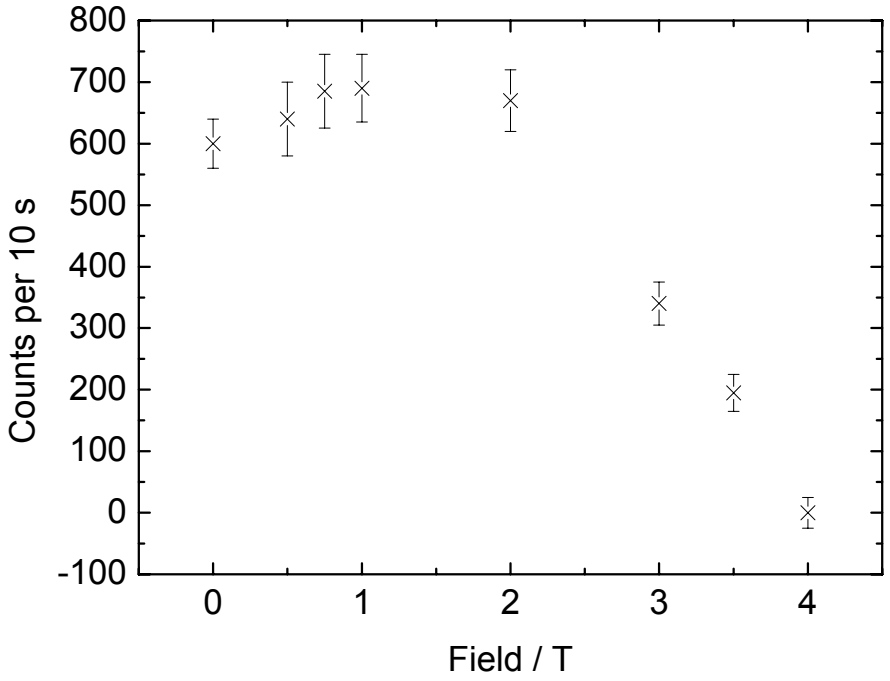

Figure 4.17: The field dependence of the intensity of the (0 1 1) magnetic Bragg peak measured at 70 mK of $(5CAP)_2CuCl_4$.

A field of 4 T was then applied in order to saturate the sample in the ferromagnetic phase. The dispersion curve was mapped out at base temperature (0.07 K) in this regime by scanning energy transfer at a fixed momentum transfer and then scanning momentum transfer for a fixed energy transfer. For the fixed momentum transfer scans, measurements were made at (0, 0, 0.9), (0, -0.1, 0.9) and (0, -0.2, 0.9) points in reciprocal space, and the energy transfer was scanned between 0.15 and 0.7 meV. Fixed energy transfer scans were measured at energy transfers of 0.35 meV, 0.30 meV and 0.25 meV scanning along the <0 *k* 0.9> direction in reciprocal space. The zero field data were subtracted from the data taken at 4 T and the peaks fitted with a Gaussian function. This was then used to plot the dispersion in the ferromagnetic phase, away from the zone centre (antiferromagnetic zone boundary), as shown in figure 4.18. When the energy of the dispersion was plotted as a function of momentum transfer along the <0 *k* 0.9> direction, the energy of the dispersion at

the zone centre was found to be less than the expected value of $g\mu_B H$. This implies that there is some anisotropy in this system.

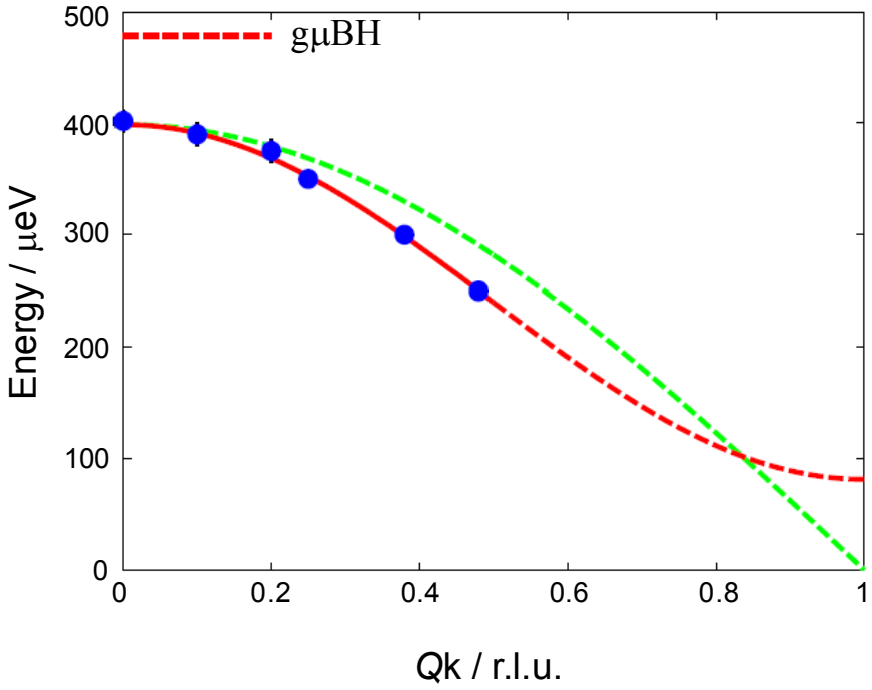

Figure 4.18: The magnon dispersion in the ferromagnetic phase of $(5CAP)_2CuCl_4$ plotted along the <0 *k* 0.9> direction, compared with the expected energy of the excitation at the zone centre, $g\mu_B H$.

4.6 Discussion

It has been noted before that both the materials studied in this chapter have significant inter-plane magnetic exchange[21]. Although the structure has a layered form, with the 5CAP ligands separating planes of CuX_4^{2-} tetrahedra (X = Cl, Br), the pathways for intra- and inter-plane exchange, respectively J and J', are not particularly dissimilar, all passing through Cu-*X*-*X*-Cu bridges. Our measurements reveal a ratio of in-plane to out-of-plane Br-Br distances of 1.17 at 10 K (with individual values 4.23 and 4.84 Å respectively), while Hammar *et al.* found this ratio to be 1.138 for X = Cl (with individual values of in-plane and out-of-plane Cl-Cl

separations 4.34 and 4.94 Å respectively)[19]. There are relatively few materials in which superexchange through Cu-*X*-*X*-Cu (*X* = Cl, Br) bridges exists, and has been characterised[47, 48]. These exceptions include ACuCl$_3$ materials (A = Rb, Cs) with a distorted hexagonal perovskite structure in which there are chains of distorted, face-sharing $CuCl_6^{4-}$ octahedra lying along the *c*-axis. Analysis of susceptibility and ESR data for the caesium salt[49-52], yielded values of intra- and interchain exchange J/k_B = 28 K and J'/k_B = -5 K respectively, while the Cl-Cl distance in the interchain Cu-Cl-Cl-Cu pathway was 3.596 Å. The bromide analogues have quite different structures[53, 54], and no such comparisons may be made, although there are other chainar ACuBr$_3$ materials in which Br-Br contacts may provide exchange pathways – for example $(C_6H_{11}NH_3)CuBr_3$ (cyclohexyl ammonium tribromocuprate(II) - CHAB)[55-57]. Here the strength of the interchain exchange interaction is of the order of 0.1-0.01 K, and may contain contributions from dipole-dipole coupling (the in-chain exchange is ferromagnetic), as well as small contributions from superexchange, which might propagate either through Cu-Br-Br-Cu pathways, or through hydrogen bonds from Br to both protons of the $-NH_2$ groups. In the former pathway the Br-Br separation is approximately 5.05 Å, while the Br-D separation in a deuterated form of the latter is 2.33-2.44 Å[56]. Similar behaviour is found for the corresponding chloride, $(C_6H_{11}NH_3)CuBr_3$ (CHAC) with interchain exchange interaction about half that in CHAB, Cl-Cl separation in a potential Cu-Cl-Cl-Cu pathway of 4.94 Å, and Cl-D bond lengths for a potential Cu-Cl-D-N-D-Cl-Cu pathway of 2.41-2.42 Å[58].

It is often stated that superexchange strength decreases rapidly with increasing separation of the orbitals that convey the spin information, but there have been relatively few attempts to quantify the relationship, and these are limited to specific types of exchange pathway, none of which are directly applicable to the present case. Where a relationship has been established, it has commonly been found to take the form $J \sim r^{-n}$, where the exponent n typically ranges from 9 to 12, and is most commonly 10[59-61]; it should be noted that most of this work applies to 180° M-O-M or M-F-M bridges. If we apply this relationship with $n = 10$, and take r to refer just to the X-X separation, we find ratios of J'/J of 0.27 and 0.21 for X = Cl and Br respectively. Perhaps fortuitously this corresponds closely to calculated values for this ratio using an empirical relation based on Quantum Monte Carlo (QMC) calculations for anisotropic cubic lattices in which the exchange (J') is weaker along one cell axis than the other two (J)[62]. For values $0.001 \leq J'/J \leq 1$, it was proposed that for $S = ½$ the following relationship holds:

$$T_N = 2.30\, J/(2.43 - \ln(J'/J)) \qquad (4.3)$$

Values of J'/J calculated either with this expression, or for smaller values of J'/J, an extended variant, are given in table 4.1 for selected 2D QHAFSLs. Note that within the *ab*-layers, there is just one short Br-Br separation between $CuBr_4^{2-}$ units, but two such between layers[21], so the ratio J'/J in the implementation of the QMC method should be replaced by $2J'/J$, where each exchange constant refers to a single exchange pathway. It should also be noted that the disposition of magnetic atoms and exchange pathways between layers is quite different in these materials compared

to La_2CuO_4 and related, layered cuprates, as well as in CFTD and CFTH. In these other materials, copper sites in one layer are displaced by (½, ½) relative to those in adjacent layers, and the different interlayer exchange interactions sum to zero. Both these factors conspire to make J'/J larger for both $(5CAP)_2CuX_4$ compounds.

Other exchange pathways may also be significant in these materials. For the bromide, the shortest separation between Br and D atoms co-ordinated to nitrogen is 2.303 Å. In addition, exchange may propagate *via* the 5CAP molecules: there are several different D-Br separations (table A3 in appendix A1), the smallest being 2.302 Å (D(5) – Br(2)), and several in the range 2.65 – 2.8 Å (D(2a) – Br(2), D(5) - Br(2), D(3) – Br(2)). Similar pathways have been shown to be responsible for exchange interactions between Cu^{2+} ions of the order of 1 – 2 cm^{-1} ($J/k_B \cong 1.2$ - 2.9 K)[63]. Of course the materials studied here differ from those in previous studies in being predominantly deuterated. However, this is expected to lead to relatively small changes in exchange interactions, with a modest reduction anticipated when H is substituted by D[64, 65]. Figure 4.19 shows these hydrogen bonds for $(d_6\text{-}5CAP)_2CuBr_4$, together with the shortest Br-Br separations. This points to methods of improving the magnetic anisotropy through the use of longer, less-conjugated organic species. Although, 5CAP is likely to play a role in the formation of this particular type of structure, possibly through relatively weak electrostatic interactions involving its π system; therefore replacement by quite a different organic species could lead to quite different structures.

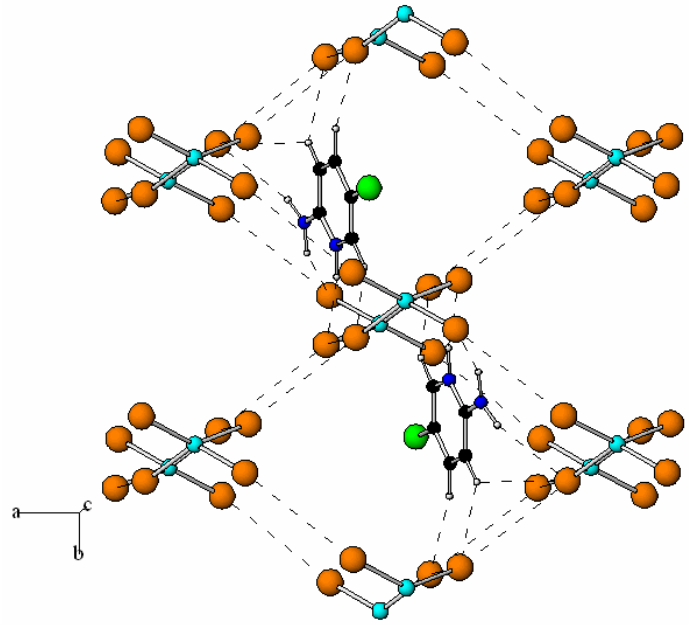

(a)

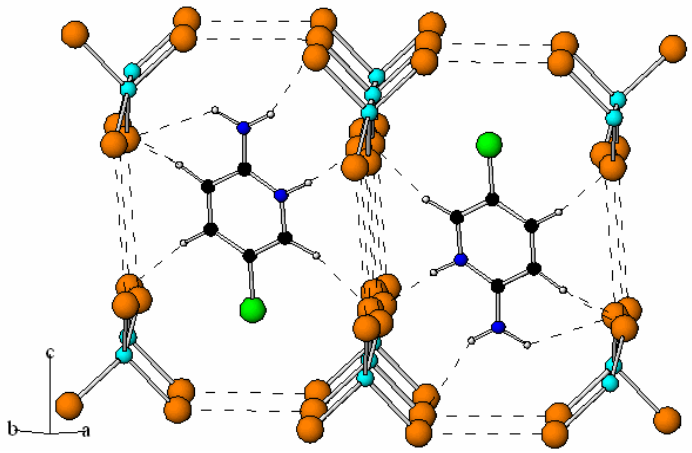

(b)

Figure 4.19: Crystal structure of $(5CAP)_2CuBr_4$ viewed (a) nearly parallel and (b) perpendicular to the *c*-axis along ***a***+***b***, with closest Br-Br separations and shortest Br-D separations indicated by dashed lines.

4.7 Conclusions

We have used a number of different techniques to look at the structural and magnetic properties of the model two-dimensional $S = ½$ square lattice Heisenberg antiferromagnets $(5CAP)_2CuX_4$ (where X = Cl or Br). Single-crystal neutron

diffraction experiments have been performed to study the nuclear and magnetic structure of deuterated samples of $(d_6\text{-}5CAP)_2CuCl_4$ and $(d_6\text{-}5CAP)_2CuBr_4$. Muon spin rotation was used in conjugation with neutron diffraction to study the critical behaviour of the sub-lattice magnetisation, and inelastic neutron scattering was used to look at the three-dimensional nature of the exchange and the magnetic dispersion in the ferromagnetic phase.

Our studies of the magnetic properties of the fully deuterated compounds, $(d_6\text{-}5CAP)_2CuCl_4$ and $(d_6\text{-}5CAP)_2CuBr_4$ confirm previous susceptibility studies that demonstrated antiferromagnetic coupling within and between the magnetic layers, with a modest degree of anisotropy: application of a recently-derived empirical relationship between J, J' and T_N indicates J'/J to be of the order of 0.1 (*i.e.* the ratio of the total inter- to intraplane exchange coupling is 0.2 when account is taken of the relative number of inter- and intraplane exchange pathways). The inelastic neutron scattering experiment that was performed on a partially deuterated crystal of $(5CAP)_2CuCl_4$ shows that the three-dimensional nature of the dispersion is in agreement with this value. Consideration of the crystal structure of the bromide indicates that the 5CAP molecules may also play a role in intra- and interlayer coupling, being hydrogen-bonded to Br as well as providing a conjugated system for delocalisation of spin polarisation. Similar effects almost certainly come into play in the chloride analogues.

The critical exponents for the sublattice magnetisation for both materials are compatible with those expected for layered magnets near a 3D ordering transition, and the general features of the *H-T* phase diagram of the chloride up to 5 T, as well as the static spin structure of the bromide all appear quite conventional. Our results provide the foundation for further work to explore non-classical behaviour in applied magnetic fields where *H/J* is large[7], particularly through further inelastic neutron scattering from larger, deuterated crystals. Such work is currently in progress. Nevertheless, there is still a need to produce better examples of model 2D QHAFSL, and in particular to decrease the ratio *J'/J* while keeping J/k_B below 5 K (corresponding to a saturation field of 15 T – the maximum currently achievable for neutron scattering). One way ahead could be to add bulky functional groups to the 5CAP molecules, but the probability that a similar structure will form is low, so until there is a quantum leap in the power of computational prediction of the structure of molecular materials we rely on intuition and the synthesis of many new compounds with $S = ½$ centres to provide such models[66]. One such compound that has recently been synthesised is $[BDTA]_2[CuCl_4]$ (BDTA = benzo-1,3,2-dithiazolyl)[67], which has a value of J/k_B of 0.018 K, and heat capacity measurements indicate that *J'/J* is relatively small. This material is potentially very interesting as the diamagnetic Zn analogue crystallises in a very similar structure (contrary to the case for the $(5CAP)_2ZnCl_4$). This indicates that the scope for doping the magnetic lattice of this compound with diamagnetic impurities, in order to study the effect of these on any magnetic ordering, is great.

4.8 References

[1] Manousakis, E., *Rev. Mod. Phys.*, 1991, **63**(1): 1-62.

[2] Shirane, G., Endoh, Y., Birgeneau, R. J., Kastner, M. A., Hidaka, Y., Oda, M. *et al.*, *Phys. Rev. Lett.*, 1987, **59**(14): 1613-1616.

[3] Anderson, P. W., *Science*, 1987, **235**(4793): 1196-1198.

[4] Kim, Y. J., Aharony, A., Birgeneau, R. J., Chou, F. C., Entin-Wohlman, O., Erwin, R. W. *et al.*, *Phys. Rev. Lett.*, 1999, **83**(4): 852-855.

[5] Christensen, N. B., Rønnow, H. M., McMorrow, D. F., Harrison, A., Aeppli, G., Perring, T. G. *et al.*, *submitted*, 2005.

[6] Osano, K., Shiba, H. and Endoh, Y., *Prog. Theor. Phys.*, 1982, **67**(4): 995-1014.

[7] Zhitomirsky, M. E. and Chernyshev, A. L., *Phys. Rev. Lett.*, 1999, **82**(22): 4536-4539.

[8] Chernyshev, A. L., Chen, Y. C. and Neto, A. H. C., *Phys. Rev. B*, 2002, **65**(10): art. no. 104407.

[9] Vajk, O. P., Mang, P. K., Greven, M., Gehring, P. M. and Lynn, J. W., *Science*, 2002, **295**(5560): 1691-1695.

[10] Sandvik, A. W., *Phys. Rev. B*, 2002, **66**(2): 024418.

[11] Bonner, J. C. and Fisher, M. E., *Phys. Rev.*, 1964, **135**(3A): A640.

[12] Harrison, A., Clarke, S. J., Mason, T. E. and Visser, D., *J. Magn. Magn. Mater.*, 1992, **104**: 557-558.

[13] Clarke, S. J. and Harrison, A., *J. Phys.-Condens. Matter*, 1992, **4**(29): 6217-6226.

[14] Clarke, S. J., Harrison, A., Mason, T. E., McIntyre, G. J. and Visser, D., *J. Phys.-Condens. Matter*, 1992, **4**(4): L71-L76.

[15] Clarke, S. J. and Harrison, A., *J. Magn. Magn. Mater.*, 1995, **140**: 1627-1628.

[16] Rønnow, H. M., McMorrow, D. F. and Harrison, A., *Phys. Rev. Lett.*, 1999, **82**(15): 3152-3155.

[17] Rønnow, H. M., McMorrow, D. F., Harrison, A., Youngson, I. D., Coldea, R., Perring, T. G. *et al.*, *J. Magn. Magn. Mater.*, 2001, **236**(1-2): 4-5.

[18] Rønnow, H. M., McMorrow, D. F., Coldea, R., Harrison, A., Youngson, I. D., Perring, T. G. *et al.*, *Phys. Rev. Lett.*, 2001, **87**(3): art. no. 037202.

[19] Hammar, P. R., Dender, D. C., Reich, D. H., Albrecht, A. S. and Landee, C. P., *J. Appl. Phys.*, 1997, **81**(8): 4615-4617.

[20] Matsumoto, T., Miyazaki, Y., Albrecht, A. S., Landee, C. P., Turnbull, M. M. and Sorai, M., *J. Phys. Chem. B*, 2000, **104**(43): 9993-10000.

[21] Woodward, F. M., Albrecht, A. S., Wynn, C. M., Landee, C. P. and Turnbull, M. M., *Phys. Rev. B*, 2002, **65**(14): art. no. 144412.

[22] Endoh, Y., Yamada, K., Birgeneau, R. J., Gabbe, D. R., Jenssen, H. P., Kastner, M. A. *et al.*, *Phys. Rev. B*, 1988, **37**(13): 7443-7453.

[23] Coldea, R., Hayden, S. M., Aeppli, G., Perring, T. G., Frost, C. D., Mason, T. E. *et al.*, *Phys. Rev. Lett.*, 2001, **86**(23): 5377-5380.

[24] Greven, M., Birgeneau, R. J., Endoh, Y., Kastner, M. A., Matsuda, M. and Shirane, G., *Z. Phys. B-Condens. Mat.*, 1995, **96**(4): 465-477.

[25] Burger, N., Fuess, H. and Burlet, P., *Solid State Commun.*, 1980, **34**(11): 883-886.

[26] Yasuda, C., Todo, S., Hukushima, K., Alet, F., Keller, M., Troyer, M. *et al.*, *Phys. Rev. Lett.*, 2005, **94**(21): 217201.

[27] http://www.isis.rl.ac.uk/muons/musr/index.htm

[28] Collins, M. F., *Magnetic Critical Scattering*. Oxford Series on Neutron Scattering in Condensed Matter, ed. 1989, (Oxford University Press: New York).

[29] Bramwell, S. T. and Holdsworth, P. C. W., *J. Phys.: Condens. Matter*, 1993, **5**: L53-L59.

[30] Keimer, B., Belk, N., Birgeneau, R. J., Cassanho, A., Chen, C. Y., Greven, M. *et al.*, *Phys. Rev. B*, 1992, **46**(21): 14034-14053.

[31] Bondah-Jagalu, V., Harrison, A., Visser, D. and McIntyre, G. J., *Personal Communication*, 2002.

[32] http://www.ill.fr/YellowBook/D10/

[33] Zeyen, C. M. E., Chagnon, R., Disdier, F. and Morin, H., *Revue De Physique Appliquee*, 1984, **19**(9): 789-791.

[34] Lehmann, M. S., Kuhs, W. F., McIntyre, G. J., Wilkinson, C. and Allibon, J. R., *J. Appl. Crystallogr.*, 1989, **22**: 562-568.

[35] Allen, F. H., Watson, P. G., Brammer, L. and Other, A. N., in *International Tables for Crystallography, Vol. C*, Ed. by: Wilson, A. J. C. and Prince, E., 1999, (Kluwer Academic Press: Dordrecht). p. 788.

[36] Place, H. and Willett, R. D., *Acta Crystallogr. Sect. C-Cryst. Struct. Commun.*, 1987, **43**: 1050-1053.

[37] Sears, V. F., in *Methods of Experimental Physics*, Ed. by: Price, K. S. D. L., 1986, (Academic Press: Orlando). p. 521.

[38] Becker, P. J. and Coppens, P., *Acta Crystallogr. Sect. A*, 1974, **A 30**(Mar): 129-147.

[39] Bramwell, S. T. and Holdsworth, P. C. W., *J. Appl. Phys.*, 1993, **73**(10): 6096-6098.

[40] Bramwell, S. T. and Holdsworth, P. C. W., *Phys. Rev. B*, 1994, **49**(13): 8811-8814.

[41] Thio, T. and Aharony, A., *Phys. Rev. Lett.*, 1994, **73**(6): 894-897.

[42] Harrison, A., Collins, M. F., Abudayyeh, J. and Stager, C. V., *Phys. Rev. B*, 1991, **43**(1): 679-688.

[43] http://www.hmi.de/bensc/instrumentation/instrumente/e4/e4.gif

[44] Harrison, A. and Feyerherm, R., *Personal Communication*, 2002.

[45] Hahn, T., ed. *Space-group symmetry*. 3rd Edition ed. International Tables for Crystallography. Vol. A. 1992, (Kluwer academic: Dordrecht)

[46] http://www.ill.fr/YellowBook/IN14/

[47] Singh, A., Tesanovic, Z., Tang, H., Xiao, G., Chien, C. L. and Walker, J. C., *Phys. Rev. Lett.*, 1990, **64**(21): 2571-2574.

[48] Rosov, N., *Phys. Rev. Lett.*, 1991, **67**(14): 1938.

[49] Singh, A., Tesanovic, Z., Tang, H., Xiao, G., Chien, C. L. and Walker, J. C., *Phys. Rev. Lett.*, 1991, **67**(14): 1939.

[50] Kopietz, P., *Phys. Rev. Lett.*, 1992, **68**(23): 3480-3483.

[51] Collins, M. F. and Petrenko, O. A., *Can. J. Phys.*, 1997, **75**(9): 605-655.

[52] de Jongh, L. J. and Miedema, A. R., *Adv. Phys.*, 2001, **50**(8): 947-1170.

[53] Tazuke, Y., Tanaka, H., Iio, K. and Nagata, K., *J. Phys. Soc. Jpn.*, 1981, **50**(12): 3919-3924.

[54] Hyodo, H., Iio, K. and Nagata, K., *J. Phys. Soc. Jpn.*, 1981, **50**(5): 1545-1550.

[55] Tanaka, H., Schotte, U. and Schotte, K. D., *J. Phys. Soc. Jpn.*, 1992, **61**(4): 1344-1350.

[56] Maruyama, S., Tanaka, H., Narumi, Y., Kindo, K., Nojiri, H., Motokawa, M. *et al.*, *J. Phys. Soc. Jpn*, 2001, **70**(3): 859-865.

[57] Inoue, M., Kishita, M. and Kubo, M., *Inorg. Chem.*, 1967, **6**(5): 900-902.

[58] Li, T. I. and Stucky, G. D., *Inorg. Chem.*, 1973, **12**(2): 441-445.

[59] Kopinga, K., Tinus, A. M. C. and de Jonge, W. J. M., *Phys. Rev. B*, 1982, **25**(7): 4685-4690.

[60] de Vries, G. C., Helmholdt, R. B., Frikkee, E., Kopinga, K., de Jonge, W. J. M. and Godefroi, E. F., *J. Phys. Chem. Solids*, 1987, **48**(9): 803-811.

[61] Kopinga, K., Delica, T. and Leschke, H., *Phys. Rev. B*, 1989, **40**(10): 7239-7246.

[62] Groenendijk, H. A., Blote, H. W. J., Vanduyneveldt, A. J., Gaura, R. M., Landee, C. P. and Willett, R. D., *Physica B & C*, 1981, **106**(1): 47-58.

[63] Bloch, D., *J. Phys. Chem. Solids*, 1966, **27**: 881-885.

[64] de Jongh, L. J. and Block, R., *Physica*, 1975, **79B**: 568-593.

[65] Bramwell, S. T., *J. Phys.: Condens. Matter*, 1990, **2**: 7527-7536.

[66] Luque, A., Sertucha, J., Lezama, L., Rojo, T. and Roman, P., *J. Chem. Soc.-Dalton Trans.*, 1997,(5): 847-854.

[67] Staniland, S. S., Harrison, A., Robertson, N., Kamenev, K. V. and Parsons, S., *Inorg. Chem.*, 2006, **45**(15): 5767-5773.

5 Jarosites

5.1 Introduction

As discussed in chapter 2, the magnetic properties of materials containing the kagome lattice are particularly interesting to study due to the high degeneracy of the ground state. For this a good model system is needed, and one such example is the jarosite family of minerals. The naturally occurring mineral jarosite has the formula $KFe_3(SO_4)_2(OH)_6$, but the series has the general formula $AB_3(XO_4)_2(OH)_6$, where *A* is a univalent cation, *B* is a trivalent cation and *X* is an element capable of forming four bonds to oxygen atoms in a tetrahedral co-ordination geometry. The *B* ions in the structure form a perfectly planar kagome lattice, and if chosen to be a magnetic ion, can give a good system with which to test kagome lattice theory. The magnetic properties of the system are mainly altered by varying *B*, and examples of elements used to fully or partially replace the Fe occupying this site include Al, Cr, V or Ga[1-4]. This variety of elements enables the lattice to be diamagnetically diluted or the spin quantum number, *S*, to be varied from $S = 1$ for V to $S = 5/2$ for Fe. The cations situated on the *A* site can be varied in order to vary the structure of the product and also the possible exchange interactions. Species that have been used include K^+, Na^+, Rb^+, Ag^+, NH_4^+ and H_3O^+[2, 5, 6].

The work contained in this chapter concerns studies of the ordered potassium iron jarosite ($KFe_3(SO_4)_2(OH)_6$) and the spin glass hydronium iron jarosite ($(H_3O)Fe_3(SO_4)_2(OH)_6$), and their deuterated analogues.

5.2 Previous Work

The most studied of the family of jarosites are the iron jarosites (B = Fe), where the iron is in the S = 5/2 spin state and nearest neighbour spins are coupled antiferromagnetically. With the exception of the hydronium analogue ($A = H_3O^+$, D_3O^+)[2, 5, 7-12], all the members of this series ($A = K^+$, Na^+, Rb^+, Ag^+, NH_4^+…)[6, 11, 13-19] exhibit an ordering transition at temperatures around 60 K where the spins order into a $\mathbf{q} = 0$ array[14] of positive chirality[18]. Hydronium jarosite on the other hand exhibits no long range ordering transition down to temperatures of 1.4 K although it does show a spin-glass transition at 13.8 K[8]. One proposed reason for this difference in behaviour is connected with the occupation of the kagome lattice. With the exception of the hydronium jarosite, which has a lattice occupation of around 97 %[9], the occupation of the kagome lattice by iron in the hydrothermally synthesised members of the jarosite series is found to be around 90 %. One explanation for the fact that only the hydronium jarosite exhibits no long range order, is that there is very little iron site disorder in the lattice. The effect of introducing disorder by doping the lattice with diamagnetic ions has been shown to result in long range order at low temperatures[9, 20, 21]. Another possible explanation is that proton transfer from the A cations introduces a degree of random magnetic exchange, which may be enough to destabilise long range order. A recent development in the field has been the use of redox based techniques in jarosite synthesis[3, 4, 6, 22]. Using this technique, stoichiometrically pure single crystals of iron jarosites with $A = Na^+$, K^+, Rb^+ and NH_4^+, have been synthesised, and show a transition to a long-range ordered state at $T_N \sim 65$ K, despite their full lattice occupancy.

The other magnetic members of the jarosite family, where $B = Cr^{3+}$ or V^{3+}, have also been studied in some detail[3, 4, 19, 23-27]. It is found that the Cr systems are weakly antiferromagnetic, whereas the V analogues have a nearest neighbour ferromagnetic exchange pathway.

The thermodynamic properties and static structures of the jarosites are now understood in some detail[5, 8, 9, 13, 14, 16, 24, 27, 28], but it is desirable to more accurately determine the strength of the magnetic coupling, *J*, and the nature of any other factors affecting the exchange. Experimentally, the measurement of the spin wave dispersion, and the comparison with available models, enables *J* to be accurately determined, along with parameters describing any further interactions. Theoretically, a number of people have discussed the spin wave dispersion expected from a two-dimensional kagome lattice[18, 29, 30]. In additional to the spin waves expected in an ideal two-dimensional Heisenberg kagome antiferromagnet with nearest neighbour exchange, the effects of further exchange[30], large *S* quantum fluctuations[29] and spin anisotropy[18] have been considered.

Despite all this theoretical work, the only experimental study of spin waves in the jarosites has been carried out by Nishiyama and co-workers[18]. Using NMR spectroscopy to investigate the temperature dependence of the sub-lattice magnetisation, they have shown that there is a spin wave present in potassium iron jarosite. The decrease of the spin-lattice relaxation rate with decreasing temperature is explained by a two-magnon process with an energy gap of the magnon dispersion.

5.2.1 Structure of the Jarosites

The jarosite minerals crystallise in the rhombohedral space group $R\bar{3}m$. Potassium iron jarosite has unit cell parameters a = 7.300 Å and c = 17.116 Å[14], whereas the hydronium analogue has a = 7.325 Å and c = 16.915 Å[2]. The structure of jarosites is shown in figure 5.1. The *B* site cations are co-ordinated by O atoms in a distorted octahedral geometry. These octahedra are interlinked, by corner sharing, in such a way that the *B* cations are situated on perfect kagome planes, depicted in figure 5.1 (b). The planes are well separated from each other by the *A* cations and sulfate tetrahedra. The coupling between atoms within the kagome planes occurs via a superexchange pathway mediated by the oxygen in the hydroxide groups, leading to an antiferromagnetic interaction in the case of $B = Fe^{3+}$. If $A = H_3O^+$ or NH_4^+, the symmetry of the cation forces it to be disordered over two symmetry related sites, rather than being situated at the origin of the unit cell.

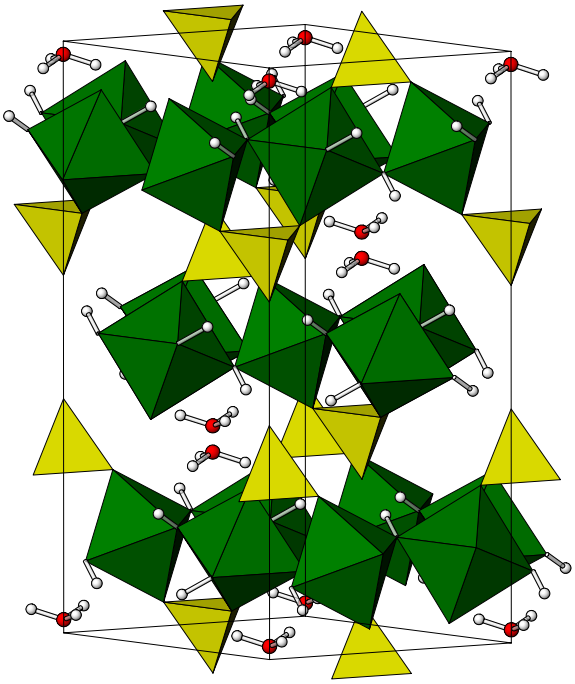

(a)

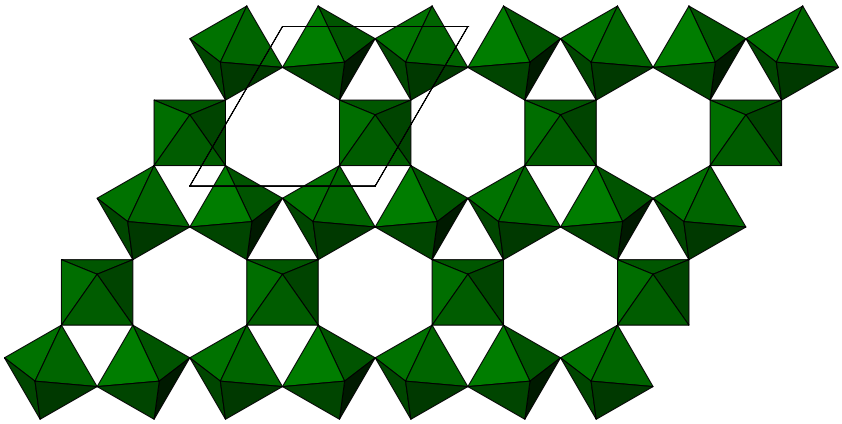

(b)

Figure 5.1: The hydronium jarosite structure (a) unit cell with the *c*-axis in the vertical direction showing MO_6 octahedra (dark green), SO_4 tetrahedra (yellow), H atoms (white) and O atoms (red), (b) view down the *c*-axis showing corner sharing MO_6 octahedra forming kagome layers.

5.3 Experimental

This section outlines the various experiments that have been performed on two members of the jarosite family, potassium iron jarosite $KFe_3(SO_4)_2(OH)_6$, which

undergoes a Néel transition to a long range ordered state, and the spin glass hydronium iron jarosite $(H_3O)Fe_3(SO_4)_2(OH)_6$. As neutron scattering experiments have been performed on both these samples, their perdeuterated analogues have been used.

5.3.1 Syntheses and Redeuteration

This section outlines the details of the various sample preparations, along with an experiment performed in order to investigate ways to improve the sample quality for neutron scattering experiments.

5.3.1.1 Synthesis of Anhydrous Iron (III) Sulfate – $Fe_2(SO_4)_3$

$Fe_2(SO_4)_3{\cdot}xH_2O$ (50 g, Fisons) was placed in a 1 l round bottom flask with conc. H_2SO_4 (500 ml, Fisher 98 %), and heated with two Bunsen burners until the acid started to boil. H_2O and some of the H_2SO_4 were distilled off as the acid is boiled for four hours. The resulting mixture was left to cool, with the solid turning white. The H_2SO_4 was then filtered off on a sintered glass funnel, and the solid washed again with conc. H_2SO_4, and sucked dry by the use of a water pump, followed by two washings with acetone. The resulting white solid (anhydrous $Fe_2(SO_4)_3$) was then dried in a vacuum oven overnight.

5.3.1.2 Synthesis of Deuteronium Iron Jarosite – $(D_3O)Fe_3(SO_4)_2(OD)_6$ – Sample 1

Anhydrous iron sulfate, $Fe_2(SO_4)_3$ (7.00 g, 17.5 mmol) was dissolved in D_2O (80 ml, Aldrich, 99 % D) at 70 ºC for 3.5 hours under a flow of nitrogen. The resulting mixture was transferred to a 125 ml PTFE lined stainless steel bomb and heated at 155 ºC for 63 hours. The resulting precipitate was washed with D_2O, filtered and dried overnight in a vacuum oven to leave a fine ochre powder, $(D_3O)Fe_3(SO_4)_2(OD)_6$ (0.8252 g, 1.69 mmol, 14.5 % yield), which was characterised by X-ray powder diffraction.

5.3.1.3 Synthesis of Deuteronium Alunite – $(D_3O)Al_3(SO_4)_2(OD)_6$

In order to differentiate between the magnetic and nuclear neutron scattering from deuteronium iron jarosite, a comparison was made with the scattering from a diamagnetic analogue. The deuteronium alunite to be used as a diamagnetic analogue was prepared using an established method[1]. Anhydrous aluminium sulfate, $Al_2(SO_4)_3$ (4.25 g, 12.42 mmol, Fisons) was dissolved in D_2O (25ml, Aldrich, 99 % D) under reflux. $MgCO_3$ (1.2 g, 14.23 mmol, Aldrich 99.9 %) was added to raise the pH of the solution to approximately 3.5. The mixture was stirred until all the $MgCO_3$ had dissolved. After cooling, the solution was divided equally between two 23 ml PTFE lined stainless steel bombs and heated at 155 ºC for 72 hours. The resulting mixture was filtered and then dried under vacuum overnight, to produce a white powder, $(D_3O)Al_3(SO_4)_2(OD)_6$ (1.55 g, 3.84 mmol, 46.4 % yield), which was characterised by X-ray powder diffraction.

5.3.1.4 Synthesis of Potassium Iron Jarosite – $KFe_3(SO_4)_2(OD)_6$

The experiments performed on $KFe_3(SO_4)_2(OD)_6$ reported in this chapter, used samples synthesised by Keith Pettigrew[31] in the following manner: K_2SO_4 (2.88 g, 16.5 mmol, Rectapur, 99 %) and $Fe_2(SO_4)_3 \cdot 5H_2O$ (23.68 g, 79 mmol, Aldrich, 97 %) were dissolved in D_2O (100 ml, Apollo, 99.92 % D). The solvent was removed by rotary evaporation. The remaining sticky residue was dissolved again in D_2O (100 ml). D_2SO_4 (0.49 g) was added and the solution was put in a PTFE-lined container within a stainless steel bomb. The bomb was placed inside a precision muffle furnace at 140 ± 0.5 °C for 24 hours. The precipitate was filtered off under nitrogen, washed with D_2O and dried well in a vacuum oven to give a yield of 8.5 g.

5.3.1.5 Synthesis of Deuteronium Iron Jarosite – $(D_3O)Fe_3(SO_4)_2(OD)_6$ – Sample 2

In order to study the effects of deuterium exchange within jarosite samples, a sample of deuteronium iron jarosite, synthesised by Keith Pettigrew[31] according to the following scheme, was used:

$Fe_2(SO_4)_3 \cdot 5H_2O$ (40.000 g) was dissolved in D_2O and the solvent removed by rotary evaporation. The remaining sticky residue was re-dissolved in D_2O and the solution made up to 300 ml. The solution was preheated in a PTFE-lined stainless steel bomb at 70 °C for 4 hours to solubilise the iron sulfate, before being heated at 155 °C for 4 hours to precipitate the jarosite. After cooling, the ochre product was washed with D_2O and dried in a vacuum furnace at 120 °C for two hours.

5.3.1.6 Redeuteration of Deuteronium Iron Jarosite – $(D_3O)Fe_3(SO_4)_2(OD)_6$ (Sample 2) – Sample 3

$(D_3O)Fe_3(SO_4)_2(OD)_6$ (1.00 g, sample 2) was placed into a 23 ml PTFE-lined stainless steel bomb with D_2O (10 ml, Aldrich, 99 % D). This was heated at 155 ºC for 16 hours. The resulting precipitate was washed with D_2O, filtered and dried in a vacuum oven overnight to leave a fine ochre powder, $(D_3O)Fe_3(SO_4)_2(OD)_6$.

5.3.1.7 Neutron Diffraction

We have suspected for some time that the quality of deuterated jarosite samples degrades over time, due to exchange of the deuterium with atmospheric hydrogen. In order to investigate whether this process is reversible, attempts were made to redeuterate a deuteronium jarosite sample (see section 5.3.1.6). To test and compare the level of deuteration in the different deuteronium jarosite samples, neutron diffraction experiments were performed on the D20 neutron diffractometer at the ILL by our collaborator Dirk Visser.

5.3.1.7.1 Experimental

D20 is a very high intensity two-axis diffractometer situated on a thermal neutron guide. A vertical focussing germanium monochromator Ge(115) was used with a take-off angle of 120° to give an incident neutron wavelength of 1.88 Å. The neutrons are then scattered by the sample, and pass on to the position sensitive ^3He

detector which covers an angular range of 153.6°. A schematic diagram of D20 is shown in figure 5.2 below.

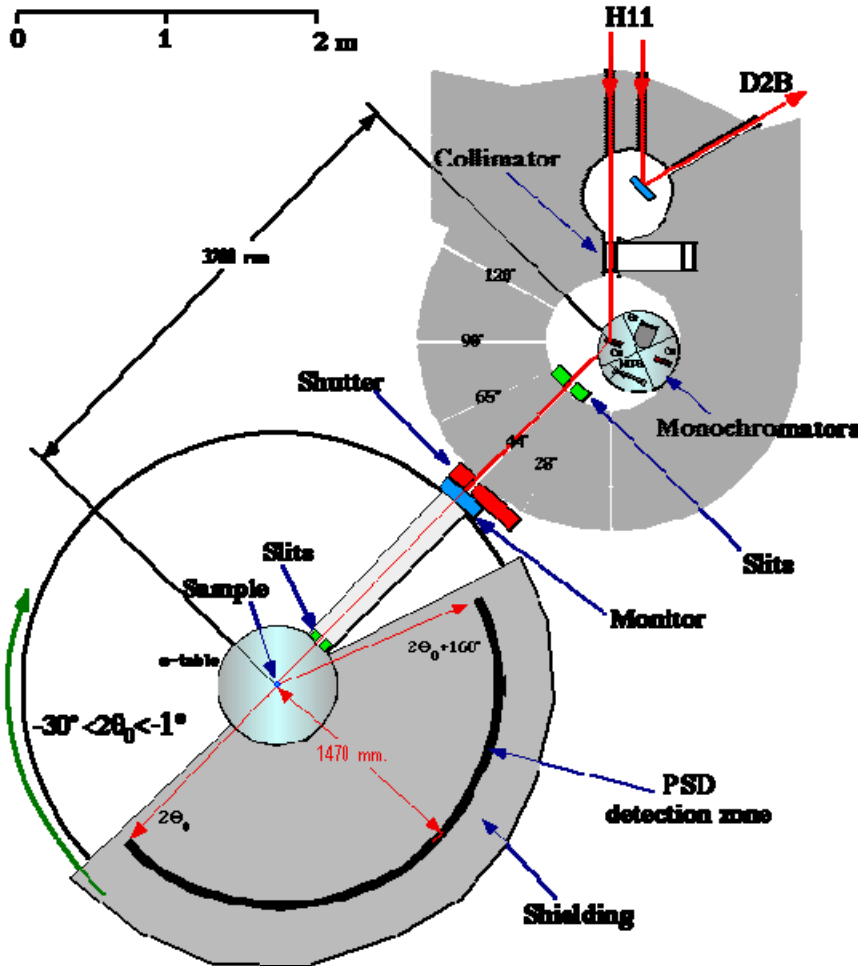

Figure 5.2: A schematic diagram of the D20 spectrometer at the ILL. Diagram taken from reference [32].

5.3.1.7.2 Results

The neutron scattering from three different samples, a recently synthesised sample (sample 1), an old sample, where there had been a significant amount of sample degradation due to hydrogen uptake (sample 2) and the same sample (2) redeuterated (sample 3), was measured at room temperature on D20. The resulting diffraction patterns were refined using the GSAS structure refinement programme[33]. There

are two different hydrogen sites in deuteronium jarosite, these are the H_3O^+ / D_3O^+ (H1 / D1) site on the *A* cation, and the OH^- / OD^- (H2 / D2) site of the iron ligands. During the Rietveld refinement process, all structural parameters were allowed to refine, in addition to the H / D ratio on the two different hydrogen sites and the iron site occupancy, with the exception of the position of the H1 / D1 site in sample 2, which was constrained. Plots of the Rietveld refinements of the three diffraction patterns are shown below, along with a table summarising the key results.

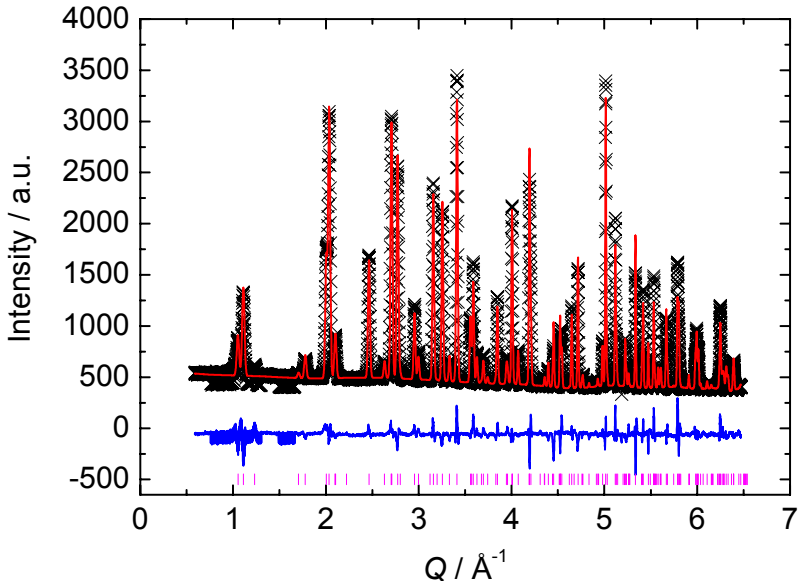

(a)

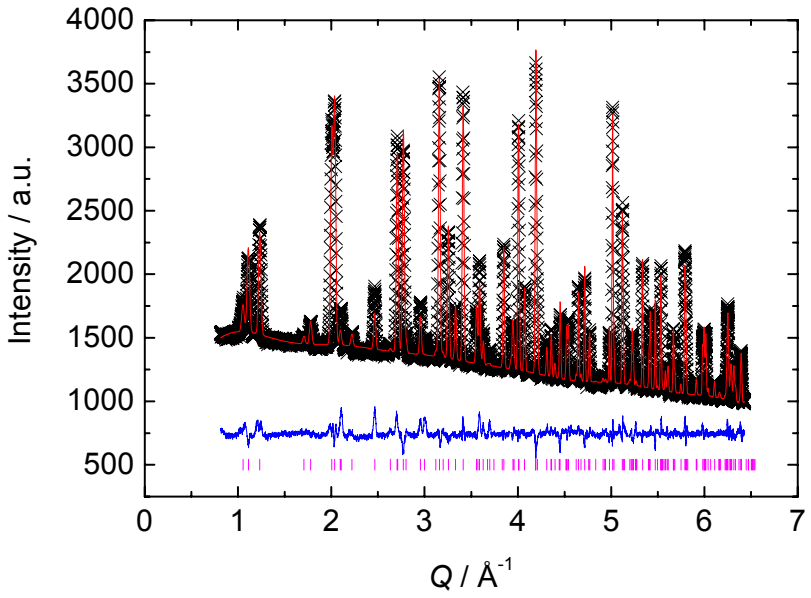

(b)

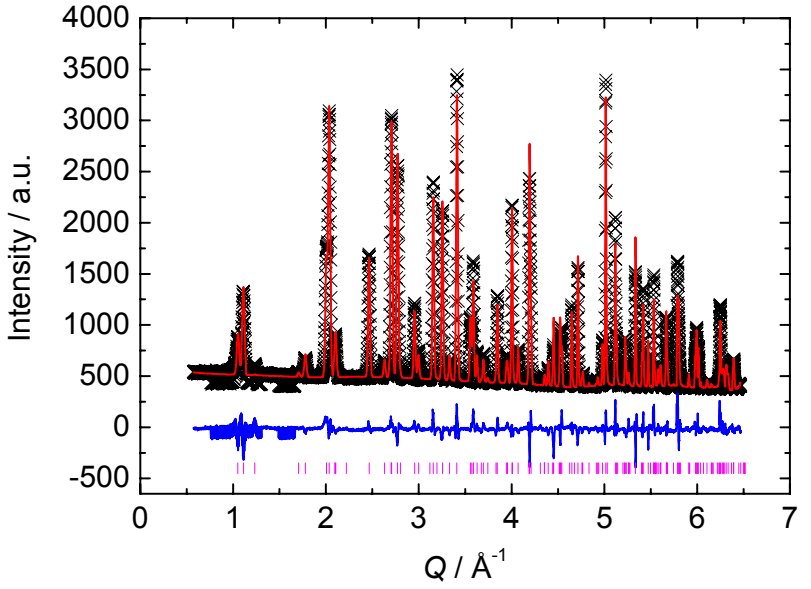

(c)

Figure 5.3: Plots showing the measured intensity (black crosses), calculated intensity (red line), difference (blue line) and Bragg reflection positions (magenta tick marks) for Rietveld refinements of neutron diffraction patterns measured on the D20 diffractometer of three samples of $(D_3O)Fe_3(SO_4)_2(OD)_6$ (a) a recently synthesised sample (sample 1), (b) an old sample (sample 2) and (c) a redeuterated sample (sample 3).

Sample	Fe Occupancy (%)	D1 Occupancy (%)	D2 Occupancy (%)
1	92.2(5)	75.6(10)	87.5(6)
2	96.4(5)	34.2(4)	47.3(3)
3	93.0(5)	80.4(10)	92.3(7)

Table 5.1: Refined site occupancies in three deuteronium jarosite samples. The figures in brackets indicate the errors in the final digit(s).

These results show that reboiling a sample in D_2O is a successful way of improving the D / H ratio in deuteronium jarosite samples by a significant amount, even above the levels present in the recently synthesised sample. This indicates that a degree of H / D exchange is likely to have taken place even in the recently synthesised sample, and that the additional step in the synthesis provides valuable results when making samples suitable for study by neutron scattering. On the other hand, this retreatment appears to be coupled with a slight loss in the iron occupancy.

5.3.2 D.c. Susceptibility Measurements Under Pressure

In order to study whether the application of pressure to a system delicately balanced on the boundary of order and disorder, has the effect of perturbing the system in some way, d.c. susceptibility measurements were made on potassium iron jarosite under applied pressure.

5.3.2.1 Experimental

The measurements were made on a Quantum Design $MPMS_2$ SQUID magnetometer. A powder sample of $KFe_3(SO_4)_2(OH)_6$ was inserted into a PTFE capsule along with a small chip of lead to act as a pressure calibrant and 'Daphne 7373' oil[34] to act as a

pressure transmitting medium. This was then inserted into a Be-Cu clamp cell, described in detail in chapter 3. The susceptibility was measured as a function of temperature in an applied field of 100 Oe, at a number of different applied pressures. The pressure was calibrated by the pressure dependence of the superconducting phase transition of the lead chip.

5.3.2.2 Results

The susceptibility was measured at five different applied pressures, and is plotted over the region of the Néel temperature (T_N) in figure 5.4 below:

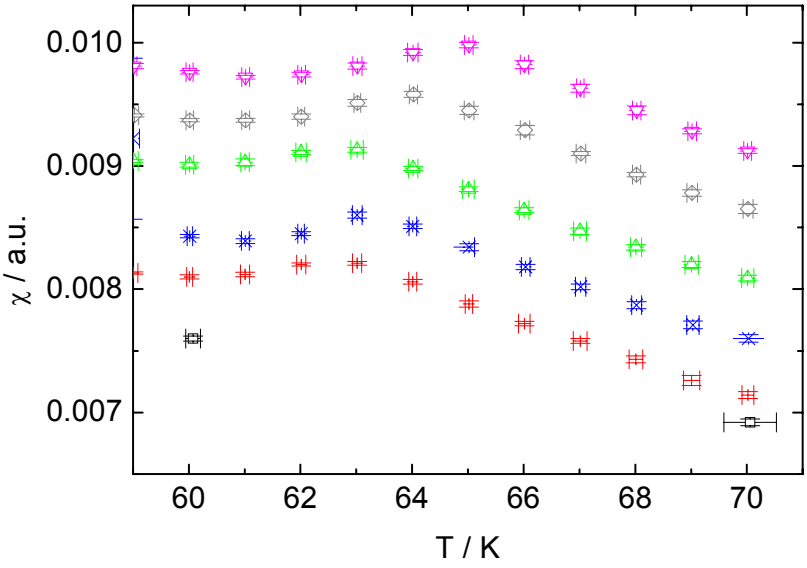

Figure 5.4: Plot of the temperature dependence of the susceptibility of $KFe_3(SO_4)_2(OH)_6$ measured at various applied pressures: (a) ambient pressure (black squares), (b) 1.1 kbar (red plus signs), (c) 1.66 kbar (blue crosses), (d) 1.68 kbar (green upward triangles), (e) 2.3 kbar (grey diamonds) and (f) 4.7 kbar (magenta downward triangles). The plots at different pressures are offset for clarity.

The pressure dependence of T_N is plotted in the phase diagram below (figure 5.5). As the pressure is increased by almost 5 kbar over the range of the experiment, T_N increases by over 2 K.

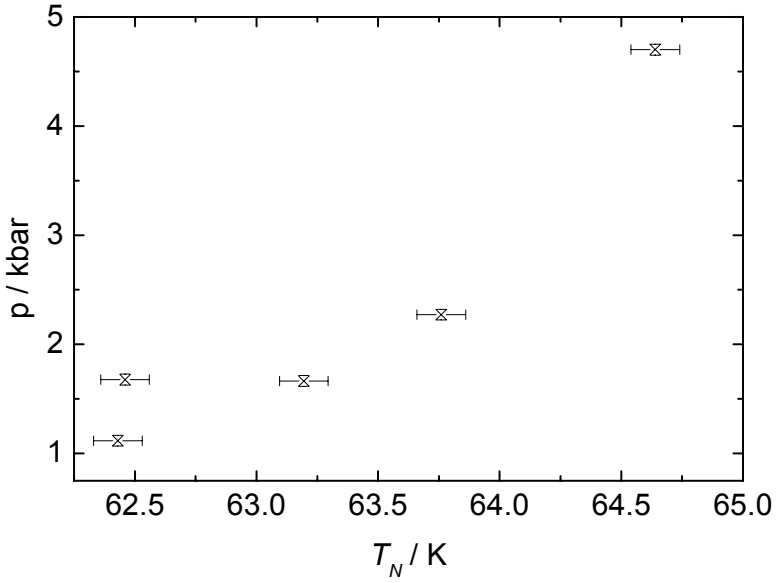

Figure 5.5: Pressure dependence of T_N of $KFe_3(SO_4)_2(OH)_6$.

5.3.2.3 Discussion

The fact that there is an increase in T_N with increasing pressure is compatible with the fact that the iron-iron distances are likely to be decreased. This would increase the orbital overlap, and is therefore likely to increase the degree of superexchange between the metal centres. There is unlikely to be a simple dependence between the applied pressure and T_N, as there are many different factors that affect T_N. It has been proposed[35] that in the case of a layered Heisenberg magnet, T_N can be estimated from the intra- (J_0) and inter-plane coupling (J_1) as:

$$T_N = 4\pi J_0 / \ln(J_0 / J_1)\,. \tag{5.1}$$

This relationship indicates that the ratio of inter-layer to intra-layer coupling is important in determining T_N, and hence will be affected by the ratio of the associated

inter-atomic distances. As the application of pressure to a layered system is likely to favour compression between the layers over compression within the layers, J_1 is likely to be affected to the greatest extent, resulting in this term having the greatest effect on T_N. In order to investigate the extent to which the intra- and inter-plane iron-iron distances affect T_N, a magnetic study such as this needs to be coupled with a parallel structural study. In model kagome systems such as the jarosites, any long range order will be very sensitive to additional terms in the spin Hamiltonian beyond the nearest neighbour interactions, which not only include further-neighbour exchange, but also terms such as the Dzyaloshinskii-Moriya interaction[36] (discussed further in section 5.3.3.5.2), and ligand-field effects that appear as single-ion anisotropy terms (discussed further in section 5.3.3.5.1).

5.3.3 Inelastic Neutron Scattering of Potassium Iron Jarosite

In order to investigate the spin wave spectrum of potassium iron jarosite, a powder sample of $KFe_3(SO_4)_2(OD)_6$ was measured on the time of flight spectrometers, IN4 at the ILL and subsequently MARI at ISIS.

5.3.3.1 IN4 at the ILL

IN4 is a thermal neutron, direct geometry spectrometer working in the neutron energy range 6 – 100 meV. After the high energy neutrons have been removed by the two background choppers, the incident energy is selected by Bragg reflection from a crystal monochromator; Cu or pyrolytic graphite (PG) can be used to give

incident wavelengths in the range 0.8 – 3.8 Å. The arrangement of the monochromator is such that the neutrons are focussed onto the sample, maximising the flux. The neutrons then pass through a Fermi chopper rotating at speeds of up 40000 rpm (> 800 Hz), which forms well defined pulses of neutrons. After scattering from the sample, the neutrons then continue to the bank of ^{3}He detectors, covering a scattering angle of 120°. IN4 has an energy resolution of between 2 - 5 % $\Delta E/E$. A schematic diagram of the layout of IN4 is shown in figure 5.6.

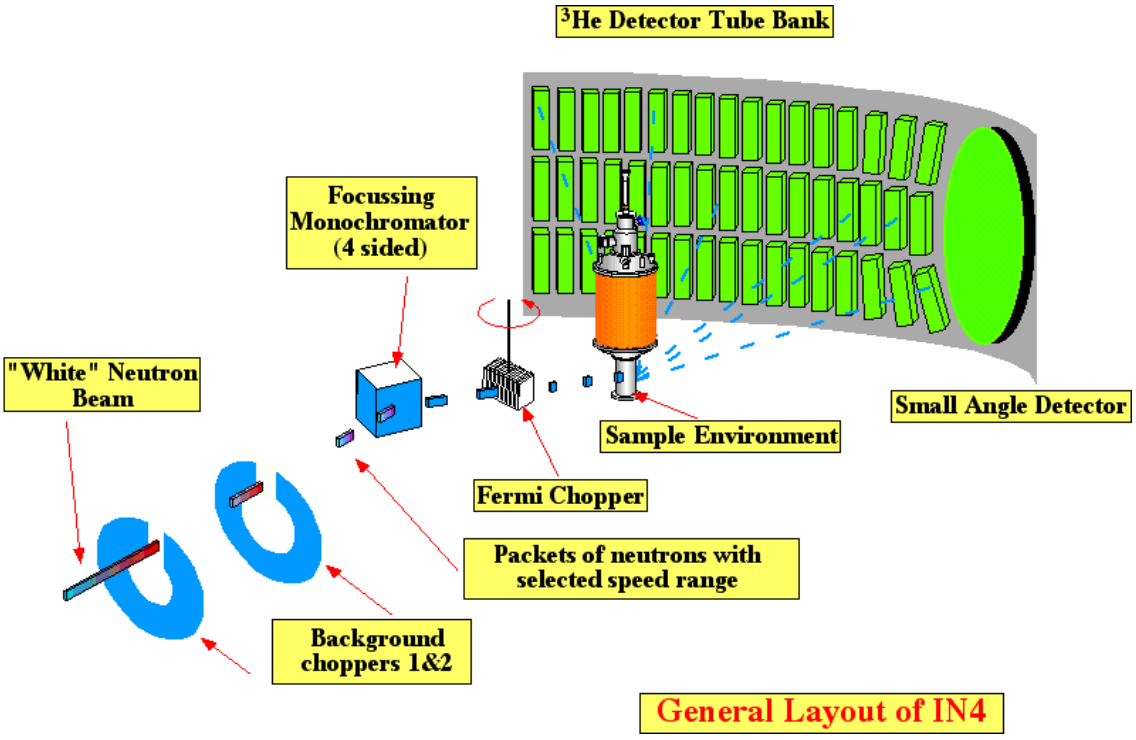

Figure 5.6: Schematic diagram showing the layout of the IN4 spectrometer at the ILL, taken from reference [37].

5.3.3.1.1 Experimental

The experiment performed on IN4 was carried out in a helium cryostat, enabling temperatures between 1.5 and 300 K to be reached. The sample was mounted on a

sample stick in the form of a thin circular disc, wrapped in aluminium foil. An incident neutron wavelength of 1.3 Å was used, which is equivalent to 48 meV, and the scattering as a function of momentum and energy transfer was measured at temperatures ranging from 1.5 K to 250 K, with a number of measurements taken around T_N.

5.3.3.2 MARI at ISIS

Various areas of Q and ω space could not be probed by IN4 in the experimental setup used. Therefore a further experiment was performed on the MARI spectrometer at the ISIS facility in order to probe the lower Q region at 10 meV and to resolve excitations down to 1 meV from the elastic scattering.

MARI is a direct geometry time of flight chopper spectrometer at the pulsed neutron spallation source, ISIS. It is able to cover a range of incident neutron energy from 9 – 1000 meV. After the neutrons have left the methane moderator, two choppers are used to cut out the background. The first chopper (made of Nimonic alloy) is used to cut out the high energy neutrons and a 50 Hz disc chopper is used to suppress the flux of delayed neutrons. The pulse of neutrons then passes to the Fermi chopper. The purpose of this chopper is to monochromate the incident pulse of neutrons. The rotation frequency and the slit package of this chopper can be altered in order for the incident neutron energy, the flux and the resolution of the experiment to be varied. For this experiment, a gadolinium chopper was used, which is optimised for low incident energies (< 200 meV), and therefore leads to better resolution than the

sloppy chopper at these incident energies. The neutrons are then scattered from the sample and pass on to an array of 922 ^{3}He detectors located in an arc under the sample space. These detectors cover a scattering angle of 3° to 135°. A schematic diagram of the MARI instrument is shown in figure 5.7 below.

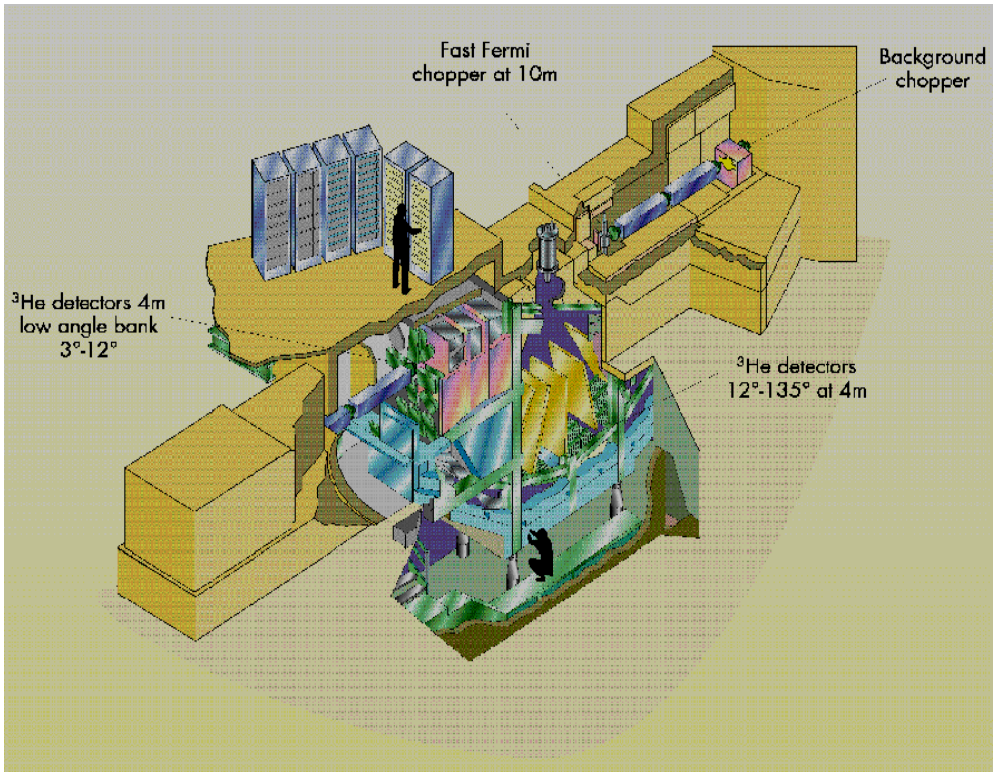

Figure 5.7: Schematic diagram showing the layout of the MARI spectrometer at ISIS, taken from reference [38].

5.3.3.3 Experimental

The experiment performed on MARI was carried out in a closed cycle refrigerator (CCR) at a temperature of 5 K. The sample was wrapped in aluminium foil and placed in an annular geometry into an aluminium sample can. The scattering was measured as a function of momentum and energy transfer at three different incident energies: 60 meV, 15 meV and 8 meV.

5.3.3.4 Results

The imaginary part of the susceptibility $\chi''(Q,\omega)$ was calculated from the dynamic structure factor $S(Q,\omega)$, using the detailed balance condition:

$$\chi''(Q,\omega) = (1-\exp(-\hbar\omega / k_B T))S(Q,\omega)\,. \tag{5.2}$$

Plots of $\chi''(Q,\ \omega)$ calculated from the data measured on IN4, over a range of temperatures, with an incident neutron energy of 48 meV, are shown in figure 5.8 below:

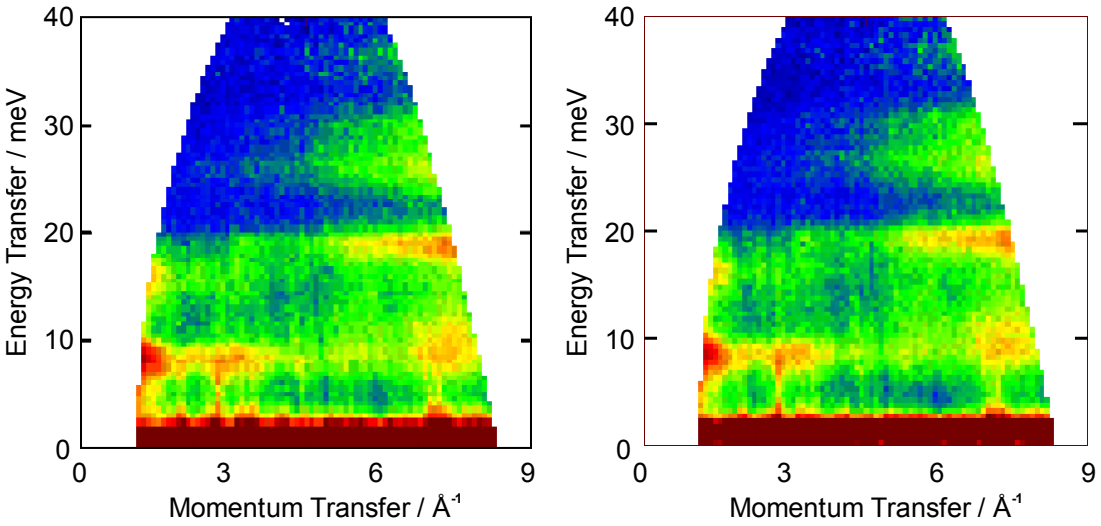

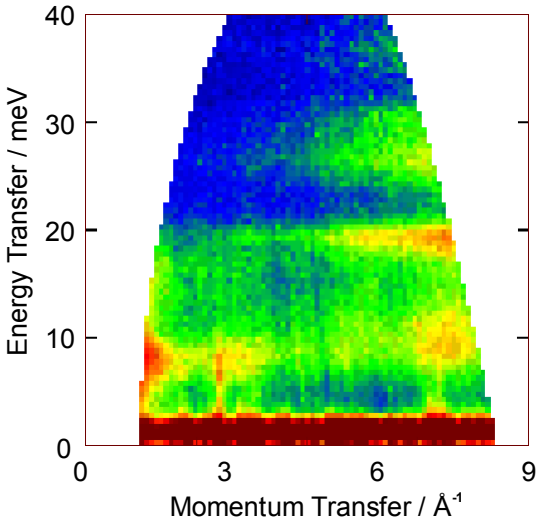
Energy Transfer / meV
Momentum Transfer / Å-1
0
10
20
30
40
0
3
6
9

(c)

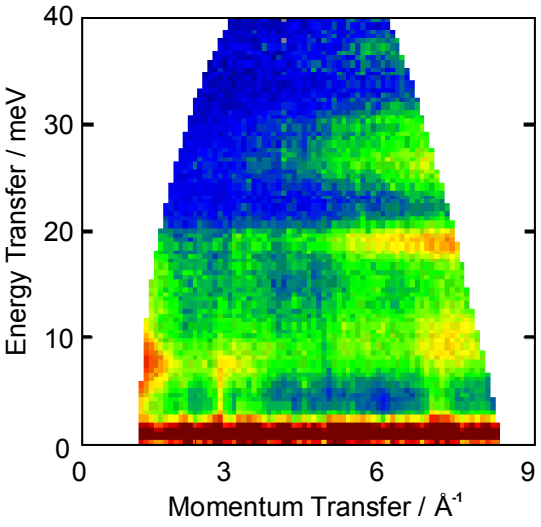
Energy Transfer / meV
Momentum Transfer / Å-1
0
10
20
30
40
0
3
6
9

(d)

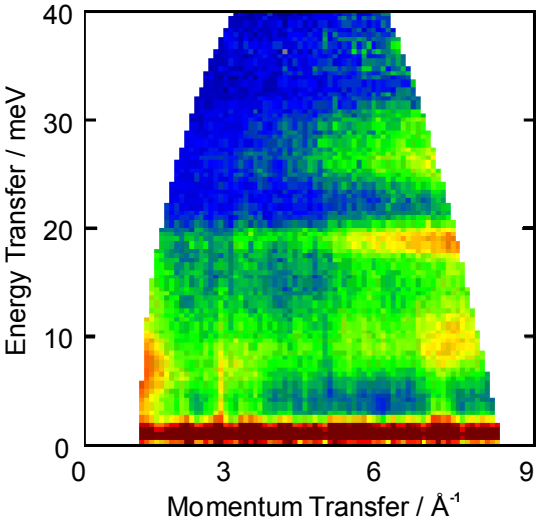
Energy Transfer / meV
Momentum Transfer / Å-1
0
10
20
30
40
0
3
6
9

(e)

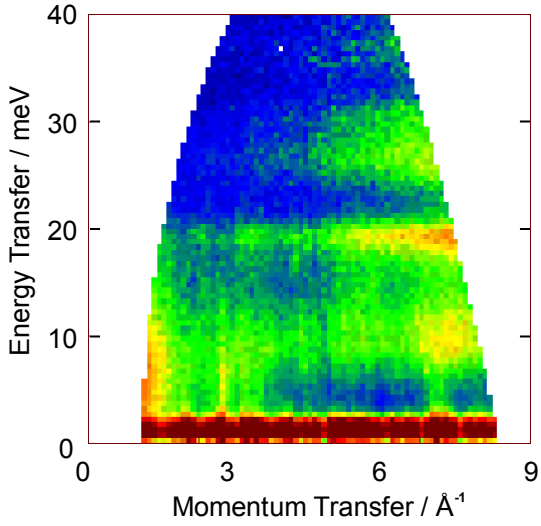
Energy Transfer / meV
Momentum Transfer / Å-1
0
10
20
30
40
0
3
6
9

(f)

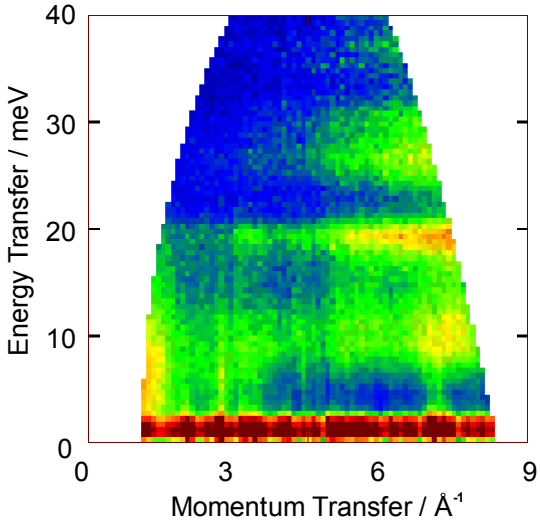
Energy Transfer / meV
Momentum Transfer / Å-1
0
10
20
30
40
0
3
6
9

(g)

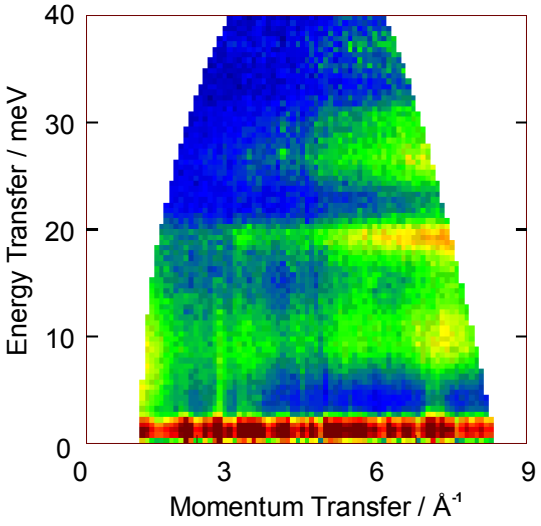
Energy Transfer / meV
Momentum Transfer / Å-1
0
10
20
30
40
0
3
6
9

(h)

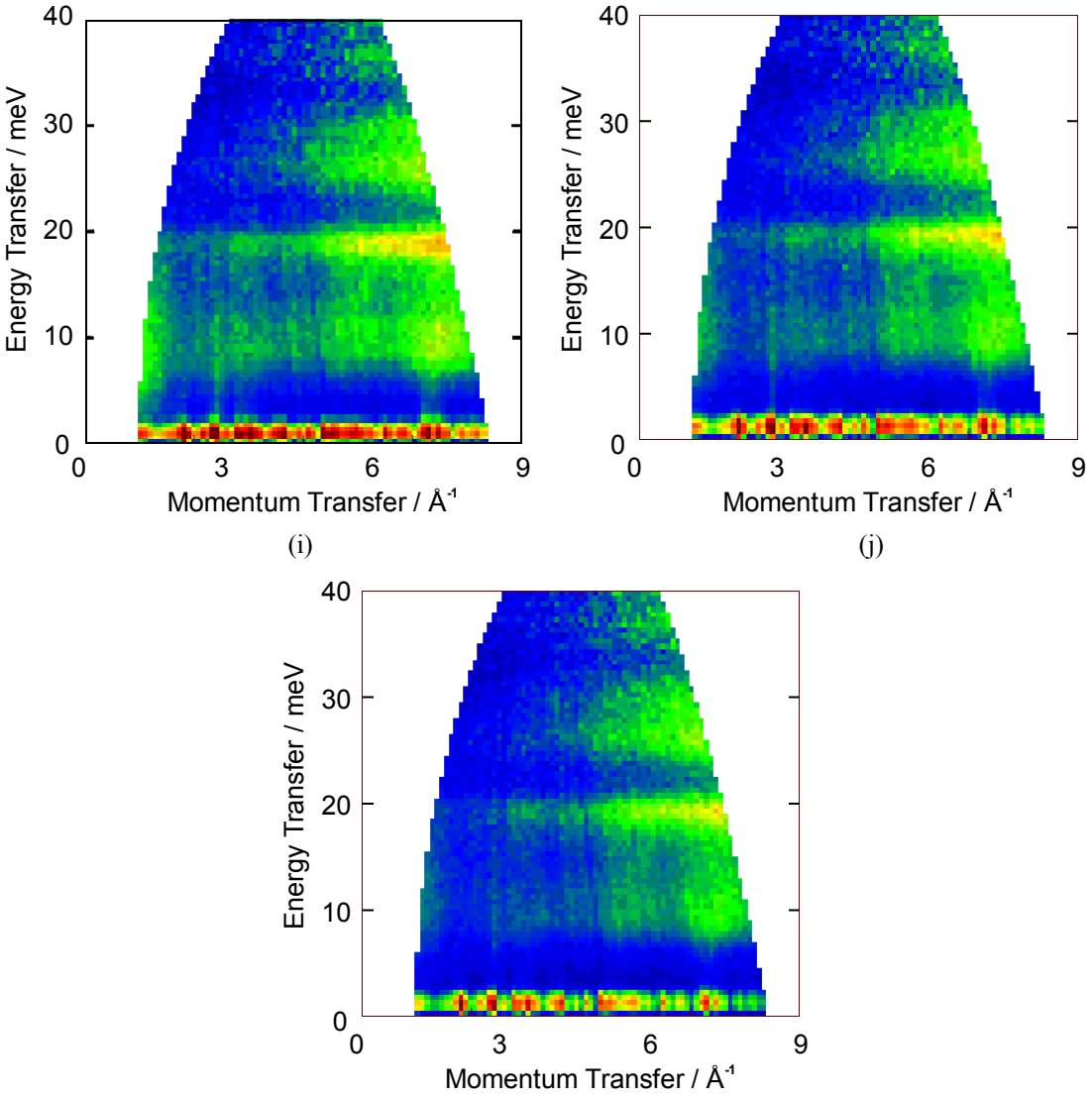

Figure 5.8: Plots of $\chi''(Q,\omega)$ of $KFe_3(SO_4)_2(OD)_6$ measured on IN4 using an incident neutron energy of 48 meV at the following temperatures: (a) 1.5 K, (b) 25 K, (c) 40 K, (d) 50 K, (e) 57.5 K, (f) 65 K, (g) 80 K, (h) 100 K, (i) 150 K, (j) 200 K and (k) 250 K.

Plots were also made of $\chi''(Q,\omega)$ calculated from the data taken at 20 K on MARI at three different incident energies, and are shown in figure 5.9:

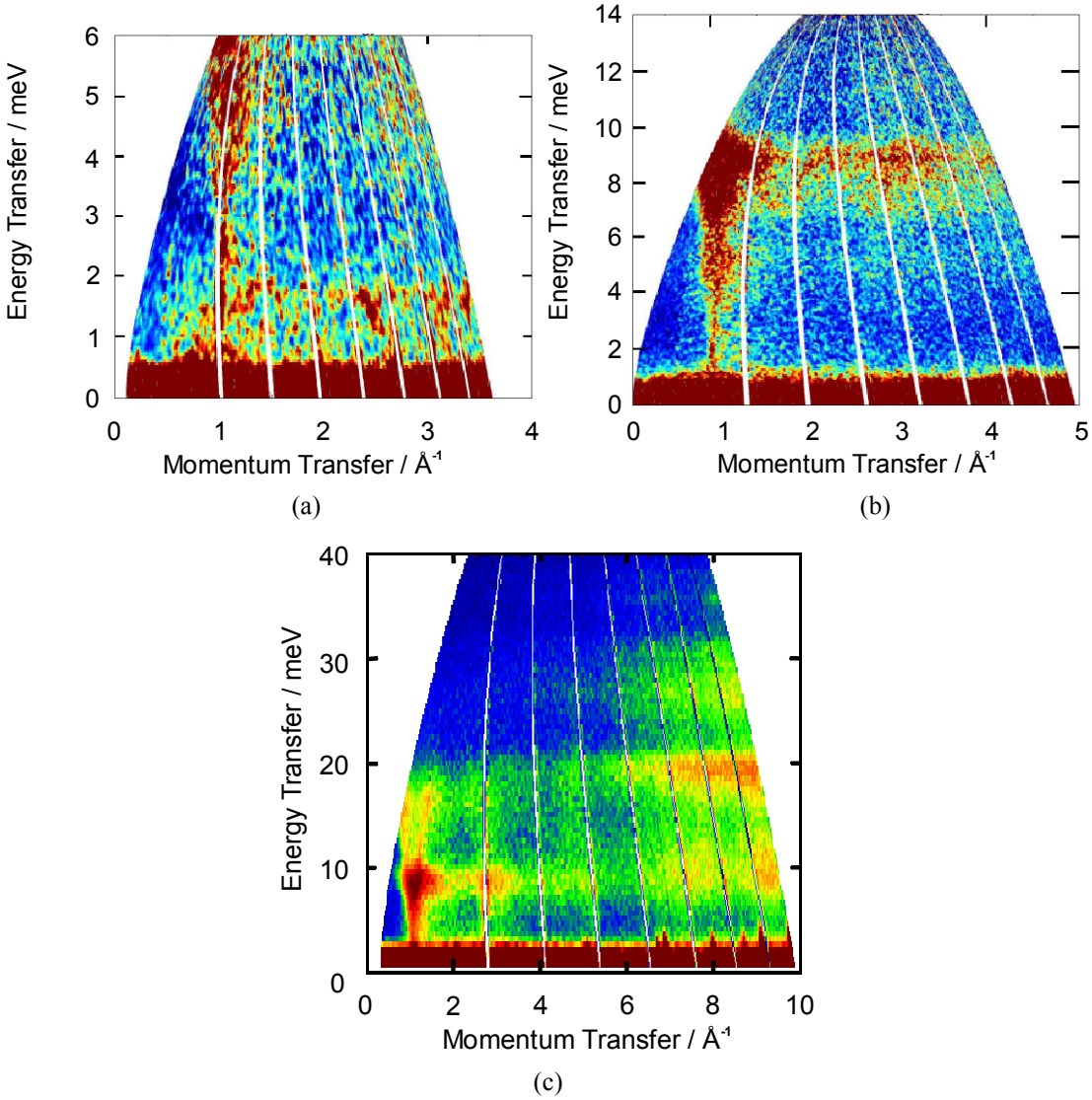

Figure 5.9: Plots of $\chi''(Q,\omega)$ of $KFe_3(SO_4)_2(OD)_6$ measured on MARI at a temperature of 20 K using the following incident neutron energies: (a) 8 meV, (b) 15 meV and (c) 60 meV.

Below T_N (64 K), a weakly dispersive mode can be observed at ~ 7 meV, with an intensity that is modulated in Q (see figures 5.8 (a)-(e) & 5.9). There are clear maxima in the regions of Q = 1 Å^{-1} and 3 Å^{-1}. In the MARI data, dispersive modes can be seen rising from a point centred near Q = 1 Å^{-1}, and stretching towards the possible zone boundary energy (see figure 5.9). Above an energy of 10 meV, there are two branches, which correspond to $\boldsymbol{\tau} \pm \mathbf{q}$ (see figure 5.9 (c)). There is a feature in the data measured with an incident energy of 8 meV (figure 5.9 (a)) at

1.7 ± 0.4 meV, which could correspond to the zero-energy mode lifted in energy. On warming through T_N these distinct modes disappear (see figure 5.8 (f) – (k)).

If it is assumed that the coupling between the kagome layers is negligible, only the symmetry of the problem in the *ab*-planes needs to be considered. The real lattice vectors are then: $\mathbf{a} = a\mathbf{x}$ and $\mathbf{b} = -(a/2)\mathbf{x}+(\sqrt{3}a/2)\mathbf{y}$, where a (= 7.23 Å), is the edge of the real lattice in the $\mathbf{q} = 0$ structure (equal in potassium iron jarosite to twice the nearest-neighbour iron-iron separation), and reciprocal lattice and orthogonal vectors **x** and **y** are displayed in figure 5.10 (c). The reciprocal lattice then has vectors $\mathbf{a}^*/2\pi = (1/a)\mathbf{x} + (1/\sqrt{3}a)\mathbf{y}$ and $\mathbf{b}^*/2\pi = (2/\sqrt{3}a)\mathbf{y}$, which for potassium iron jarosite leads to a second Brillouin zone centred at $Q = 4\pi/\sqrt{3}a = 1.00$ Å^{-1} – compatible with the observed position of the first intensity maximum in the neutron data.

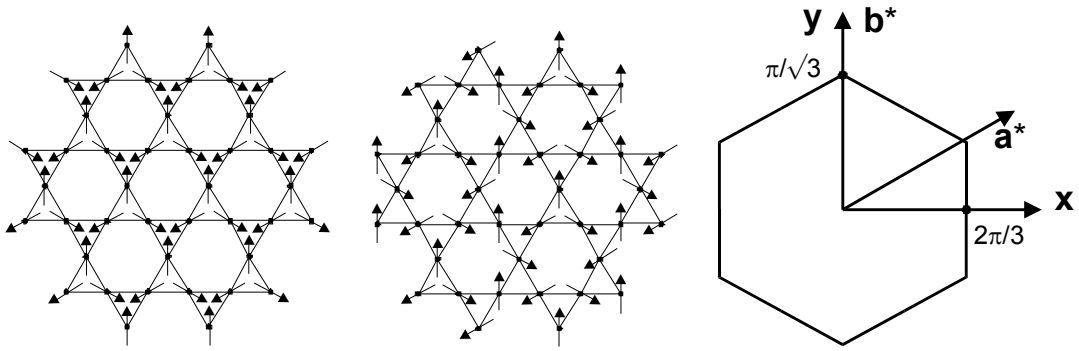

(a) (b) (c)

Figure 5.10: The kagome lattice, with (a) the $\mathbf{q} = 0$ array, (b) the √3 x √3 spin configuration, and (c) the reciprocal lattice vectors and extent of the first Brillouin zone for the purely two-dimensional real-lattice cell of edge a together with the definition of the co-ordinate axes **x** and **y**.

In principle one could model such data to obtain leading parameters in the magnetic Hamiltonian if an expression for $S(Q,\omega)$ was available and a powder average taken;

in the absence of such an expression it is unreliable to assume that some of the more distinct dispersive elements correspond to specific modes.

A second feature may also be distinguished at low temperature at approximately twice the energy of the weakly-dispersive mode, with a similarly flat dependence on Q, though it is also broader in energy and less intense. This is most likely to reflect the zone-boundary energy of the one-magnon excitation spectrum, though it could also be some form of two-magnon excitation. Figure 5.11 displays cuts through the data along an energy axis, centred at Q = 1.75 Å^{-1}, as a function of temperature, clearly revealing a mode centred near 8 meV, and the broader feature centred near 16 meV, at temperatures below T_N.

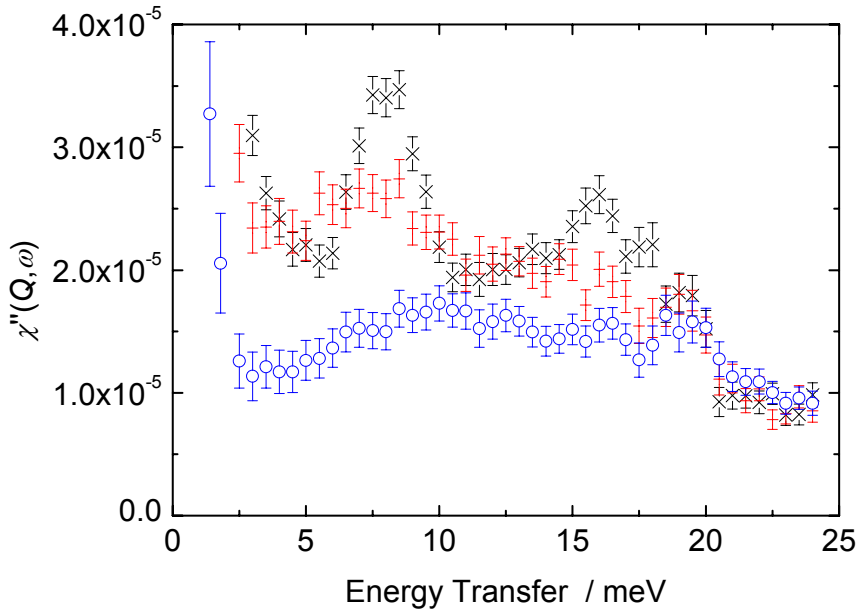

Figure 5.11: Cuts made through χ''(Q,ω) at Q = 1.75 Å^{-1} for $KFe_3(SO_4)_2(OD)_6$ as measured on IN4 at temperatures: 1.5 K (black crosses), 57.5 K (red plus signs) and 150 K (blue circles).

In order to further understand the data measured on the powder sample, these were studied in conjunction with data measured on a natural, single crystal sample of

$KFe_3(SO_4)_2(OH)_6$ on the triple axis spectrometer IN8 at the ILL. These data were measured by another member of our research group, Gareth Oakley[39]. Due to the small size of the sample (14.9 mg) and the high level of protonation, alone, these data proved inconclusive, but in combination with the powder data, it has been possible to map out the in plane dispersion. This is shown in figure 5.12 below:

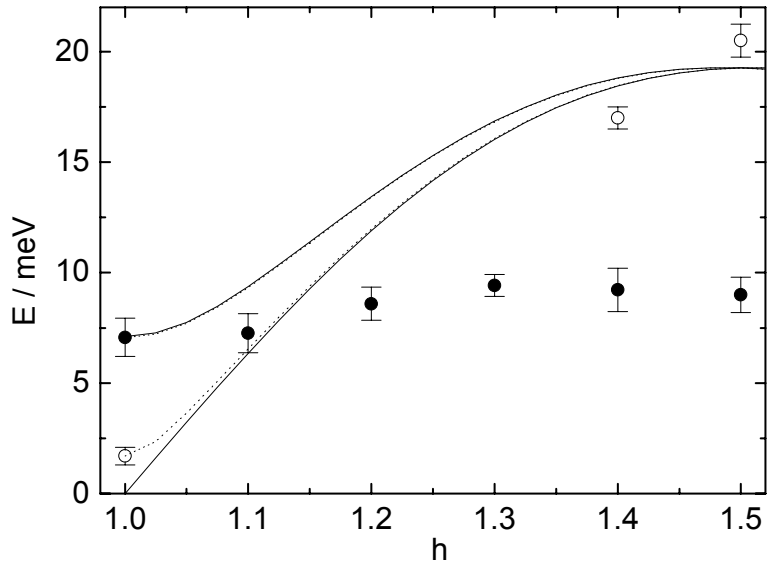

Figure 5.12: Dispersion of excitations observed in potassium iron jarosite along **Q** = (*h h* 1.5) from a combination of single crystal and powder data. A weakly dispersive mode is depicted by the solid circles and a strongly dispersive mode by the open circles. The dotted lines represent spin-wave branches calculated for the crystal field (CF) model and solid lines those calculated for the Dzyaloshinskii-Moriya (DM) model. The upper branches calculated using the DM model obscure branches calculated using the CF model.

5.3.3.5 Calculations and Discussion

In order to further understand the nature of any interactions within potassium iron jarosite, the experimentally measured spin-wave dispersion is compared with existing expressions. The dominant interaction is undoubtedly the nearest-neighbour exchange, J_1, which alone would lead to the following Hamiltonian:

$$\mathcal{H} = J_1 \sum_{<i,j>} S_i \cdot S_j \,, \tag{5.3}$$

where the sum is over all spins *i*, and their nearest-neighbours *j*. Consideration of this Hamiltonian gives three branches in the Brillouin zone for the **q** = 0 structure: one is a non-dispersive, zero-energy mode (ε_1), and the other two (ε_2, ε_3) are degenerate, and disperse to a maximum energy $2J_1S$ at the zone boundary [30, 40].

By investigating both the various exchange pathways, and the collective properties of the iron jarosites, it has been concluded that inter-plane exchange, *J'*, is much less than J_1 [22]; further-neighbour in-plane exchange interactions J_2 and J_3 are likely to be intermediate between J_1 and *J'*. Dispersion relations have been derived for antiferromagnets with up to third further-neighbour interactions within the kagome layers[30, 40]. Other perturbations to the simple Hamiltonian (equation 5.3) that have been considered are single-ion anisotropies arising from crystal field (CF) terms[18], and a Dzyaloshinskii-Moriya (DM) interaction[36, 41]. Both these terms raise the energy of the non-dispersive, zero-energy mode, and may also perturb the energy of the dispersive modes[42]. The effects of introducing either of these two terms into the Hamiltonian are considered below, in an attempt to explain the observation of the flat mode at around 8 meV.

5.3.3.5.1 Single-ion Anisotropy and the Crystal Field Model

The high-spin Fe^{3+} ion, for which crystal field effects would normally be weak, in jarosite lies in an axially distorted octahedral local co-ordination geometry. Combined with finite spin-orbit coupling, this can lead to additional single-ion anisotropy terms of the following form appearing in the Hamiltonian[18]:

$$\mathscr{H} = D\sum_i (S_i^{z'})^2 - E\sum_i (S_i^{x'})^2 - (S_i^{y'})^2, \tag{5.4}$$

where *x'*, *y'* and *z'* refer to a mutually orthogonal local co-ordinate system in which z' is the unique axis of the axially-distorted co-ordination octahedron of iron, and *x'* and *y'* bisect the angle O-Fe-O for those atoms in the equatorial plane of the canted FeO_6 octahedra. Dispersion relations have been derived for this case[18] as follows:

$$\varepsilon_i(\mathbf{q}) = S\sqrt{(J_1(2-\lambda_i(\mathbf{q}) + 2(E-D) + 2(E+D)\cos^2\theta)(2J_1(1+\lambda_i(\mathbf{q})) + 2(D+E)(2\cos^2\theta - 1)}\,, \tag{5.5}$$

where θ is the canting of the *z'*-axis from the crystallographic *c*-axis, and the values of $\lambda_i(\mathbf{q})$ are:

$$\lambda_1 = -1\,; \tag{5.6}$$

$$\lambda_{2,3} = \frac{1}{2}\left(1 \pm \sqrt{-3 + 4\left(\cos^2 q_x + \cos^2\left(\frac{q_x - \sqrt{3}q_y}{2}\right) + \cos^2\left(\frac{q_x + \sqrt{3}q_y}{2}\right)\right)}\right), \tag{5.7}$$

where q_x and q_y are components of **q** in directions **x** and **y** in the reciprocal lattice as defined in section 5.3.3.4 and illustrated in figure 5.10 (c).

For D, $E << J_1$, this anisotropy has the effect of raising the energy of the zero-energy mode of the simple kagome antiferromagnet to an energy of:

$$\varepsilon_1 = S\sqrt{6J_1(D+E)(2\cos^2\theta - 1)}\,. \tag{5.8}$$

D and E also have an influence on the most stable spin array, favouring the **q** = 0 structure over the √3 × √3 spin structure, and further selecting +1 or -1 chirality, depending on the sign of E (figure 5.13). Finally, competition between D, E and J_1 may lead to spin-canting, with the angle δ between the spins and the *xy*-planes when D, $E << J_1$ given by[18]:

$$\sin\delta \cong \frac{D+E}{3J_1}\sin 2\theta\,. \tag{5.9}$$

Iron jarosites studied to date have a **q** = 0 spin structure of +1 chirality as far as the projection of moments in the *ab*-plane are concerned, and some degree of canting towards the *c*-axis, depending on the temperature. Magnetisation measurements yield an estimate of the canted angle in the low-temperature phase to be at least 0.65(6)° at 50 K[22], and zero-field magnetic polarimetry indicates that the upper limit for any canting is of the order of 1° at 20 K [43]. This latter result was for the

same sample for which the current single crystal inelastic neutron scattering data are reported.

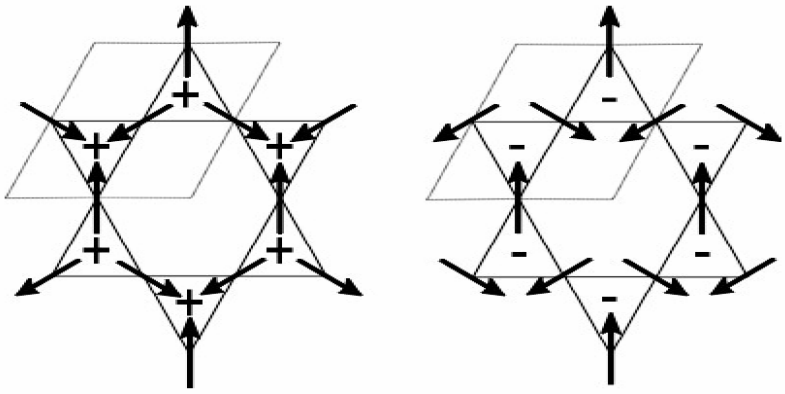

(a) (b)

Figure 5.13: Different forms of the **q** = 0 spin structures of the kagome lattice in the jarosite structure. The rhombus depicts the nuclear unit cell projected onto the *ab*-plane with the *b*-axis horizontal, while (a) and (b) possess a uniform chirality +1 and -1 respectively.

For the more strongly dispersive modes ($\varepsilon_{2,3}$) the values of energy were calculated in terms of J_1, D and E using $\lambda_{2,3}$ as defined in equation 5.7, while the energy of the zone-centre mode at 7 meV was attributed to the weakly dispersive branch (ε_1) and its energy calculated using the value of λ_1 given in equation 5.6. The value of θ was taken to be 21° based on neutron diffraction data taken on the same sample at 20 K[43]. Values of J_1, D and E were then optimized through least-squares fitting of the appropriate expressions to the data, yielding the following values: $J_1 = 3.50(3)$ meV, $D = 0.47(2)$ meV and $E = 0.038(2)$ meV. These result in an estimate of the spin canting angle $\delta = 1.86°$ from equation 5.9, which is significantly larger than the upper limit determined experimentally.

5.3.3.5.2 Dzyaloshinskii-Moriya Interactions

A DM interaction, which is discussed in more detail in chapter 2, introduces the following term to the Hamiltonian:

$$\sum_{<i,j>} \mathbf{D}_{ij} \cdot \mathbf{S}_i \times \mathbf{S}_j \,. \tag{5.10}$$

Here, the vector $\mathbf{D}_{ij}$ may have components both parallel (D_{xy}) and perpendicular (D_z) to the kagome layers, as the canting of the FeO_6 octahedra means that the D_{xy} component is not forbidden by symmetry. The balance between D_{xy}, D_z and J_1, determines the most stable spin-structure. A positive value of D_z favours the $\mathbf{q} = 0$ spin-array with +1 chirality, and similarly a negative value favours that with -1 chirality (see figure 5.13). The D_{xy} term favours canting of the moments out of the kagome layers. The canting angle η may be estimated from the values of D_{xy} and D_z and J_1 using the expression:

$$\tan(2\eta) = \frac{2D_{xy}}{\sqrt{3}J_1 + D_z} \,. \tag{5.11}$$

D_{xy} and D_z may also influence the spin-wave dispersion, with D_z raising the energy of the zero-energy mode so that it becomes[41, 42]:

$$\varepsilon_1 = 2S\sqrt{6\sqrt{3}J_1 D_z + 18D_z^2} \,. \tag{5.12}$$

The same spin-wave excitations as were used in the analysis in the previous section with the CF model, were fitted to equations 5.12 and 5.13; the closest dispersion relation available in the literature for a kagome antiferromagnet with a DM term[42]:

$$\varepsilon_i(\mathbf{q}) = S\sqrt{2\left(J_1\left(1+\lambda_i\left(\mathbf{q}\right)\right)+D_z\sqrt{3}\right)\left(J_1+D_z\sqrt{3}\right)\left(2-\lambda_i\left(\mathbf{q}\right)\right)}\,, \qquad (5.13)$$

where $\lambda_i(\mathbf{q})$ is as given in equations 5.6 and 5.7. The presence of a term D_{xy} will produce a gap at the zone centre for the more strongly dispersing branches, but without any explicit expression to do this, we chose not to fit the data to the lower energy excitation at **Q** = (1.0 1.0 1.5). The result of this analysis is illustrated in figure 5.12, and yields the following optimized parameters: J_1 = 3.33(5) meV and D_z = 0.21(1) meV. There are two further caveats to this analysis: first, both DM and CF terms may co-exist, and although it has been argued that the CF terms are likely to be substantially smaller than the DM terms[36], they may still give rise to significant errors in the optimized DM parameters; second, the fact that the mode whose energy is 7 meV at (1.0 1.0 1.5) weakly disperses indicates that further neighbour exchange is significant.

The *xy* component of **D** may be estimated from the canting angle, assuming it to be the dominant factor determining this parameter. Using a value η = 1° to provide an upper limit for the sample on which our spin-wave data were taken[43], we find from

equation 5.11 that the upper limit on $|D_{xy}|$ is 0.10(2) meV; note that this analysis is unable to provide the sign of D_{xy}[42].

5.3.4 Inelastic Neutron Scattering of Deuteronium Iron Jarosite

In order to investigate the energy spectrum in the spin glass deuteronium iron jarosite, as a function of Q and temperature, a sample was investigated on the MARI spectrometer at ISIS. This spectrometer has been described in detail in section 5.3.3.2.

5.3.4.1 Experimental

The experiments on MARI were carried out using a closed cycle refrigerator (CCR) in order to reach temperatures between ~ 15 K and 300 K. A powder sample of $(D_3O)Fe_3(SO_4)_2(OD)_6$ was wrapped in aluminium foil and placed in an annular geometry, in order to minimise multiple scattering, in an aluminium sample can filled with helium. A chopper slit package with wide slits, known as a *sloppy* chopper, was chosen, as this has a reasonably good resolution for all available incident energies. The chopper frequency was chosen in order to have incident energies initially of 40 meV and then of 10 meV, when it was decided to look at low energy transfers more closely. $S(Q,\omega)$ was measured at a number of different temperatures ranging from 15 K to 240 K. In order to distinguish between the magnetic and nuclear scattering from the iron jarosite, a powder sample of the

diamagnetic analogue $(D_3O)Al_3(SO_4)(OD)_6$ was also measured in the same experimental configuration in order to act as a phonon blank.

5.3.4.2 Results

For each of the temperatures measured, using an incident neutron energy of 40 meV, the total scattering was plotted, and is shown in figure 5.14 below:

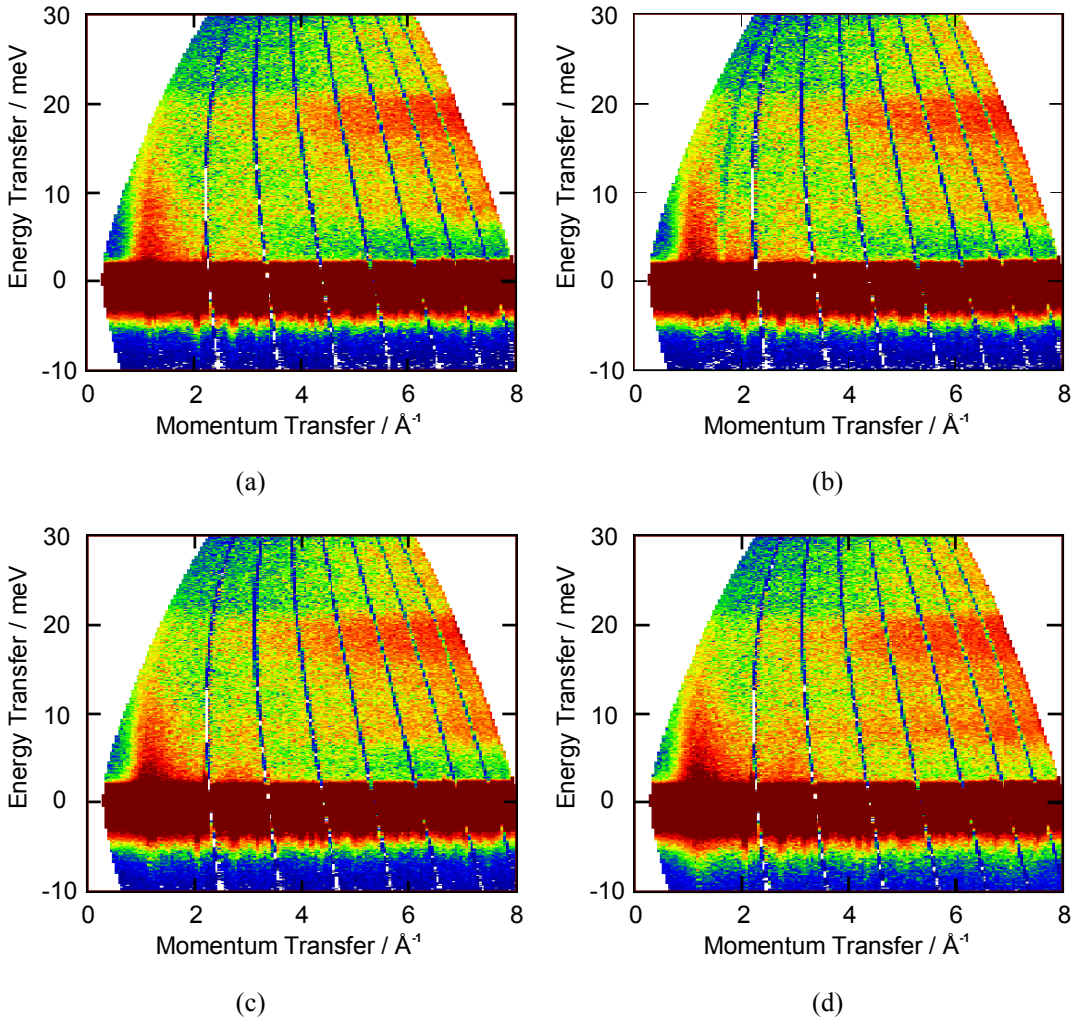

(a) (b)

(c) (d)

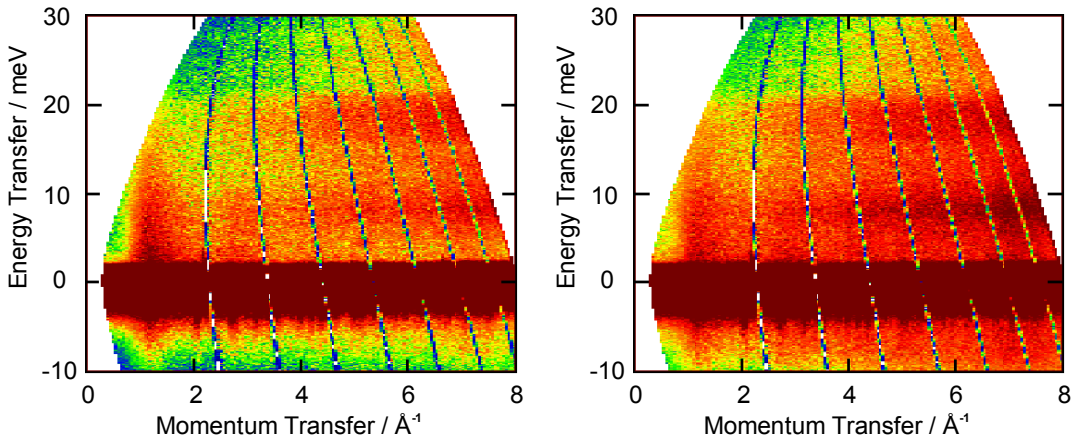

(e) (f)

Figure 5.14: Plots of $S(Q,\omega)$ of $(D_3O)Fe_3(SO_4)_2(OD)_6$ measured on MARI using an incident neutron energy of 40 meV at the following temperatures: (a) 14.5 K, (b) 21 K, (c) 36.1 K, (d) 61.3 K, (e) 121 K and (f) 238 K.

In contrast to the distinct spin waves observed at low values of momentum transfer in potassium iron jarosite, there is no evidence of any distinct modes in deuteronium iron jarosite, even at the lowest temperatures measured. Instead, the magnetic scattering observed at these wavevectors is broad and featureless in the energy transfer direction. This magnetic scattering is very similar in form to the nuclear scattering that is obtained from a liquid, implying that there is little or no freezing of the moments.

In order to investigate the temperature dependence of the scattering along the energy axis, the data were integrated over the range $0.6 \leq Q \leq 2.0$ Å^{-1}, where the magnetic scattering is maximal, and converted into $\chi''(Q,\omega)$ using the relationship shown in equation 5.2. This integration was performed after the data had been corrected for all background and phonon scattering. Figure 5.15 shows the energy dependence of the magnetic component of $\chi''(Q,\omega)$ for all the temperatures measured:

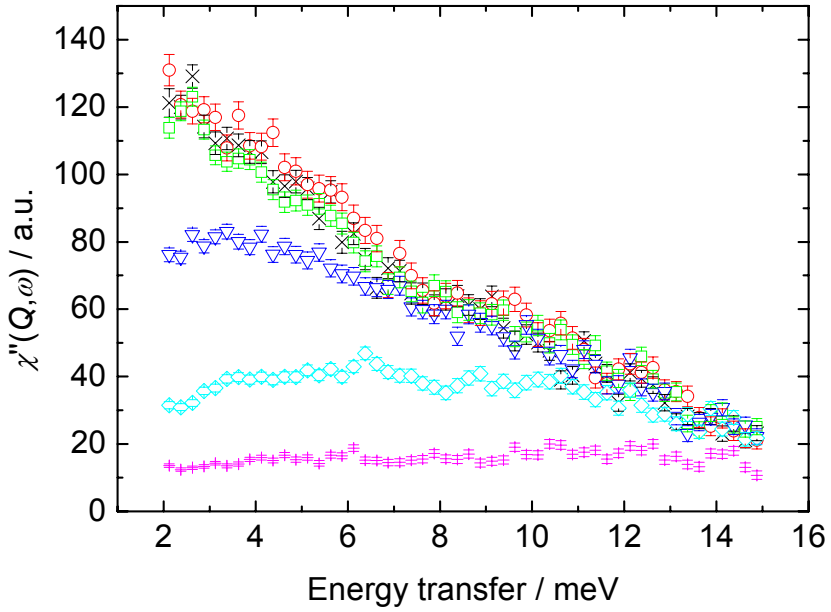

Figure 5.15: χ"(Q,ω) integrated over the Q range 0.6 ≤ Q ≤ 2.0 Å^{-1} measured in $(D_3O)Fe_3(SO_4)_2(OD)_6$ on the MARI spectrometer with an incident neutron energy of 40 meV at temperatures: 14.5 K (black crosses), 21.0 K (red circles), 36.1 K (green squares), 61.3 K (blue triangles), 121 K (cyan diamonds) and 238 K (magenta plus signs).

In order to describe the broadening of the elastic response due to fluctuating spins, for each of the temperatures, fits were made to a quasielastic Lorentzian function, which is appropriate for paramagnets[44]:

$$\chi''(Q,\omega) = \frac{\chi'(Q)\omega\Gamma}{\omega^2 + \Gamma^2}, \tag{5.14}$$

where χ'(Q) is the Q-dependent static susceptibility (*i.e.* for $\omega = 0$) and Γ the inverse relaxation rate of the spins. Plots of the fits to the data measured at each temperature are shown in figure 5.16 below:

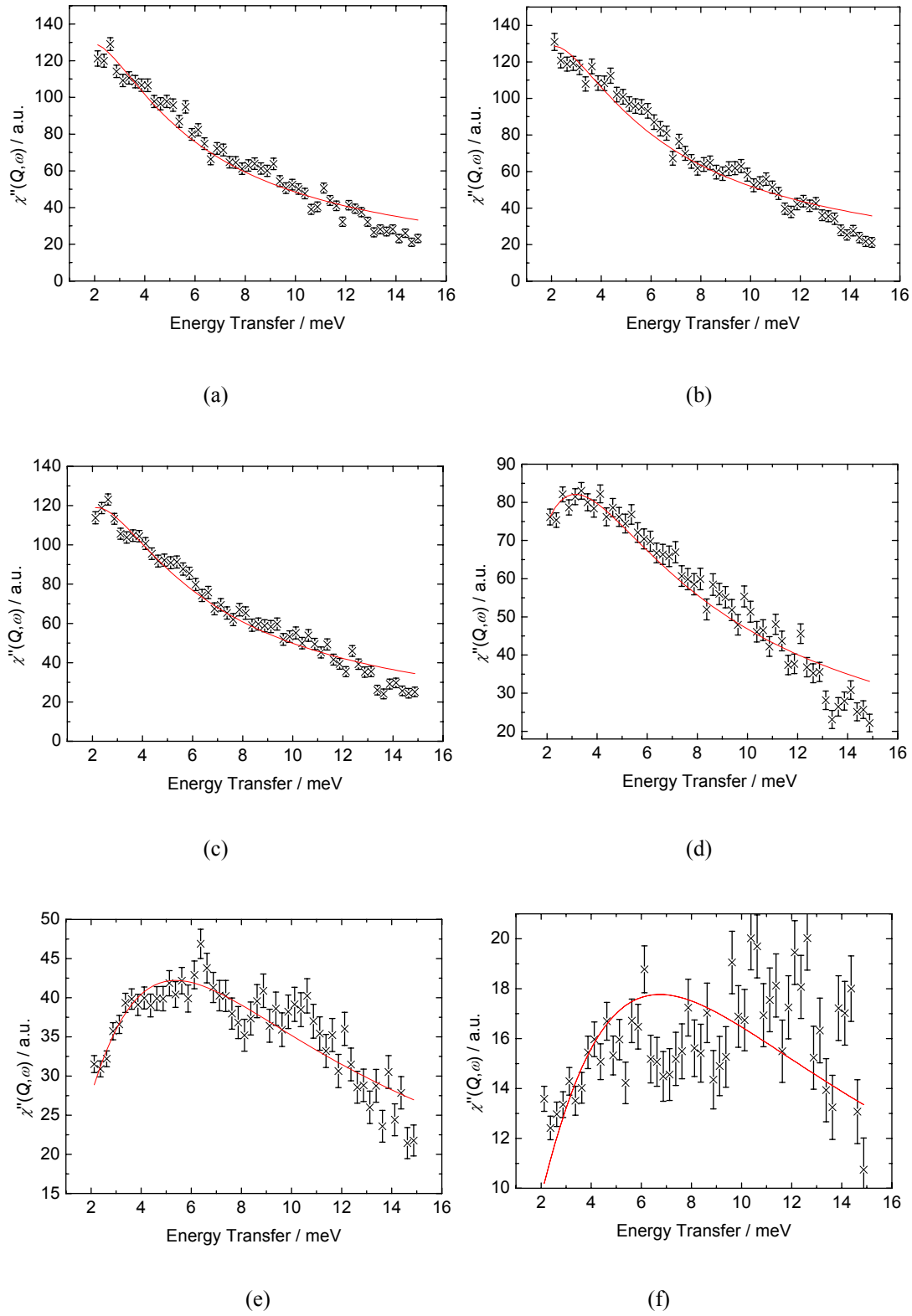

Figure 5.16: $\chi''(Q,\omega)$ integrated over the Q range $0.6 \leq Q \leq 2.0$ Å^{-1} measured in $(D_3O)Fe_3(SO_4)_2(OD)_6$ on the MARI spectrometer with an incident neutron energy of 40 meV, shown by the black crosses, and fits to a quasielastic Lorentzian (equation 5.14), shown by the red line at temperatures: (a) 14.5 K, (b) 21.0 K, (c) 36.1 K, (d) 61.3 K, (e) 121 K and (f) 238 K.

The temperature dependence of the two fitted parameters $\chi'(Q)$ and Γ, was determined and plotted in figures 5.17 and 5.18 below:

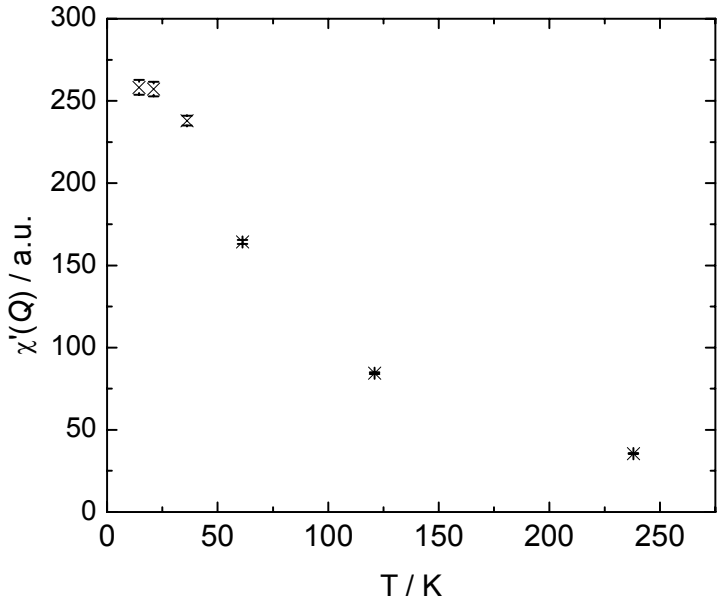

Figure 5.17: Temperature dependence of $\chi'(Q)$ as determined by fits of $\chi''(Q,\omega)$ measured in $(D_3O)Fe_3(SO_4)_2(OD)_6$ to equation 5.14.

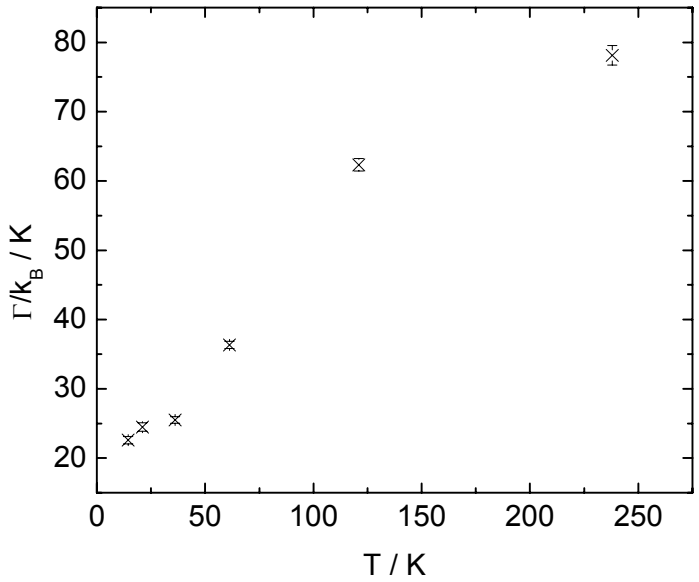

Figure 5.18: Temperature dependence of Γ as determined by fits of $\chi''(Q,\omega)$ measured in $(D_3O)Fe_3(SO_4)_2(OD)_6$ to equation 5.14.

The temperature dependence of the static susceptibility over the *Q*-range investigated is similar in form to the d.c. susceptibility over the same range in temperature[5]; rising in a Curie-Weiss type manner with decreasing temperature until the influence of short-range correlations is observed below 20 K. On increasing temperature, the characteristic relaxation rate increases, as would be expected for a conventional paramagnet; however for such a system, Γ would be expected to increase at the same rate as the temperature. The rate of increase of Γ with increasing *T* is lower than expected for a paramagnetic system. Longer spin relaxation times are associated with the increase in cluster formation, as can be found in spin glass systems[45]. This behaviour is similar to that observed in another spin glass system $ZnCr_2O_4$[46].

The quasielastic Lorentzian function to which the data have been fitted, assumes that there is one characteristic relaxation rate within the sample. Attempts were also made to fit the data to the Bernhoeft function[47], which assumes that there is a distribution of relaxation rates, but it was found that this function did not model the data as successfully as the quasielastic Lorentzian.

5.4 Conclusions and Further Work

The experiments performed on the synthesis and redeuteration of deuteronium iron jarosite have shown that it is possible to significantly improve the sample quality by boiling in D_2O. This is a very useful result, as it has the potential to greatly improve the quality of the data collected from neutron scattering experiments, therefore

optimising the use of neutron beam time. This technique also has the potential to be applied to other similar systems.

Our measurements of the susceptibility of potassium iron jarosite under pressure, have shown that T_N increases under compression. This is in agreement with the fact that the superexchange pathways within the jarosite sample are likely to be strengthened by the application of pressure as the ions are pushed closer together. It would be interesting to investigate this change in susceptibility with applied pressure in parallel with a structural study, in order to investigate whether it is the inter- or intra-plane interactions that are affecting this transition, or the effect of additional terms in the Hamiltonian, such as the DM interaction. Currently it is not certain whether it is the inter-plane coupling or the DM interaction that drives the onset of long range order in experimental kagome systems; a study of both the structural and magnetic properties of such materials under applied pressure could help resolve this. As T_N of an ordered system has been raised by the application of pressure, it would be interesting to investigate whether the application of pressure to a system that does not undergo a conventional ordering transition at ambient pressure, can induce long range order in that system. This has been observed in the pyrochlore system $Tb_2Ti_2O_7$[48], but also studying the spin glass hydronium iron jarosite under pressure could give important insights into the jarosite system.

Using TOF inelastic neutron scattering from a deuterated powder sample of potassium iron jarosite, coherent magnetic excitations have been observed, and their

temperature dependence investigated. These confirm those seen in a natural single crystal sample. The spin-wave spectrum contains modes that disperse strongly in the a^*b^*-plane, as well as weakly dispersive modes whose energy scale depends both on the exchange and smaller terms in the Hamiltonian such as components of a DM interaction or single-ion anisotropy. Appropriate spin-wave dispersion relations were fitted to the most distinct excitations. A model in which the principal perturbations to the simple near-neighbour kagome antiferromagnet arose from CF effects yields the optimized parameters: J_1 = 3.50(3) meV, D = 0.47(2) meV and E = 0.038(2) meV; these in turn yield an estimate of the spin canting angle $\delta = 1.86°$. A second model in which a DM term D_z was present yielded the parameters: J_1 = 3.33(5) meV and D_z = 0.21(1) meV; these parameters, together with a measured upper limit on any spin-canting out of the kagome layers, provide an estimate of 0.10(2) meV for $|D_{xy}|$. The value of J_1 deduced from susceptibility data[30] using a series-expansion based on the simplest Hamiltonian (equation 5.3) was 3.9 meV[49], slightly higher than has been found by neutron scattering. Discrepancies between the parameters may reflect the absence of further-neighbour exchange in our models.

In order to further investigate the nature of these spin waves, a deuterated crystal of sufficient size to perform further inelastic neutron scattering measurements would be required. This would allow the investigation of the dispersion of the various magnon modes and their structure factors, and, together with theory that enables the calculation of these properties for a Hamiltonian that includes not only DM and single-ion anisotropy terms, but also further-neighbour in-plane exchange, and the presence of canting of moments out of the kagome layers, a greater understanding of

this system could be gained. This could allow us to determine whether classical theory is sufficient to explain the static and dynamic properties of classical kagome antiferromagnets.

The dynamic response of a powder sample of deuteronium iron jarosite has been investigated by TOF inelastic neutron scattering. Down to the lowest temperatures measured, there is no evidence of scattering from coherent spin waves (as have been observed in the other members of the jarosite family studied); in contrast the response in energy is broad. In order to model the characteristic relaxation rate of the spins, the data were fitted to a quasielastic Lorentzian function. Although the relaxation rate increases with increasing temperature, this increase is not as rapid as would be expected for uncorrelated spins. This picture is consistent with the behaviour of spin glasses. This experiment shows that the properties of deuteronium iron jarosite (and by inference, the hydronium analogue) differ from other iron jarosites, as there is no onset of long-range order, but glassy behaviour is exhibited. One possible explanation for this is that there is a degree of proton transfer from the H_3O^+ / D_3O^+ cations in the structure to the oxygen atom in the nearest-neighbour Fe-O-Fe bridges, causing a degree of random magnetic exchange. This added degree of disorder could be enough to destabilise long range order.

5.5 References

[1] Lager, G. A., Swayze, G. A., Loong, C. K., Rotella, F. J., Richardson, J. W. and Stoffregen, R. E., *Can. Mineral.*, 2001, **39**: 1131-1138.

[2] Wills, A. S., *PhD Thesis*. 1996, University of Edinburgh.

[3] Papoutsakis, D., Grohol, D. and Nocera, D. G., *J. Am. Chem. Soc.*, 2002, **124**(11): 2647-2656.

[4] Grohol, D. and Nocera, D. G., *J. Am. Chem. Soc.*, 2002, **124**(11): 2640-2646.

[5] Wills, A. S. and Harrison, A., *J. Chem. Soc.-Faraday Trans.*, 1996, **92**(12): 2161-2166.

[6] Grohol, D., Nocera, D. G. and Papoutsakis, D., *Phys. Rev. B*, 2003, **67**(6): art. no.-064401.

[7] Wills, A. S., Oakley, G. S., Visser, D., Frunzke, J., Harrison, A. and Andersen, K. H., *Phys. Rev. B*, 2001, **6409**(9): art. no.-094436.

[8] Wills, A. S., Harrison, A., Mentink, S. A. M., Mason, T. E. and Tun, Z., *Europhys. Lett.*, 1998, **42**(3): 325-330.

[9] Wills, A. S., Harrison, A., Ritter, C. and Smith, R. I., *Phys. Rev. B*, 2000, **61**(9): 6156-6169.

[10] Oakley, G. S., Pouget, S., Harrison, A., Frunzke, J. and Visser, D., *Physica B*, 1999, **267-268**: 145-148.

[11] Oakley, G. S., Visser, D., Frunzke, J., Anderson, K. H., Wills, A. S. and Harrison, A., *Physica B*, 1999, **267 - 268**: 142-144.

[12] Harrison, A., Kojima, K. M., Wills, A. S., Fudamato, Y., Larkin, M. I., Luke, G. M. *et al.*, *Physica B*, 2000, **289**: 217-220.

[13] Inami, T., Maegawa, S. and Takano, M., *J. Magn. Magn. Mater.*, 1998, **177**: 752-753.

[14] Inami, T., Nishiyama, M., Maegawa, S. and Oka, Y., *Phys. Rev. B*, 2000, **61**(18): 12181-12186.

[15] Keren, A., Kojima, K., Le, L. P., Luke, G. M., Wu, W. D., Uemura, Y. J. *et al.*, *Phys. Rev. B*, 1996, **53**(10): 6451-6454.

[16] Maegawa, S., Nishiyama, M., Tanaka, N., Oyamada, A. and Takano, M., *J. Phys. Soc. Jpn.*, 1996, **65**(9): 2776-2778.

[17] Nishiyama, M. and Maegawa, S., *Physica B*, 2003, **329-333**: 1065-1066.

[18] Nishiyama, M., Maegawa, S., Inami, T. and Oka, Y., *Phys. Rev. B*, 2003, **67**: 24435.

[19] Nocera, D. G., Bartlett, B. M., Grohol, D., Papoutsakis, D. and Shores, M. P., *Chem. Eur. J.*, 2004, **10**: 3850-3859.

[20] Harrison, A., Wills, A. S. and Ritter, C., *Physica B*, 1998, **241-243**: 722-723.

[21] Earle, S. J., Ramirez, A. P. and Cava, R. J., *Physica B*, 1999, **262**: 199-204.

[22] Bartlett, B. M. and Nocera, D. G., *J. Am. Chem. Soc.*, 2005, **127**: 8985-8993.

[23] Ballou, R., Canals, B., Elhajal, M., Lacroix, C. and Wills, A. S., *Phys. Stat. Sol. (b)*, 2003, **236**(2): 240-245.

[24] Inami, T., Morimoto, T., Nishiyama, M., Maegawa, S., Oka, Y. and Okumura, H., *Phys. Rev. B*, 2001, **6405**(5): art. no.-054421.

[25] Keren, A., *Phys. Rev. B*, 1994, **50**(14): 10039-10042.

[26] Lee, S. H., Broholm, C., Collins, M. F., Heller, L., Ramirez, A. P., Kloc, C. *et al.*, *Phys. Rev. B*, 1997, **56**(13): 8091-8097.

[27] Morimoto, T., Nishiyama, M., Maegawa, S. and Oka, Y., *J. Phys. Soc. Jpn.*, 2003, **72**(8): 2085-2090.

[28] Townsend, M. G., Longworth, G. and Roudaut, E., *Phys. Rev. B*, 1986, **33**(7): 4919 - 4926.

[29] Chubukov, A., *Phys. Rev. Lett.*, 1992, **69**(5): 832-835.

[30] Harris, A. B., Kallin, C. and Berlinsky, A. J., *Phys. Rev. B*, 1992, **45**(6): 2899-2919.

[31] Pettigrew, K. G., *PhD Thesis*. 2002, University of Edinburgh.

[32] http://www.ill.fr/YellowBook/D20/

[33] Larsen, A. C. and von Dreele, R. B., *GSAS General Structure Analysis System*. 1994: University of California.

[34] Murata, K., Yoshino, H., Yadav, H. O., Honda, Y. and Shirakawa, N., *Rev. Sci. Instrum.*, 1997, **68**(6): 2490-2493.

[35] Pokrovsky, V. L. and Uimin, G. V., in *Magnetic Properties of Layered Transition Metal Compounds*, Ed. by: de Jongh, L. J., 1990, (Kluwer Academic Publishers: Dordrecht).

[36] Elhajal, M., Canals, B. and Lacroix, C., *Phys. Rev. B*, 2002, **66**: 014422.

[37] http://www.ill.fr/YellowBook/IN4/

[38] http://www.isis.rl.ac.uk/excitations/mari

[39] Coomer, F. C., Harrison, A., Oakley, G. S., Kulda, J., Stewart, J. R., Stride, J. A. *et al.*, *J. Phys.: Condens. Matter*, 2006, **18**: 8847 - 8858.

[40] Asakawa, H. and Suzuki, M., *Physica A*, 1994, **205**(4): 687-701.

[41] Ballou, R., Canals, B., Elhajal, M., Lacroix, C. and Wills, A. S., *J. Magn. Magn. Mater.*, 2003, **262**: 465-471.

[42] Elhajal, M., *PhD Thesis*. 2002, Université Joseph Fourier - Grenoble 1.

[43] Harrison, A., Oakley, G. S., Pettigrew, K. G., de Vries, M., McIntyre, G. J., LeLièvre-Berna, E. *et al.*, *Phys. Rev. B*, 2006: In prep.

[44] Lovesey, S. W., *Theory of Neutron Scattering from Condensed Matter*. Vol. 2. International Series of Monographs in Physics, ed. 1984, (Oxford University Press: New York).

[45] Mydosh, J. A., *Spin Glasses: An Experimental Introduction*, ed. 1993, (Taylor & Francis: London - Washington DC).

[46] Ratcliff II, W., Lee, S.-H., Broholm, C., Cheong, S.-W. and Huang, Q., *Phys. Rev. B*, 2002, **65**(22): 220406.

[47] Bernhoeft, N., *J. Phys.: Condens. Matter*, 2001, **13**(39): R771-R816.

[48] Mirebeau, I., Goncharenko, I. N., Cadavez-Peres, P., Bramwell, S. T., Gingras, M. J. P. and Gardner, J. S., *Nature*, 2002, **420**: 54-57.

[49] Grohol, D., Matan, K., Cho, J.-H., Lee, S.-H., Lynn, J. W., Nocera, D. G. *et al.*, *Nature Materials*, 2005, **4**(4): 323-328.

6 Volborthite

6.1 Introduction

We have seen in previous chapters that the two-dimensional systems studied behave in a largely classical manner, and exhibit relatively conventional ground states. In order to further destabilise the ground state of magnetic materials, a combination of geometric frustration, low lattice dimensionality and low magnetic moment is believed to lead to non-classical ground states and excitations. A possible model system manifesting these properties is the $S = ½$ kagome lattice antiferromagnet. In recent years this system has attracted a considerable amount of theoretical interest[1-8]. It is believed that there is no long range order in this system at $T = 0$ [1], even when interactions between planes are considered[6]. It is believed that the ground state consists of some form of singlets, and that the system has a spin gap of the order of $J/20$ [8] (where J is the coupling constant). There is thought to be a band of singlet states within this gap, and a band of triplet excitations at higher energies; one consequence of this is that much of the magnetic contribution to the heat capacity at low temperature is relatively insensitive to magnetic fields. However, the nature of the band of singlets is still unclear, as is the precise energy scale of both magnetic and non-magnetic fluctuations. Therefore there is considerable interest in finding physical realisations of this system.

One approach to finding an $S = ½$ kagome system would be to continue the jarosite family of compounds, by finding a transition metal atom, B, such that B^{3+} is an $S = ½$ species. The best candidate for this would be B = Ti. Unfortunately, as the jarosite

minerals are made by hydrothermal methods, any such species also would need to be stable in solution, and Ti^{3+} has a tendency to oxidise in solution forming the thermodynamically stable TiO_2 compound. The pH required to stabilise the Ti^{3+} ion in solution is too low to favour jarosite formation. Therefore, the search must be widened to include other materials containing the kagome lattice. To date there are only reports of magnetic measurements on three materials that may model this system. One is the copper co-ordination compound $[Cu_3(titmb)_2(OCOCH_3)_6]\cdot 6H_2O$ [9]. Unfortunately, this material contains a high proportion of hydrogen, making it very difficult and expensive to make samples that are suitable for study by neutron scattering. Another, that has come to light in the past year is the mineral herbertsmithite[10], $ZnCu_3(OH)_6Cl_2$, which provides great scope for future investigations. The third material is the naturally occurring mineral volborthite, $Cu_3V_2O_7(OH)_2\cdot 2H_2O$ [11, 12].

6.2 Previous Studies of Volborthite

6.2.1 Structure of Volborthite

The structure of volborthite, $Cu_3V_2O_7(OH)_2\cdot 2H_2O$, was determined by Lafontaine *et al*.[12]; it crystallises in the monoclinic space group *C*2/*m* with unit cell parameters a = 10.607 Å, b = 5.864 Å, c = 7.214 Å and β = 94.88°. There are two formula units per unit cell. The structure of volborthite is shown in figure 6.1. It consists of perfectly planar layers of copper (II) ions surrounded by oxygen atoms in a slightly distorted octahedral geometry. The arrangement of these octahedra is such

that the copper ions are arranged on a slightly distorted kagome lattice. This distortion is manifested as a slight shortening of the Cu-Cu distance along the direction of the *b*-axis, resulting in Cu atoms situated on isosceles triangular arrays. The shorter Cu - Cu distance within the isosceles triangle is 2.937 Å and the two longer distances are 3.031 Å. These layers are separated by pyrovanadate pillars, formed by two corner-sharing tetrahedra of oxygen atoms co-ordinated about vanadium (V) (which has been determined to be diamagnetic by NMR studies[13]). Water is intercalated between the layers. The interlayer Cu – Cu distance is 7.214 Å – the length of the *c*-axis. The dominant pathway for magnetic exchange is almost certainly *via* the in-plane Cu – O – Cu pathway.

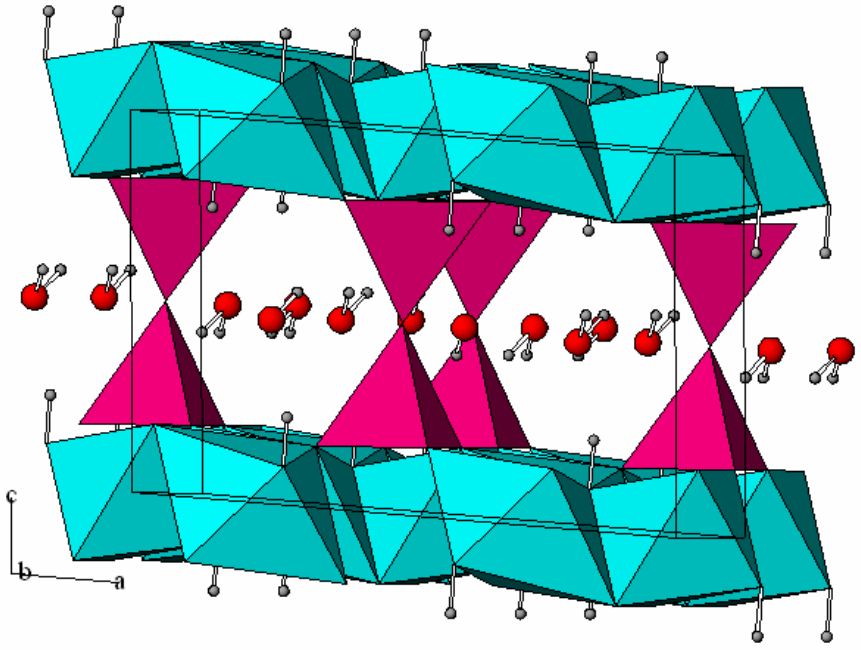

(a)

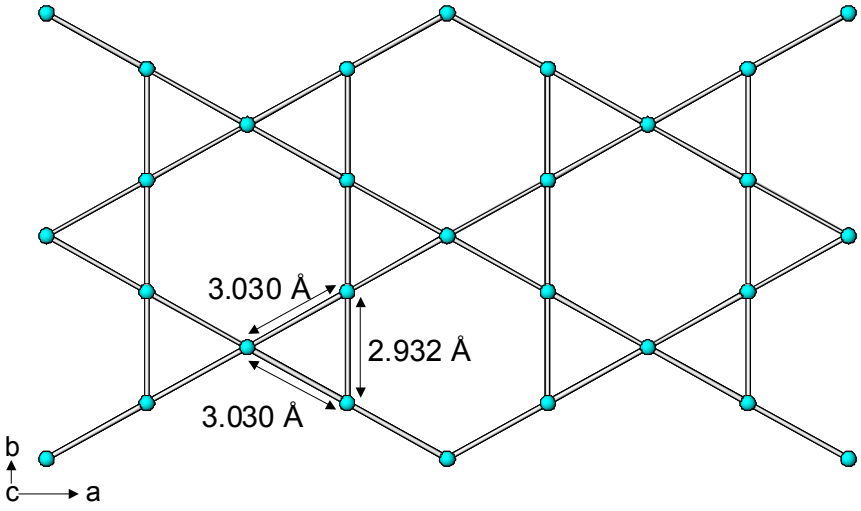

(b)

Figure 6.1: (a) Unit cell structure of volborthite, with the CuO_6 octahedra shown in turquoise, the VO_4 tetrahedra shown in pink and oxygen in red and hydrogen in grey and (b) the distorted kagome layers of Cu(II) ions in volborthite.

6.2.2 Magnetic Properties

The magnetic susceptibility and specific heat capacity of volborthite were measured by Hiroi and co-workers[13]. The magnetic susceptibility shows that volborthite is antiferromagnetic, with θ = -115 K leading to a value of J/k_B = 84.1 K, but no

evidence of any long-range order down to 1.8 K. This was confirmed by heat capacity measurements, which show no anomaly above 1.8 K, but a broad maximum at around 20 K, corresponding to the onset of short-range ordering. ^{51}V NMR spectra measured at a variety of temperatures and frequencies indicate that the vanadium ions are diamagnetic, and that the system is near a quantum critical point between Néel ordered and disordered ground states. Further NMR investigations by Bert *et al*.[14, 15] indicate that volborthite is a spin liquid with a disordered ground state, but with a small amount of well defined short-range order – possibly corresponding to the $\sqrt{3}$ x $\sqrt{3}$ structure.

Fukaya *et al*.[16] have studied both pure and Zn doped volborthite using μSR. During the experiment, a longitudinal field of 100 G was applied in order to decouple nuclear dipolar fields. No oscillations were observed in the muon relaxation asymmetry, implying that there was no long range order of the Cu spins down to a temperature of 50 mK or lower. The Cu spins were found to be fluctuating down to a temperature of at least 50 mK, due to the persistent relaxation of the muon relaxation asymmetry in longitudinal fields, H_{LF}, greater than 100 G. In order to quantify the temperature dependence of the muon decay asymmetry relaxation, the data were fitted with an exponential decay function of relaxation rate, λ, although it was acknowledged that this function did not model the data particularly well. The origin of this anomalous behaviour, found in so-called "undecouplable Gaussian" μSR line shapes, has not yet been fully understood. The temperature dependence of the relaxation rate, shown in figure 6.2, shows that with decreasing temperature, λ increases from 4 K downwards, reaching saturation at around 1 K. This suggests that

dynamic spin fluctuations on Cu persist below 1 K in a quantum (temperature independent) process.

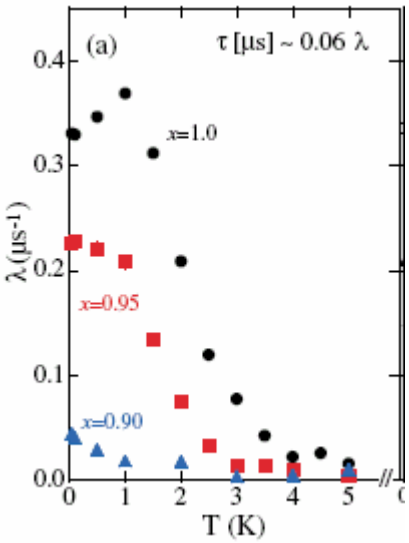

Figure 6.2: Temperature dependence of the relaxation rate λ of the x = 1.0, 0.95 and 0.90 samples of $(Cu_xZn_{1-x})_3V_2O_7(OH)_2{\cdot}2H_2O$ in H_{LF} =100 G. For the instantaneous local field width H_Δ ~ 35 G, the correlation time becomes $\tau[\mu s] \sim 0.06\lambda\ [1/\mu s]$[16].

Bert *et al.*[14, 15, 17] have also studied both pure and Zn doped volborthite using μSR. Their results show a nearly static component to the muon relaxation, which is decoupled in a field of 50 G. This they attribute to muons implanting close to the intercalated water molecules, and experiencing the proton nuclear dipolar field. They also measure a dynamic component that remains down to the lowest temperatures measured (<< 1 K), shown by a component of the muon relaxation that is not easily decoupled with an external field of up to 1600 G and attributed to Cu^{2+} electron spin magnetism. The muon depolarisation rate, λ, as a function of temperature was found by fitting an exponential decay to the muon relaxation asymmetry, and is shown in figure 6.3. The samples were measured in a longitudinal field of 100 G, in order to isolate the dynamic component of the signal. The depolarisation rates found for the Zn doped samples show a similar temperature

dependence to those found by Fukaya *et al*.[16], but for the undoped sample Bert and co-workers measure a much greater relaxation rate at low temperatures, although the temperature at which the relaxation rate saturates is similar.

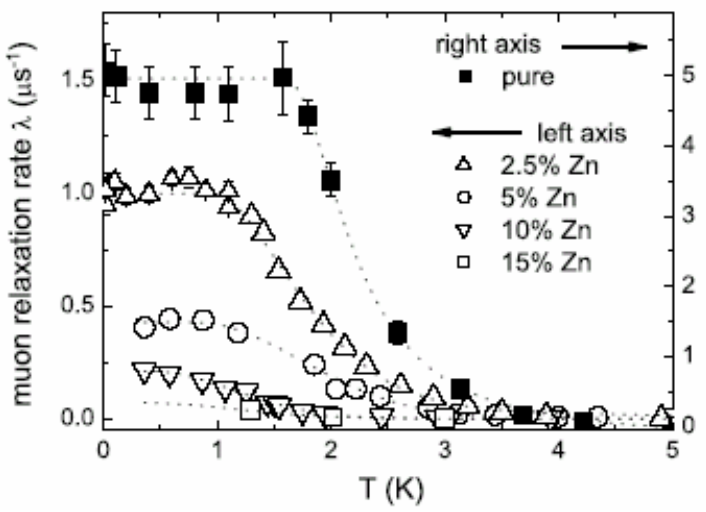

Figure 6.3: Muon depolarization rate λ as a function of the temperature for all the samples studied. The pure sample data are associated with the right-hand axis[15].

6.3 Experimental

Results of previous experiments on volborthite have established that most of the moments remain fluxional down to very low temperatures, while a small degree of spin freezing may occur[13-17]. There is still some disagreement about the timescale of any fluxional behaviour; further experiments have been performed and reported in this chapter, in order to clarify this. Neither the nature of any spin freezing in the ground state, nor the energy scale of any spin gap, have been conclusively reported in the literature. The best way to investigate such properties involves using neutron scattering techniques. For such experiments, good quality samples containing low levels of hydrogen are required. In this chapter the

progressive attempts to make fully deuterated samples of volborthite along with results of various neutron scattering experiments are reported.

6.3.1 Syntheses

6.3.1.1 Synthesis of Volborthite, $Cu_3V_2O_7(OH)_2{\cdot}2H_2O$ – Sample V1

Volborthite was synthesised using an established method[13]. Copper (II) oxide (2.390 g, 30.0 mmol, Lancaster, 99 %) was dissolved in H_2SO_4 (30 ml, 1 M) at 40 °C. V_2O_5 (1.815 g, 10.0 mmol, Acros Organics, 99.6 %) was then added to this solution, and dissolved at 40 °C. After dissolution had occurred, the pH of the solution was increased to 5.4 by the addition of NaOH solution (~ 1 M). The temperature was then increased to 95 °C, and the pale green suspension was stirred at this temperature for a period of 42 hours. The resulting green powder was then washed with water, filtered and dried in a vacuum desiccator to give a yield of 4.55 g.

6.3.1.2 Syntheses of Deuterated Volborthite

In neutron scattering experiments the amount of incoherent scattering needs to be minimised in order to increase the signal to noise ratio, and hence decrease the counting time required. This is particularly important when performing inelastic or diffuse neutron scattering experiments as the scattered neutron flux is much lower than in conventional diffraction experiments. In a $S = ½$ sample such as volborthite, the magnetic scattering is also very low in comparison with the nuclear scattering, so

the level of incoherent scattering must be kept to a minimum to ensure that any magnetic scattering is not obscured. When using polarised neutrons, there is the additional problem that incoherent scatterers have the effect of depolarising the neutron beam, which will decrease the efficiency of any such experiment. As hydrogen has a large incoherent scattering cross-section, the amount of hydrogen in a sample needs to be kept to a minimum. For samples that naturally contain hydrogen, as high a proportion of this as possible should be replaced by deuterium. The syntheses reported throughout this chapter show attempts made to maximise the D / H ratio in volborthite samples, and are included in the experimental details for the respective experiment. For each sample that was made, an idea of the level of deuteration was only obtained during the neutron scattering experiment, and for some of the samples was found to be much lower than desired. Further steps were then taken to improve the synthesis and therefore the level of deuteration within the sample.

6.3.2 D.c. Susceptibility of Volborthite

6.3.2.1 Experimental

For purposes of sample characterisation, the magnetisation of a powder sample of protonated volborthite was measured in a gelatine capsule mounted in a straw, in a Quantum Design $MPMS_2$ SQUID magnetometer. The applied field was 100 Oe, and the susceptibility was measured as a function of temperature between 2 and 340 K, and is shown in figure 6.4. There was found to be no difference between field cooled

and zero field cooled measurements or between samples with differing levels of deuteration.

6.3.2.2 Results

A broad cusp is observed in the susceptibility at around 20 K, and below that there is a rapid increase in susceptibility. This is consistent with a Curie tail, possibly arising due to incomplete copper lattice occupancy. The data measured above 200 K were fitted to the Curie Weiss law with a constant background, giving a Curie constant of 1.52(5) emu K mol^{-1}, corresponding to an effective moment of 2.0 μ_B per Cu^{2+} ion, and a Weiss constant of -128(7) K. For a spin only ion, this value of the effective moment gives a value of $g = 2.32(4)$, which is slightly higher than that of 2.2 found by Hiroi *et al*.[13], but within the range $2.0 \leq g \leq 2.3$ expected for Cu(II)[18]. The data measured at temperatures below 4 K were also fitted to the Curie Weiss law with a constant background, giving $C = 0.120(6)$ emu K mol^{-1}, corresponding to 8 % of the Cu^{2+} in the sample.

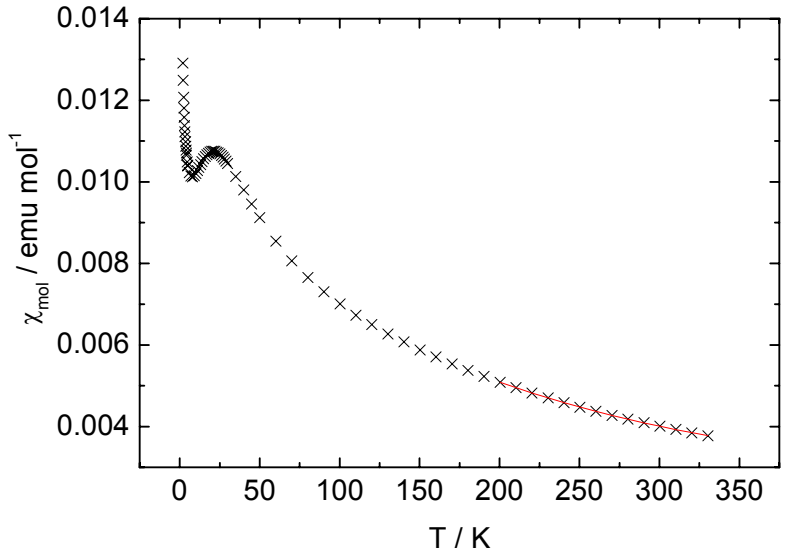

Figure 6.4: D.c. susceptibility (black crosses) of volborthite measured in an applied field of 100 Oe and Curie-Weiss fit (red line) to data over range $200 \leq T \leq 340$ K with $C = 1.52(5)$ emu K mol^{-1} and $\theta = -128(7)$ K.

6.3.3 MuSR

6.3.3.1 Experimental

In order to investigate the nature of any spin freezing in volborthite, muon spin rotation experiments were carried out on the MuSR spectrometer at the pulsed muon source at ISIS. This work was carried out in the majority before the publication of other such results, but was then also used to investigate the discrepancies between the work of Fukaya *et al*.[16] and Bert *et al*.[14, 15, 17]. Instrumental details of this spectrometer are given in chapter 4. Seven 13 mm diameter pellets of ~ 2 mm in thickness of protonated volborthite powder were pressed. Six pellets were arranged around a central pellet and mounted onto a plate with silicone grease and covered with a thin sheet of silver foil. This sample plate was then placed into an Oxford Instruments cryostat, enabling temperatures as low as 1.5 K to be reached. A second

experiment was performed where the sample plate was loaded into a dilution refrigerator which has a base temperature of 40 mK.

6.3.3.2 Results

After the sample had been cooled to base temperature, the field dependence of the muon decay asymmetry was measured at 0.049 K in fields from $0 \leq H \leq 2500$ G. This is shown in figure 6.5.

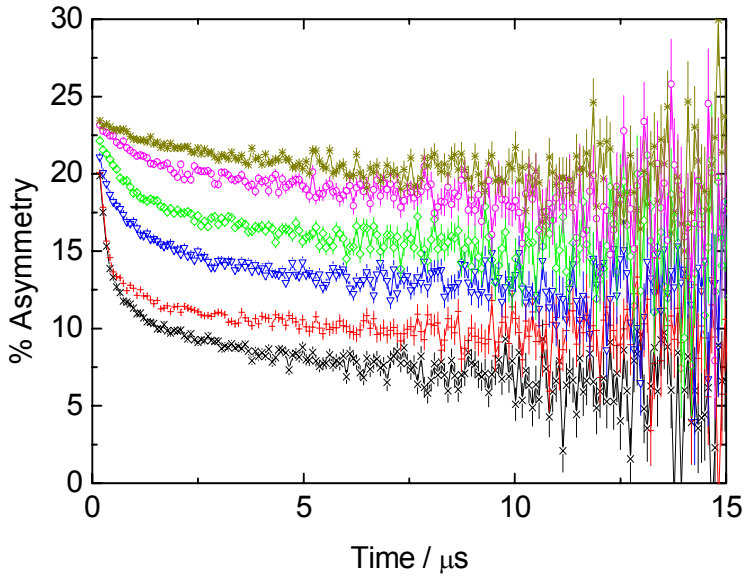

Figure 6.5: Muon decay asymmetry in volborthite measured at $T = 0.049$ K, with longitudinal applied fields shown as: 0 G (black crosses), 50 G (red plus signs), 250 G (blue triangles), 500 G (green diamonds), 1250 G (pink circles) and 2500 G (yellow stars).

Even at this lowest temperature, there is no evidence of the muon experiencing long range magnetic order, which would be shown by oscillations in the muon decay asymmetry. As the applied field is increased, relaxation of the muon decay asymmetry flattens out – this is indicative of the spins within the sample aligning with the applied field. As the shape of the decay asymmetry is changed in low applied fields, this indicates that a significant proportion of the spins within the

sample are frozen at low temperatures. It is possible that nuclear dipolar fields contribute towards the static field; in order to decouple such fields a longitudinal field of at least 50 G was applied to the sample during the experiment. The temperature dependence of the muon decay asymmetry was measured in such a field, and is shown in figure 6.6.

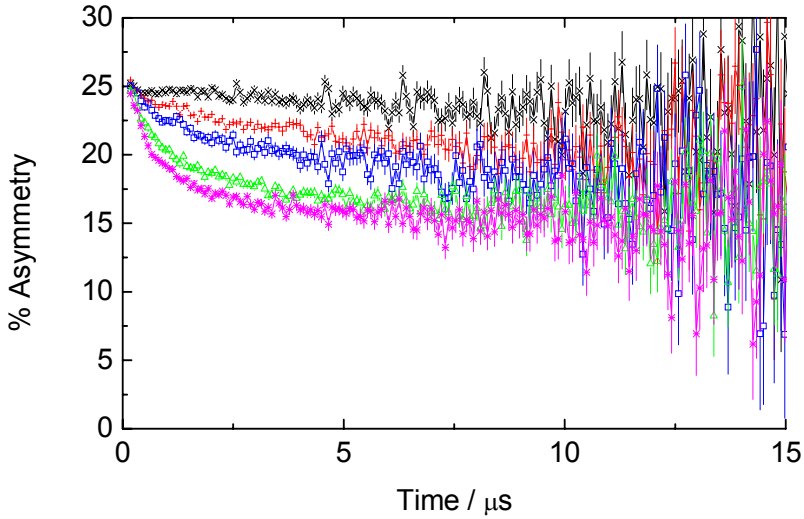

Figure 6.6: Muon decay asymmetry in volborthite measured in a longitudinal applied field of $H = 50$ G, at different temperatures shown as: 5.2 K (black crosses), 4.2 K (red plus signs), 3.3 K (blue squares), 2.3 K (green triangles) and 1.8 K (pink stars).

As the temperature is decreased, the muon relaxation rate increases, indicating a slowing down of the spin dynamics. At high temperatures the muon relaxation asymmetry decays as a stretched exponential, which is the behaviour seen in spin glasses above T_g. At lower temperatures, the muon relaxation asymmetry could no longer be well described by a stretched exponential function, as the initial decay was too fast (see figure 6.7). This is indicative of the increase of static components of the spin.

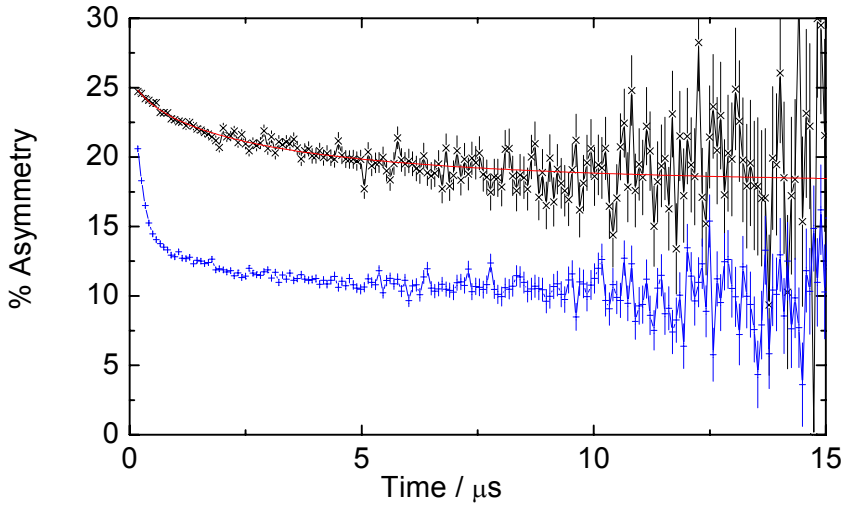

Figure 6.7: Muon decay asymmetry in volborthite measured in a longitudinal applied field of 50 G at 3.4 K (black crosses) and 0.066 K (blue plus signs) with a stretched exponential fit to the high temperature data shown in red.

In this regime the data were fitted to the Keren function[19] (see chapter 3), which models both static and dynamic spin behaviour, with a constant background. The parameter Δ quantifies the static moment and ν the dynamic moment within the sample. The data measured at a temperature of 2.5 K in a longitudinal field of 50 G are shown in figure 6.8, along with a fit to the Keren function with a constant background.

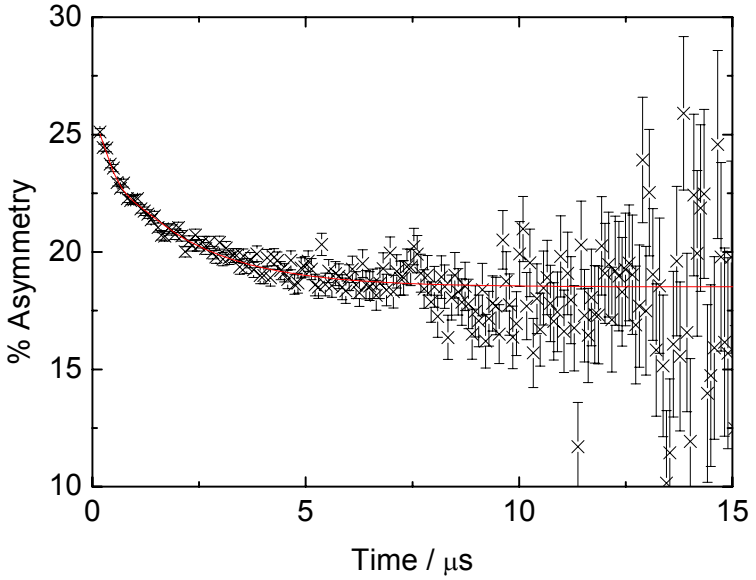

Figure 6.8: Muon decay asymmetry in volborthite measured at T = 2.5 mK in a longitudinal applied field of 50 G (black crosses), and a fit to the Keren function[19] with a constant background (red line).

The temperature dependence of Δ and ν have been plotted, see figures 6.9 and 6.10, in order for trends to be observed.

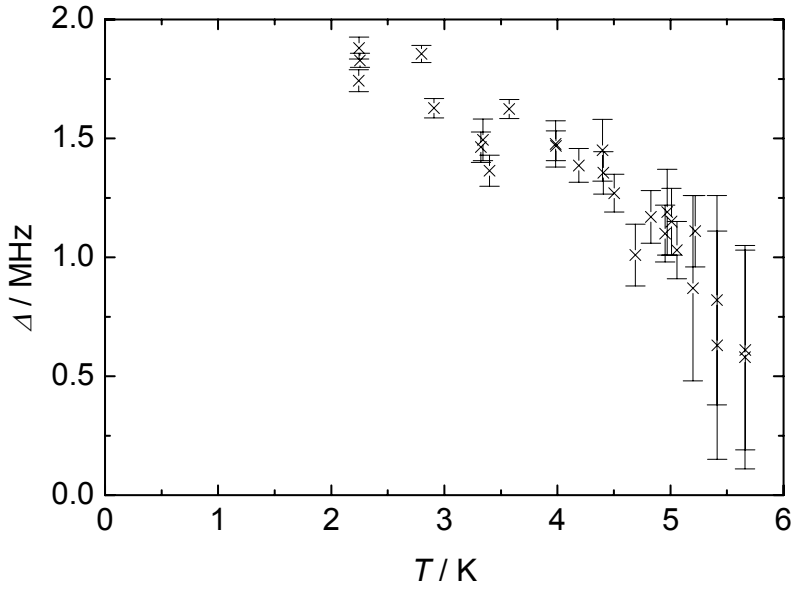

Figure 6.9: Plot of the temperature dependence of the static component, Δ, of fits to the Keren function for volborthite measured in a longitudinal applied field of 50 G.

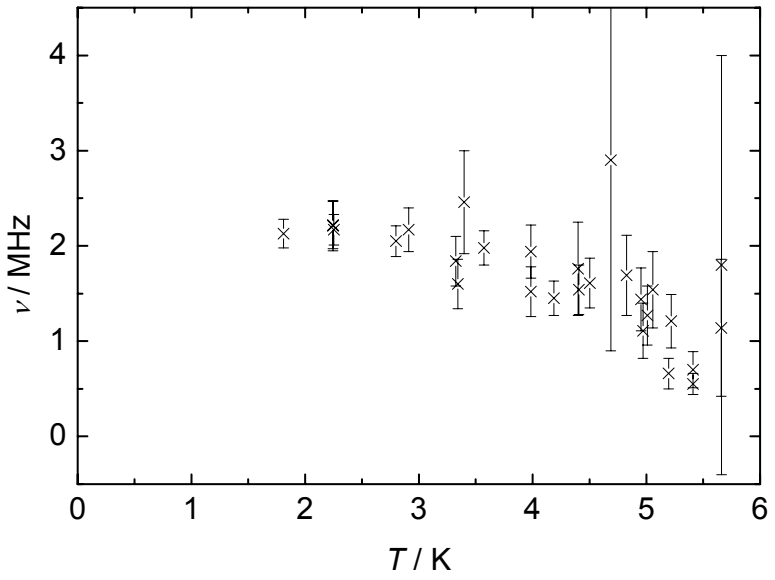

Figure 6.10: Plot of the temperature dependence of the dynamic component, ν, of fits to the Keren function for volborthite measured in a longitudinal applied field of 50 G.

The data shows increasing values of both Δ and ν with decreasing temperature, indicating that both the static and dynamic components of the moment increase as the temperature is lowered. This appears not to be physical, although one explanation for the dynamic character increasing with decreasing temperature, with the static character also increasing is that more of the spin dynamics slow down and enter the timescale measurable by μSR as the temperature decreases.

6.3.4 Neutron Spin Echo

In order to further investigate the timescale of any magnetic fluctuations in volborthite, a neutron spin echo experiment was carried out on the IN11 spectrometer at the ILL. A schematic diagram of this instrument is shown in figure 6.11.

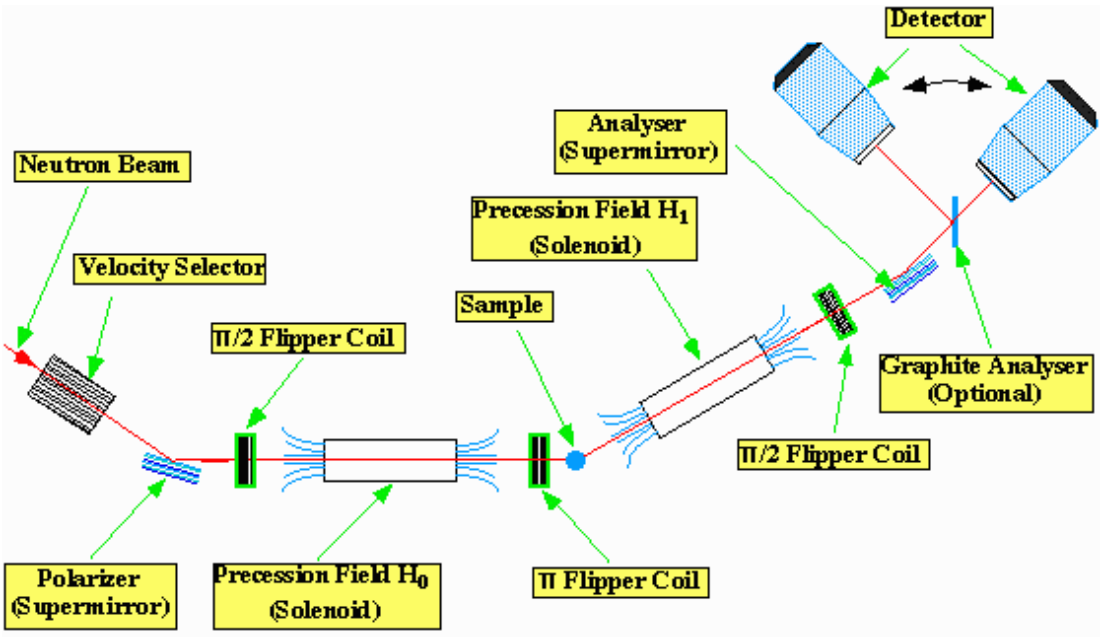

Figure 6.11: Schematic diagram showing the layout of the IN11 spectrometer at the ILL taken from reference [20].

IN11 is situated on a cold neutron source at the ILL, and the incident neutron wavelength (5.5 Å for this experiment) is chosen by a velocity selector. The incident neutron beam is then polarised in a direction parallel to the incident beam direction by a Fe / Ag supermirror to a level of 99 %. The neutron polarisation is then flipped by a π/2 flipper coil in order for it to lie perpendicular to the precession field in the first solenoid, about which the neutrons will precess. The neutrons are then scattered by the sample, where the polarisation is also π-flipped (either by the sample itself or by the use of a π flipper) in such a way that the polarisation remains perpendicular to the direction of propagation. A second precession field causes the neutrons to precess in the opposite direction. The length and field of the coils is such that neutrons of exactly the same velocity will undertake precisely the same number of precessions in each coil, but if the neutrons have been scattered inelastically, the polarisation of the neutrons at the end of the second coil will not be fully restored.

The polarisation is flipped by a further $\pi/2$ flipper, to determine the proportion of neutrons which have their initial polarisation restored. The polarisation is then analysed by a Co / Ti supermirror, before passing on to a detector. The multi-detector configuration of the instrument, IN11c, was used in order to maximise the count rate and investigate a broad range of *Q*. The multidetector covers an angular range of 30° and two positions were used in this experiment to provide two ranges in *Q*: 0.1 – 0.7 $Å^{-1}$ (low *Q*) and 0.95 – 1.35 $Å^{-1}$ (high *Q*). The high *Q* position is centred on 1.1 $Å^{-1}$; this is the *Q* vector corresponding to twice the nearest neighbour distance within the Cu lattice, which is the correlation distance expected for antiferromagnetic interactions.

6.3.4.1 Sample Synthesis – Sample V2

For the neutron spin echo and other neutron scattering experiments, a sample of volborthite with reduced levels of hydrogen was synthesised. The sample was synthesised as for the protonated sample, V1, described in section 6.3.1.1, but the 1 M solutions of H_2SO_4 and NaOH were made by solution in D_2O in place of H_2O. The entire synthesis was carried out under a nitrogen atmosphere created by flowing nitrogen over the reaction mixture in the glass apparatus throughout the synthesis. The resulting powder was dried at room temperature under vacuum.

6.3.4.2 Experimental

For this experiment a powder sample of volborthite was loaded into a Cu sample can, which was placed in an ILL ^3He / ^4He dilution fridge. Measurements were taken at

two temperatures: 52 mK (the base temperature of the dilution fridge) and 6 K (the temperature at which MuSR experiments indicate that the spin fluctuations start to slow down). In order to maximise the signal to noise ratio of the data, measurements were made at only six points in Fourier time.

6.3.4.3 Results

For the three experimental configurations described in the previous section, the scattering intensity measured as a function of Fourier time and momentum transfer ($S(q,t)$), was plotted relative to the elastic scattering intensity ($S(q,0)$) for six different points in Fourier time. A summary of the data is shown in figure 6.12.

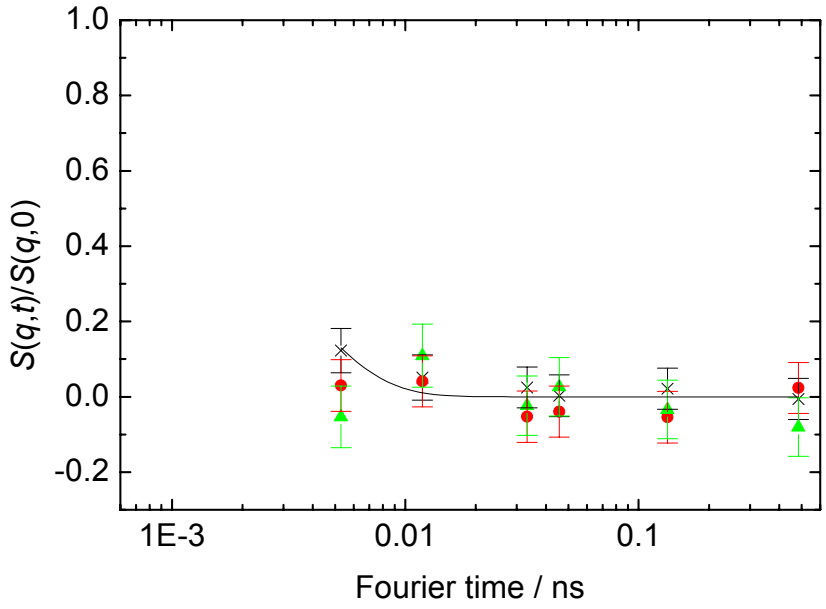

Figure 6.12: Plot of $S(q,t)$ / $S(q,0)$ versus Fourier time in volborthite for three experimental configurations: $T = 6$ K & $0.95 \leq q \leq 1.35$ Å^{-1} (green triangles), $T = 52$ mK & $0.1 \leq q \leq 0.7$ Å^{-1} (red circles) and $T = 52$ mK & $0.95 \leq q \leq 1.35$ Å^{-1} (black crosses), with an exponential fit to the latter, giving a correlation time of 2.6 ps (shown by the black line).

Within the error of the measurement, both the high temperature measurement and the low Q, low temperature measurement, were consistent with a time dependent

scattering intensity of zero. This is indicative of the spin-spin relaxation occurring on a timescale faster than can be measured by this neutron spin echo experiment. The high Q, low temperature data were fitted to an exponential decay. This indicated that at this temperature the relaxation has slowed down into the timescale of the measurement with a spin-spin correlation time of 2.6(2) ps.

6.3.5 XYZ-Polarised Diffuse Neutron Scattering

In order to investigate the form of the static magnetic correlations in volborthite, neutron scattering experiments were performed on the D7 spectrometer at the ILL. D7 is a spectrometer that has been designed to specifically study diffuse scattering from materials[21]. The instrument can employ full 3-directional "*XYZ*"-polarisation analysis, which enables the scattering to be separated into nuclear-spin-incoherent, nuclear and magnetic components. This means that D7 is particularly useful for studying diffuse magnetic scattering.

A focussing pyrolytic graphite monochromator is situated in the cold source neutron guide at the ILL to select an incident wavelength of 3.1 Å, 4.8 Å or 5.8 Å. Scattered neutrons of higher wavelength are subsequently removed by a cooled beryllium filter. The neutron beam is then polarised using a supermirror polarizer. A supermirror contains alternating layers of magnetic and non-magnetic materials, which reflect the neutrons of a particular polarisation and transmit or absorb neutrons of the opposite polarisation. This results in a spin polarised neutron beam being produced. The direction of the neutron spins are manipulated by a Mezei π flipper

(an arrangement of coils that can alter the polarisation direction of a neutron by π radians) followed by a set of orthogonal *XYZ* field coils (which allow the incident beam polarisation direction to be defined). The neutrons are then scattered by the sample, and pass on to the detector banks. These consist of removable supermirror analysers situated in front of ^{3}He detector tubes. A schematic diagram of the D7 spectrometer is shown in figure 6.13.

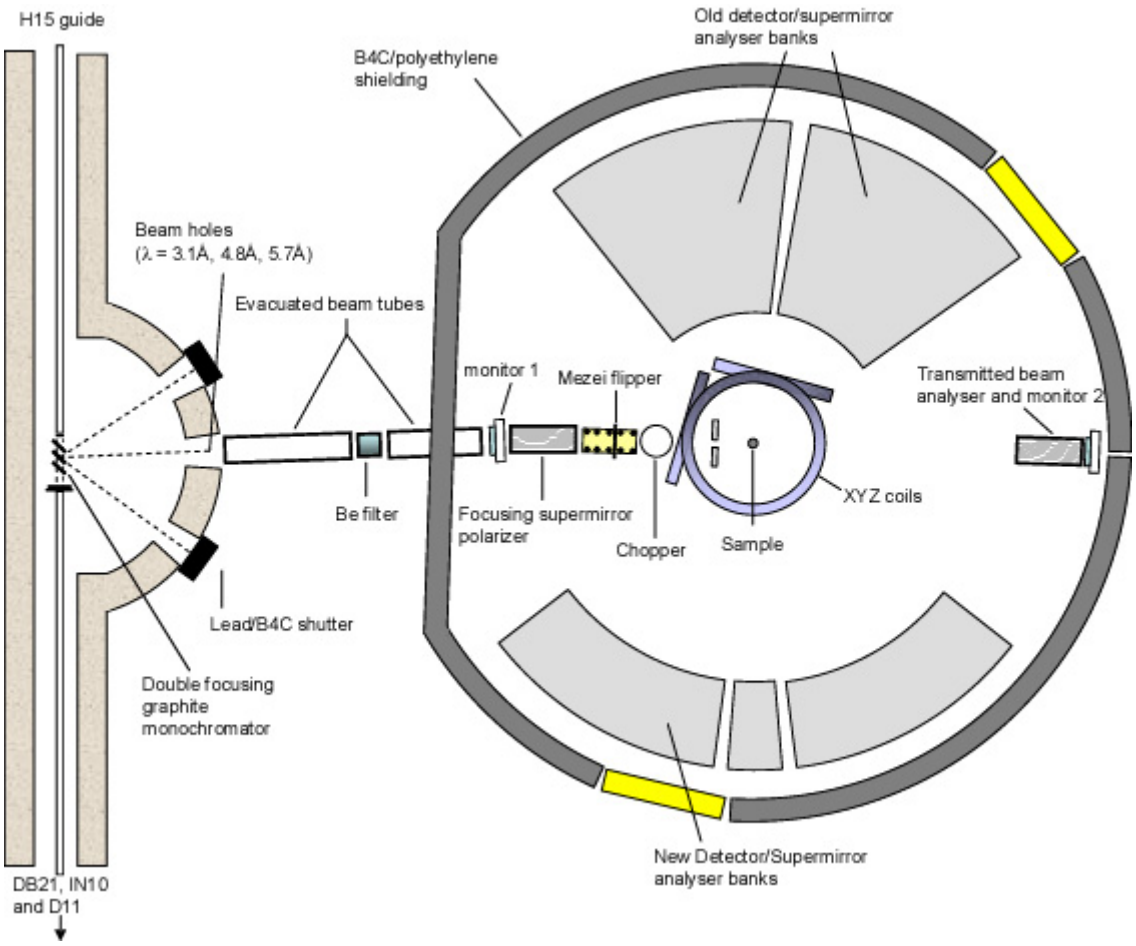

Figure 6.13: Schematic diagram showing the layout of the D7 spectrometer at the ILL taken from reference [22].

6.3.5.1 First D7 Experiment

The first D7 experiment with volborthite was performed using an incident neutron wavelength of 4.8 Å. The measurement on the first sample (V2) indicated that the H/D ratio was unacceptably high for a polarised neutron scattering experiment. Successive attempts were then made to reduce the H/D ratio in the sample, resulting in measurements on further samples (V3 & V4), during the allocated experimental period. The following sections contain details of the various syntheses and the levels of deuteration after each step.

6.3.5.1.1 Sample Synthesis – Sample V2

The first sample measured was the sample measured in the neutron spin echo experiment, and the synthesis is described in section 6.3.4.1.

6.3.5.1.2 Results – Sample V2

The spin incoherent scattering was plotted, along with the nuclear and magnetic scattering, as a function of Q (figure 6.14). The level of spin incoherent scattering was then used to calculate the total quantity of hydrogen in the sample.

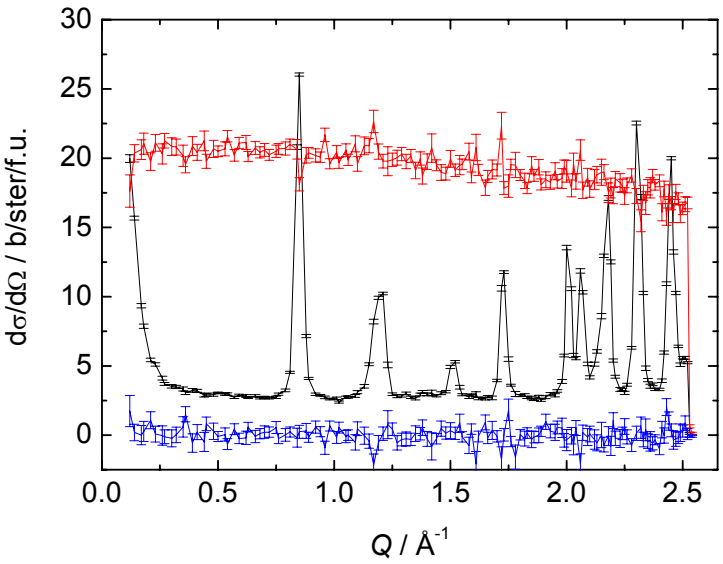

Figure 6.14: Nuclear (black, middle), spin incoherent (red, upper) and magnetic (blue, lower) scattering from volborthite sample V2.

The level of spin incoherent scattering in this sample corresponds to ~ 3 H atoms per formula unit, a hydrogen level of 50 %. The percentage occupancy of hydrogen on the two different crystallographic sites in volborthite were determined by Rietveld refinement (see figure 6.15) of the nuclear scattering using the software GSAS[23], giving a hydrogen occupancy on the -OH site (H1) = 40(3) % and an occupancy on the interlayer H_2O site (H2) = 25.6(8) %. As these figures are lower than the amount of hydrogen calculated from the spin incoherent scattering, it is likely that there is a significant amount of hydrogen contained in water adsorbed onto the surface of volborthite. The high overall level of hydrogen in the sample may have arisen due to exchange with atmospheric water during the sample synthesis.

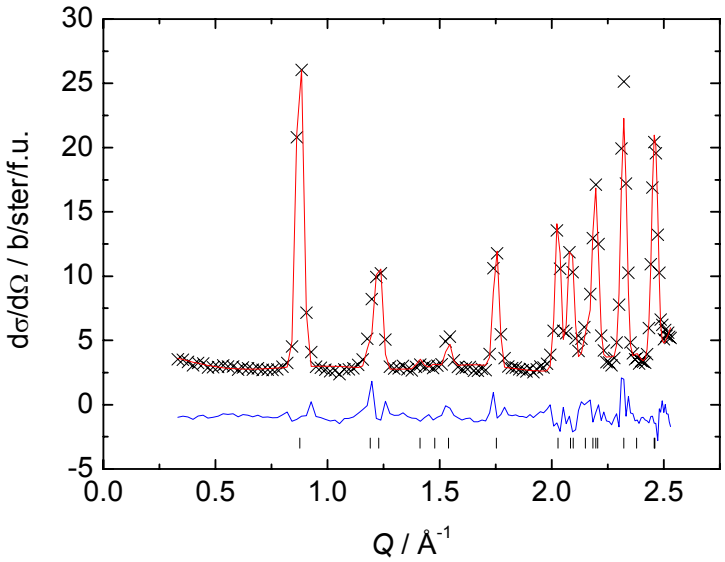

Figure 6.15: Plot showing the measured intensity (black crosses), calculated intensity (red line, upper) and difference (blue line, lower) from the Rietveld refinement of the nuclear scattering from volborthite sample V2.

6.3.5.1.3 Sample Synthesis – Sample V3

In order to remove any water adsorbed onto the surface of the sample, sample V2 (2 g) was heated at 90 °C for two hours under vacuum to yield sample V3.

6.3.5.1.4 Results – Sample V3

The level of spin incoherent scattering in sample V3 (see figure 6.16) corresponds to ~ 2.5 H per formula unit (or 40 %), showing that the overall H level has been lowered by heating under vacuum.

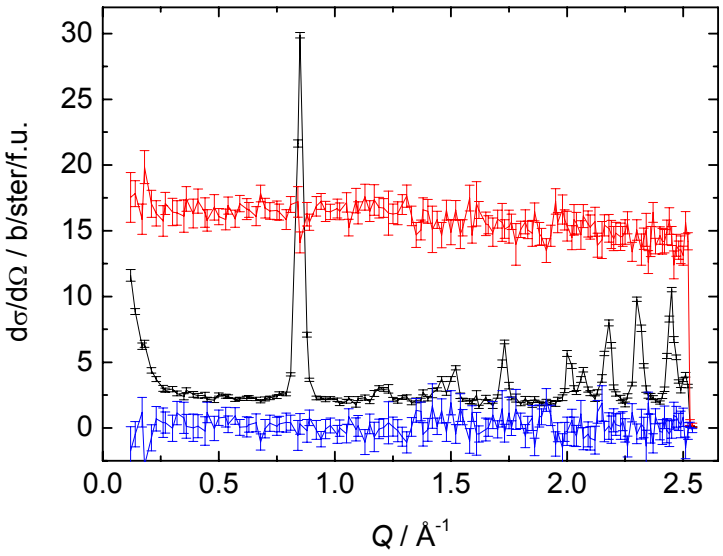

Figure 6.16: Nuclear (black, middle), spin incoherent (red, upper) and magnetic (blue, lower) scattering from volborthite sample V3.

A Rietveld refinement (shown in figure 6.17) of the nuclear scattering from sample V3 gave hydrogen levels of: H1 = 61(5) % and H2 = 47(8) %. Although the overall level of hydrogen in the sample was lowered, the amount on the crystallographic sites has increased. One explanation for this could be that heating has provided the driving force for the protons in any adsorbed water to exchange with deuterium atoms in the structure.

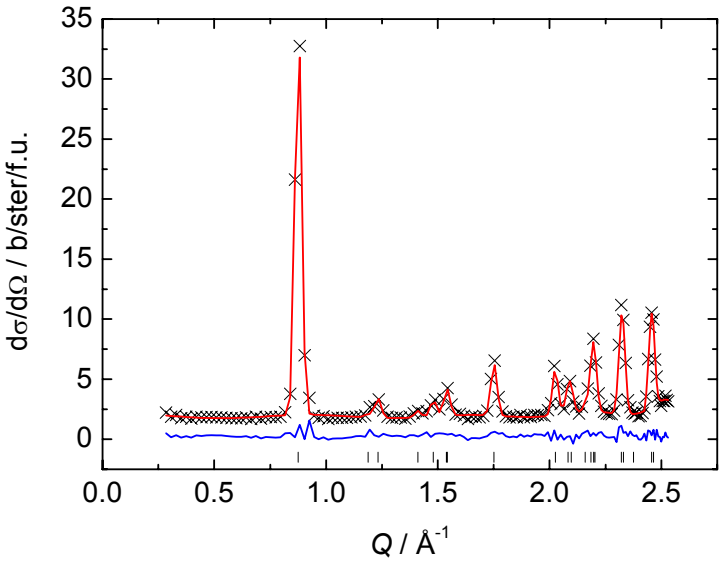

Figure 6.17: Plot showing the measured intensity (black crosses), calculated intensity (red line, upper) and difference (blue line, lower) from the Rietveld refinement of the nuclear scattering from volborthite sample V3.

6.3.5.1.5 Sample Synthesis – Sample V4

In order to increase the deuterium content of the sample, sample V3 (5 g) was heated under reflux in D_2O (100 ml) under a nitrogen stream for 16 hours. Most of the excess D_2O was removed by filtration, and then the resulting slurry was dried in a vacuum oven at 95 °C over three hours before being left to cool under vacuum over a period of five hours, yielding sample V4.

6.3.5.1.6 Results – Sample V4

The level of spin incoherent scattering in sample V4 (see figure 6.18) shows that the hydrogen level in this sample has been reduced to a level of 0.1 H per formula unit (or 2 %).

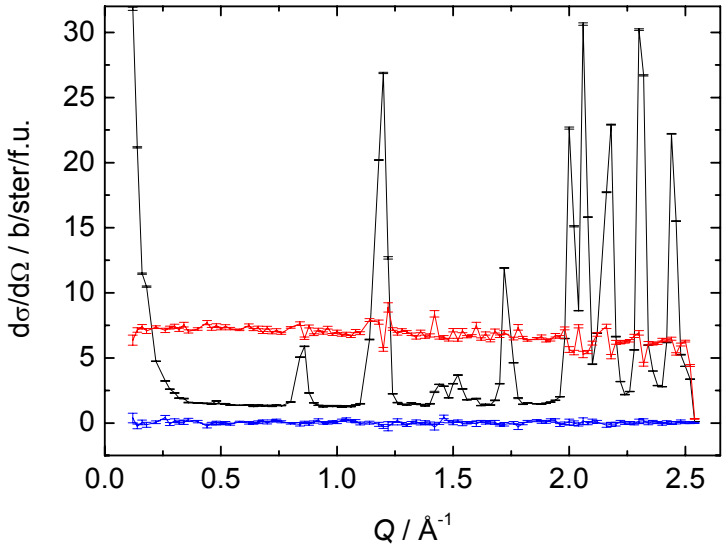

Figure 6.18: Nuclear (black, middle), spin incoherent (red, upper) and magnetic (blue, lower) scattering from volborthite sample V4.

A Rietveld refinement (see figure 6.19) of the nuclear scattering also showed that within the error of the refinement, the sample was 100 % deuterated on each of the crystallographic sites (H1 = - 6(4) % and H2 = 1(2) %).

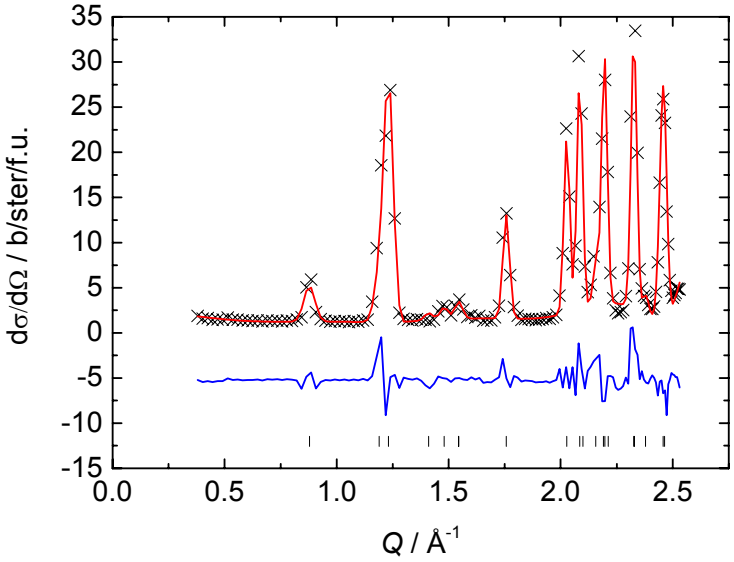

Figure 6.19: Plot showing the measured intensity (black crosses), calculated intensity (red line, upper) and difference (blue line, lower) from the Rietveld refinement of the nuclear scattering from volborthite sample V4.

6.3.5.2 Second D7 Experiment

As the first experiment on D7 gave very little information about the magnetism in volborthite in the allocated experimental time, due to the redeuteration attempts, a second experiment was performed. The information on sample deuteration learned during the first experiment was put into practice in order to make a sample with a higher level of deuteration for this second experiment.

6.3.5.2.1 Sample Synthesis – Sample V5

Samples V6 and V7 (20 g) (see section 6.3.6.2.1) were combined together and divided between four 23 ml PTFE lined stainless steel bombs. The liners were then filled with D_2O and heated at 90 °C overnight. The D_2O was then drained in a closed cabinet, and replaced with fresh D_2O, and the heating process repeated. The D_2O was then removed by filtration in a closed cabinet, and then the sample was dried by heating at 90 °C in a vacuum oven. The oven was flooded with nitrogen before the sample was removed.

6.3.5.2.2 Experimental

The second D7 experiment was run with an incident neutron wavelength of 3.1 Å. 18.21 g of sample V5 was placed in an aluminium sample can, and into a CCR. Measurements were made with *XYZ*-polarisation analysis over a range of temperatures, from base temperature (2.7 K) to 200 K. Each measurement was taken over three detector positions, covering a range of 0.24 – 3.92 $Å^{-1}$ in Q, with each temperature taking 24 hours to measure. As the experiment was performed without

time of flight analysis, $S(Q)$ was integrated over the energy window of the instrument at this wavelength, an integration over the energy range $-20 \leq \omega \leq 8.5$ meV.

6.3.5.2.3 Results

The magnetic contribution of the scattering was separated from the nuclear scattering and the nuclear-spin-incoherent scattering using *XYZ*-polarisation analysis. A plot showing the relative intensities of these three different scattering cross sections measured at a temperature of 2.7 K is shown in figure 6.20.

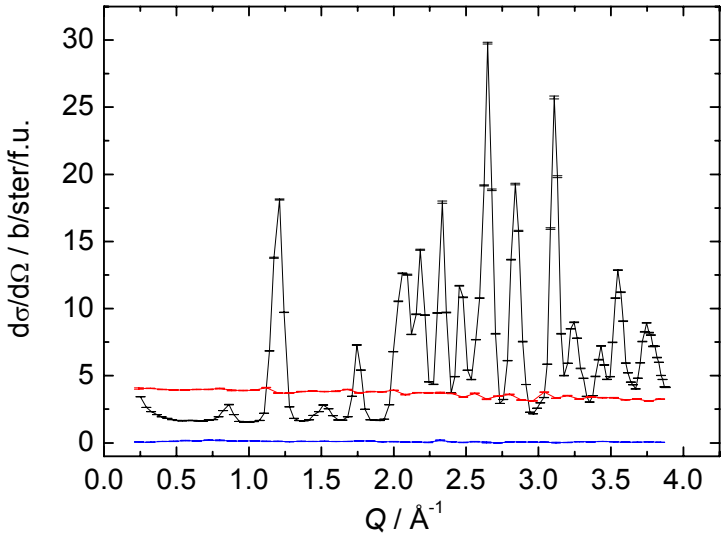

Figure 6.20: Nuclear (black, middle), spin incoherent (red, upper) and magnetic (blue, lower) scattering from volborthite at 2.7 K.

In order to model the nature of the magnetic correlations within volborthite and to quantify the amount of magnetic scattering, the data were fitted to a shell model for the magnitude of magnetic scattering[24, 25], see equation 6.1:

$$\frac{d\sigma}{d\Omega} = 0.049\left(f(Q)\right)^2 g^2 S(S+1)\sum_{i=0}^{n} z_i \frac{\langle S_0.S_i \rangle}{S(S+1)}\left(\frac{\sin\left(Q.r_i\right)}{Q.r_i}\right), \qquad (6.1)$$

where f(Q) is the form factor for the magnetic ions[26] (in the case of volborthite, Cu^{2+}), S is the spin on each magnetic ion, z_i is the number of neighbouring atoms in the ith shell at a distance r_i (in Å) from the central atom and $\langle S_0 \cdot S_i \rangle$ is the correlation between the spin on the central ion and one in the ith shell. For two spins perfectly ferromagnetically aligned, $\langle S_0 \cdot S_i \rangle = 1$, and for perfect antiferromagnetic alignment, $\langle S_0 \cdot S_i \rangle = -1$; $\langle S_0 \cdot S_i \rangle = 0$ when the two spins are lying perpendicular to each other. This function models the relative significance of the magnetic correlations from successive shells of further neighbours. For the fitting, the copper lattice in volborthite was treated as a perfect kagome lattice with a nearest neighbour Cu-Cu distance of 3 Å, and the g-value was fixed at 2. Fits were made over the first three nearest neighbour shells, as fitting over further shells did not improve the quality of the fits. Plots showing these fits to the data can be seen in figure 6.21.

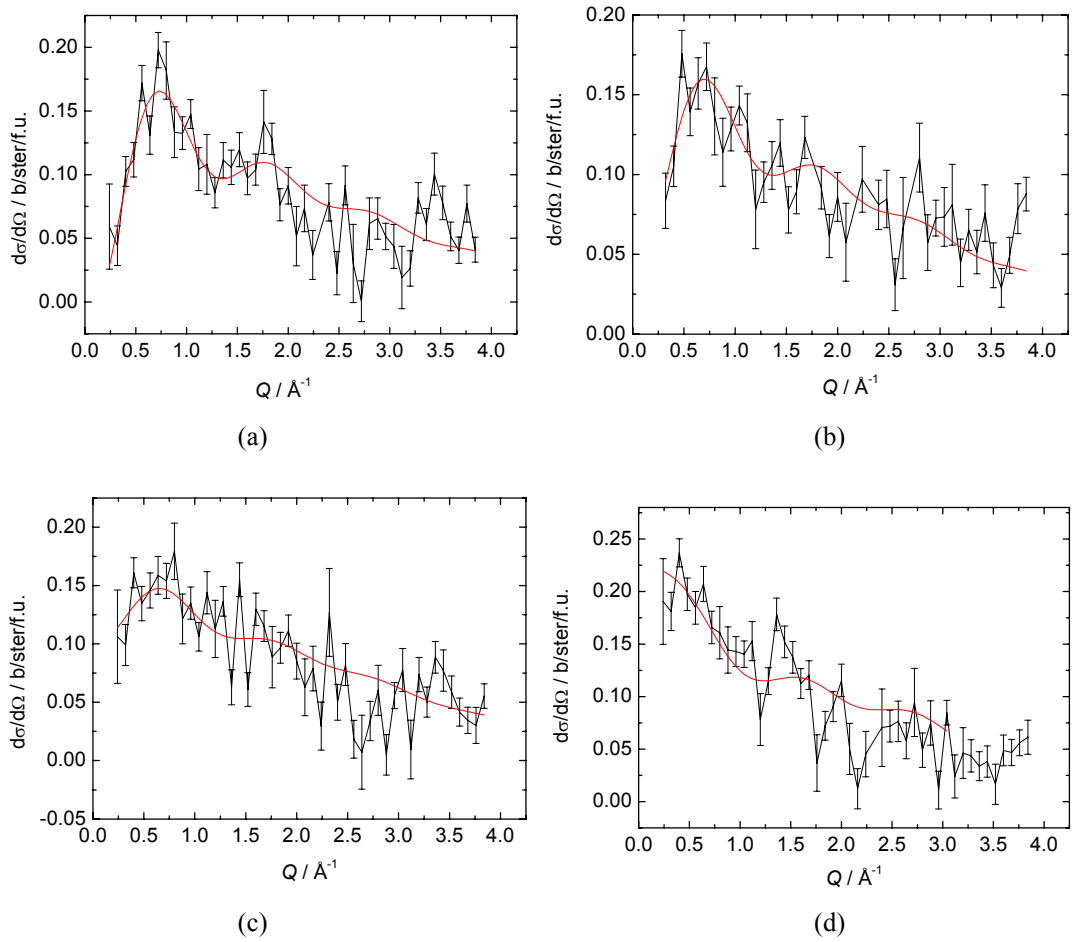

Figure 6.21: Magnetic component of scattering (black) plotted as a function of Q and fit to equation 6.1 (red) for volborthite measured at temperatures: (a) T = 2.7 K, (b) T = 15 K, (c) T = 50 K and (d) T = 200 K.

For each of the temperatures at which measurements were made, the total spin contributing to the magnetic scattering was found to be around 0.5 per formula unit. This is the value of S expected for each copper ion, of which there are three per formula unit, thus implying that a significant amount of the magnetic scattering from volborthite is found outside the energy window of D7 in this experimental configuration. The energy range over which the scattering is integrated covers the range $-20 \leq \omega \leq 8.5$ meV, and the shape of the window in Q and ω is shown below (figure 6.22).

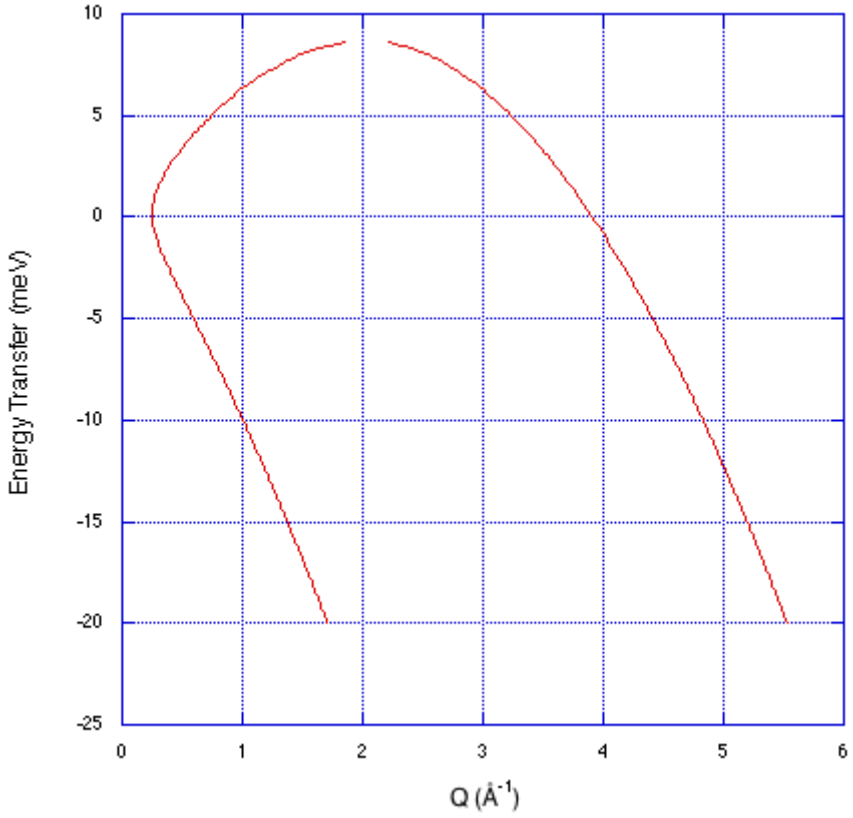

Figure 6.22: The window in Q and ω of D7 for an incident neutron wavelength of λ = 3.05 Å. Integrations in energy are performed over the area on the inside of the red lines.

The temperature and distance dependence of the different correlation parameters are shown in figures 6.23 and 6.24 respectively.

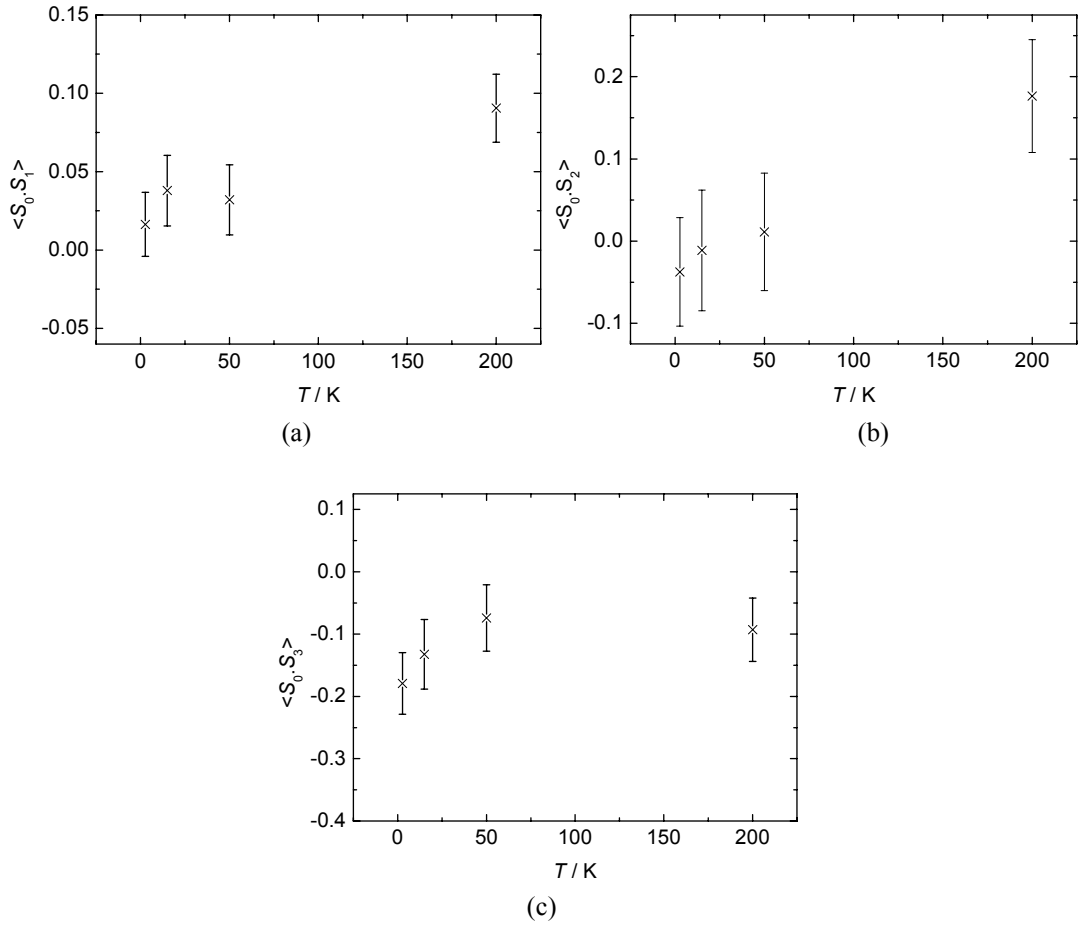

Figure 6.23: Temperature dependence of the spin correlation parameters (a) $\langle S_0 \cdot S_1 \rangle$, (b) $\langle S_0 \cdot S_2 \rangle$ and (c) $\langle S_0 \cdot S_3 \rangle$ obtained from fits to equation 6.1.

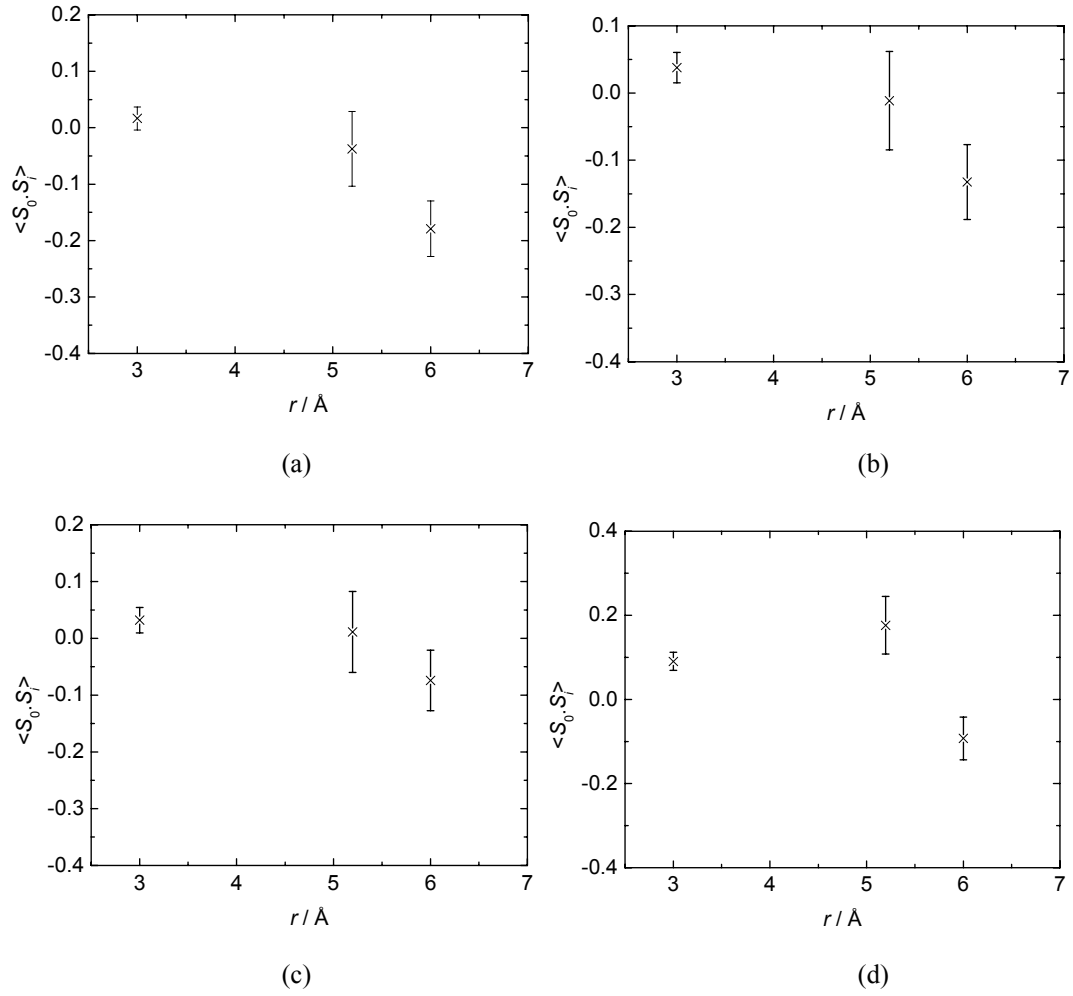

Figure 6.24: Distance dependence of the spin correlation parameters $\langle S_0 \cdot S_i \rangle$ obtained from fits to equation 6.1 for data measured at temperatures: (a) $T = 2.7$ K, (b) $T = 15$ K, (c) $T = 50$ K and (d) $T = 200$ K.

It can be seen that at all temperatures the dominant correlation is between the third nearest neighbours, which is at a distance of 6 Å. This correlation is weakly antiferromagnetic in character, becoming even weaker with increasing temperature. The nearest neighbour correlation is negligible at low temperature which is compatible with either there being no correlation between individual spins, or with the spins lying approximately perpendicular to each other. As the temperature is increased, this correlation becomes slightly more ferromagnetic in character. The second nearest neighbour correlation is negligible at all temperatures apart from at

200 K, where it is slightly ferromagnetic in character. Further discussion of these results can be found in section 6.4.

6.3.6 Time of Flight Inelastic Neutron Scattering

In order to investigate the nature of any spin gap in volborthite, time of flight inelastic neutron scattering experiments were carried out. Initially an experiment was carried out on the time of flight spectrometer, DCS, at the National Institute for Standards and Technology (NIST) Center for Neutron Research, in order to investigate the energy scales at which further investigations should be concentrated. Two further experiments were then carried out on higher flux instruments, IN4 at the ILL and MARI at ISIS, in order to investigate in further depth any magnetic scattering. Improvements in the sample synthesis meant that the quality of the samples progressed with each experiment performed.

6.3.6.1 DCS at NIST

A powder sample of volborthite was measured by collaborators, Jason Gardner and Georg Ehlers, on the time of flight spectrometer, DCS, at NIST to provide a preliminary map of $S(Q,\omega)$. The sample used was V2, whose synthesis is described in section 6.3.4.1. DCS is a cold neutron, disc chopper spectrometer, and is shown schematically in figure 6.25. After the fast neutrons from the beam have been removed by the "optical filter" design of the neutron guide (no direct line of sight to the cold neutron source), and further by a cooled pyrolytic graphite filter, a pulsed, monochromatic beam of neutrons is produced by a 9 m long system of seven disc

choppers. After the neutrons have been scattered by the sample, they are detected by an array of 913 ^{3}He detectors covering angles of -30° to -5° and 5° to 140° at a distance of 4 m from the sample.

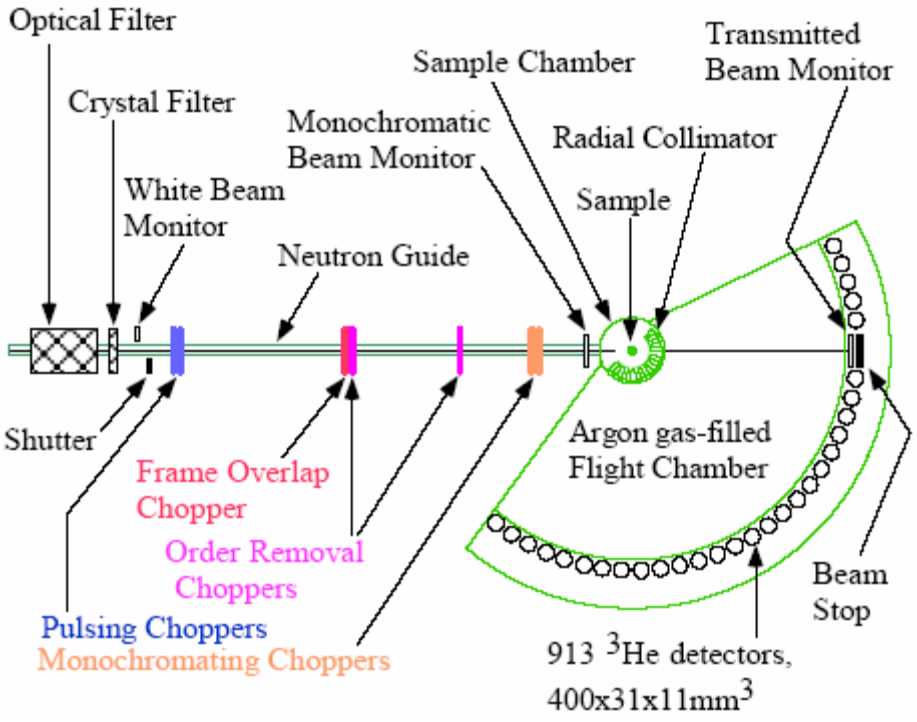

Figure 6.25: Schematic diagram showing the layout of the DCS spectrometer at NIST taken from reference [27].

Initially, measurements were made at an incident neutron wavelength of 2.4 Å (an incident energy of 14.2 meV), in order to survey $S(Q, \omega)$. This was carried out at two temperatures, 2 K and 50 K. A subtraction was made of the high temperature data from the low temperature data, shown in figure 6.26, revealing a feature lying at around 5 meV, with higher intensity at low values of Q.

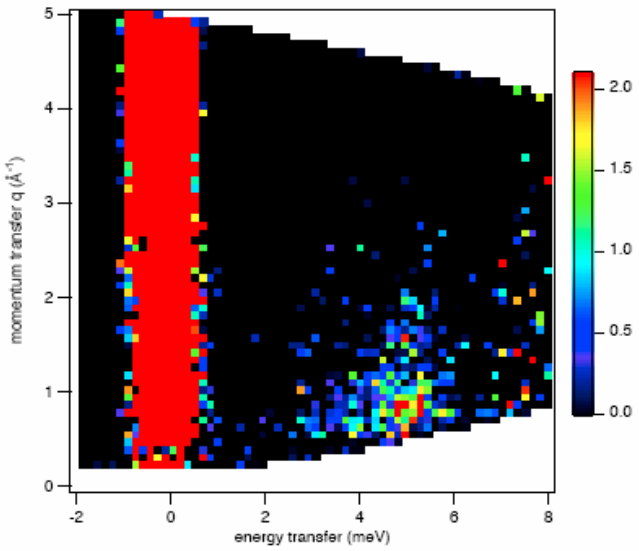

Figure 6.26: Difference between $S(Q,\omega)$ measured in volborthite at 2 K and 50 K, with the intensity scale shown in arbitrary units.

The incident neutron wavelength was then increased to 6 Å (≡ 2.27 meV), and $S(Q, \omega)$ measured at a range of temperatures, in order for the quasielastic signal to be probed. A subtraction of the low temperature (2 K) dataset from datasets measured at higher temperatures (*e.g.* 105 K) reveal that the width of the quasielastic scattering increases with increasing Q as shown in figure 6.27.

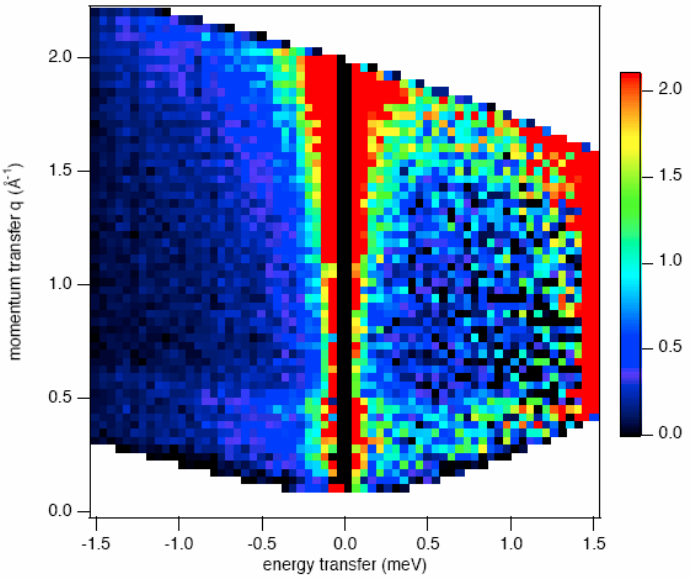

Figure 6.27: Difference between $S(Q,\omega)$ measured in volborthite at 105 K and 2 K with the intensity scale shown in arbitrary units.

At this incident wavelength, cuts were also taken through the elastic line at a variety of temperatures, in order to assess the sample quality. These are shown in figure 6.28. The relative sizes of the peaks in the elastic line (*c.f.* figures 6.29 (b) & (c)) show that, although the sample is of a high crystallinity, the level of deuteration is not significant. No evidence of magnetic ordering, in the form of additional Bragg peaks at low temperature, was found.

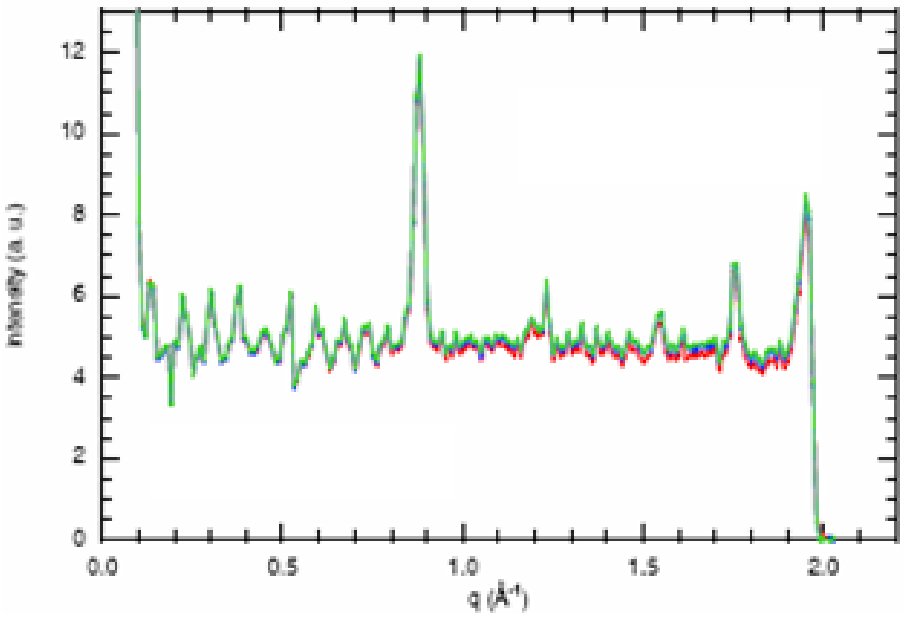

Figure 6.28: Integration over the elastic line in volborthite over the range $-0.3 \leq \omega \leq 0.3$ meV at $T = 1.5$ K (green), $T = 60$ K (blue) and $T = 120$ K (red).

6.3.6.2 IN4 at the ILL

In order to further investigate the excitation observed at NIST, a sample of volborthite was measured on the higher flux time of flight spectrometer, IN4, at the ILL. Further details of the IN4 spectrometer can be found in chapter 5.

6.3.6.2.1 Sample Syntheses

Two sample preparation methods were employed for this experiment. The reasons for this were two-fold; a fault occurred during the first synthesis which meant that the sample quality could not be guaranteed. A second synthesis was then carried out, but due to time constraints, the sample could not be reboiled in D_2O (a step ascertained to be important to maximise the sample quality) before the neutron experiment. The quality of both the samples was then assessed on IN4 at the start of the experiment.

6.3.6.2.1.1 Synthesis of 'Deuterated' Volborthite – Sample V6

Copper (II) oxide (2.390 g, 30.0 mmol, Lancaster, 99 %) was dissolved in D_2SO_4 (2.02 ml, Aldrich, 98 %) and D_2O (79 ml, Aldrich, 99.9 atom % D) at 40 °C under a flow of nitrogen. V_2O_5 (1.815 g, 10.0 mmol, Acros Organics, 99.6 %) was then added to this solution, and dissolved at 40 °C. After dissolution had occurred, the pH of the solution was increased to 5.4 by the addition of NaOD (Aldrich, 99 + atm % D) solution in D_2O (~ 1 M). The temperature was then increased to 95 °C, and the pale green suspension was stirred at this temperature for a period of 42 hours under a nitrogen flow, which was interrupted for a period due to a technical fault. The D_2O was then removed by filtration and replaced with fresh D_2O, and sample V2 was added. The resulting suspension was heated at 95 °C with stirring under a nitrogen flow for 24 hours. The sample was then washed with D_2O, filtered and dried at room temperature under vacuum.

6.3.6.2.1.2 Synthesis of 'Deuterated' Volborthite – Sample V7

Copper (II) oxide (2.390 g, 30.0 mmol, Lancaster, 99 %) was dissolved in D_2SO_4 (2.02 ml, Aldrich, 98 %) and D_2O (79 ml, Aldrich, 99.9 atom % D) at 40 °C under a flow of nitrogen. V_2O_5 (1.815 g, 10.0 mmol, Acros Organics, 99.6 %) was then added to this solution, and dissolved at 40 °C. After dissolution had occurred, the pH of the solution was increased to 5.4 by the addition of NaOD (Aldrich, 99 + atm. % D) solution in D_2O (~ 1 M). The temperature was then increased to 95 °C, and the pale green suspension was stirred at this temperature for a period of 42 hours under a nitrogen flow. The resulting green powder was then washed with D_2O, filtered, and dried at room temperature under vacuum.

6.3.6.2.2 Experimental

Initially 12.10 g of sample V6 was placed into a 15 mm diameter aluminium sample can. Using an incident neutron wavelength of 2.2 Å, $S(Q, \omega)$ of this sample was measured at a temperature of 1.5 K. An integration over the elastic line, from -0.5 meV to 0.5 meV, was made in order to obtain a measure of the level of deuteration in the sample, this is shown in figure 6.29. The sample was then replaced with 7.00 g of sample V7; this was measured at 1.5 K with a similar experimental configuration, and the elastic line examined. By inspection of the relative intensities of the (0 0 1) (Q = 0.87 Å^{-1}) and (1 1 0) (Q = 1.23 Å^{-1}) reflections and comparison with neutron powder diffraction intensities simulated in GSAS[23] for fully deuterated and fully protonated volborthite, it was qualitatively determined that the level of deuteration in sample V6 was higher. 12.85 g of sample V6 was

reloaded into the sample can. $S(Q, \omega)$ was measured as a function of temperature for three different temperatures; 1.5 K, 15 K and 50 K for 16 hours per temperature.

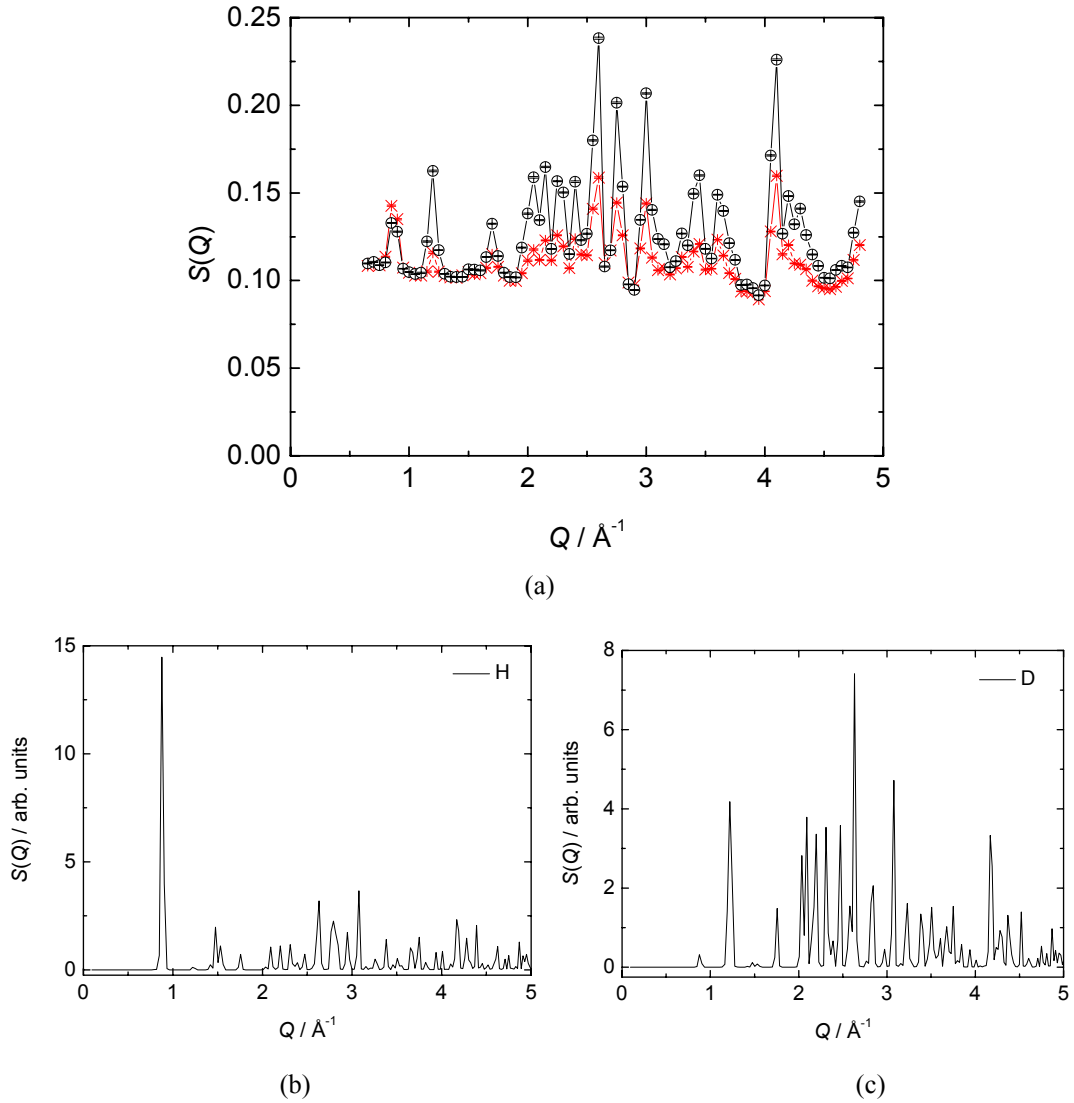

Figure 6.29: (a) Integration over the elastic line in two volborthite samples: V6 (black circles) and V7 (red crosses) over the range $-0.5 \leq \omega \leq 0.5$ meV and simulated diffraction patterns for (b) fully hydrogenated and (c) fully deuterated volborthite.

6.3.6.2.3 Results

The $S(Q,\omega)$ data have been converted into $\chi''(Q,\omega)$ by application of the detailed balance condition for $\omega > 0$:

$$S(Q,\omega) = \frac{1}{1-\exp(-\hbar\omega / k_B T)} \chi''(Q,\omega). \tag{6.2}$$

Plots of χ"(Q,ω) are shown for the three temperatures measured, in figure 6.30.

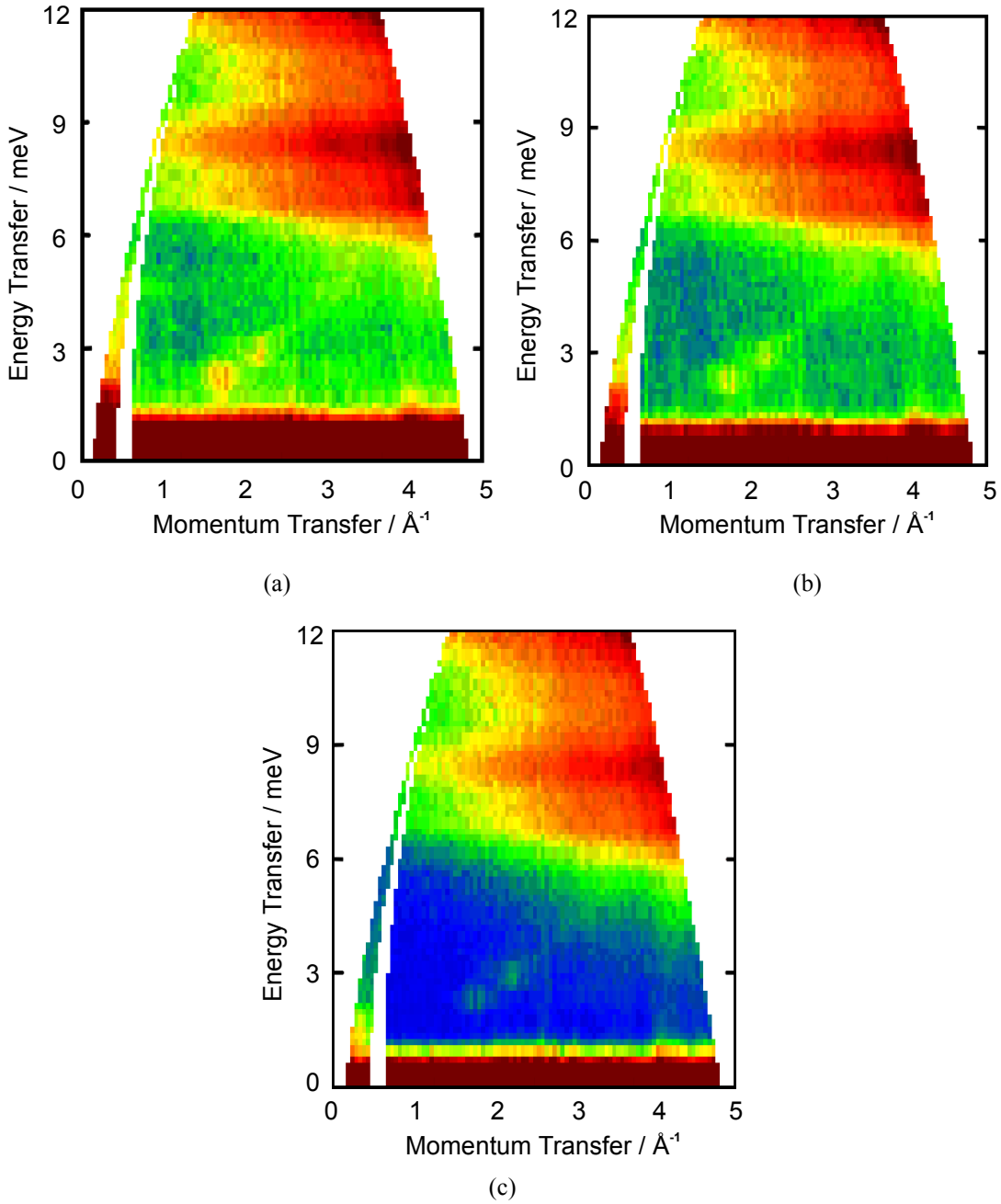

Figure 6.30: χ"(Q,ω) measured in volborthite on the IN4 spectrometer at temperatures (a) T = 5 K, (b) T = 15 K, (c) T = 50 K.

At low temperature (1.5 K), a sharp excitation is observed at ~ 4.5 meV with a width of approximately 1.5 meV. This excitation is non dispersive, but its intensity decreases with increasing Q (see also figure 6.33), implying that this is a magnetic excitation. At 15 K, there is still an excitation at the same energy, but the intensity is much lower. $S(Q,\omega)$ was integrated along the momentum transfer axis over the range $0.8 \leq Q \leq 1.0$ Å^{-1}, and plotted as a function of energy transfer for the three temperatures; this is shown in figure 6.31.

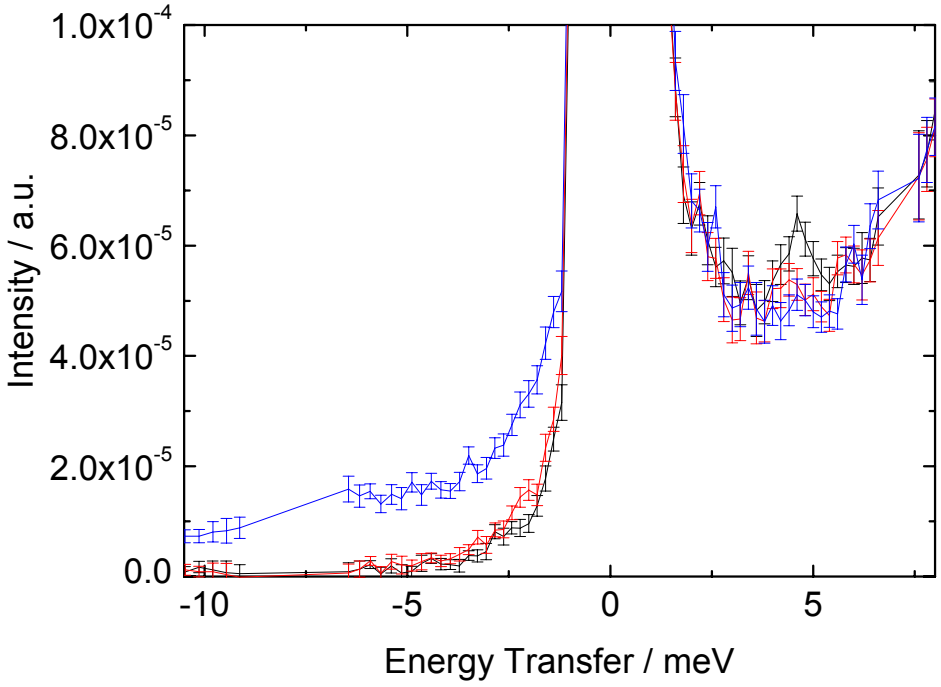

Figure 6.31: $S(Q,\omega)$ integrated over the Q range $0.8 \leq Q \leq 1.0$ Å^{-1} measured in volborthite on the IN4 spectrometer at temperatures $T = 5$ K (black), $T = 15$ K (red), $T = 50$ K (blue).

On subtracting the higher temperature (50 K) data from the lower temperature (5 K) data, the excitation is also seen in the neutron energy gain side of the spectra, at both 1.5 K and 15 K. This is seen most distinctly in subtractions of two $S(Q,\omega)$ plots; the plots resulting from the subtraction of the 50 K dataset from both the 1.5 K and 15 K datasets are shown in figure 6.32.

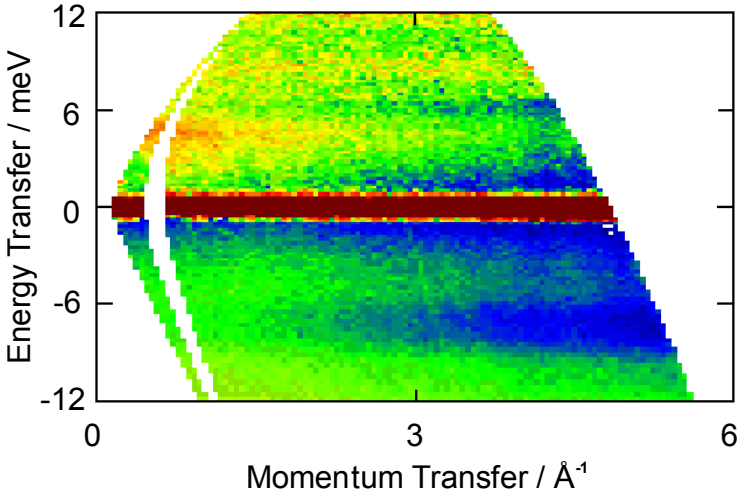

(a)

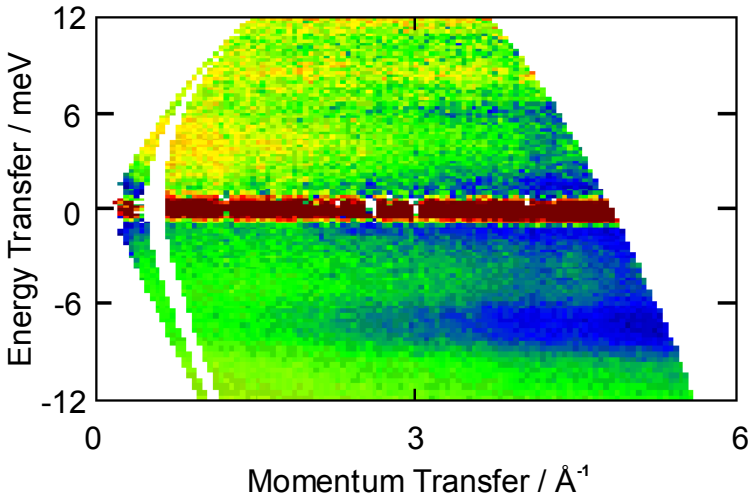

(b)

Figure 6.32: Subtractions of two $S(Q,\omega)$ plots measured at different temperatures of volborthite on IN4 (a) 5 K minus 50 K and (b) 15 K minus 50 K.

After subtraction of the data measured at 50 K from that measured at 1.5 K, an integration was made over the energy transfer range of 4.4 meV $\leq \omega \leq$ 4.8 meV (see figure 6.33). This shows that the intensity of the excitation decreases with increasing Q in accordance with the Cu^{2+} form factor squared, which implies the absence of any magnetic correlations.

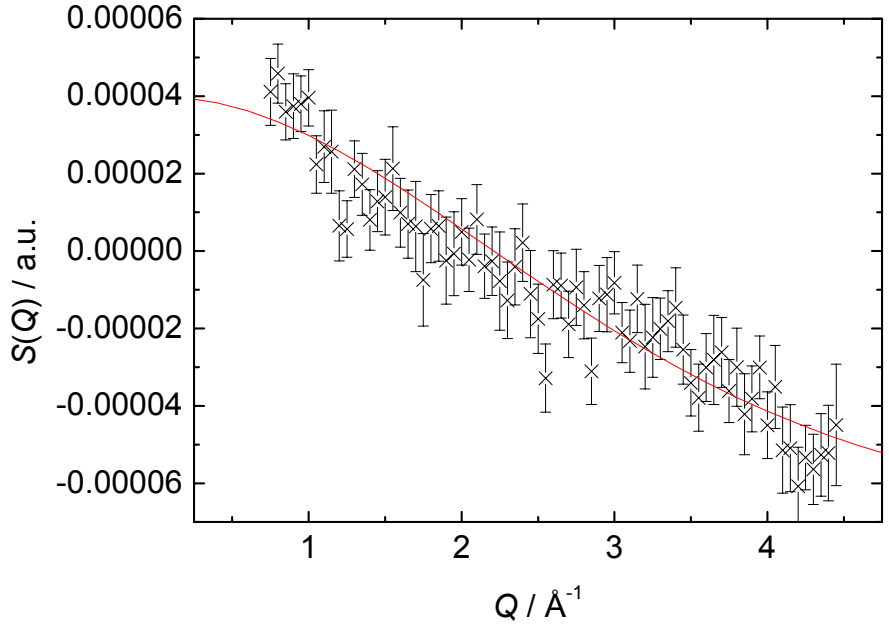

Figure 6.33: $S(Q,\omega)$ at 1.5 K minus $S(Q,\omega)$ at 50 K integrated over the energy transfer range $4.4 \leq \omega \leq 4.8$ meV measured in volborthite on the IN4 spectrometer (black crosses) and a fit to the Cu^{2+} form factor (red line).

6.3.6.3 MARI at ISIS

MARI is a direct geometry time of flight chopper spectrometer at the pulsed neutron spallation source, ISIS. Further details of this instrument can be found in chapter 5. For this experiment, the 'sloppy chopper' was used for all but the lowest temperature measurement. The sloppy chopper is optimised for use over a wide range of frequencies, but has poorer resolution – achieved by having wide slits. For the lowest temperature measurement, a gadolinium chopper was used, which is optimised for low incident energies (< 200 meV), and therefore leads to better resolution than the sloppy chopper at these incident energies.

6.3.6.3.1 Synthesis of Fully Deuterated Volborthite, $Cu_3V_2O_7(OD)_2 \cdot 2D_2O$ – Sample V8

Samples of both fully hydrogenated and partially deuterated volborthite (50 g) synthesised previously by a number of different methods (samples V1 – V7), were placed into a 125 ml capacity PTFE-lined container within a stainless steel bomb. The remaining space in the liner was then filled with D_2O (Aldrich, 99.9 atom % D) (~ 30 ml). The bomb was heated at 95 °C in a furnace for 18 hours. The D_2O was then decanted and replaced with fresh D_2O, and heated again. This process was repeated a further five times. The resulting slurry was placed, with additional D_2O (~ 50 ml), into a silica tube. The D_2O was then removed under vacuum at elevated temperature (< 95 °C) over a period of two days. This process resulted in a fully deuterated product as shown by the MARI experiment.

6.3.6.3.2 Experimental

Initially 21.37 g of volborthite was placed in an aluminium sachet into an aluminium sample can, in an annular configuration. This was placed into a top-loading closed cycle refrigerator (CCR). Whilst cooling to base temperature (4.8 K), the hydrogen recoil line was measured using an incident energy of 700 meV, with a sloppy chopper rotation frequency of 600 Hz. The recoil line shows the Q dependence of the energy of a nucleus recoiling from an incident neutron. The energy of the recoil line is found to be proportional to Q^2/m, where m is the mass of the nucleus[28]. Analysis of the recoil line showed that it lay closer to that expected for a deuterium nucleus than that expected for a hydrogen nucleus, showing that the level of H in the

sample was insignificant. Integrations over the elastic line for $-0.5 \leq \omega \leq 0.5$ meV (shown for the dataset measured at 5 K in figure 6.34) also confirm that the level of hydrogen in the sample was negligible.

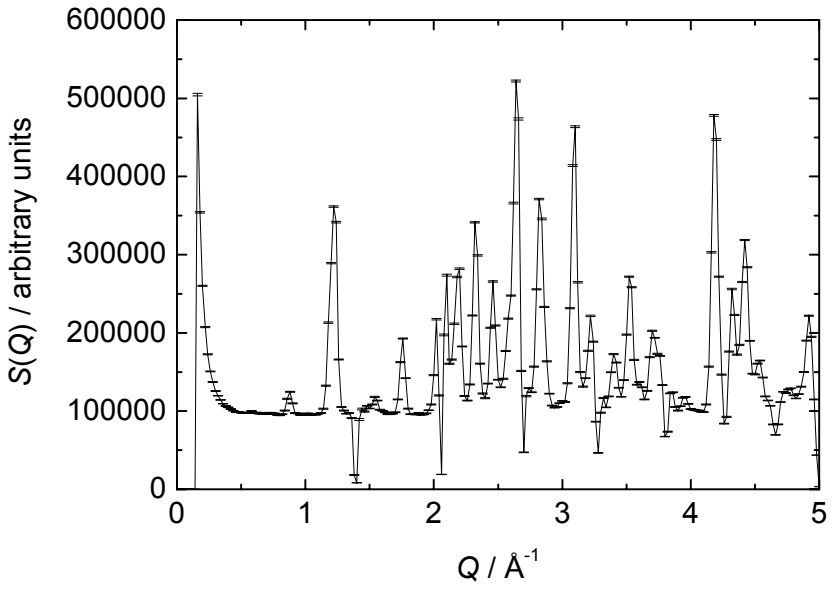

Figure 6.34: Integration of $S(Q,\omega)$ over the elastic line ($-0.5 \leq \omega \leq 0.5$ meV) for volborthite measured at a temperature of 5 K on the MARI spectrometer.

After cooling to 4.8 K, the spectrum was measured using an incident energy of 15 meV and a sloppy chopper frequency of 150 Hz. Additional sample was then added, in another aluminium sachet, to the same sample can, bringing the total sample mass to 48.35 g. Initially, only part of the sample was used in order to minimise multiple scattering, but the remaining sample was added when this was found not to be a problem. $S(Q,\omega)$ was then measured as a function of temperature from 4.8 K to 300 K.

For the lowest temperature measurement, taken at 1.7 K, 49.78 g of powdered volborthite was placed in two aluminium foil sachets into an aluminium sample can. This was then loaded into a top loading CCR containing a low temperature insert.

Using a Gd chopper frequency of 300 Hz, $S(Q,\omega)$ was measured for an incident neutron energy of 15 meV.

6.3.6.3.3 Results

For each of the temperatures measured, $\chi''(Q,\omega)$ was plotted, as shown in figure 6.35.

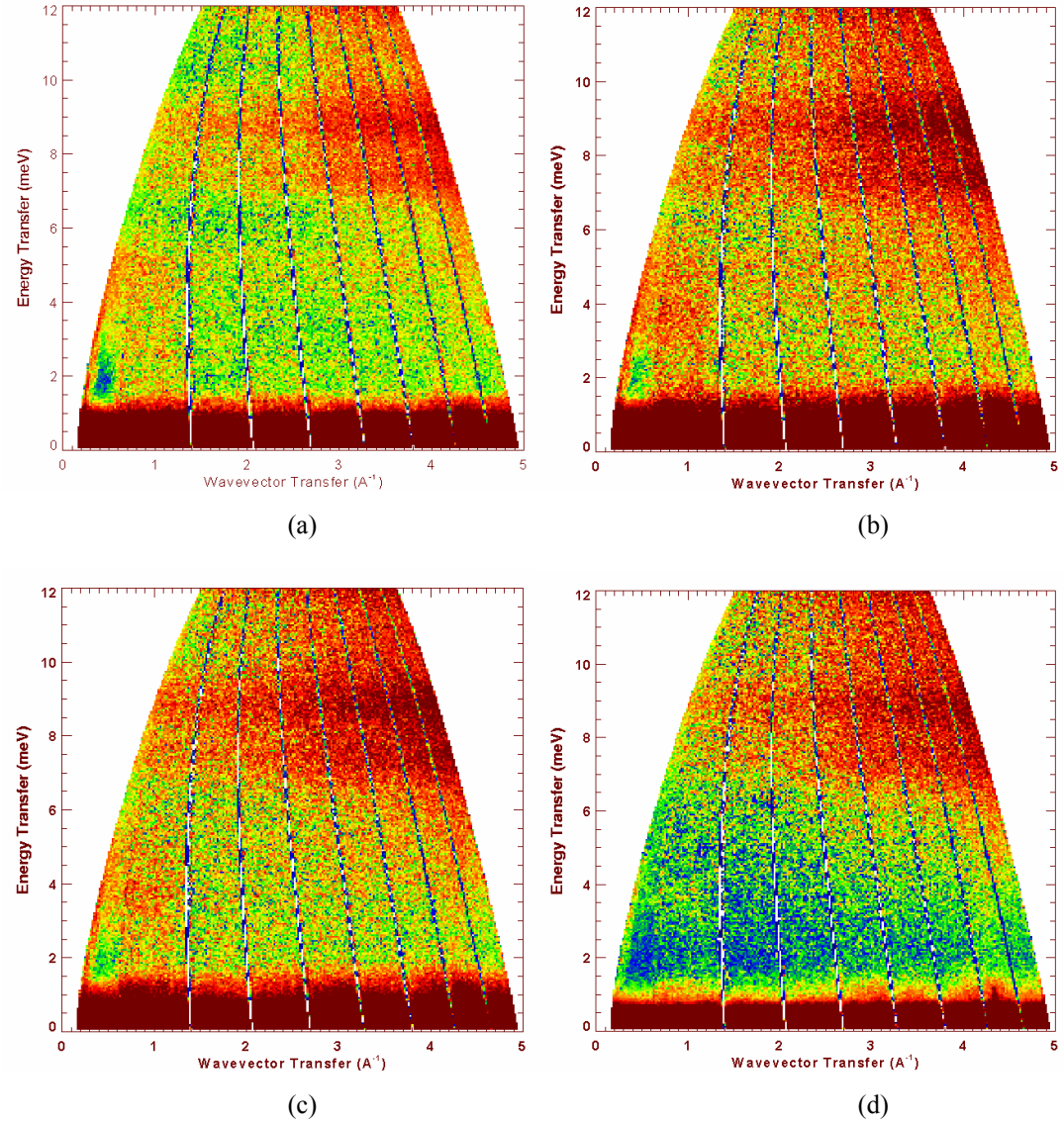

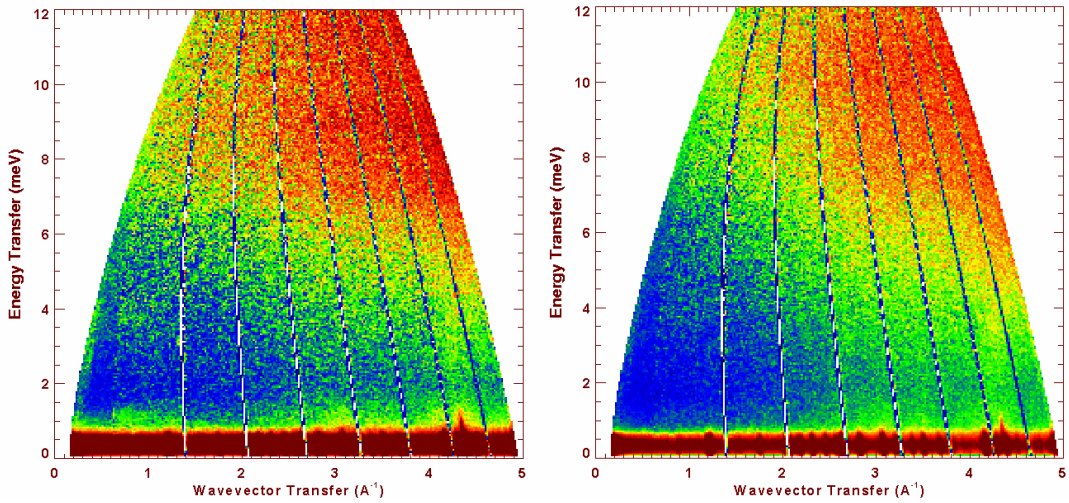

(e) (f)

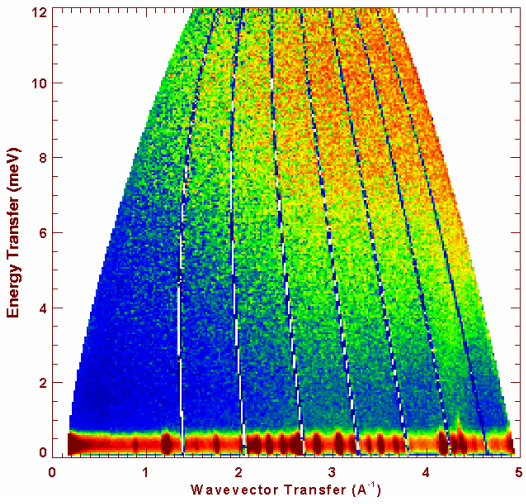

(g)

Figure 6.35: $\chi''(Q,\omega)$ measured in volborthite on the MARI spectrometer at temperatures: (a) 1.7 K, (b) 5 K, (c) 15 K, (d) 50 K, (e) 100 K, (f) 200 K and (g) 300 K.

Cuts through the low Q region, $0.7 \leq Q \leq 1.2$ Å^{-1}, of the plots of $S(Q,\omega)$ (shown in figure 6.36) reveal two features at low energy transfers: one at an energy of around 3 meV and another closer to 5 meV. The feature at lower energy is temperature independent. As the temperature scale of the subtracted spectra is of the same order as J in this system, we would expect any magnetic features to exhibit temperature dependence. Therefore, we conclude that this mode is non-magnetic in origin. As this mode has not been observed in experiments on samples with lower levels of

deuteration, one possibility is that this is due to a framework vibration – any hydrogen in the sample would obscure this type of mode.

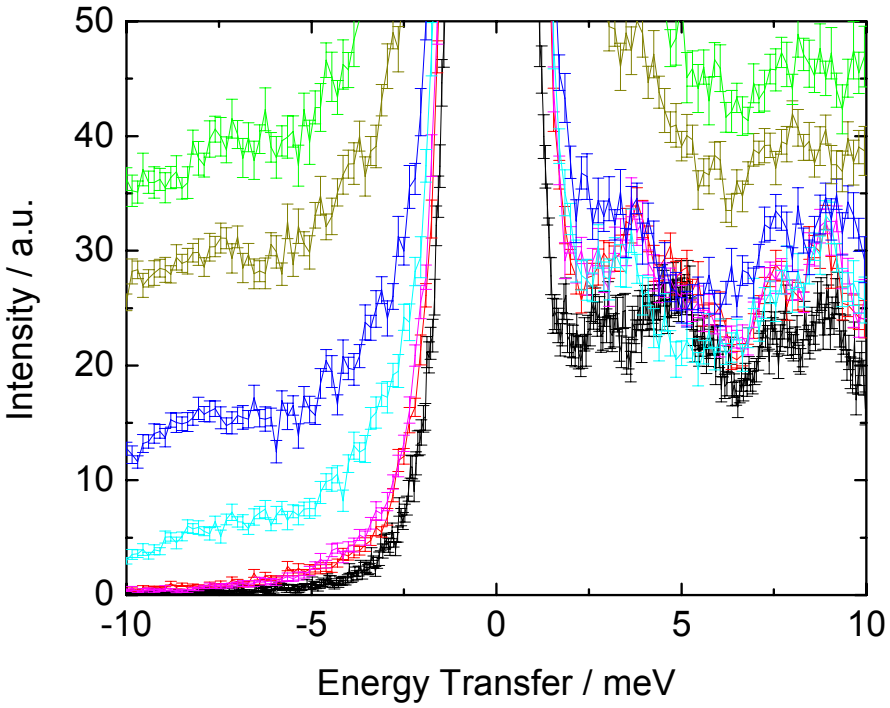

Figure 6.36: $S(Q,\omega)$ integrated over the Q range $0.7 \leq Q \leq 1.2$ Å^{-1} measured in volborthite on the MARI spectrometer at temperatures $T = 1.7$ K (black), $T = 5$ K (red), $T = 15$ K (pink), $T = 50$ K (pale blue), $T = 100$ K (dark blue), $T = 200$ K (yellow) and $T = 300$ K (green).

There is a less intense mode present at an energy of ~ 5 meV. This mode is temperature dependent, and has also been observed in previous experiments on IN4 at the ILL and DCS at NIST. It is proposed that this is a magnetic feature. One possible explanation is that it corresponds to the energy gap between a non-magnetic, singlet ground state, and a magnetic, triplet excited state. A further feature exhibiting temperature dependence can be observed at 9 meV. The intensity of these two features is found to decrease with increasing Q. This behaviour is consistent with these modes being magnetic in character, as the intensity of such modes would be modulated by the form factor.

6.4 Discussion

The results obtained from the experiments on volborthite reported in this chapter have enabled us to draw up a picture of its magnetic properties. There is no evidence of long range static magnetic order in volborthite even down to temperatures as low as 50 mK. Any long range static magnetic order would manifest itself as magnetic Bragg peaks in the magnetic channel of the spectra measured on D7, as well as the presence of oscillations in the muon decay asymmetry observed in MuSR experiments. This is consistent with predictions made by Lecheminant *et al*.[1] and Schmalfuß *et al*.[6] of no long range order at $T = 0$ in the $S = ½$ Heisenberg kagome antiferromagnet.

Despite there being no onset of long range order in volborthite, there is evidence of a degree of spin freezing at low temperatures. With decreasing temperature, the degree of spin freezing increases. This can be seen from the increase in the proportion of the component of the MuSR signal that can be attributed to the static moment. In the same MuSR experiments, the fluxional moment also appears to increase on cooling. This is likely to be due to an increasing proportion of spins slowing down to relax on the time scale of the muon experiment; any fluxional behaviour occurring over a time scale shorter than 0.176 μs is too rapid to be measured by MuSR in the experimental configuration used. This again would support the idea that with decreasing temperature, the spin dynamics slow down, but that a large proportion remain fluxional down to low temperatures.

The results of the neutron spin echo experiment also support the hypothesis of the system remaining highly fluxional to very low temperatures, but with a slowing down of the spin fluctuations with decreasing temperature. This is shown by the spin-spin correlation time for a Q range of 0.95 – 1.35 $Å^{-1}$ slowing down to a time of 2.6 ps as the temperature is lowered to 50 mK.

The nature of any spin freezing in volborthite was investigated by the diffuse polarised neutron scattering experiments. Although there are no magnetic Bragg peaks observed down to the lowest experimental temperatures, the scattering in the magnetic channel at different temperatures do not follow a simple form factor dependence (which would be expected for non-interacting spins), but exhibit features indicative of the build up of short range spin correlations. When these were fitted to a pairwise correlation model, the dominant interaction was found to be an antiferromagnetic interaction between third-nearest-neighbour spins (or twice the nearest neighbour distance). The fact that the dominant interaction is antiferromagnetic is consistent with the value of θ found in d.c. susceptibility measurements. One possible explanation for the dominant interaction being over a distance of two nearest neighbour distances is that it arises from two spins excited to a triplet state interacting with a neighbouring pair. This is also consistent with the shorter range correlations being more ferromagnetic in character. As the temperature is increased, the interactions all become more ferromagnetic in character. This would be consistent with the singlets being excited into triplet states, and the longer range interactions becoming less significant as the spins gain more thermal energy in comparison with their coupling energy, J.

As a significant proportion of the spin expected in volborthite was not found in the energy range of the D7 spectrometer, it is likely that there is significant population of excited magnetic states, even at the low temperatures measured. This could possibly correspond to the ladder of triplet states predicted in this kind of system. Another possible explanation is that the fluctuations in the singlet ground state are occurring on a timescale faster than can be observed by neutrons.

In the configuration of the D7 spectrometer that was used, it is impossible to tell whether the spin correlations observed in volborthite are from a ground state configuration or that of an excited state. An important experiment to perform in the future would be to perform time of flight analysis on the diffracted neutrons, in order to obtain an $S(Q,\omega)$ map of purely the magnetic scattering. This would give an insight into how the magnetism in volborthite is distributed in energy as well as Q-space.

A degree of insight into how the magnetism is distributed in energy was obtained from the inelastic neutron scattering experiments. The only feature that was observed in the region of momentum and energy transfer space probed, that is likely to be magnetic in nature, is a relatively sharp, dispersionless feature at 5 meV. As the intensity of this feature has a form factor like dependence with Q, and also decreases with increasing temperature, it is highly likely to be magnetic and correspond to the spin gap energy below the triplet excited states. Waldtmann *et al*.[8] predicted that any spin gap would have an energy of $J/20$, which for volborthite would be at an energy of 4.2 K or 0.35 meV. This value is over an

order of magnitude lower than we have found. One possible explanation for this discrepancy is that any calculations have been performed on a perfect kagome lattice. Volborthite has a slight distortion to this ideal lattice, with a nearest neighbour distance, r_1 = 2.93 Å and next nearest neighbour distance, r_2 = 3.03 Å. Although this distortion is small, it may be enough to favour interactions in one direction over the others. In many materials an empirical relationship has been established between J and r, of the form $J \propto r^{-n}$, where n is typically 10[29]. When this relationship is applied to volborthite, the ratio of the coupling constant for the nearest neighbour, J_1, versus the next nearest neighbour, J_2, is found to give $J_1 / J_2 = 1.4$. One way to determine whether this imbalance in exchange within the kagome type lattice is indeed enough to explain the discrepancy between the experimental and theoretical results would be to perform calculations on this slightly distorted lattice. To date, no calculations on this type of distorted kagome lattice have been reported in the literature.

6.5 Conclusions and Further Work

As we have seen through the experiments reported in this chapter, despite the strong antiferromagnetic coupling between spins in volborthite, there is no evidence of any long range magnetic order down to temperatures as low as 50 mK. Instead there is a slowing down of the spin dynamics and a build up of short range correlations. These short range correlations are dominated by an antiferromagnetic interaction over a range of 6 Å, which corresponds to the third-nearest-neighbour correlation. This correlation remains significant up to temperatures as high as 200 K. In order to

investigate these correlations further an interesting experiment to perform in the future would be an *XYZ*-polarised neutron scattering experiment with time of flight analysis. This would enable the magnetic scattering from volborthite to be resolved in both energy and momentum transfer space.

There appears to be a spin gap in volborthite at 5 meV, which is at a much higher energy than that of $J/20$ predicted by theorists. One possible explanation for this is the fact that the volborthite lattice is slightly distorted from the perfect kagome lattice. In order to see whether this is indeed the case, it would be necessary to compare the behaviour of volborthite with calculations performed on the distorted lattice.

Although volborthite is a very interesting system in itself, there are questions as to whether it is a good model for a kagome system due to its lattice distortion. The search for an $S = ½$ kagome system must therefore continue in order for the theories for this type of system to be rigorously tested. The recently synthesised mineral herbertsmithite[10] may well provide such a model and would be a good starting point for further investigations.

6.6 References

[1] Lecheminant, P., Bernu, B., Lhuillier, C., Pierre, L. and Sindzingre, P., *Phys. Rev. B*, 1997, **56**(5): 2521-2529.

[2] Sindzingre, P., Misguich, G., Lhuillier, C., Bernu, B., Pierce, L., Waldtmann, C. *et al.*, *Phys. Rev. Lett.*, 2000, **84**(13): 2953-2956.

[3] Syromyatnikov, A. V. and Maleyev, S. V., *Phys. Rev. B*, 2002, **66**(13): art.-no. 132408.

[4] Zeng, C. and Elser, V., *Phys. Rev. B*, 1995, **51**(13): 8318-8324.

[5] Mila, F., *Phys. Rev. Lett.*, 1998, **81**(11): 2356-9.

[6] Schmalfuss, D., Richter, J. and Ihle, D., *Phys. Rev. B*, 2004, **70**: art. -no. 184412.

[7] Elstner, N. and Young, A. P., *Phys. Rev. B*, 1994, **50**(10): 6871-6.

[8] Waldtmann, C., Everts, H.-U., Bernu, B., Lhuillier, C., Sindzingre, P., Lecheminant, P. *et al.*, *Eur. Phys. J.*, 1998, **2**: 501-507.

[9] Honda, Z., Katsumata, K. and Yamada, K., *J. Phys.-Condes. Matter*, 2002, **14**(38): L625-L629.

[10] Shores, M. P., Nytko, E. A., Bartlett, B. M. and Nocera, D. G., *J. Am. Chem. Soc.*, 2005, **127**: 13462-3.

[11] Strupler, N., *Annales De Chimie France*, 1965, **10**(7-8): 345.

[12] Lafontaine, M. A., Lebail, A. and Ferey, G., *J. Solid State Chem.*, 1990, **85**(2): 220-227.

[13] Hiroi, Z., Hanawa, M., Kobayashi, N., Nohara, M., Takagi, H., Kato, Y. *et al.*, *J. Phys. Soc. Jpn.*, 2001, **70**(11): 3377-3384.

[14] Bert, F., Bono, D., Mendels, P., Ladieu, F., Duc, F., Trombe, J.-C. *et al.*, *Phys. Rev. Lett.*, 2005, **95**: art. -no. 087203.

[15] Bert, F., Bono, D., Mendels, P., Trombe, J.-C., Millet, P., Amato, A. *et al.*, *J. Phys.-Condes. Matter*, 2004, **16**(11): S829-S834.

[16] Fukaya, A., Fudamoto, Y., Gat, I. M., Ito, T., Larkin, M. I., Savici, A. T. *et al.*, *Phys. Rev. Lett.*, 2003, **91**(20): art. no.-207603.

[17] Bert, F., Mendels, P., Bono, D., Olariu, A., Ladieu, F., Trombe, J.-C. *et al.*, *Physica B*, 2006, **374-375**: 134-137.

[18] Carlin, R. L., *Magnetochemistry*, ed. 1986, (Springer-Verlag: Berlin).

[19] Keren, A., *Phys. Rev. B*, 1994, **50**(14): 10039-10042.

[20] http://www.ill.fr/YellowBook/IN11/

[21] Schärpf, O. and Capellmann, H., *Phys. Stat. Sol. (a)*, 1993, **135**: 359 - 379.

[22] http://www.ill.fr/YellowBook/D7/

[23] Larsen, A. C. and von Dreele, R. B., *GSAS General Structure Analysis System*. 1994: University of California.

[24] Rainford, B. D., *Journal De Physique*, 1982, **43**(C-7): 33-43.

[25] Stewart, J. R., Ehlers, G., Wills, A. S., Bramwell, S. T. and Gardner, J. S., *J. Phys.-Condes. Matter*, 2004, **16**(28): L321-L326.

[26] Brown, P. J., in *International Tables of Crystallography C*, 1992, (Kluwer Academic Publishers: Dordrecht).

[27] http://www.ncnr.nist.gov/instruments/dcs/dcs_post.html

[28] Squires, G. L., *Introduction to the Theory of Thermal Neutron Scattering*, ed. 1978, (Cambridge University Press: New York).

[29] Bloch, D., *J. Phys. Chem. Solids*, 1966, **27**: 881-885.

A1 Appendix

Details of the structural refinement of $(5CAP)_2CuBr_4$ performed by Garry McIntyre.

A1.1 Crystal structure at 10 K

Two complete sets of unique structural reflections to $\sin(\theta)/\lambda = 0.40$ Å^{-1} were scanned at 10 K with a wavelength of 2.3604 Å (1134 reflections), as well as one nearly complete set of unique reflections in the range $0.40 = \sin(\theta)/\lambda = 0.61$ Å^{-1} at a wavelength of 1.5318 Å (1152 reflections). Background[1] and Lorentz corrections were applied. Absorption corrections were made by Gaussian integration using the calculated attenuation coefficients $\mu = 0.0528$ and $0.0386\ mm^{-1}$, at 2.3604 and 1.5318 Å respectively, with account taken of the exchange of the labile amine deuterium atoms discussed below, giving a transmission range of 0.851 - 0.952. Averaging over symmetry equivalents gave 523 and 1083 unique reflections at 2.3604 and 1.5318 Å respectively. The reflections h 0 l, l odd, which are systematically absent in space group $C2/c$, all showed small but significant contributions, of similar magnitude to the nearly constant discrepancy between the observed and calculated F^2 of allowed reflections noted in preliminary refinements of the crystal structure. We attributed this to multiple diffraction, which we could correct by subtraction of a mildly Q-dependent contribution from all observed F^2[2]. Since the three-dimensional count distribution around each reflection was observed, the centroids of all scanned reflections could be found. Least-squares matching of the observed and calculated coordinates of the centroids of the 707 strongest reflections at 2.3604 Å gave cell parameters a = 12.9032(8) Å, b = 8.7577(6) Å, c = 15.8324(11) Å and $\beta = 94.171(6)°$.

Structure refinements were made using programs based on the Cambridge Crystallographic Subroutine Library[3], with starting coordinates taken from the room-temperature X-ray structure[4]. In all refinements the quantity minimised was $\Sigma w(|F_{obs}| - |F_{calc}|)^2$, using weights according to $w = [\sigma^2(F_{obs}^2)]^{-1}$, where σ^2 was derived

from Poisson counting statistics and the population statistics within each group of equivalent reflections where these existed. Neutron scattering lengths assumed for Cu, Br, Cl, N, C and D were 7.718, 6.79, 9.579, 9.36, 6.648 and 6.674 fm[5]. In preliminary refinements the occupation factors of all D sites were varied to allow for possible exchange with H during or since growth of the crystal. Indeed, this was indicated for the labile sites D(1), D(2a) and D(2b) attached to N atoms, and in later refinements two occupation factors were varied, one for D(1) and a common factor for the chemically equivalent D(2a) and D(2b). The refined occupation factors (0.79 and 0.78) correspond to 14% exchange with H. It was also necessary to model the thermal displacement of all deuterium sites anisotropically, due to the significant libration of these atoms even at 10 K. Several isotropic extinction models within the Becker & Coppens' (1974) formalism[6] were tried. The best agreement between observed and calculated data was for a type-I model with a Lorentzian distribution of mosaic blocks. The most severe extinction correction y, ($|F_{obs,\ corrected}|^2 = y|F_{obs}|^2$), was 0.42. There were 101 variable parameters in the final structural refinement; two scale factors, the angular mosaic width, the positional and thermal displacement parameters for all 27 atoms in the asymmetric unit, and the two site occupation factors for the labile deuterium atoms. The agreement indicators following the final refinement were $R(F) = \Sigma|\Delta|/\Sigma F_{obs} = 0.039$, $wR(F) = (\Sigma w\Delta 2/\Sigma w F_{obs}^2)^{1/2} = 0.031$, and $\chi^2 = \Sigma w\Delta^2/\Sigma(n\text{-}p) = 5.95$, where $\Delta = F_{obs} - |F_{calc}|$, and n and p are the number of observations and number of parameters respectively.

A1.2 Magnetic structure at 1.8 K

A limited survey of reciprocal space at 1.8 K revealed the presence of additional reflections that did not satisfy the *C*-centring operator of the structural space group. The strongest were (0 1 1), (1 0 1) and (0 1 –1), which were about 0.02 % the intensity of the strongest structural reflection, while (1 0 –1) and all reflections with $l = 0$ were unobservable. 56 reflections with $h + k = 2n + 1$ to $\sin(\theta)/\lambda = 0.229$ Å^{-1} were scanned at both 1.8 K and 10 K at the wavelength of 2.3604 Å. To remove the contribution from the small half-wavelength contamination, the integrated intensity of each reflection was obtained by a Gaussian fit to the difference between the ω

projections of corresponding scans at 1.8 K and 10 K. Lorentz and absorption corrections were applied as described above. No correction for multiple scattering was necessary since either the operative reflection or cooperative reflection must also fail to satisfy the *C*-centring operation, and is therefore too weak to lead to a significant multiple-scattering contribution.

	x	*y*	*z*	*g*	U_{eq}
Cu	0	0.0050(2)	0.25		0.0009(4)
Br(1)	0.1384(1)	0.0898(2)	0.3464(1)		0.0022(4)
Br(2)	-0.1055(1)	-0.1085(2)	0.3509(1)		0.0020(4)
Cl	0.0760(1)	0.4096(1)	0.1712(1)		0.0048(3)
N(1)	0.1271(1)	0.2423(1)	-0.0530(1)		0.0033(3)
N(2)	0.1867(1)	0.3381(2)	-0.1770(1)		0.0056(3)
C(1)	0.1602(1)	0.3611(2)	-0.0983(1)		0.0024(4)
C(2)	0.1636(1)	0.5075(2)	-0.0589(1)		0.0025(4)
C(3)	0.1383(1)	0.5221(2)	0.0229(1)		0.0033(4)
C(4)	0.1061(1)	0.3931(2)	0.0679(1)		0.0030(4)
C(5)	0.0996(1)	0.2541(2)	0.0281(1)		0.0035(4)
D(1)	0.1220(2)	0.1359(2)	-0.0812(1)	0.788(8)	
D(2)	0.1862(2)	0.6050(2)	-0.0956(1)		
D(3)	0.1401(2)	0.6329(2)	0.0534(1)		
D(5)	0.0745(2)	0.1501(2)	0.0576(1)		
D(2a)	0.1771(2)	0.2367(3)	-0.2067(1)	0.777(6)	
D(2b)	0.2213(2)	0.4217(3)	-0.2078(1)	0.777(6)	

Table A1: Fractional atomic coordinates, atomic occupation factor (*g*), and equivalent isotropic displacement parameters (Å^2) for $(5CAP)_2CuBr_4$ at 10 K. The occupation factor is used to treat exchange of H for D at the more labile sites. The form of the displacement factor was $\exp(-2\pi^2 \Sigma_i\Sigma_j U_{ij}\mathbf{h}_i\mathbf{h}_j a_i^* a_j^*)$; $U_{eq} = (U_{11} + U_{22} + U_{33})/3$.

	U11	*U22*	*U33*	*U23*	*U12*	*U13*
D(1)	0.0166(15)	0.0051(13)	0.0123(13)	-0.0035(9)	-0.0005(10)	-0.0023(10)
D(2)	0.0228(11)	0.0103(9)	0.0147(9)	0.0023(8)	0.0014(8)	-0.0035(9)
D(3)	0.0212(11)	0.0082(9)	0.0165(9)	-0.0047(8)	0.0000(9)	-0.0011(9)
D(5)	0.0233(11)	0.0101(9)	0.0144(10)	0.0029(8)	0.0028(9)	-0.0053(9)
D(2a)	0.0229(16)	0.0096(13)	0.0156(13)	-0.0073(10)	0.0046(11)	-0.0042(11)
D(2b)	0.0222(15)	0.0134(13)	0.0105(11)	0.0033(10)	0.0053(10)	-0.0047(11)

Table A2: Anisotropic thermal displacement parameters ($Å^2$) for the deuterium sites in $(5CAP)_2CuBr_4$ at 10 K.

$CuBr_4$:

Cu – Br(1)	2.382(2)	Br(1) – Cu – Br(1)^i	143.7(1)
Cu – Br(2)	2.390(2)	Br(1) – Cu – Br(2)	98.0(1)
		Br(2) – Cu – Br(1)^i	97.9(1)
		Br(2) – Cu – Br(2)^i	130.8(2)

5-chloro-2-aminopyridinium:

Cl – C(4)	1.714(2)
N(1) – C(1)	1.351(2)
C(1) – C(2)	1.425(2)
C(2) – C(3)	1.364(2)
C(3) – C(4)	1.415(2)
C(4) – C(5)	1.371(2)
C(5) – N(1)	1.360(2)
N(1) – D(1)	1.033(3)
C(1) – N(2)	1.331(2)
N(2) – D(2a)	1.007(3)
N(2) – D(2b)	1.002(3)
C(2) – D(2)	1.084(3)
C(3) – D(3)	1.084(3)
C(5) – D(5)	1.084(3)

Hydrogen bonds:

D(5) … Br(2)^{i} 2.702(3)	C(5) – D(5) … Br(2)^{i} 153.9(9)
C(5) … Br(2)^{i} 3.707(3)	
D(1) … Br(1)^{ii} 2.302(3)	N(1) – D(1) … Br(1)^{ii} 170(2)
N(1) … Br(1)^{ii} 3.324(2)	
D(2) … Br(2)^{iii} 2.876(3)	C(2) – D(2) … Br(2)^{iii} 117.4(4)
C(2) … Br(2)^{iii} 3.509(2)	
D(2) … Br(1)^{iv} 2.879(3)	C(2) – D(2) … Br(1)^{iv} 147.4(7)
C(2) … Br(1)^{iv} 3.842(2)	
D(3) … Br(2)^{i} 2.779(3)	C(3) – D(3) … Br(2)^{i} 167(2)
C(3) … Br(1)^{i} 3.474(2)	
D(2a) … Br(2)^{v} 2.650(3)	N(2) – D(2a) … Br(2)^{v} 142.9(7)
N(2) … Br(2)^{v} 3.506(2)	
D(2b) … Br(2)^{iii} 2.868(3)	N(2) – D(2b) … Br(2)^{iii} 128.6(6)
N(2) … Br(2)^{iii} 3.580(2)	

Table A3: Selected interatomic distances (Å) and angles (°) for $(5CAP)_2CuBr_4$ at 10 K. Standard deviations are given in parentheses. Superscripts on the atom symbols denote positions equivalent to those given in table A2: (i) –x, y, 1/2 + z; (ii) x, -y, -1/2 – z; (iii) 1/2 + x, 1/2 -y, -1/2 – z; (iv) –x, 1 + y, 1/2 + z; (v) –x, -y, -z.

A1.3 References

[1] Wilkinson, C., Khamis, H. W., Stansfield, R. F. D. and McIntyre, G. J., *J. Appl. Crystallogr.*, 1988, **21**: 471-478.

[2] Luzon, J., Dobe, C. and Barratt, J., *Personal Communication*, 2002.

[3] Matthewman, J. C., Thompson, P. and Brown, P. J., *J. Appl. Crystallogr.*, 1982, **15**(Apr): 167-173.

[4] Woodward, F. M., Albrecht, A. S., Wynn, C. M., Landee, C. P. and Turnbull, M. M., *Phys. Rev. B*, 2002, **65**(14): art. no. 144412.

[5] Sears, V. F., in *Methods of Experimental Physics*, Ed. by: Price, K. S. D. L., 1986, (Academic Press: Orlando). p. 521.

[6] Becker, P. J. and Coppens, P., *Acta Crystallogr. Sect. A*, 1974, **A 30**(Mar): 129-147.

A2 Appendix

A2.1 Publications

F. C. Coomer, V. Bondah-Jagalu, K. J. Grant, A. Harrison, G. J. McIntyre, H. M. Rønnow, R. Feyerherm, T. Wand, M. Meißner, D. Visser and D.F. McMorrow, *'Neutron diffraction studies of magnetic correlations in the S = ½ square Heisenberg antiferromagnets (d6-5CAP)$_2$CuCl$_4$ and (d6-5CAP)$_2$CuBr$_4$'* Submitted to Physical Review B, 2005.

F. C. Coomer, A. Harrison, G. S. Oakley, J. Kulda, J. R. Stewart, J. A. Stride, B. Fåk, J. W. Taylor and D. Visser, *'Inelastic neutron scattering study of magnetic excitations in the kagome antiferromagnet potassium jarosite'. J. Phys.: Condens. Matter* **18**(39) (4 October 2006) 8847-8858.

http://ej.iop.org/links/r1FLVnVzO/hKFoekNj2xG0EgF5av5vpA/cm6_39_015.pdf